Wissenschaftliche Mitteilungen

aus dem
Institut für Meteorologie der Universität Leipzig

ISBN **978-3-9814401-7-1**

Meteorologische Arbeiten (XXIV) und Jahresbericht 2018 des Instituts für Meteorologie der Universität Leipzig

Hrsg.: Armin Raabe, Manfred Wendisch

Leipzig 2019 **Band 57**

Wissenschaftliche Mitteilungen aus dem Institut für Meteorologie der Universität Leipzig Bd. 57 (2019)

Wissenschaftliche Mitteilungen aus dem Institut für Meteorologie der Universität Leipzig Bd. 57 (2019)

Cloud thermodynamic phase detection with the GLORIA limb imager during the StratoClim campaign in the Asian monsoon

Carlsen, T.[1,*], Bartolome Garcia, I.[2], Ehrlich, A.[1], Ungermann, J.[2], Wendisch, M.[1]

[1]) Institute for Meteorology, Stephanstr. 3, 04103 Leipzig, E-Mail: tim.carlsen@geo.uio.no
[2]) Institut für Energie- und Klimaforschung – Stratosphäre (IEK-7), Forschungszentrum Jülich GmbH, Jülich, Germany
[*]) Now at: Department of Geosciences, University of Oslo, Oslo, Norway

Summary: One major source of uncertainty in current climate projections is the effect of clouds on the Earth's climate system due to a direct influence on the radiative energy budget as well as through complex feedback mechanisms. The radiative properties of clouds are governed by their microphysical properties, e.g. the thermodynamic phase. However, the interactions of cloud and aerosol particles leading to complex vertical structures of the thermodynamic phase and their influence on the optical properties of clouds are not yet fully understood. Therefore, measurements with the Gimballed Limb Observer for Radiance Imaging of the Atmosphere (GLORIA) are utilized during the StratoClim (Stratospheric and upper tropospheric processes for better climate predictions) campaign in the Asian monsoon to detect cloud thermodynamic phase in the terrestrial infrared wavelength range for cloud-side observations.

Zusammenfassung: Der Einfluss von Wolken auf das Klimasystem der Erde bildet einen großen Unsicherheitsfaktor in aktuellen Klimaprojektionen durch einen direkten Effekt auf den Strahlungshaushalt sowie über komplexe Feedbackmechanismen. Die Streueigenschaften von Wolken werden durch deren mikrophysikalische Eigenschaften (z.B. die thermodynamische Phase) bestimmt. Allerdings sind die Wechselwirkungen zwischen Wolken- und Aerosolpartikeln, welche zu komplexen vertikalen Strukturen der thermodynamischen Phase führen und damit die optischen Eigenschaften der Wolke beeinflussen, noch nicht endgültig verstanden. Deshalb werden in dieser Studie Messungen mit dem Gimballed Limb Observer for Radiance Imaging of the Atmosphere (GLORIA) während der Messkampagne StratoClim (Stratospheric and upper tropospheric processes for better climate predictions) in der asiatischen Monsunregion verwendet, um die thermodynamische Phase von Wolken aus Wolkenseitenbeobachtungen im terrestrischen infraroten Wellenlängenbereich abzuleiten.

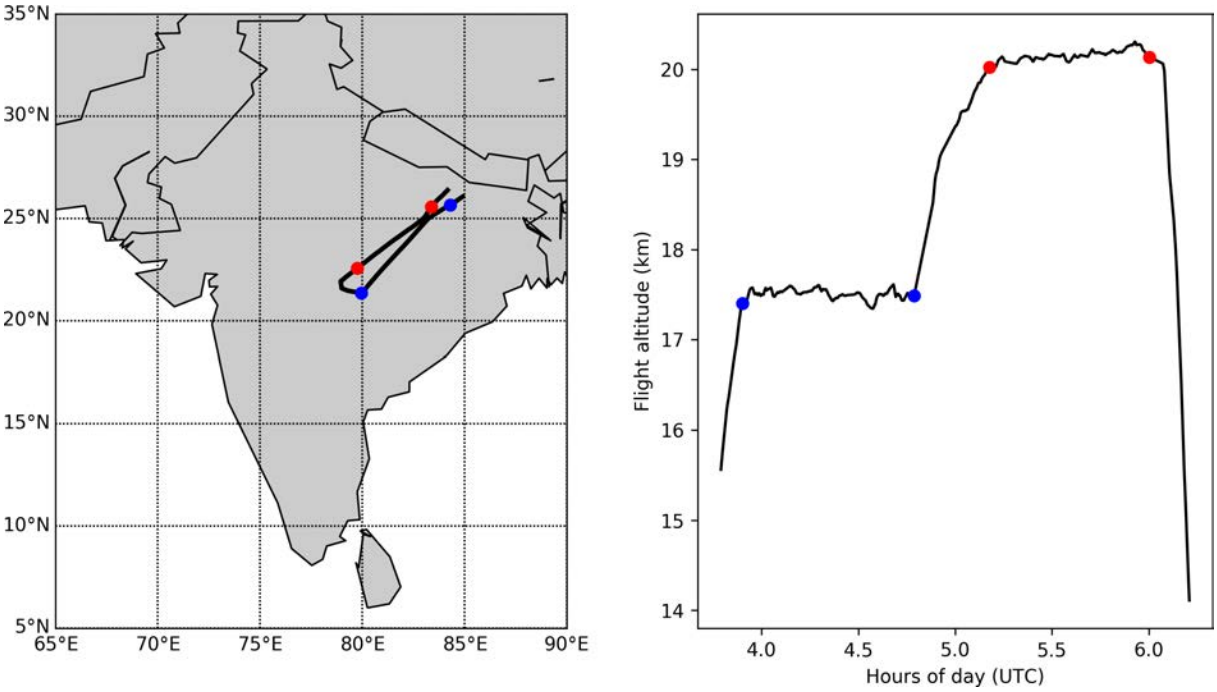

Fig. 1: ***Left:*** *Map of the flight track on 31 July 2017.* ***Right:*** *Corresponding flight altitude. The colored circles correspond to their counterparts on the left image and indicate the relation between temporal and spatial domain.*

1. Introduction

Clouds influence the Earth's climate system by affecting the hydrological cycle, redistributing latent heat, and altering the radiative energy budget. The radiative properties of clouds are governed by their optical, macrophysical (e.g., frequency of occurence, cloud vertical extent), and microphysical (e.g., cloud droplet size distribution, thermodynamic phase) properties. Cloud particles consist of either liquid water, ice, or a mixture of the two. At the microphysical level, the interactions of cloud and aerosol particles lead to highly dynamic systems with respect to phase transitions from liquid water to ice, the depth of the mixed-phase layer, processes of particle growth, the formation of warm and cold rain, and variations in the cloud droplet size distribution. These processes lead to a complex vertical microphysical structure and a variable cloud particle size in particular in deep convective clouds (e.g., Jäkel et al., 2017). The optical properties between liquid water and ice differ and the phase transition is particularly relevant for the formation of precipitation (e.g., Rosenfeld et al., 2008). Consequently, aerosol particles modify the radiative effects (due to the difference in optical properties of liquid water and ice clouds), the lifetime, and the formation of precipitation of the clouds (Twomey, 1977; Albrecht, 1989). These effects cover a wide range of temporal and spatial scales (Rosenfeld et al., 2014). Imaging spectroradiometers provide cloud-side observations for a variety of different viewing angles instantaneously and, thus, are suitable for studying profiles of the microphysical structure of clouds. Jäkel et al. (2017) investigated vertical profiles of particle phase in tropical deep convective clouds exploiting differences in the imaginary part of the refractive index of liquid water and ice in the near-infrared wavelength range. Analogously, the thermodynamic phase can be inferred from the

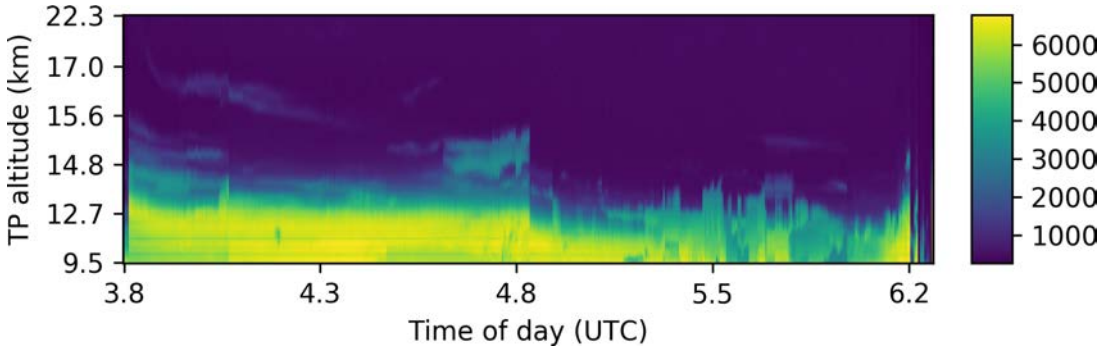

Fig. 2: Radiance profiles along flight track at wavenumber 770 cm^{-1} *in dependence of time of day and the tangent point (TP) altitude as measured by GLORIA on 31 July 2017. The radiance is color-coded in units* $\mathrm{nW\,cm^{-2}\,sr^{-1}\,cm}$.

difference in brightness temperature between 11 and 8.5 $\mu\mathrm{m}$ in the terrestrial infrared wavelength region (e.g., Martins et al., 2011). This was, among others, demonstrated by Chylek et al. (2006) who retrieved the cloud thermodynamic phase using the Moderate Resolution Imaging Spectroradiometer (MODIS) for nadir viewing geometry. Within this study, measurements with the Gimballed Limb Observer for Radiance Imaging of the Atmosphere (GLORIA) are utilized during the StratoClim (Stratospheric and upper tropospheric processes for better climate predictions) campaign in the Asian monsoon to detect cloud thermodynamic phase in the terrestrial infrared wavelength range for cloud-side observations.

2. Measurements and instrumentation

The StratoClim campaign aimed at improving the understanding of key processes in the upper troposphere and lower stratosphere (UTLS) region. It comprised an aircraft campaign in the Asian monsoon based at Kathmandu, Nepal, during July and August 2017 and measurements at a tropical ground station on Palau Island. The airborne instrumentation was installed on the Russian high-altitude aircraft M55 Geophysica. This study focuses on the third research flight on 31 July 2017. The flight track is shown in Fig. 1. The flight covered two main legs over Northeast India in altitudes of 17.5 km and 20 km, respectively.

The GLORIA instrument combines a Fourier transform spectrometer with a 2-D detector array (128×48 pixel) covering the spectral range between 7-13 $\mu\mathrm{m}$ utilizing in-flight calibration with two blackbodies and a 3-axis compensation for aircraft movement. The measured spectral radiance (in units $\mathrm{W\,m^{-2}\,sr^{-1}\,\mu m^{-1}}$) is available as the row average for 127 super pixels for each image. In total, 413 images were taken by GLORIA during the flight.

3. Methodology

Figure 2 shows the measured radiance at wavenumber 770 cm^{-1} in dependence of the time of day and the tangent point (TP) altitude for the research flight on 31 July 2017. In general, the aircraft flew above an optically thick cloud layer emitting the highest radiance values. The GLORIA instrument observed the cloud scene from the side and

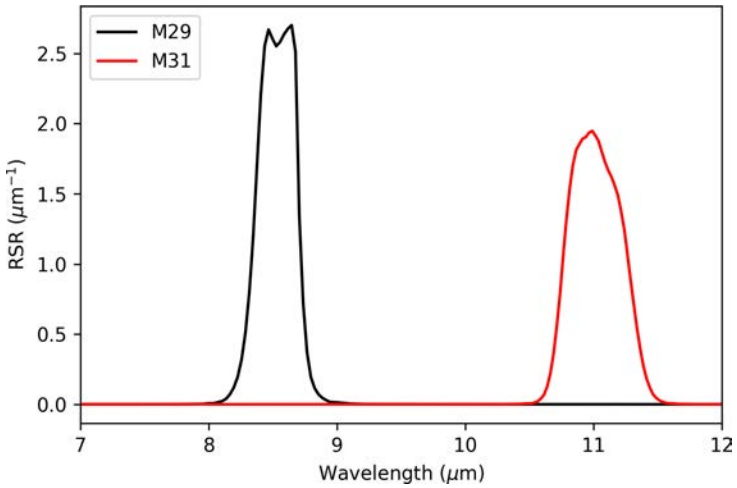

Fig. 3: Relative spectral response functions (in $\mu\mathrm{m}^{-1}$) in dependence of wavelength for the two MODIS channels M29 (black) and M31 (red).

from above. From time to time, thin cirrus clouds above the cloud layer were observed. At around 4:50 UTC, a discontinuity in the measured radiances is visible due to an abrupt change in flight altitude (from 17.5 to 20 km, compare Fig. 1) and the corresponding change in viewing geometry.

The data analysis comprises (1) the spectral band integration with respect to MODIS channels M29 and M31, (2) the calculation of the brightness temperatures at M29 and M31, and (3) the detection of the thermodynamic phase using the brightness temperature difference method.

3.1 Spectral band integration

To lower the data amount following the very fine spectral sampling of up to 0.0625 cm^{-1} within the spectral range of 770 to 1400 cm^{-1}, spectral band integration with respect to the MODIS channels M29 and M31 (in the terrestrial infrared) is performed. The choice of the satellite channels (e.g., Chylek et al., 2006) is based on the spectral behavior of the complex refractive indices of water and ice. At M29 (8.4-8.7 µm) no difference and at M31 (10.8-11.3 µm) a strong difference between the refractive indices is found. In addition, the ozone band at approximately 9.5 µm is avoided. Furthermore, spectrally close bands minimize the effect of the cloud particle size (Chylek et al., 2006). The relative spectral response (RSR) functions of the two MODIS channels M29 and M31 are shown in Fig. 3. The central wavelengths are 8.55 and 11 µm, respectively.

The band integration is done by integrating the spectral radiance with respect to the RSR functions of the two MODIS channels.

3.2 Calculation of brightness temperature

The brightness temperature T_B can be calculated from the spectral radiance $I(\lambda)$ using Planck's law:

$$T_\mathrm{B} = \frac{hc}{k_\mathrm{B}\lambda} \cdot \left\{ \ln\left[\frac{2hc^2}{\lambda^5(\mathrm{sr})I(\lambda)} + 1 \right] \right\}^{-1} . \qquad (1)$$

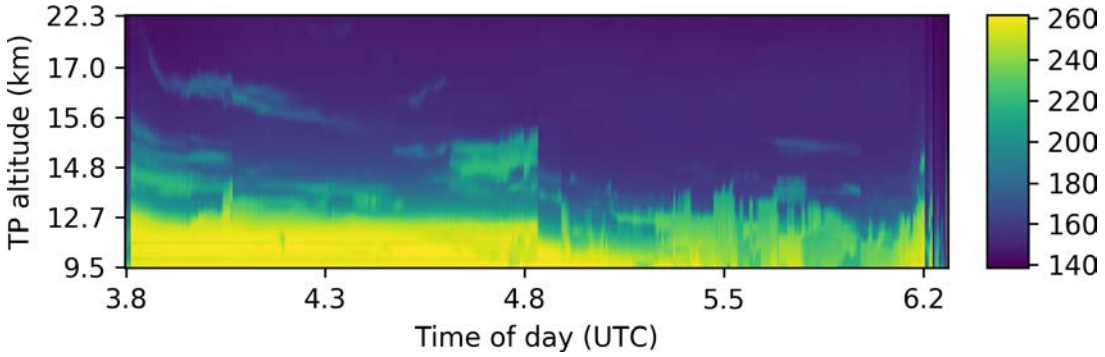

Fig. 4: Brightness temperature profiles along flight track for MODIS channel M31 in dependence of time of day and the tangent point (TP) altitude as measured by GLORIA on 31 July 2017. The brightness temperature is color-coded in units K.

Herein, h denotes the Planck constant ($6.6262 \cdot 10^{-34}$ Js), k_B is the Boltzmann constant ($1.3806 \cdot 10^{-23}\,\mathrm{J\,K^{-1}}$), c the speed of light in vacuum ($2.997925 \cdot 10^{8}\,\mathrm{m\,s^{-1}}$), and λ the wavelength.

For the channel M31, the brightness temperature profiles along the flight track are shown in Fig. 4. Analogously to the emitted radiance, the cloud fields exhibit higher brightness temperatures than the clearsky above.

3.3 Thermodynamic phase detection

The brightness temperature difference (BTD) is calculated as,

$$\mathrm{BTD} = T_{\mathrm{B,M29}} - T_{\mathrm{B,M31}}\,. \tag{2}$$

A preliminary cloud detection selects cloudy pixels as seen by GLORIA based on the cloud index as demonstrated by Spang et al. (2008). The cloud index is calculated as the ratio of spectral radiance at $830\,\mathrm{cm^{-1}}$ (atmospheric window region) and $792\,\mathrm{cm^{-1}}$ (dominated by CO_2 emission). Cloud indices below the threshold of 2 indicated the presence of clouds.

For all cloudy pixels, the thermodynamic phase is retrieved based on the decision matrix following Baum et al. (2000). A BTD below -1.0 K indicates liquid water within the cloud. In contrast, BTD values above 0.5 K indicate ice.

4. Results and discussion

Figure 5a shows the brightness temperature difference for the research flight on 31 July 2017. The preliminary cloud detection is illustrated in Fig. 5b and is in agreement with the visual estimation. Cloudy pixels where ice was detected are shown in green in Fig. 5c. Cloud particles were detected as ice for all cirrus clouds above the cloud layer. In the top parts of the convective cloud layer, ice was detected. The comparison with Fig. 4 shows for the convective layer mostly constant brightness temperatures indicating a view from the top. However, e.g. during the time marked with a black rectangle in Fig. 5c (5:48-5:53 UTC), some periods with cloud-side observations occured. This can be deduced from the change of the brightness temperature with TP altitude.

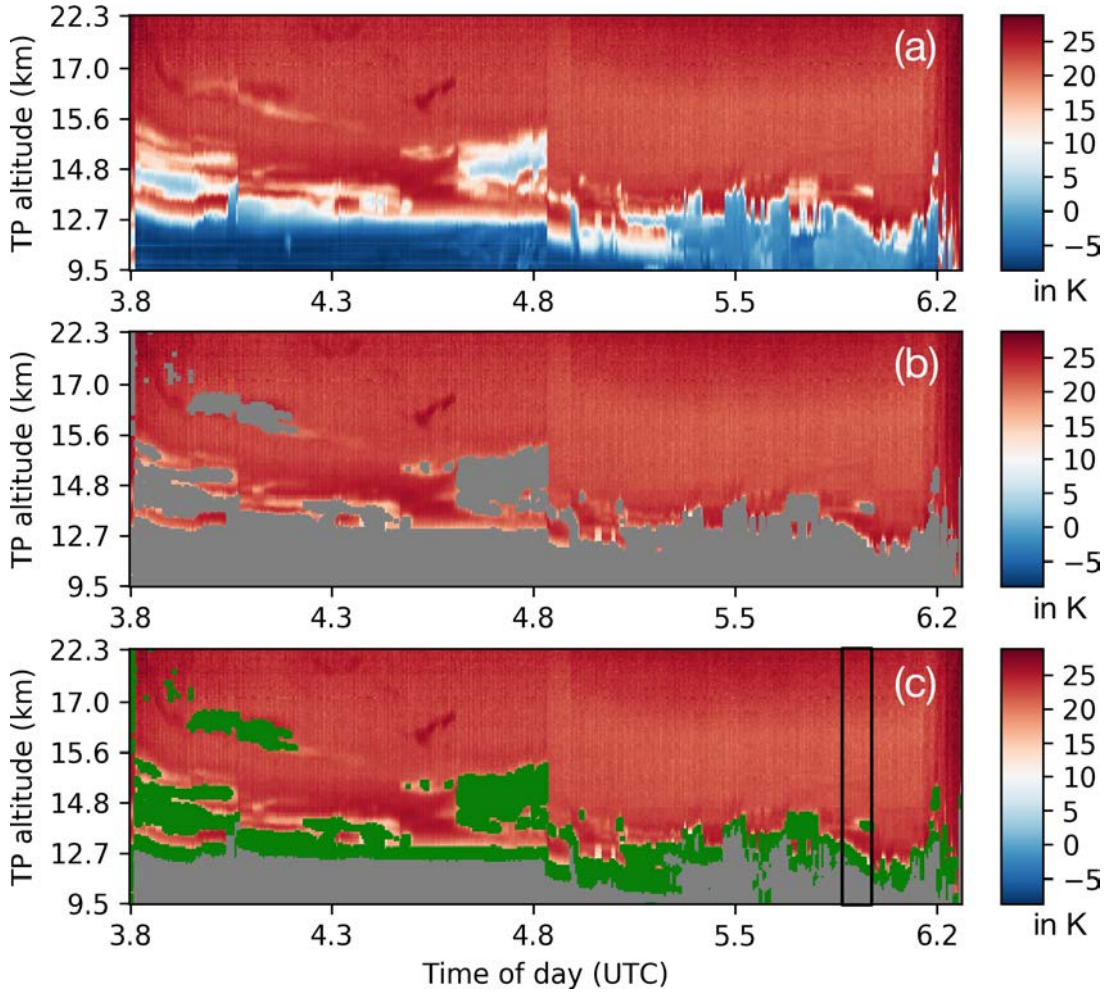

Fig. 5: ***(a)*** *Brightness temperature difference BTD (in* K*) along flight track on 31 July 2017.* ***(b)*** *Same as in a. In addition, cloudy pixels are shown in gray.* ***(c)*** *Same as in b. In addition, pixels where ice was detected are shown in green. The black rectangle marks the time range for the detailed study in Fig. 6.*

This time period is illustrated in more detail in Fig. 6a. Ice could be detected at the cloud top and in the overlying thin cirrus cloud. Figure 6b explicitly shows the 20 vertical profiles observed with GLORIA. The brightness temperature at 8.55 µm wavelength (M29) is shown with respect to the BTD. In addition, the thresholds of BTD for the detection of liquid water, mixed-phase, and ice particles are shown. Thus, between a liquid layer and the ice layer at the cloud top, a layer with mixed-phase cloud particles could be identified. Note that the brightness temperature is shown as a vertical coordinate and is not equal to the actual air temperature.

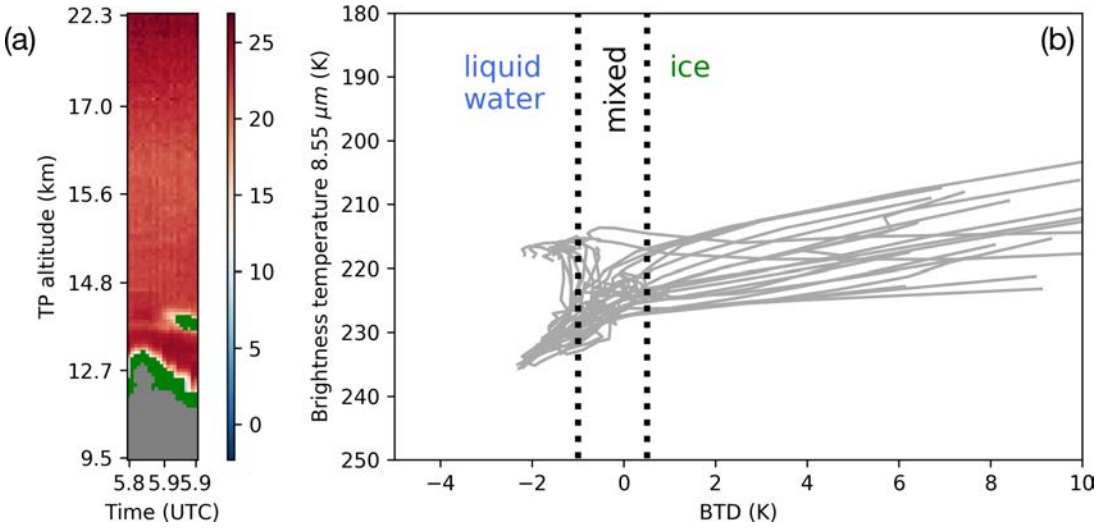

Fig. 6: ***(a)*** *Brightness temperature difference BTD (in* K*) along flight track on 31 July 2017 between 5:48* UTC *and 5:53* UTC*. The time range corresponds to the black rectangle in Fig. 5. Cloudy pixels are shown in gray. Pixels where ice was detected are shown in green.* ***(b)*** *Brightness temperature at 8.55* μm *(in K) in dependence of BTD (in K) for the 20 vertical profiles shown in (a) (gray color). In addition, BTD thresholds corresponding to liquid water, mixed-phase, and ice detection are illustrated with black dashed lines.*

5. Conclusions

The study demonstrates the feasibility of the cloud thermodynamic phase retrieval utilizing brightness temperature differences for limb observations in the terrestrial infrared wavelength region with the GLORIA instrument. Future research efforts with the GLORIA instrument could be extended to legs with lower flight altitudes yielding better viewing geometry for cloud-side observations.

6. Bibliography

Albrecht, B. A.: Aerosols, Cloud Microphysics, and Fractional Cloudiness, Science, 245, 1227–1230, doi:10.1126/science.245.4923.1227, 1989.

Baum, B., Soulen, P., Strabala, K., King, M., Ackerman, S., Menzel, W., and Yang, P.: Remote sensing of cloud properties using MODIS airborne simulator imagery during SUCCESS. 2. Cloud thermodynamic phase, J. Geophys. Res., 105, 11 781–11 792, doi:10.1029/1999JD901090, 2000.

Chylek, P., Robinson, S., Dubey, M. K., King, M. D., Fu, Q., and Clodius, W. B.: Comparison of near-infrared and thermal infrared cloud phase detections, J. Geophys. Res., 111, D20 203, doi:10.1029/2006JD007140, 2006.

Jäkel, E., Wendisch, M., Krisna, T., Ewald, F., Koelling, T., Jurkat, T., Voigt, C., Cecchini, M., Machado, L., Afchine, A., Costa, A., Kraemer, M., Andreae, M., Poeschl, U., Rosenfeld, D., and Yuan, T.: Vertical distribution of the particle phase in tropical

deep convective clouds as derived from cloud-side reflected solar radiation measurements, Atmos. Chem. Phys., 17, 9049–9066, doi:10.5194/acp-17-9049-2017, 2017.

Martins, J. V., Marshak, A., Remer, L. A., Rosenfeld, D., Kaufman, Y. J., Fernandez-Borda, R., Koren, I., Correia, A. L., Zubko, V., and Artaxo, P.: Remote sensing the vertical profile of cloud droplet effective radius, thermodynamic phase, and temperature, Atmos. Chem. Phys., 11, 9485–9501, doi:10.5194/acp-11-9485-2011, 2011.

Rosenfeld, D., Lohmann, U., Raga, G. B., O'Dowd, C. D., Kulmala, M., Fuzzi, S., Reissell, A., and Andreae, M. O.: Flood or drought: How do aerosols affect precipitation?, Science, 321, 1309–1313, doi:10.1126/science.1160606, 2008.

Rosenfeld, D., Liu, G., Yu, X., Zhu, Y., Dai, J., Xu, X., and Yue, Z.: High-resolution (375 m) cloud microstructure as seen from the NPP/VIIRS satellite imager, Atmos. Chem. Phys., 14, 2479–2496, doi:10.5194/acp-14-2479-2014, 2014.

Spang, R., Hoffmann, L., Kullmann, A., Olschewski, F., Preusse, P., Knieling, P., Schroeder, S., Stroh, F., Weigel, K., and Riese, M.: High resolution limb observations of clouds by the CRISTA-NF experiment during the SCOUT-O3 tropical aircraft campaign, Adv. Space Res., 42, 1765–1775, doi:10.1016/j.asr.2007.09.036, 2008.

Twomey, S.: The influence of pollution on the shortwave albedo of clouds, J. Atmos. Sci., 34, 1149–1152, doi:10.1175/1520-0469(1977)034<1149:TIOPOT>2.0.CO;2, 1977.

Comparison of simulated and observed horizontal inhomogeneities of optical thickness of Arctic stratus

Schäfer, M.[1], Loewe, K.[2], Ehrlich, A.[1], Hoose, C.[2], Wendisch, M.[1]

[1]) Leipzig Institute for Meteorology, Stephanstr. 3, 04103 Leipzig, Germany, E-Mail: michael.schaefer@uni-leipzig.de

[2]) Institute of Meteorology and Climate Research, Karlsruhe Institute of Technology, Karlsruhe, Germany

Summary: Two-dimensional horizontal fields of cloud optical thickness derived from airborne measurements of solar spectral, reflected radiance are compared with semi-idealized large eddy simulations (LESs) of Arctic stratus performed with the Consortium for Small-scale Modeling (COSMO) atmospheric model. The measurements were collected during the Vertical Distribution of Ice in Arctic Clouds (VERDI) campaign carried out in Inuvik, Canada, in April/May 2012. The input for the LESs is obtained from collocated dropsonde observations of a persistent Arctic stratus above the sea-ice-free Beaufort Sea. Simulations are performed for spatial resolutions of 50 m (1.6 km by 1.6 km domain) and 100 m (6.4 km by 6.4 km domain). Macrophysical cloud properties, such as cloud top altitude and vertical extent, are well captured by the COSMO simulations. However, COSMO produces rather homogeneous clouds compared to the measurements, in particular for the simulations with coarser spatial resolution. For both spatial resolutions, the directional structure of the cloud inhomogeneity is well represented by the model. This study was first published by Schäfer et al., 2018.

Zusammenfassung: Zweidimensionale horizontale Felder optischer Dicken abgeleitet aus flugzeuggetragenen Messungen der spektralen, solaren, reflektierten Strahldichte über Arktischem Stratus werden mit teilidealisierten Large Eddy Simulationen (LES) im Atmosphärenmodel des Consortium for Small-scale Modeling (COSMO) verglichen. Die Messungen stammen von der Vertical Distribution of Ice in Arctic Clouds (VERDI) Kampagne in Inuvik, Kanada, im April/Mai 2012. Fallsonden-Beobachtungen eines beständigen arktischen Stratus über dem eisfreien Beaufort Meer bilden die LES-Eingangsdaten. Die Simulationen wurden mit räumlichen Auflösungen von 50 m (1.6 km × 1.6 km Gebiet) und 100 m (6.4 km × 6.4 km Gebiet) durchgeführt. Makroskopische Wolkeneigenschaften (Wolkenhöhe, -ausdehnung) wurden von COSMO erfasst. Allerdings produziert COSMO verglichen zu den Beobachtungen (besonders bei grober räumlicher Auflösung) eher homogenere Wolken. Gerichtete Strukturen der Inhomogenitäten wurden mit beiden räumlichen Auflösungen gut erfasst. Diese Studie wurde als erstes von Schäfer et al., 2018 veröffentlicht.

1. Introduction

Arctic clouds are expected to be a major contributor to the so-called Arctic amplification (Serreze and Barry, 2011; Wendisch et al., 2017) and therefore need to be represented

adequately in model projections of the future Arctic climate (Vavrus, 2004). Especially, low-level Arctic stratus are of importance (Wendisch et al., 2013), because they occur quite frequently (around 40 %; Shupe et al., 2011), typically persist over several days or even weeks (Shupe et al., 2011), and, on annual average, warm the Arctic surface (Shupe and Intrieri, 2004). The numerous physical and microphysical processes that determine the properties of Arctic stratus are complexly linked to each other and still not understood in full detail (Morrison et al., 2012).

Dynamic factors (updrafts), which increase the actual supersaturation in the cloud beyond the equilibrium values for both liquid water and ice, and a steady supply of water vapor from above the cloud, stabilize Arctic stratus (Shupe et al., 2008). This facilitates the simultaneous existence and formation of both phases (Korolev, 2007). While in updrafts super-cooled liquid water droplets and ice crystals grow, and the cloud top cooling causes downward vertical motion, the Wegener–Bergeron–Findeisen process may dominate. Therefore, small-scale structures may evolve in down- and updraft regions of the stratus, which can be important to understand microphysical processes keeping the cloud to persist for a longer period. Additionally, Arctic stratus shows microphysical inhomogeneities, which typically occur on horizontal and vertical scales within tens of meters (Lawson et al., 2010). These small-scale structures and cloud inhomogeneities lead to three-dimensional (3-D) radiative effects, which can be parameterized using inhomogeneity parameters (Iwabuchi and Hayasaka, 2002).

Unfortunately, the understanding of Arctic cloud processes is impeded by a paucity of comprehensive observations caused by a lack of basic research infrastructure and the harsh Arctic environment (Shupe et al., 2011). Therefore, observation of small-scale cloud structures within the Arctic Circle are sparse. Satellite observations are typically too coarse to resolve scales below 250 m. Space-borne passive remote sensing observations suffer from contrast problems over highly reflecting surfaces (snow and sea ice; Ehrlich et al., 2017). Ground-based remote sensing measurements with radar and lidar typically point only in zenith direction and are not able to provide the horizontal two-dimensional (2-D) structure of clouds. In comparison, airborne spectral imaging observation of reflected solar radiation provides areal measurements with a spatial resolution down to several meters (Schäfer et al., 2015). Bierwirth et al. (2013) used such airborne measurements of reflected solar spectral radiance to retrieve 2-D fields of cloud optical thickness τ of Arctic stratus and demonstrated their strong spatial variability. From similar measurements, Schäfer et al. (2017a) analyzed the directional variability of Arctic stratus. The few analyzed cases revealed that 1-D statistics are not sufficient to quantify the variability of horizontal cloud inhomogeneities.

Likewise, treating small-scale inhomogeneities using reanalysis data and atmospheric models is difficult. Global reanalysis products have relatively coarse spatial resolutions (40 km and larger; Lindsay et al., 2014) and therefore do not resolve small-scale features. Furthermore, in numerical weather prediction and climate models, the representation of the temporal evolution of mixed-phase clouds is not always adequate (Barrett et al., 2017). Especially, areas of up- and downdrafts in Arctic stratus, which are typically in the range of less than 1 km, cannot be resolved but need to be parameterized. To realistically simulate the spatial structure of these clouds, large eddy simulations (LESs) with a spatial resolution of 100 m or less and high vertical resolution ($\approx$ 20 m within atmospheric boundary layer, ABL) are needed. Those LESs can resolve

the vertical motion of turbulent eddies in the ABL representing the inhomogeneities in the cloud top structure, which can be seen in the amount of liquid water.
Previous LES studies focused, for instance, on cloud top entrainment (Mellado, 2017) and emphasized the behavior of changes in the spatial resolution on the liquid water path (Pedersen et al., 2016). Kopec et al. (2016) discussed two main processes: the radiative cooling and wind shear. The radiative cooling sharpened the inversion, while wind shear at the top of the ABL caused the turbulence in the capping inversion.

LESs are helpful to investigate small-scale structures in Arctic stratus under controlled conditions. Here, results from the Consortium for Small-scale Modeling (COSMO) model are evaluated, which is adjusted to an LES setup with a high horizontal and vertical resolution to resolve the structures of Arctic stratus (Loewe et al., 2017). For the Arctic Summer Cloud Ocean Study (ASCOS), Loewe et al. (2017) validated COSMO for simulations with a spatial resolution of 100 m with respect to droplet/ice crystal number concentrations and surface energy fluxes. Cloud inhomogeneities were not validated due to the lack of observational data from ASCOS.

In this study, which was first published by Schäfer et al., 2018, 2-D fields of cloud optical thickness (Sect. 2.2), retrieved from airborne imaging spectrometer measurements, obtained during the Vertical Distribution of Ice in Arctic Clouds (VERDI) campaign, are used to analyze small-scale cloud inhomogeneities. Those are then compared to COSMO simulations using the same model setup as proposed by Loewe et al. (2017) with 64 by 64 grid points and 100 m spatial resolution as well as a setup with 32 by 32 grid points and higher spatial resolution of 50 m. For that, data measured by dropsondes served as input for semi-idealized simulations of clouds using COSMO-LES (Sects. 2.3 and 3). These fields are compared with COSMO results with respect to their cloud inhomogeneity (Sects. 4 and 5). Observations and modeling are aimed to quantify the horizontal cloud top structures, which are discussed in Sect. 5.

2. Airborne measurements

2.1 Vertical Distribution of Ice in Arctic clouds (VERDI) campaign

VERDI was based in Inuvik, Canada, and was conducted in April/May 2012. The data were collected aboard the Polar 5 research aircraft of the Alfred Wegener Institute, Helmholtz Centre for Polar and Marine Research (AWI). The measurement flights were carried out in the region over the Beaufort Sea, which was mostly covered by sea ice, but also included sea-ice-free areas (polynyas). Mostly stratiform, low-level liquid and mixed-phase clouds within a temperature range of -19°C to 0°C were investigated (Costa et al., 2017). Here, the analysis is focused on a persistent cloud layer probed on 4 consecutive days from 14 to 17 May 2012. The applied measurements were performed in close vicinity (less than 50 km) over constant surface conditions (open ocean; polynyas). The persistent cloud cover in the respective area decreased continuously from day to day with cloud top altitude decreasing from about 880 m on 14 May to around 200 m on 17 May (Klingebiel et al., 2015; Schäfer et al., 2015, 2017a). The Polar 5 research aircraft was equipped with a set of cloud and aerosol in situ and remote sensing instruments (Schäfer et al., 2015; Klingebiel et al., 2015). Atmospheric profiles of temperature, humidity, wind speed, and direction were derived from dropsondes, which were regularly released during all flights.

2.2 Horizontal fields of cloud optical thickness

The qualitative and quantitative description of the cloud inhomogeneities is performed using 2-D fields of cloud optical thickness τ. The 2-D fields of τ are retrieved from 2-D fields of reflected solar spectral radiance, which were collected with the imaging spectrometer AisaEAGLE (Schäfer et al., 2013, 2015). Using those data, Schäfer et al. (2017a) retrieved 10 cases of 2-D fields of τ (Schäfer et al., 2017b). From those 10 cases, four are selected for the comparison with the LES results obtained from COSMO. Figure 1 illustrates sections (1.2 km by 3.0 km) of these cases. The full widths and lengths of these 2-D fields range from 1.7 to 26.8 km. Their spatial resolution is between 2.6 and 3.6 m (depending on the vertical distance between aircraft and cloud).

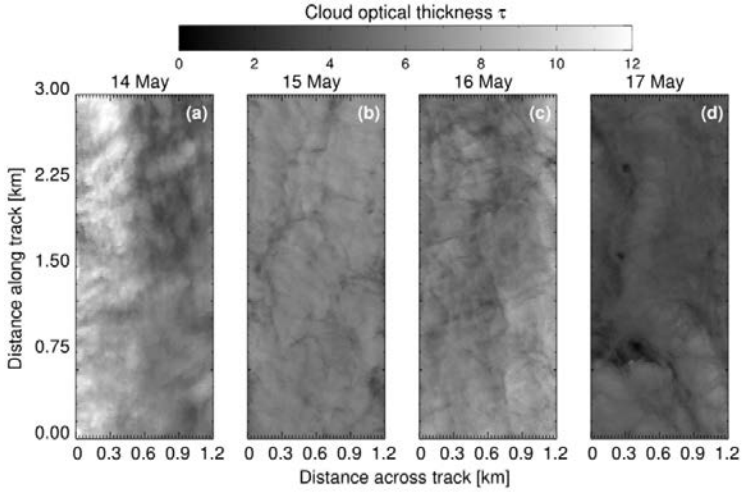

Fig. 1. Sections (1.2 by 3.0 km) of fields of τ to illustrate the daily variability of the horizontal cloud inhomogeneities during VERDI on (a) 14 May 2012, (b) 15 May 2012, (c) 16 May 2012, and (d) 17 May 2012. Graph adapted from Schäfer et al. (2018).

During the time period from 14 to 17 May 2012, the areal average of τ decreased from 8.1 to 4.3 (Schäfer et al., 2017a). In particular, from 15 to 17 May 2012, a reduction of the horizontal cloud inhomogeneity is visible, which is confirmed by Schäfer et al. (2017a), who also found a reduction of cloud inhomogeneity during those 4 consecutive days. Directional features, which are prominent on 14 May, seem to be reduced as well.

2.3 Vertical profiles of atmospheric parameters

During each measurement flight, Vaisala dropsondes (type RD94) were released to sample profiles of meteorological parameters – air pressure (p, ± 0.4 hPa), air temperature (T, ± 0.2°C), relative humidity (RH, ± 2 %), wind speed (v, ± 0.5 ms^{-1}), and wind direction (WD) – below the aircraft, which typically operated at about 3 km altitude to sample the entire cloud and ABL structure. The potential temperature (Θ), RH, v, and WD profiles for the four investigated cases are displayed in Fig. 2.

From 14 to 15 May, the cloud top inversion increased from 810 to 880 m, while for the subsequent 2 days, the inversion layer decreased to 440 m on 16 May and to 200 m on 17 May 2012 (Fig. 2a). In conjunction with the decrease of the cloud top altitude, the cloud base decreased as well until it almost reached the surface on 17 May. The relative humidity (Fig. 2b) confirms the initial increase and consecutive decrease of the cloud top and base altitudes. The inversion strength decreased over the time from

about 5 to 1 K, mainly because the temperature of the surface layer continuously decreased; the ABL became more stable. Figure 2c illustrates that the near-surface wind increased during the 4 days from about 1 to 10 ms^{-1}. Except for the case on 14 May, the daily increase of the near-surface wind speed is observed as well in higher altitudes to up to 1 km, which is related to low-level jets for the days from 15 to 17 May.

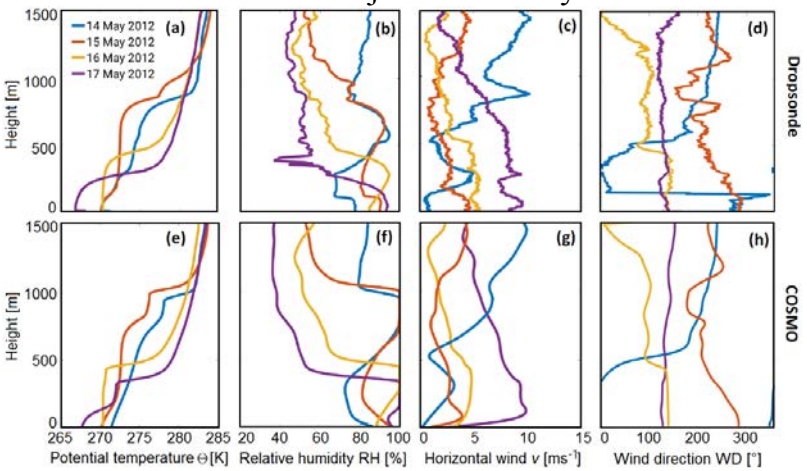

Fig. 2: (a, e) Potential temperature, (b, f) relative humidity, (c, g) wind speed, and (d, h) wind direction for the four investigated cases. The dropsonde data are shown in the first row (a–d), the 2 h domain-averaged profiles after spin-up time of the simulations in the second row (e–h). Graph adapted from Schäfer et al. (2018).

3. Simulations

3.1 COSMO: general setup

COSMO is a non-hydrostatic, limited-area atmospheric forecast model (Schättler et al., 2015). Here, it is used in a semi-idealized LES setup, which follows the description by Loewe et al. (2017), based on Ovchinnikov et al. (2014), and Paukert and Hoose (2014). The two-moment cloud microphysics scheme by Seifert and Beheng (2006) predicts the number densities and masses of six hydrometeor types. The different ice-phase hydrometeor growth processes are parameterized. The radiative transfer is described by a two-stream radiation scheme (Ritter and Geleyn, 1992). It is calculated every 2 s and has a direct cloud radiative feedback. A 3-D prognostic turbulence scheme describes the turbulent fluxes of heat, momentum, and mass by a first-order closure after Smagorinsky and Lilly (Herzog et al., 2002; Langhans et al., 2012). The horizontal size of the model domain used by Loewe et al. (2017) was 6.4 x 6.4 km with a spatial resolution of 100 m. For the comparison with the imaging spectrometer measurements analyzed here, the spatial resolution is also increased to 50 m for additional model runs. In those cases, the domain size is reduced to 32 by 32 grid points (1.6 km x 1.6 km) for computational constraints. The vertical height range of 22 km is divided into 166 levels, which are more dense for the ABL with a typical vertical resolution of around 15 m. The initialization profiles of temperature, humidity, wind speed, and wind direction are based on dropsonde data. The surface of the model is open ocean and the surface fluxes depend on the surface temperature (273.5 K for sea-water surface). ERA-Interim reanalysis data from the European Centre for Medium-Range Weather Forecasts have been used to complete the profiles above the altitude where the dropsondes were released. Other model parameters include the description of the large-scale subsidence, the relaxation to fixed cloud droplet number concentration (CDNC), and ice crystal

number concentration (ICNC). The spin-up time was set to 2 h following Ovchinnikov et al. (2014). The CDNCs are based on measurements of the Small Ice Detector (SID-3; Vochezer et al., 2016). During the four investigated days, CDNCs of 90 to 100 cm^{-3} were observed. The ICNC were assumed to be one particle per liter according to observations of mixed-phase Arctic stratus during the Indirect and Semi-Direct Aerosol Campaign (Ovchinnikov et al., 2014). The inversion height of the temperature, $z(T_{in})$, is necessary for the description of the large-scale subsidence in the model and is represented by the inversion height of the dropsonde profiles.

3.2 Domain-averaged cloud properties and temporal evolution

The liquid water content (LWC) and ice water content (IWC) was simulated for the four selected cases. The simulated clouds consisted mostly of liquid water droplets except for 15 May, in which more IWC was built. The cloud top height is around 1000 m for 14 and 15 May, 450 m and 350 m on 16 and 17 May. It increases over time in all four simulations because of entrainment of air through the top of the ABL.

The four simulations show differences in the temperature, relative humidity, and wind speed profiles (Fig. 2e–g), which in general agree with the initial dropsonde profiles after spin-up (Fig. 2a–c). The height of the ABLs and the strength of the inversions are lower in the simulations of 16 and 17 May. For the simulation on 17 May, a second inversion develops in the ABL near the surface between 60 and 150 m. The ABL structure is well mixed in the simulation of 16 May, shows a wind shear from around 150 to 100° (Fig. 2g), and a decrease of v with height above the cloud top height, which is also seen in the dropsonde profiles (Fig. 2c).

The simulated mixed-phase clouds of the four cases have a liquid water path (LWP) around 35 to 50 g m^{-2} with highest LWP in the simulation of 14 May, which increases towards 50 g m^{-2}. The simulation of 15 May has the lowest LWP values and the LWP remains very stable until the end of the simulation. The ice water path and the snow water path of all four simulations are small, which fits well with observations.

In the following, fields of simulated cloud optical thickness (τ_{sim}) are compared to retrieved fields of cloud optical thickness from measurements (τ_{meas}). The τ_{sim} is calculated within COSMO considering the LWP and the solar spectrum. It cannot be expected that COSMO is capable of reproducing the detailed spatial and temporal cloud evolutions, which are captured by the observed fields of τ, accurately. Therefore, besides the comparison of observed and simulated clouds with regard to macrophysical cloud features of the individual cases, statistical bulk parameters describing the horizontal cloud inhomogeneities and their directional structures will be compared.

4. Quantification of cloud inhomogeneities

4.1 One-dimensional statistical bulk parameters

For the quantitative description of the cloud inhomogeneities from the simulated (τ_{sim}) and measurement-based (τ_{meas}) fields of τ, statistical techniques are applied. Following Schäfer et al. (2017a), a statistical quantitative measure of the cloud inhomogeneity is derived using the mean ($\bar{\tau}$) and standard deviation (σ_τ) of the particular τ field and a 1-D inhomogeneity parameter ρ_τ (Davis et al., 1999; Szczap et al., 2000), given by:

$$\rho_\tau = \frac{\sigma_\tau}{\bar{\tau}}. \quad (1)$$

A homogeneous cloud is characterized by $\rho_\tau = 0$. Higher values of ρ_τ indicate more pronounced cloud inhomogeneity. However, it has no predefined upper limit. Therefore, ρ_τ only sustains a quantitative significance, when its values for different cases are compared to each other.

4.2 Two-dimensional autocorrelation analysis

Two-dimensional autocorrelation analysis is applied to quantify typical scales of cloud inhomogeneities and to identify directional patterns of the cloud structures (Schäfer et al., 2017a). For this, each field of τ is correlated with itself, while it is shifted pixel by pixel (observations) or grid point by grid point (simulations) against itself. The resulting correlation coefficients after each shift are in the range between -1 (perfect negative correlation) and +1 (perfect positive correlation). Correlation coefficients with values of 0 identify no correlation. Here, only the degree of correlation matters and not its algebraic sign. Therefore, similar to Schäfer et al. (2017a), squared autocorrelation functions P^2_τ are used to avoid ambiguous interpretations with P^2_τ between 0 and 1.

The particular correlation coefficients at the derived distances identify the similarity of the horizontal cloud structures. If the cloud is horizontally homogeneous, the correlation coefficients stay constant over large distances. If the cloud is rather inhomogeneous, the correlation coefficients already drop at closer distances. Therefore, P^2_τ as a function of distances is a measure of the size of the dominant cloud structures. A quantitative value for the distance, at which cloud structures are different from each other (namely decorrelated), is the decorrelation length ξ_τ (Schäfer et al., 2017a). It is the distance, at which P^2_τ drops to:

$$P^2_\tau(\xi_\tau) = \frac{1}{e^2}. \quad (2)$$

In a 2-D autocorrelation function, ξ_τ can differ depending on the orientation, if the cloud structures have a predominant orientation. To quantify this directionality, ξ_τ is calculated along ($\xi_\tau^{\updownarrow}$) and across ($\xi_\tau^{\leftrightarrow}$) the predominant direction. The larger the differences, the more cloud structures are orientated.

Figure 4a shows a section of an observed field of τ_{meas}, retrieved from the measurements on 15 May. The selected section has a swath of 1.3 km (oriented in y direction) and a length of 6 km (oriented in x direction). Figure 4b shows the corresponding field of τ_{sim} (6 km by 6 km, adapted to the selected length of the measurement case), which is simulated with COSMO for the case of 15 May. For comparability reasons, both fields of τ are normalized by their maximum.

Although the swath (y direction) of the field of τ_{meas} is smaller by a factor of almost 5 compared to the field of τ_{sim}, larger cloud structures of similar size and shape are obvious in both fields of τ_{meas} and τ_{sim}. However, with 488 spatial pixels along the swath and a field of view of 37°, AisaEAGLE's spatial resolution is approximately 1.3 m for a target in a distance of 1 km. Thus, the spatial resolution of AisaEAGLE is relatively high, compared to the spatial resolution of 100 m from COSMO. Thereby, the exact pixel size of AisaEAGLE depends on the distance between aircraft and cloud,

which leads to pixel sizes between 2.6 and 3.6 m for the four investigated cases. Due to the 30 to 40 times higher spatial resolution of AisaEAGLE, compared to COSMO, the measurements show cloud features, which cannot be resolved by COSMO. Those features may have an effect on the statistical and spatial comparison of the fields of τ.

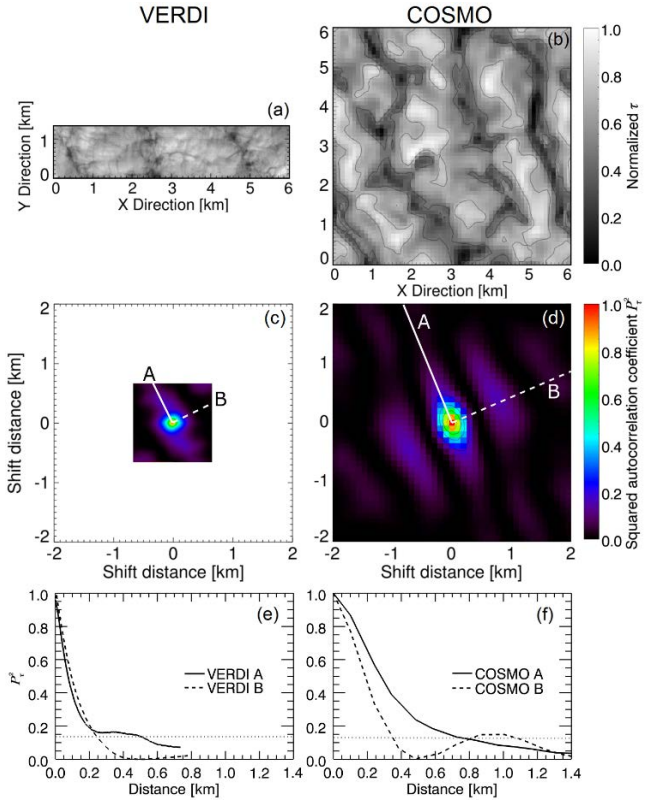

To quantify the size and orientation of the represented cloud structures in the observations and simulations, Fig. 3c and d show the calculated squared 2-D autocorrelation coefficients P^2_{τ}. To calculate them, different numbers of lags (shifts) have to be applied for $P^2_{\tau,meas}$ and $P^2_{\tau,sim}$. The applied field of τ_{meas} consists of 2700 by 450 spatial pixels. Therefore, restricted by the shorter side, 225 by 225 (half of swath pixel number, calculated into x and y direction) lags are chosen for the calculation of the 2-D $P^2_{\tau,meas}$. The COSMO results consist of 64 by 64 grid points. This allows 32 by 32 lags for the calculation of $P^2_{\tau,sim}$.

Fig. 3: (a–b) Horizontal fields of normalized τ_{meas} (VERDI) and τ_{sim} (COSMO) for 15 May 2012. (c–d) 2-D $P^2_{\tau,meas}$ and $P^2_{\tau,sim}$, calculated for fields of τ displayed in panels (a) and (b). (e–f) 1-D P^2_{τ} along (straight white line in panels c and d) and across (dashed white line in panels c and d) predominant directional structure. The grey dotted line illustrates the threshold for the estimation of $\xi_{\tau}^{\updownarrow}$ and $\xi_{\tau}^{\leftrightarrow}$. Schäfer et al. (2018).

The resolved domains and spatial resolutions displayed in Fig. 3c and d show significant differences, which reveals that a direct comparison is difficult. Applying the 2-D autocorrelation analysis to the observations allows to resolve small-scale cloud structures with high spatial resolution (approximately 2.7 m) but only within a narrow spatial range below 1 km. The same analysis for COSMO delivers $P^2_{\tau,sim}$ with lower spatial resolution of 100 m but over a larger spatial range (about 3.2 km). Thus, also large-scale cloud structures are covered by COSMO (purple stripes in Fig. 3d) but not in the observations. Therefore, the large-scale structures cannot be compared between observations and simulations. With respect to a comparison of the small-scale structures, the spatial resolution and domain size of both data sets need to be conformed for a direct comparison. Furthermore, Fig. 3c and d show predominant directional features of the cloud structures. Their lengths and widths are derived from 1-D autocorrelation functions along (straight white line in Fig. 3c and d) and across (dashed white line in Fig. 3c and d) those predominant directional structures. The derived $\xi_{\tau}^{\updownarrow}$ and $\xi_{\tau}^{\leftrightarrow}$ show an overall agreement but still differ from each other. For the observations, $\xi_{\tau}^{\updownarrow}$ and $\xi_{\tau}^{\leftrightarrow}$

reach distances of approximately 500 and 250 m, respectively. Contrarily, for the simulations, $\xi_\tau^{\updownarrow}$ and $\xi_\tau^{\leftrightarrow}$ reach distances of approximately 800 and 400 m, respectively. This is a further indication that it is necessary to make the fields of τ_{meas} and τ_{sim} conform. This is done by (i) averaging the fields of τ_{meas} to the spatial resolution of the fields of τ_{sim}, and (ii) improving the spatial resolution of the simulations themselves to 50 m.

5. Comparison of modeled against observed cloud structures

5.1 Magnitude of inhomogeneity

Both, measurements and simulations, show the highest areal averaged τ on 14 May with $\tau_{meas} = 7.8 \pm 1.5$ and $\tau_{sim} = 7.9 \pm 0.6$ at 50 m spatial resolution and $\tau_{meas} = 8.1 \pm 1.2$ and $\tau_{sim} = 6.9 \pm 0.5$ at 100 m spatial resolution, which indicate an overall agreement. During the following days, the large-scale subsidence led to a decrease of the cloud top altitude and geometrical thickness, and lower values of τ and σ_τ. For these days, the model and observations are still in agreement. However, the finer resolved simulations (50 m) lead to better agreement between measurements and simulations.

Regarding the cloud inhomogeneity, the 1-D inhomogeneity parameter ρ_τ does not compare well for the simulations with 100 m spatial resolution (detailed values can be found in Schäfer et al., 2018). The results for the COSMO simulations show lower 1-D inhomogeneity parameters (more homogeneous) by a factor of 2, compared to the measurements. The agreement improves with the finer spatial resolution of 50 m. The reason might be that the lower inhomogeneity derived from COSMO for both resolutions is caused by its effective resolution, which is three times 50 (100) m (Skamarock, 2004). Although the pixel size of AisaEAGLE is adapted to the COSMO spatial resolution, COSMO's effective resolution is larger.

However, the observations show that the cloud field became more homogeneous from 14 to 15 May as indicated by lower values of ρ_τ, which reduce from 0.209 to 0.115. From 15 to 16 May, ρ_τ increases to 0.145, which indicates a cloud field with slightly higher inhomogeneity. Then, on 17 May, ρ_τ reduced to 0.132, showing that the cloud field became more homogeneous again. These different cases with high and low ρ_τ are reproduced by COSMO independent of the chosen spatial resolution. Larger discrepancy between modeled and observed inhomogeneity parameters only occurred on 14 May, when the observations were influenced by large-scale cloud structures.

5.2 Spatial inhomogeneity scale

The 2-D autocorrelation functions are calculated to compare the typical spatial scales and the directional character of the small-scale cloud inhomogeneities (no large-scale inhomogeneities like roll convection) of observations and simulations. The 2-D autocorrelation coefficients ($P^2_{\tau,meas}$; $P^2_{\tau,sim}$) for each case are shown in Fig. 4e–h for the measurements and in Fig. 4m–p for the simulations (50 m spatial resolution).

Additionally, representative fields of normalized τ_{meas} (Fig. 4a–d) and τ_{sim} (Fig. 4i–l) are added. The 2-D autocorrelation analysis was applied to the simulated fields of τ_{sim} orientated in a north–south and west–east grid. The orientation of the observations is determined by the flight direction. Therefore, the orientation of the fields of τ_{meas} and $P^2_{\tau,meas}$ are rotated into the direction of the COSMO grid. One-dimensional

P^2_τ values are calculated manually along the dominant direction (straight red and blue lines) and across it (dashed red and blue lines). For $P^2_{\tau,meas}$ (red) and $P^2_{\tau,sim}$ (blue), the results are displayed in Fig. 4q-t.

The observations on 14 May are influenced by a largescale cloud structure, which is caused by large-scale dynamic forcing and leads to an increase of the autocorrelation coefficients for distances larger than 800 m. Furthermore, during this day, a significant directional structure from northwest to southeast is observed. Along this direction, the cloud field stays homogeneous over a wide range (ξ_τ = 800 m). Across this predominant structure, the small-scale cloud structures reach a decorrelation length of ξ_τ = 300 m. During the following days, the orientation of the directional structure turns eastwards in the observations. The differences between $\xi_\tau^{\updownarrow}$ and $\xi_\tau^{\leftrightarrow}$ decrease. This characterizes a weakening of the directional structure of the cloud field.

Comparing the results for $P^2_{\tau,sim}$ with $P^2_{\tau,meas}$ reveals that the large-scale cloud structure is not well simulated for the case of 14 May. This results most probably from the small domain size of COSMO, which is fixed over the same location, when averaging the $P^2_{\tau,sim}$ over a set of time steps. Contrarily, the averages of $P^2_{\tau,meas}$ from the measurements are performed over a set of squared domains along the flight track. Thus, the chance to cover also larger structures is higher for the measurements compared to the simulations. However, the small-scale directional structures are well simulated. On 14 May, a significant directional structure from northwest to southeast is observed, which then turns eastwards for 15 to 17 May. Except on 16 May, the predominantly simulated directions of the cloud fields are almost identical to the observations.

Furthermore, the results for $P^2_{\tau,meas}$ and $P^2_{\tau,sim}$ show that COSMO simulations using a spatial resolution of 50 m produce similar sizes of the small-scale cloud structures compared to the measurements. In Fig. 4m–p, the covered areas of $P^2_{\tau,sim}$ are of similar sizes compared to the areas covered by $P^2_{\tau,meas}$ in Fig. 4e–h. A comparison of $\xi_{\tau,\,meas}$ and $\xi_{\tau,\,sim}$ along and across the dominant structures found in Fig. 4e–h and m–p reveals only minor differences. The best agreement is achieved on 15 and 17 May, when $\xi_{\tau,\,meas}$ and $\xi_{\tau,\,sim}$ show almost identically results. On 16 May, the differences are slightly larger, while on 14 May the differences are significantly larger, which might result from the insufficient simulated large-scale cloud structure. For the simulations with 100 m spatial resolution (graph not shown), the directional features still compare well between observations and simulations. As for the measurements on 14 May, a predominant northwest to southeast direction is simulated, which then turns eastwards.

Thereby, the cases on 14 May and 16 May show the strongest directional features. Although on 17 May COSMO simulates a more isotropic structure ($\xi_\tau^{\updownarrow} \approx \xi_\tau^{\leftrightarrow} \approx$ 400 m) of the cloud inhomogeneities compared to the measurements ($\xi_\tau^{\updownarrow}$ = 370 m ≠ $\xi_\tau^{\leftrightarrow}$ = 260 m), it captures the reduction of the overall directionality. Therefore, the overall results with regard to the directional structure provided by COSMO are acceptable. However, the covered areas of the 2-D autocorrelation functions, where the values of $P^2_{\tau,sim}$ are higher than e^{-2} are larger compared to the areas covered by the particular $P^2_{\tau,meas}$. Therefore, the $\xi_{\tau,\,meas}$ and $\xi_{\tau,\,sim}$ calculated along ($\xi_\tau^{\updownarrow}$) and across ($\xi_\tau^{\leftrightarrow}$) the predominant structures do not compare well. The values from the simulations

(except for $\xi_\tau^{\updownarrow}$ on 14 May) are larger compared to the values from the observations by 20 % to 30 %.

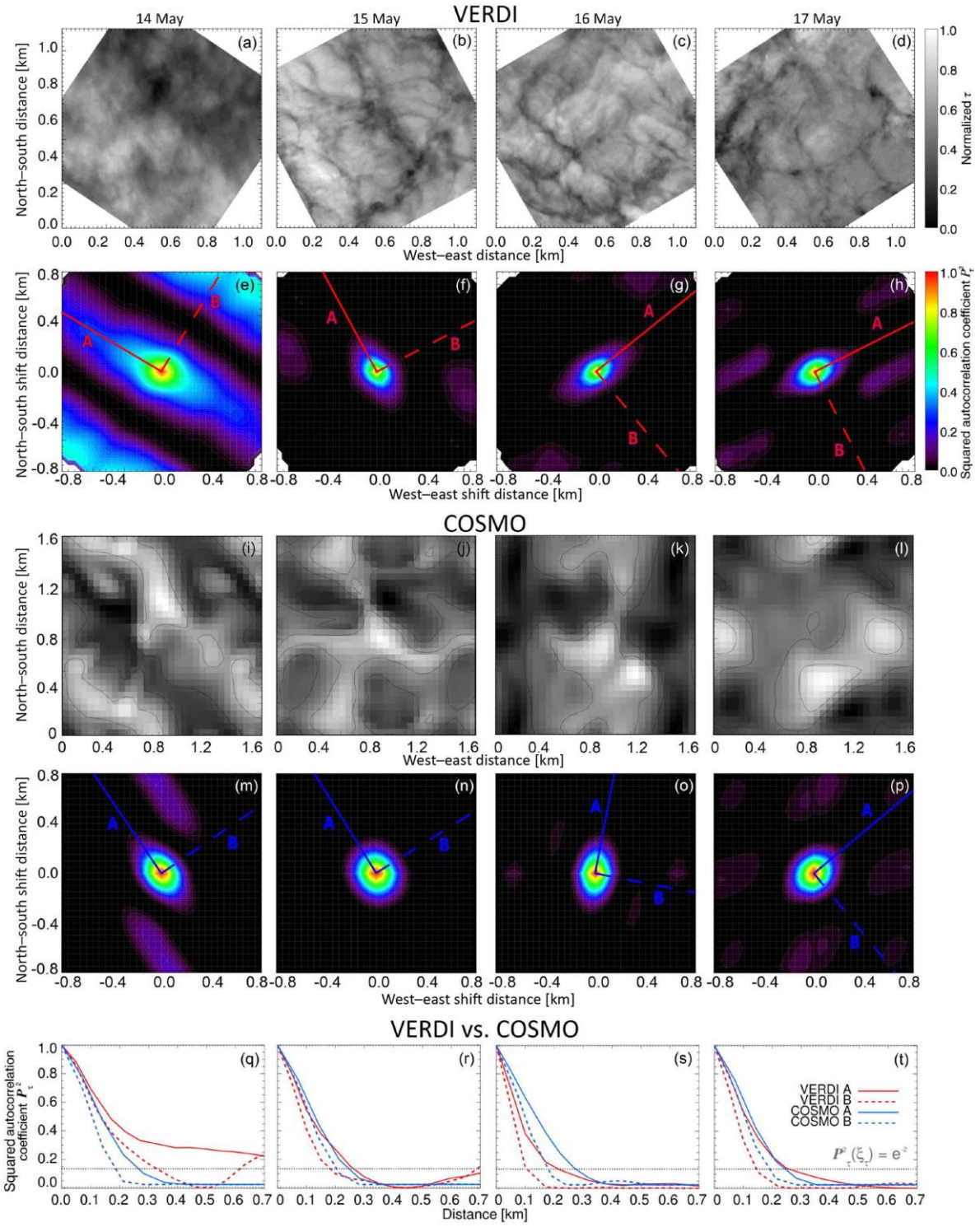

Fig. 4: (a–d) Selected sections of fields of τ_{meas} observed during VERDI from 14 to 17 May 2012. (e–h) Mean 2-D autocorrelation coefficients $P^2_{\tau,meas}$ derived for fields of τ_{meas} from VERDI. (i–l) Selected fields of τ_{sim} simulated with COSMO (50 m spatial resolution) for the VERDI cases from 14 to 17 May 2012. (m–p) Mean 2-D $P^2_{\tau,sim}$ derived for fields of τ_{sim}. (q–t) Decorrelation length ξ_τ along strongest (straight blue and red lines) and weakest (dashed blue and red lines) extents of 2-D autocorrelation coefficients derived from $P^2_{\tau,meas}$ in panels (e)–(h) and $P^2_{\tau,sim}$ in panels (m)–(p), respectively. Graph adapted from Schäfer et al. (2018).

6. Summary and conclusions:

Remote sensing of cloud optical thickness and atmospheric dropsonde measurements from the airborne VERDI campaign conducted in April/May 2012 are exploited. A persistent cloud layer was analyzed, which was probed on 4 consecutive days from 14 to 17 May 2012 in almost the same area and over constant surface conditions. The top altitude of the cloud layer decreased from about 880 m on 14 May to around 200 m on 17 May. The airborne observations obtained during these days were compared to cloud simulations with COSMO using observed and simulated 2-D cloud fields.

The dropsonde measurements were used to initialize cloud simulations with COSMO. COSMO captured the measured cloud altitude, cloud vertical extent, and retrieved cloud optical thickness. The comparison of the horizontal, small-scale cloud inhomogeneities was performed for horizontal 2-D fields of cloud optical thickness τ. For the comparison, the observed 2-D fields of τ_{meas} were averaged to the spatial resolutions of the individual simulations (50 and 100 m).

First, 1-D inhomogeneity parameters were compared. For 100 m resolution, the absolute values of cloud inhomogeneity derived from COSMO are larger by a factor of about 2, as compared to the values obtained from the observations. These differences slightly decrease when the spatial resolution of the simulations is increased by a finer grid of 50 m. However, for both spatial resolutions the cloud inhomogeneity generated by COSMO is too low. This is mainly related to (i) the larger effective spatial resolution ($\approx 3 \times 50$ m, $\approx 3 \times 100$ m) of COSMO and (ii) a mismatch in timing/spacing. For the simulations by COSMO the 1-D inhomogeneity parameters are averaged over several time steps, while for the observations the 1-D inhomogeneity parameters are averaged along the flight track. These results are in agreement with a model intercomparison by Ovchinnikov et al. (2014), who revealed that COSMO underestimates the variance of the vertical wind velocity compared to other LES models and thus may cause an underestimation of the standard deviation of τ_{sim}. However, the different magnitudes of cloud inhomogeneity of the individual days are well covered by COSMO.

Especially on 14 May, the cloud structure showed a distinct directional orientation, while on 15 to 17 May only a slight directional orientation is observed. Brümmer (1999) pointed out that such directed cloud structures are typical for Arctic stratus with cloud top altitudes below 1 km. Contrarily, for Arctic stratus with cloud top altitudes above 1.4 km, cell structures are common. Based on a new method, proposed by Schäfer et al. (2017a), a 2-D analysis using autocorrelation functions is used to examine directional features of the cloud structures. The investigations show that COSMO captures the observed directional structures of the cloud inhomogeneities. The wind directions of the individual cases show a significant correlation with the direction of the predominant structures. During the 4 investigated days, the orientation of the dominant directional structures turned eastwards by the same degree the wind direction changed. Similar results were found by Houze Jr. (1994), who stated that for changing wind shear cloud streets will be orientated along the mean wind direction.

The autocorrelation analysis was also used to derive the characteristic size of the small-scale cloud structures by estimating the decorrelation length ξ_τ, which represents

the distance at which the squared autocorrelation coefficients P^2_τ drop below e^{-2}. The decorrelation lengths P^2_τ were calculated along and across the strongest extent of the derived $P^2_{\tau,meas}$ and $P^2_{\tau,sim}$. For the COSMO simulations (50 m), the observed ξ_τ agree well with the simulations, except on 14 May. In contrast, for the simulations with a spatial resolution of 100 m, COSMO produced small-scale cloud structures with characteristic sizes that are 20 % to 30 % larger compared to the observations. However, for both resolutions, the best agreement was found for the case on 15 May 2012.

It is concluded that the wind direction and the atmospheric boundary layer structure explain the differences on 16 May. In contrast to the other 3 days, a change of the wind direction of about 50° is found close to cloud top. Additionally, the ABL was well mixed on 16 May, which increases the turbulent mixing within in the ABL, and influences the cloud top structure. Local wind field differences at the dropsonde position and the location where the imaging spectrometer measured might be the reason that this was not equally well captured by the simulations and measurements.

Cloud inhomogeneities are a challenge for cloud-resolving models. Not only the spatially averaged magnitude of inhomogeneity but also the directional structure and the interaction with large-scale cloud structures need to be reproduced in the simulations. COSMO performs well, since it correctly represents the directional structures and the general degree of cloud inhomogeneity. The presented statistical methods can also be applied to characterize larger-scale dynamic patterns, if the domain resolves them.

7. References / Literature:

Barrett, A. I., Hogan, R. J., and Forbes, R. M., 2017: Why are mixed-phase altocumulus clouds poorly predicted by large-scale models? Part 1. Physical processes, J. Geophys. Res.-Atmos., 122, 9903–9926

Bierwirth, E., Ehrlich, A., Wendisch, M., Gayet, J.-F., Gourbeyre, C., Dupuy, R., Herber, A., Neuber, R., and Lampert, A., 2013: Optical thickness and effective radius of Arctic boundary-layer clouds retrieved from airborne nadir and imaging spectrometry, Atmos. Meas. Tech., 6, 1189–1200

Brümmer, B., 1999: Roll and Cell Convection in Wintertime Arctic Cold-Air Outbreaks, J. Atmos. Sci., 56, 2613–2636, doi: 10.1175/1520-0469(1999)056<2613:RACCIW>2.0.CO;2.

Costa, A., Meyer, J., Afchine, A., Luebke, A., Günther, G., Dorsey, J. R., Gallagher, M. W., Ehrlich, A., Wendisch, M., Baumgardner, D., Wex, H., and Krämer, M., 2017: Classification of Arctic, midlatitude and tropical clouds in the mixed-phase temperature regime, Atmos. Chem. Phys., 17, 12219–12238

Davis, A., Marshak, A., Gerber, H., and Wiscombe, W., 1999: Horizontal structure of marine boundary layer clouds from centimeter to kilometer scales, J. Geophys. Res., 104, 6123–6144.

Ehrlich, A., Bierwirth, E., Istomina, L., and Wendisch, M., 2017: Combined retrieval of Arctic liquid water cloud and surface snow properties using airborne spectral solar remote sensing, Atmos. Meas. Tech., 10, 3215–3230, doi: 10.5194/amt-10-3215-2017.

Herzog, H.-J., Vogel, G., and Schubert, U., 2002: LLM – a nonhydrostatic model applied to high-resolving simulations of turbulent fluxes over heterogeneous terrain, Theor. Appl. Climatol., 73, 67–86

Houze Jr., R. A, 1994.: Cloud Dynamics, International Geophysics series, Academic Press, San Diego, USA, and London, UK, 53, p. 166.

Iwabuchi, H. and Hayasaka, T., 2002: Effects of cloud horizontal inhomogeneity on the optical thickness retrieved from moderate-resolution satellite data, J. Atmos. Sci., 59, 2227–2242.

Klingebiel, M., de Lozar, A., Molleker, S., Weigel, R., Roth, A., Schmidt, L., Meyer, J., Ehrlich, A., Neuber, R., Wendisch, M., and Borrmann, S., 2015: Arctic low-level boundary layer clouds: in situ measurements and simulations of mono- and bimodal supercooled droplet size distributions at the top layer of liquid phase clouds, Atmos. Chem. Phys., 15, 617–631, doi: 10.5194/acp-15-617-2015.

Kopec, M. K., Malinowski, S. P., and Piotrowski, Z. P., 2016: Effects of wind shear and radiative cooling on the stratocumulustopped boundary layer, Q. J. Roy. Meteor. Soc., 142, 3222–3233.

Korolev, A., 2007: Limitations of the Wegener–Bergeron–Findeisen Mechanism in the Evolution of Mixed-Phase Clouds, J. Atmos. Sci., 64, 3372–3375, doi: 10.1175/JAS4035.1.

Langhans, W., Schmidli, J., and Szintai, B., 2012: A Smagorinsky-Lilly turbulence closure for COSMO-LES: Implementation and comparison to ARPS, COSMO newsletter, 12, 20–31.

Lawson, R. P., Stamnes, K., Stamnes, J., Zmarzly, P., Koskuliks, J., Roden, C., Mo, Q., Carrithers, M., and Bland, G. L., 2010: Deployment of a Tethered-Balloon System for Microphysics and Radiative Measurements in Mixed-Phase Clouds at NyÅlesund and South Pole, J. Atmos. Ocean. Tech., 28, 656–670.

Lindsay, R., Wensnahan, M., Schweiger, A., and Zhang, J., 2014: Evaluation of seven different atmospheric reanalysis products in the arctic, J. Climate, 27, 2588–2605, doi: 10.1175/JCLID-13-00014.1.

Loewe, K., Ekman, A. M. L., Paukert, M., Sedlar, J., Tjernström, M., and Hoose, C., 2017: Modelling micro- and macrophysical contributors to the dissipation of an Arctic mixed-phase cloud during the Arctic Summer Cloud Ocean Study (ASCOS), Atmos. Chem. Phys., 17, 6693–6704.

Mellado, J. P., 2017: Cloud-Top Entrainment in Stratocumulus Clouds, Annu. Rev. Fluid Mech., 49, 145–169.

Morrison, H., de Boer, G., Feingold, G., Harrington, J., Shupe, M. D., and Sulia, K., 2012: Resilience of persistent Arctic mixed-phase clouds, Nat. Geosci., 5, 11–17.

Ovchinnikov, M., Ackerman, A. S., Avramov, A., Cheng, A., Fan, J., Fridlind, A. M., Ghan, S., Harrington, J., Hoose, C., Korolev, A., McFarquhar, G. M., Morrison, H., Paukert, M., Savre, J., Shipway, B. J., Shupe, M. D., Solomon, A., and Sulia, K., 2014: Intercomparison of large-eddy simulations of Arctic mixed-phase clouds: Importance of ice size distribution assumptions, J. Adv. Model. Earth Syst., 6, 223–248.

Paukert, M. and Hoose, C., 2014: Modeling immersion freezing with aerosol-dependent prognostic ice nuclei in Arctic mixedphase clouds, J. Geophys. Res.-Atmos., 14, 9073–9092.

Pedersen, J. G., Malinowski, S. P., and Grabowski, W. W., 2016: Resolution and domain-size sensitivity in implicit large-eddy simulation of the stratocumulus-topped boundary layer, J. Adv. Model. Earth Syst., 8, 885–903, doi: 10.1002/2015MS000572.

Ritter, B. and Geleyn, J.-F., 1992: A Comprehensive Radiation Scheme for Numerical Weather Prediction Models with Potential Applications in Climate Simulations, Mon. Weather Rev., 120, 303–325.

Schäfer, M., Bierwirth, E., Ehrlich, A., Jäkel, E., and Wendisch, M., 2015: Airborne observations and simulations of three-dimensional radiative interactions between Arctic boundary layer clouds and ice floes, Atmos. Chem. Phys., 15, 8147–8163, doi:10.5194/acp-15-8147-2015.

Schäfer, M., Bierwirth, E., Ehrlich, A., Jäkel, E., Werner, F., and Wendisch, M., 2017a: Directional, horizontal inhomogeneities of cloud optical thickness fields retrieved from ground-based and airbornespectral imaging, Atmos. Chem. Phys., 17, 2359–2372, doi:10.5194/acp-17-2359-2017.

Schäfer, M., Bierwirth, E., Ehrlich, A., Jäkel, E., Werner, F., and Wendisch, M., 2017a: Directional, horizontal inhomogeneities of cloud optical thickness fields retrieved from ground-based and airbornespectral imaging, Atmos. Chem. Phys., 17, 2359–2372, doi: 10.5194/acp-17-2359-2017.

Schäfer, M., Loewe, K., Ehrlich, A., Hoose, C., and Wendisch, M., 2018: Simulated and observed horizontal inhomogeneities of optical thickness of Arctic stratus, Atmos. Chem. Phys., 18, 13115-13133, doi:10.5194/acp-18-13115-2018

Schättler, U., Doms, G., and Schraff, C. 2015: A description of the non-hydrostatic regional COSMO-model, part VII: user's guide, available at: http://www.cosmo-model.org (last access: 11 September 2018).

Seifert, A. and Beheng, K. D., 2006: A two-moment cloud microphysics parameterization for mixed-phase clouds. Part 1: Model description, Meteorol. Atmos. Phys., 92, 45–66.

Serreze, M. C. and Barry, R. G., 2011: Processes and impacts of Arctic amplification: A research synthesis, Global Planet. Change, 77, 85–96, doi:10.1016/j.gloplacha.2011.03.004.

Shupe, M. D. and Intrieri, J. M., 2004: Cloud radiative forcing of the Arctic surface: The influence of cloud properties, surface albedo, and solar zenith angle, J. Climate, 17, 616–628.

Shupe, M. D., Kollias, P., Persson, P. O. G., and Mc- Farquhar, G. M., 2008: Vertical Motions in Arctic Mixed-Phase Stratiform Clouds, J. Atmos. Sci., 65, 1304–1321, doi:10.1175/2007JAS2479.1.

Shupe, M. D., Walden, V. P., Eloranta, E., Uttal, T., Campbell, J. R., Starkweather, S. M., and Shiobara, M., 2011: Clouds at Arctic Atmospheric Observatories. Part I: Occurrence and Macrophysical Properties, J. Appl. Meteorol. Clim., 50, 626–644, doi10.1175/2010JAMC2467.1.

Skamarock, W. C., 2004: Evaluating Mesoscale NWP Models Using Kinetic Energy Spectra, Mon. Weather Rev., 132, 3019–3032, doi:10.1175/MWR2830.1.

Szczap, F., Isaka, H., Saute, M., and Guillemet, B., 2000: Effective radiative properties of bounded cascade nonabsorbing clouds, J. Geophys. Res., 105, 20617–20633.

Vavrus, S., 2004: The Impact of Cloud Feedbacks on Arctic Climate under Greenhouse Forcing, J. Climate, 17, 603–615, doi:10.1175/1520-0442(2004)017<0603:TIOCFO>2.0.CO;2.

Vochezer, P., Järvinen, E., Wagner, R., Kupiszewski, P., Leisner, T., and Schnaiter, M., 2016: In situ characterization of mixed phase clouds using the Small Ice Detector and the Particle Phase Discriminator, Atmos. Meas. Tech., 9, 159–177, doi:10.5194/amt-9-159-2016.

Wendisch, M., Yang, P., and Ehrlich, A., 2013: Amplified climate changes in the Arctic: Role of clouds and atmospheric radiation, 132, 1–34, Sitzungsberichte der Sächsischen Akademie der Wissenschaften zu Leipzig, Mathematisch-Naturwissenschaftliche Klasse, S. Hirzel Verlag, Stuttgart/Leipzig.

Wendisch, M., Brückner, M., Burrows, J. P., Crewell, S., Dethloff, K., Ebell, K., Lüpkes, Ch., Macke, A., Notholt, J., Quaas, J., Rinke, A., and Tegen, I., 2017: Understanding causes and effects of rapid warming in the Arctic, EOS, 98, 22–26, doi:10.1029/2017EO064803.

Charakterisierung der Eigenschaften von mariner Stratocumulusbewölkung über den Azoren

Ritter, O.[1], Lauermann F.[2], Wendisch M.[3]

[1] *Institut für Meteorologie, Stephanstraße 3 04103 Leipzig, Email: oscar.ritter@web.de*
[2] *Institut für Meteorologie, Stephanstraße 3 04103 Leipzig,*
Email: felix.lauermann@uni-leipzig.de
[3] *Institut für Meteorologie, Stephanstraße 3 04103 Leipzig, Email: m.wendisch@uni-leipzig.de*

Zusammenfassung

Auf der Azoreninsel Graciosa, etwa 1600 km westlich von Portugal, betreibt das U.S. Department of Energy eine American Radiation Measurement (ARM) Station, welche mit einer Vielzahl von Messgeräten ausgestattet ist. Durch ihre Lage im subtropischen Hochdruckgürtel eignet sich diese Station gut zur Erforschung von mariner Stratocumulusbewölkung. Für eine Klimatologie der Eigenschaften dieser Bewölkung wurden Messwerte von Radiosonden, einem Ceilometer, einem Distrometer und einem Mikrowellenradiometer aus dem Zeitraum vom 01. März 2014 bis 31. August 2018 verwendet. Daraus wurde der Tages- und Jahresgang der Wolkenhöhe und -dicke, des Flüssigwasserpfades, des Entkopplungs- und Niederschlagsverhaltens und der Inversionsstärke abgeleitet. Die Auswertung basiert auf einer Methode von Zhang et al. (2010) zur Detektion von Wolkenschichten aus Radiosondenmessungen, die für die Abgrenzung mariner Stratocumulusbewölkung von anderen Wolkenarten angepasst und anschließend mit den Messungen eines Ka-Band-Wolkenradars evaluiert wurde. Während die Parameter im Tagesgang nur geringe Änderungen zwischen 00 UTC und 12 UTC aufwiesen, konnten im Jahresgang deutliche Variationen bei Wolkenhöhe, Niederschlagsverhalten, Entkopplung und Inversionstärke gezeigt werden. Die beobachteten Variationen wurden mit den Jahresgängen der solaren Einstrahlung, der Temperatur sowie der synoptischen Variabilität über den Azoren verglichen.

Summary

The U.S. Department of Energy operates an American Radiation Measurement (ARM) station on Graciosa (Azores), an island located approximately 1600 km west of Portugal. Due to the wide variety of installed measuring devices and its location in the subtropical belt of high pressure the station is well suited for studying marine stratocumulus. To derive a climatology of the properties of these clouds, data from radiosondes, a ceilometer, a disdrometer and a microwave radiometer were used for the period from 1st March 2014 to 31st August 2018 to get the daily and annual cycle of cloud height and thickness, liquid water path, precipitation, inversion strength and the presence of decoupling. The evaluation is based on a method developed by Zhang et al. (2010) to detect cloud layers from moisture profiles in the sounding data. The method was adapted for the distinction between marine stratocumulus and other cloud types. For the evaluation of the method data from a Ka-band cloud radar were used. While only minor changes occurred in the daily variability of the properties, a clear annual cycle was observed for cloud height,

precipitation, inversion strength and decoupling of the stratocumulus. The observed variations were compared with the annual cycles of solar irradiance, temperature and the synoptic patterns over the Azores.

1 Einleitung

Aufgrund der Zunahme der optischen Dicke, die mit einer Anhäufung kondensierter Wassertropfen bzw. Eispartikel einhergeht, haben Wolken einen bedeutenden Einfluss auf die lokale und globale Strahlungsbilanz. Die Kenntnis ihrer Eigenschaften sowie ihrer räumlichen und zeitlichen Variabilität bildet daher eine entscheidende Grundlage für die korrekte Implementierung dieser Wolken in numerischen Wetter- und Klimamodellen, da diese Variabilität stark zu den Prognoseunsicherheiten beiträgt. (vgl. Dufresne and Bony, 2008).

Stratocumulus (im Folgenden: Sc) bedeckt im Mittel rund 23 % der Ozean- und 12 % der Landoberfläche und hat in den subtropischen Gewässern vor den Westseiten der Kontinente seine Häufigkeitsmaxima (Wood, 2012). Um die Eigenschaften dieser Bewölkung zu quantifizieren ist es daher sinnvoll, einen Beobachtungsort in diesen Regionen auszuwählen. Dies steigerte die Attraktivität der Azoreninsel Graciosa als Standort für ein Beobachtungsprogramm der Forschungseinrichtung für atmosphärische Strahlungsmessungen (Atmospheric Radiation Measurement, ARM), das auf dem Flughafengelände im Norden der Insel im Jahr 2013 begonnen wurde und sich auf die Erfassung mariner Stratocumulusbewölkung (im Folgenden: MSc) spezialisiert (vgl. Nitschke and de Azevedo, 2015). Hier kann Stratocumulus, zum Teil in Kombination mit Cumulus, in 30-40 % des Jahres detektiert werden. (Rémillard et al., 2012). Die Wolken bilden sich dabei zum einen rückseitig von außertropischen Zyklonen, deren Zugbahnen nördlich der Azoren verlaufen und zum anderen in der feuchten marinen Grenzschicht, welche von einer stabilen Schichtung der subtropischen Hochdruckzone vertikal begrenzt wird. (Rémillard et al., 2012; Rémillard and Tselioudis, 2015).

Die hier vorgestellten Ergebnisse zur Klimatologie von MSc über der Azoreninsel Graciosa wurden im Rahmen einer Bachelorarbeit erarbeitet. Betrachtet wurden die Eigenschaften der marinen Grenzschicht (u.a. Inversionshöhe und -mächtigkeit) sowie des Sc (Wolkenhöhe und -dicke, Niederschlagsverhalten, Flüssigwasserpfad (LWP) und Entkopplung) hinsichtlich ihres Tages- und Jahresganges. Die Grundlage bildeten Messwerte von Radiosonden, einem Mikrowellenradiometer, Ceilometer und Distrometer im Zeitraum von März 2014 bis August 2018. Dazu wurde zunächst eine Auswertemethode für Radiosondenmessungen weiterentwickelt, evaluiert und anschließend in Kombination mit den weiteren Messgeräten für die Klimatologie verwendet.

2 Datengrundlage

Die Grundlage der gesamten Methodik und Auswertung bilden die Messwerte von Radiosondenaufstiegen, die mindestens 2 mal am Tag vom Observatorium auf dem Gelände des Flughafens der Insel Graciosa (39°5′29.76″ N, 28°1′32.52″ W, 15 m ü NN) gestartet wurden (Datenquelle: ARM, 2013a). Die Sonden des Typs RS92 von der Firma Vaisala zeichnen die Messdaten mit einer Frequenz von 0,5 Hz auf. Tabelle 1 zeigt die jährliche Anzahl der in mindestens 3000 m Höhe aufgestiegenen Radiosonden im Auswertungszeitraum vom 01. März 2014 bis 31. August 2018. Regelmäßige Messungen wurden nur zu den Hauptterminen 00 UTC und 12 UTC durchgeführt, weshalb ausschließlich diese Termine ausgewertet wurden. Ergänzt wurden die halbtäglichen Aufstiege durch weitere Sondenstarts, unter anderem im Rahmen von Messkampangen. Fanden diese innerhalb eines Zeitfensters von ± 1 h um den 00 UTC bzw. 12 UTC-Termin statt, wurden sie in die Auswertung einbezogen.

Tabelle 1: Anzahl der bis 3000 m vollendeten Radiosondenaufstiege im Zeitraum März 2014 - August 2018

	23.30 UTC	**05.30 UTC**	**11.30 UTC**	**17.30 UTC**	**Summe**
2014	311	-	315	-	626
2015	378	-	400	1	778
2016	407	-	410	-	817
2017	398	20	405	20	803
2018	224	20	229	19	453
Summe	**1718**	**40**	**1759**	**40**	**3557**

Zur Bestimmung und Evaluation der Wolkenuntergrenzenhöhe wurden die Messwerte eines Ceilometers verwendet (Daten: ARM, 2013b). Ergänzend zur Radiosondenmessung liefert außerdem ein 3-Kanal-Mikrowellenradiometer (MWR) mit dem Frequenzen 23,8 GHZ, 31,4 GHz und 89 GHz Informationen zum LWP (Daten: ARM, 2014a). Weiterhin wurde zur Bestimmung des Niederschlagsanteils der Datensatz eines optischen Partikelgrößen- und Geschwindigkeitsdistrometers einbezogen (Daten: ARM, 2014b). Von den genannten Messgeräten sind im gesamten Auswertezeitraum Messwerte verfügbar. Der Anteil der fehlenden Messwerte beschränkt sich für das Distrometer auf 0,5%, für das Ceilometer auf 1,6% und für das MWR auf 1,9%.

Die Evaluation und Anpassung der Auswertemethode wurde mithilfe von Messdaten eines Ka-Band-Wolkenradars (35 GHz) durchgeführt, welche für den Zeitraum vom 01. Juni 2017 bis 31. August 2017 zur Verfügung standen (Daten: ARM, 2015). In diesem Zeitraum gab es während der Radiosondenaufstiege keine Ausfälle des Wolkenradars, sodass hier eine vollständige Datenreihe vorliegt.

3 Auswertemethode

Die Grundlage der Auswertung bildet eine ursprünglich von Wang and Rossow (1995) entwickelte und von Zhang et al. (2010) angepasste Methode zur Detektion von Wolkenschichten anhand des vertikalen Feuchteverlaufs. Dafür werden Grenzwerte der relativen Feuchte (RH) definiert, um Feuchteschichten und Wolkenschichten in der Atmosphäre festzustellen. Die Grenzwerte liegen bei 92% RH für eine Feuchteschicht, 95% RH für eine Wolkenschicht und 84% als Zwischenfeuchtekriterium für den Bereich zwischen zwei detektierten Schichten. Die Grenzwerte zur Wolkenbestimmung liegen im Untersättigungsbereich, da es durch die horizontale Verlagerung der Radiosonde dazu kommen kann, dass diese eine durchbrochene Wolkenschicht in einem trockeneren Bereich passiert und im Falle von 100 % RH als Kriterium diese Schicht dann fälschlicherweise nicht als Wolkenschicht detektiert werden würde.

Die folgenden Kriterien basieren auf einer Betrachtung des vertikalen Feuchteverlaufs vom Boden her:

(1) Die Basis einer Feuchteschicht wurde markiert, wenn der Feuchtegrenzwert das erste Mal überschritten wurde, wobei unmittelbar folgende Schichten mit einer RH über dem Feuchtegrenzwert zur Feuchteschicht hinzugefügt wurden.

(2) Die Oberkante einer Feuchteschicht wurde markiert, wenn die RH unter den Feuchtegrenzwert fällt oder die Oberkante des ausgewerteten Höhenbereichs erreicht wurde.

(3) Eine Feuchteschicht galt als Wolkenschicht, wenn innerhalb der Feuchteschicht die RH mindestens einmal den Wolkengrenzwert überschritt.

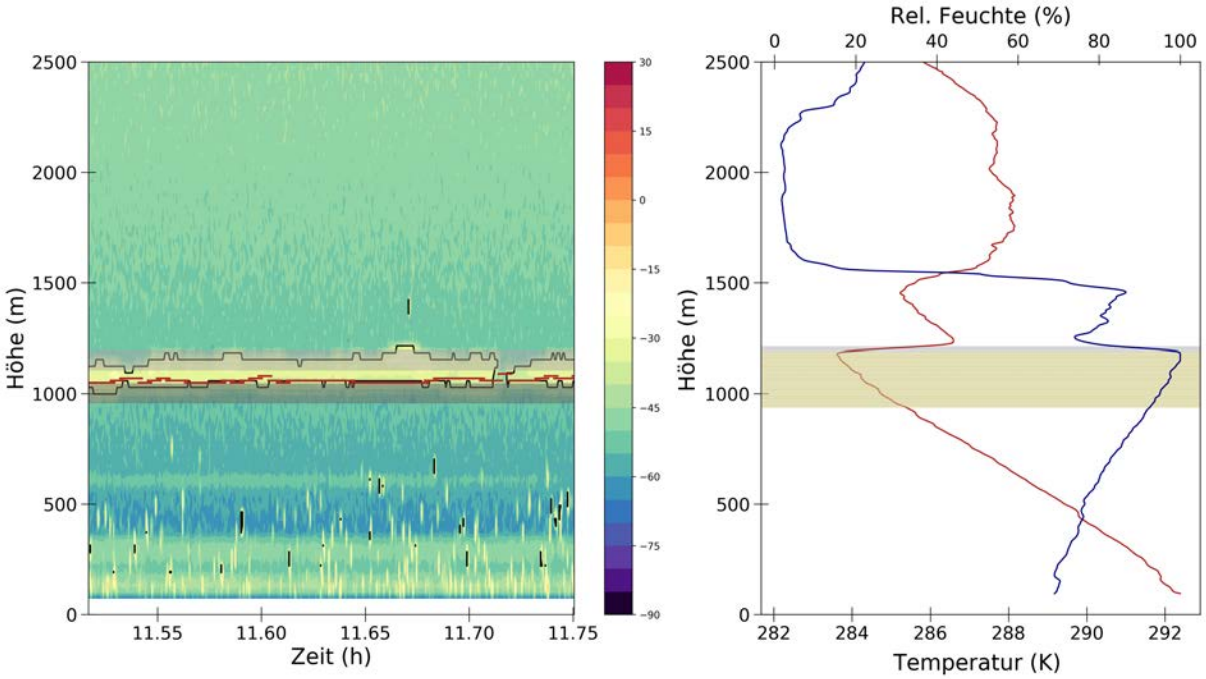

Abbildung 1: links: vom Ka-Band-Wolkenradar gemessene Reflektivität und daraus abgeleitete Wolkengrenzen (grau) sowie Wolkenuntergrenze aus Ceilometermessungen (rot), rechts: Vertikalprofil von Temperatur und relativer Feuchte aus dem Radiosondenaufstieg mit detektierten Wolkenschichten (grau) und Sc-Schichten (auf Inversion angepasste Wolkenoberkante) (beige)

(4) Die Unterkante von Wolkenschichten wurde auf 100 m Höhe festgelegt und alle Wolkenschichten mit Oberkanten unterhalb dieser Höhe aussortiert.

(5) Wolken mit weniger als 30 m Dicke wurden aussortiert (vorwiegend aufgrund der Vergleichbarkeit mit dem verwendeten Wolkenradar und zur Entfernung turbulenter Feuchtespitzen aus der Detektion).

(6) Waren zwei detektierte Wolkenschichten vertikal weniger als 100 m voneinander entfernt oder lag die RH zwischen beiden Schichten stets über dem Zwischenfeuchtekriterium, wurden sie zusammengefasst.

Zusätzlich zur Wolkenbestimmung wurde die Methode zur Unterscheidung von Stratocumulusbewölkung und anderen tiefen Wolken (v.a. Cumulus) weiterentwickelt. Dazu wurde das Temperatur- und Feuchteprofil in der Umgebung detektierter Wolkenschichten auf das Vorhandensein von Absinkinversionen überprüft. Als Kriterium für eine Absinkinversion galt ein kontinuierlicher vertikaler Temperaturanstieg über mindestens 30 m oder 1 K unter gleichzeitigen Absinken der relativen Feuchte. Nach der Bestimmung aller potentiellen Inversionen wurde in einem Höhenbereich von 150 m unterhalb und 30 m oberhalb einer vorher bestimmten Wolkenobergrenze nach einer Inversion gesucht. Konnte diese detektiert werden, galt die Wolkenschicht als Stratocumulusschicht. Nachfolgend wurde die neue Wolkenobergrenze für die detektierte Stratocumulusschicht auf die Unterkante der Temperaturinversion festgelegt. Lag dennoch eine weitere Inversion unterhalb der Stratocumulusschicht, wurde dieser MSc als entkoppelt eingestuft.

In Abbildung 1 ist das Auswerteverfahren für einen Fall mit MSc im Vergleich zur Auswertung des Ka-Band-Wolkenradars und des Ceilometers dargestellt.

3.1 Verifikation der Methode

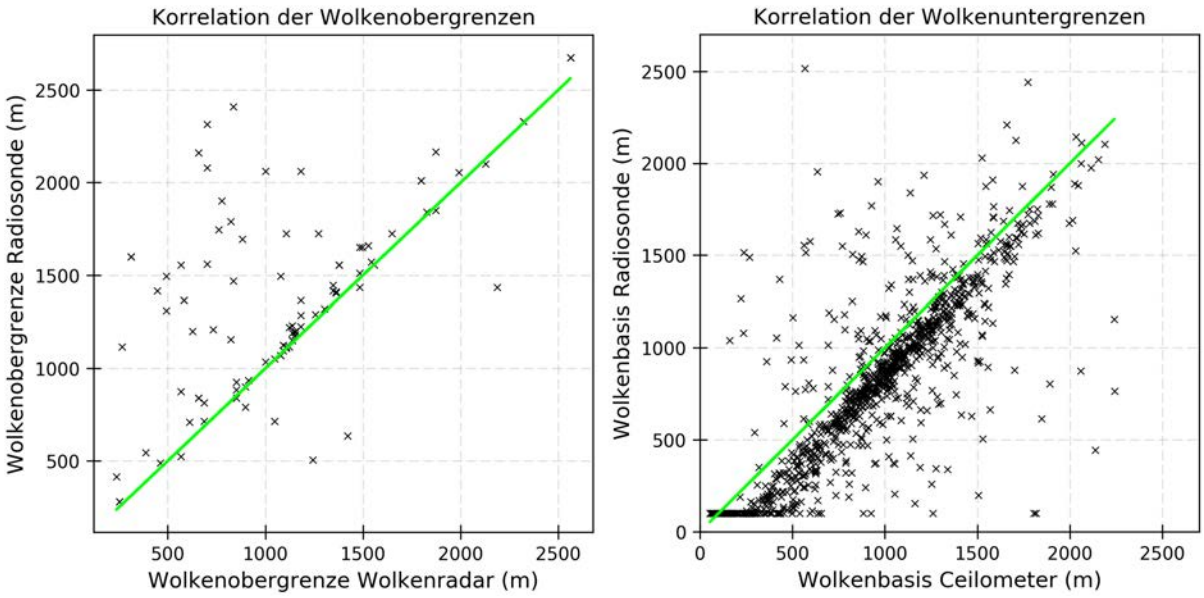

Abbildung 2: links: Evaluation mittels Radiosondenmethode ermittelten Wolkenobergrenzen im Vergleich zur Wolkenradarmessung, rechts: Evaluation der ermittelten Wolkenuntergrenzen im Vergleich zur Ceilometermessung

Die Anpassung der Methode erfolgte über einen optischen Vergleich mit den Radarbildern des Ka-Band-Wolkenradars und wurde anschließend mit den Ergebnissen des Wolkenradars und des Ceilometers korreliert. Um das Ka-Band-Wolkenradar als Referenzgerät nutzen zu können, war es notwendig, auch aus den Reflektivitätsdaten Wolkenschichten abzuleiten und sie so vom Hintergrundrauschen abzuheben. Dazu wurde als Schwellwert eine Reflektivität von -40 dB_Z ausgewählt (vgl. Grenzhäuser, 2014). Um Wolken von Fehlechos (z.B. durch Insekten) zu unterscheiden, wurde eine Wolke nur als solche angesehen, wenn die Reflektivität für mindetens zwei Zeitschritte (4 s) über dem Schwellwert lag. Die Höhen von Wolkenuntergrenzen bzw. Wolkenobergrenzen wurden anschließend über eine Häufigkeitsverteilung abgeleitet.

Abbildung 2 zeigt die mittels Radiosondenmethode ermittelten Wolkenobergrenzen im Vergleich zum Median der Wolkenobergrenzen aus dem Wolkenradar und die ermittelten Wolkenuntergrenzen im Vergleich zu den Auswertungen des Ceilometers. Die 1:1-Linie markiert den theoretischen Verlauf eines vollständigen Zusammenhangs zwischen beiden Detektionsmethoden. Für beide Vergleiche ergaben sich starke Korrelationen mit einem Korrelationskoeffizienten von 0,88 für die Wolkenobergrenzen und 0,87 für die Wolkenuntergrenzen. Auffällig sind die teils deutlichen Überschätzungen der Wolkenobergrenze durch die Radiosondenmethode. Ursächlich hierfür zeigt sich zum einen die Verfrachtung der Radiosonde mit dem Wind und zum anderen das Evaluationsverfahren beim Auftreten mehrschichtiger Sc-Bewölkung. Letzteres führt dazu, dass mehrere Wolkenschichten nur einem Median der Radarmessung zugeordnet werden.

Beim Vergleich der Wolkenuntergrenzen fällt dagegen eine systematische Unterschätzung der Radiosondenmethde auf. Als Grund wird unter anderem die Auswahl der Grenzwerte für Feuchte- und Wolkenschichten angenommen, wobei diese offenbar zu niedrig gewählt wurden. Da die Gradienten im Feuchteverlauf an der Wolkenuntergrenze oftmals schwächer sind als an der Wolkenobergrenze, zeigt sich die Abweichung hier deutlicher. Als weitere Ursachen für die zahlreichen Ausreißer nach unten gelten das Auftreten von ”virgae” unterhalb des MSc und die Fehlinterpretation flacher und sehr feuchter Grenzschichten als Wolkenschichten.

4 Ergebnisse

4.1 Tagesgang der Wolkeneigenschaften

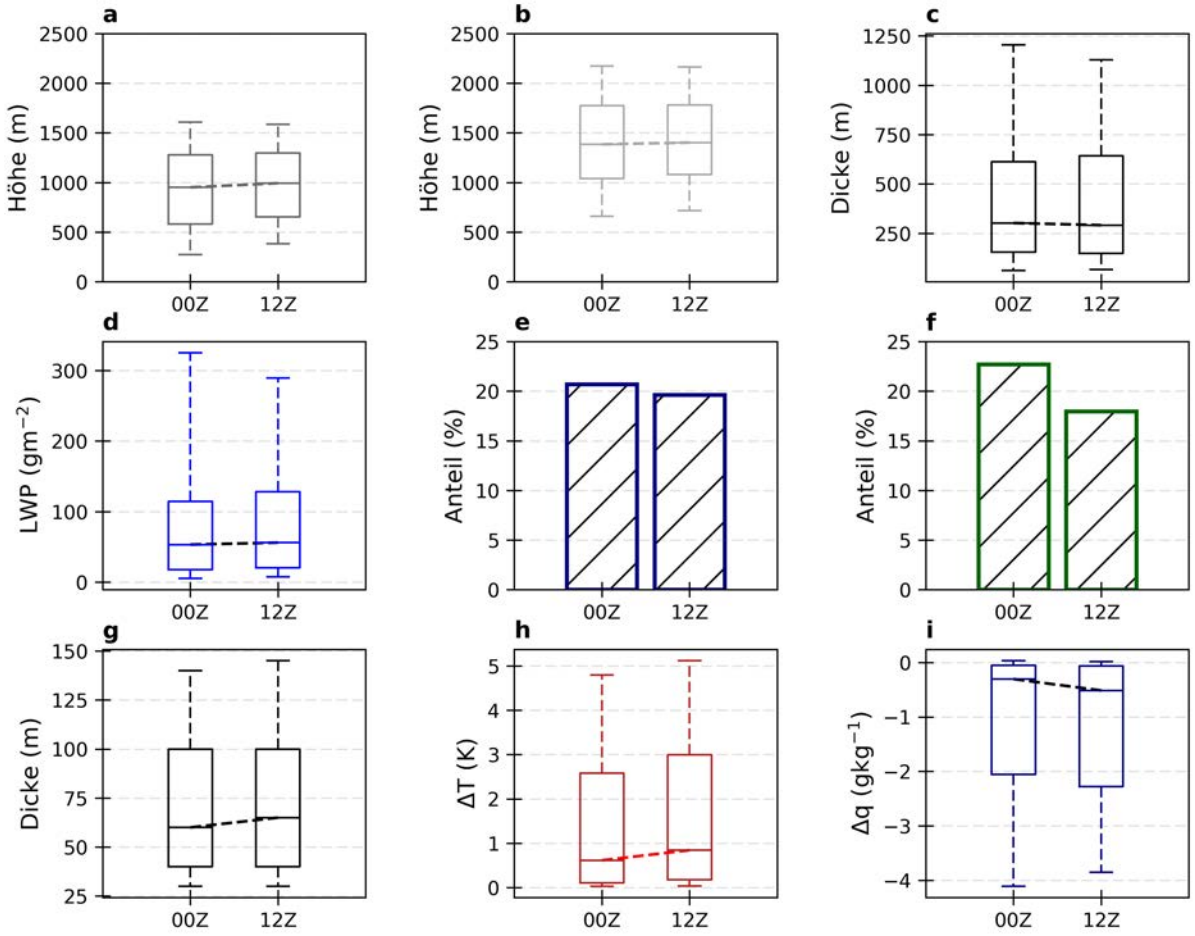

Abbildung 3: Vergleich der Wolkenuntergrenze (a), Wolkenobergrenze (b), Wolkendicke (c), des Flüssigwassergehalts (LWP) (d), der Niederschlagshäufigkeit (e), Häufigkeit von entkoppeltem MSc (f), Inversionsdicke (g), Änderung der Temperatur ΔT (h) sowie Änderung des Mischungsverhältnisses Δq innerhalb der Inversion (i) zwischen den Radiosondenaufstiegen 00 UTC und 12 UTC

Die Tagesgänge der Wolken- und Inversionseigenschaften wurden mit der Radiosondenmethode ausgewertet. Verwendet wurden alle zur Verfügung stehenden Messwerte im Auswertezeitraum vom 01. März 2014 bis 31. August 2018. Da allerdings nur die Radiosondenaufstiege um 00 UTC und 12 UTC kontinuierlich durchgeführt wurden, beschränkt sich die Darstellung auch auf diese beiden Termine.

Abbildung 3 zeigt die Auswertung der Tagesgänge, wobei sich die Diagramme a bis f auf die Wolkeneigenschaften und die Diagramme g bis i auf die Inversionseigenschaften beziehen. Für die Auswertung der Wolkenuntergrenze wurden anstelle der Radiosondenmethode die Messwerte des Ceilometers verwendet, da die systematische Abweichung der Radiosondenmethode die Ergebnisse zur sehr verfälschen würde. Die Boxplots setzen sich jeweils aus dem Median der Messwerte, dem 25. bzw. 75. Perzentil als Außenränder der Boxen und dem 10. bzw. 90. Perzentil zusammen, die die Antennen der Boxplots aufspannen. Messwerte, die außerhalb dieser Perzentile liegen, werden nicht dargestellt.

Auffällig ist eine leichte Zunahme der Wolkenhöhen (a und b)zwischen 00 UTC und 12 UTC

im Median, wobei inbesondere die Zahl sehr niedriger Unter- bzw. Obergrenzen um 12 UTC gegenüber 00 UTC abnimmt. Hier wird die Fehlinterpretation von Nebel bzw. Hochnebel als MSc vermutet. Dieser wird durch solare Einstrahlung und turbulente Wärmeströme in der Grenzschicht im Tagesverlauf oft aufgelöst. Die Mediane der Wolkendicke (c) und des LWP (d) sind dagegen weitgehend konstant, hier fällt vor allem die Abnahme des 90. Perzentils auf. Bei der Niederschlagshäufigkeit (e) kommt es dagegen im Tagesverlauf zu einer leichten Abnahme. Dies unterstreicht, dass LWP und Niederschlagsrate direkt miteinander zusammenhängen und hohe LWP notwendig sind, damit ausfallender Niederschlag auch den Boden erreicht.

Weiterhin zeigt Abbildung 3(f) einen kleineren Anteil an entkoppeltem MSc zum 12 UTC-Zeitpunkt. Die ermittelten Anteile liegen außerdem im Vergleich zur Auswertung von Rémillard et al. (2012), die in 93% der Fälle eine Übergangschicht registrieren konnten, deutlich niedriger. Hier wird die Ursache in der abweichenden Auswertemethode für entkoppelte Grenzschichten gesehen, da Rémillard et al. (2012) das Entkopplungskriterium anhand von Gradienten im Temperatur- und Feuchteverlauf und nicht anhand von Temperaturinversionen festlegten. Der beobachtete Tagesgang widerspricht der theoretischen Auffassung einer Stabilsierung der marinen Grenzschicht durch solare Einstrahlung. Allerdings ist der Aufbau einer stabilen Zwischenschicht mit einer Inversion gegenüber dem solaren Tagesgang verzögert, sodass die Entkopplung vorwiegend in den Nachmittags- und Abendstunden beobachtet werden kann (Bougeault, 1985).

Der Median der vertikalen Mächtigkeit der Inversion (g) nimmt zwischen den Auswerteterminen geringfügig zu, während die Quartile konstant bleiben. Die untere Grenze der Inversionsdicke wird dabei durch das Auswertekriterium auf 30 m festgelegt. Deutlichere Unterschiede zeigen sich beim Temperaturanstieg (h) und der Änderung des Wasserdampfmischungsverhältnisses an der Inversion (i). Sowohl die Temperatur- als auch die Feuchteänderung fällt um 12 UTC stärker als um 00 UTC aus. Auch dieses Ergebnis widerspricht der theoretischen Auffassung einer stärkeren Erwärmung der oberen Wolkenschichten durch Absorption solarer Strahlung, welche zur Abschwächung des Temperaturgradienten führen sollte. Als Ursache für die beobachtete Vergrößerung des Temperaturanstiegs zur Mittagszeit wird daher die Verzögerung der langwelligen Ausstrahlung an der Wolkenoberseite nach Sonnenuntergang angenommen, wenn die Stratocumulusdecke im Tagesverlauf aufgebrochen ist (vgl. Wyant et al., 1997). Inbesondere in den Sommermonaten führt dies zu einer Abschwächung der lokalen Abkühlung an der Wolkenobergrenze. Diese Hypothese muss allerdings durch weitere Auswertungen, inbesondere zur Abhängigkeit des Temperaturanstiegs vom Wolkenbedeckungsgrad oder dem Entkopplungsverhalten, genauer betrachtet werden.

4.2 Jahresgang der Wolkeneigenschaften

Abbildung 4 zeigt die monatliche Verteilung der Wolkeneigenschaften. Auffällig ist ein deutlicher Jahresgang der Wolkenhöhen (a und b) auch unter Einbezug der Streuung mit Maxima im April und September und einem Minimum in den Sommermonaten. Der Jahresgang zeigt keinen direkten Zusammenhang zum Jahresgang der Meeresoberflächentemperaturen oder der solaren Einstrahlung im subtropischen Nordatlantik (vgl. Yashayaev and Zveryaev, 2001). Daher wird die Ursache in der synoptischen Variabilität über den Azoren vermutet.

Im Frühjahr und Frühherbst befinden sich die Azoren oftmals rückseitig des subtropischen Hochdruckgebiets in einer südwestlichen Strömung (Mechem et al., 2018). Hier ist die untere Troposphäre oftmals noch stabil geschichtet, die Advektion wärmerer Luftmassen und die fortschreitende Umwandlung von vorhandenem MSc führt jedoch zu einem Anstieg der Grenzschichthöhe. Damit einhergehend zeigt Abbildung 4f auch einen erhöhten Anteil an entkoppeltem MSc (f) zu diesen Jahreszeiten.

In den Sommermonaten liegen die Inseln eher keilvorderseitig in einer nordwestlichen Strö-

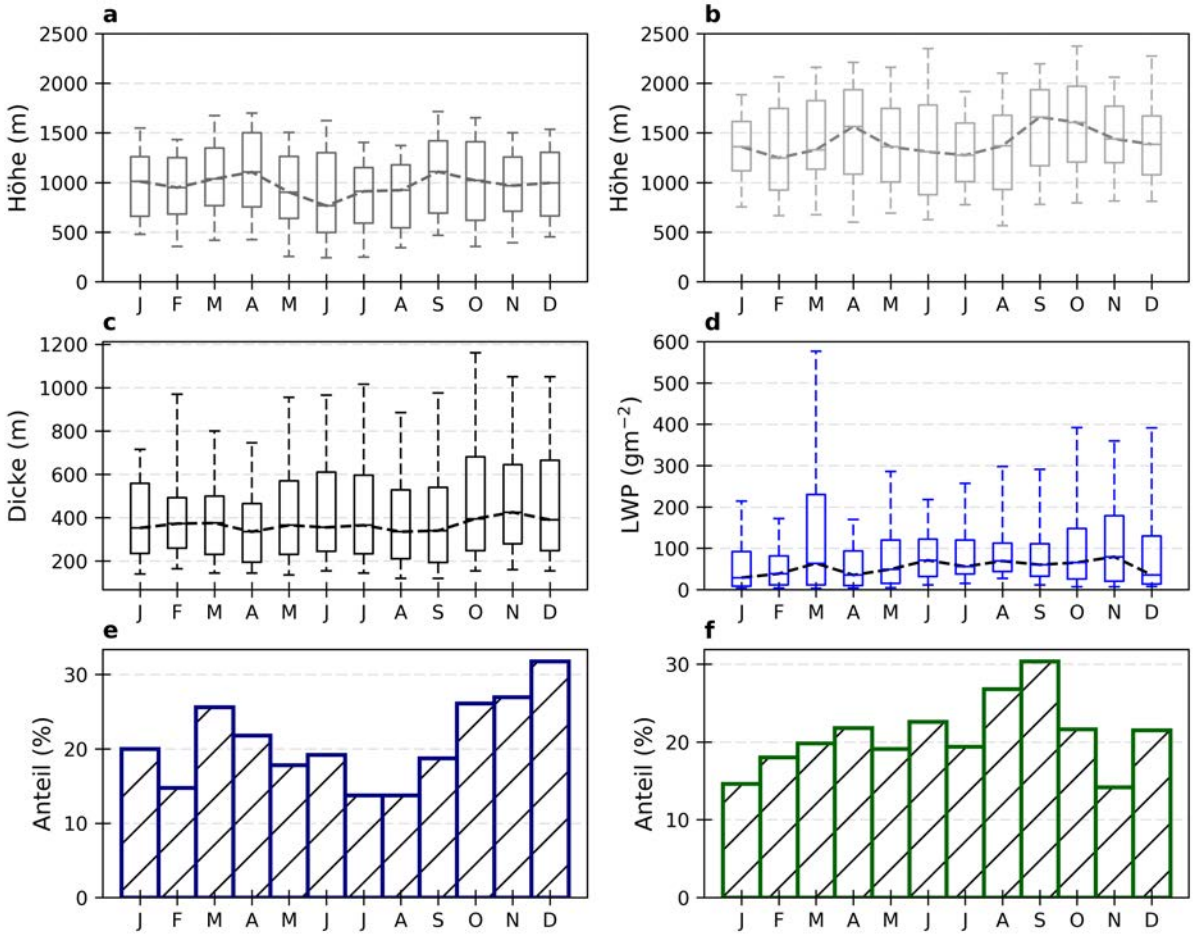

Abbildung 4: Jahresgang der Wolkenuntergrenze (a), Wolkenobergrenze (b), Wolkendicke (c), des Flüssigwasserpfades (d), der Niederschlagshäufigkeit (e) und der Häufigkeit von entkoppeltem MSc (f)

mung, wodurch unter stärkeren Absinkbewegungen kältere Luftmassen mit flachen Grenzschichten advehiert werden. Entsprechend hoch ist auch der Anteil sehr flacher Stratocumulusbewölkung an der Gesamtbewölkung in den Sommermonaten (Rémillard and Tselioudis, 2015). Allerdings führt die starke solare Einstrahlung in den Sommermonaten zu einem beschleunigten Entkopplungsprozess, sodass sich bei der Häufigkeit entkoppelter Bewölkung kein deutliches Minimum zeigt.

In den Wintermonaten wurde im Allgemeinen niedrigerer MSc beobachtet, welcher zudem seltener entkoppelt war. Hier lässt sich eine Verbindung zur verstärkten Tiefdruckaktivität unmittelbar nördlich der Azoren herstellen, wodurch die Windgeschwindigkeit und die Intensität von Kaltluftausbrüchen deutlich stärker ausfällt als in den Sommermonaten (Rémillard and Tselioudis, 2015; Mechem et al., 2018). Dadurch ist der Anteil von MSc an der Gesamtbewölkung zum einen deutlich geringer (Rémillard et al., 2012), zum anderen begünstigen verstärkte Absinkbewegungen, höhere Windgeschwindigkeiten und eine geringe solare Einstrahlung das Auftreten gut durchmischter Grenzschichten.

Die Auswertung der Wolkendicke (c) zeigt nur einen schwachen Jahresgang. Allerdings fällt der geringere Anteil vertikal mächtiger Bewölkung in den Monaten mit großen Wolkenhöhen auf. Die unteren Perzentile des LWP (d) folgen deutlich dem Jahresgang der Meeresoberflächentemperaturen (vgl. Yashayaev and Zveryaev, 2001), da bei höheren Sättigungsdampfdrücken im Falle von Kondensation auch mehr Wasserdampf umgewandelt wird. Die Statistik der ho-

hen LWP zeigt eine deutlich größere Variabilität, wobei in den Herbstmonaten und im März die größten Anteile an hohen LWP beobachtet wurden. Ein ähnlicher Verlauf wird auch beim Niederschlagsanteil (e) deutlich, der zwischen 15% im Juli und August und 30% im Dezember schwankt. Zwar ermöglichen kältere Temperaturen die Entwicklung von Niederschlägen über den Wegener-Bergeron-Findeisen-Prozess, dennoch lassen sich diese Jahresgänge zunächst nicht plausibel erklären. Hier werden Fehlinterpretationen des LWP und des Niederschlags bei Absinkinversionen unter hochreichender Aufgleitbewölkung sowie synoptische Anomalien als Ursache angenommen, welche aufgrund des kurzen Auswertezeitraumes von nur 5 Jahren die Statistik stark verfälschen können.

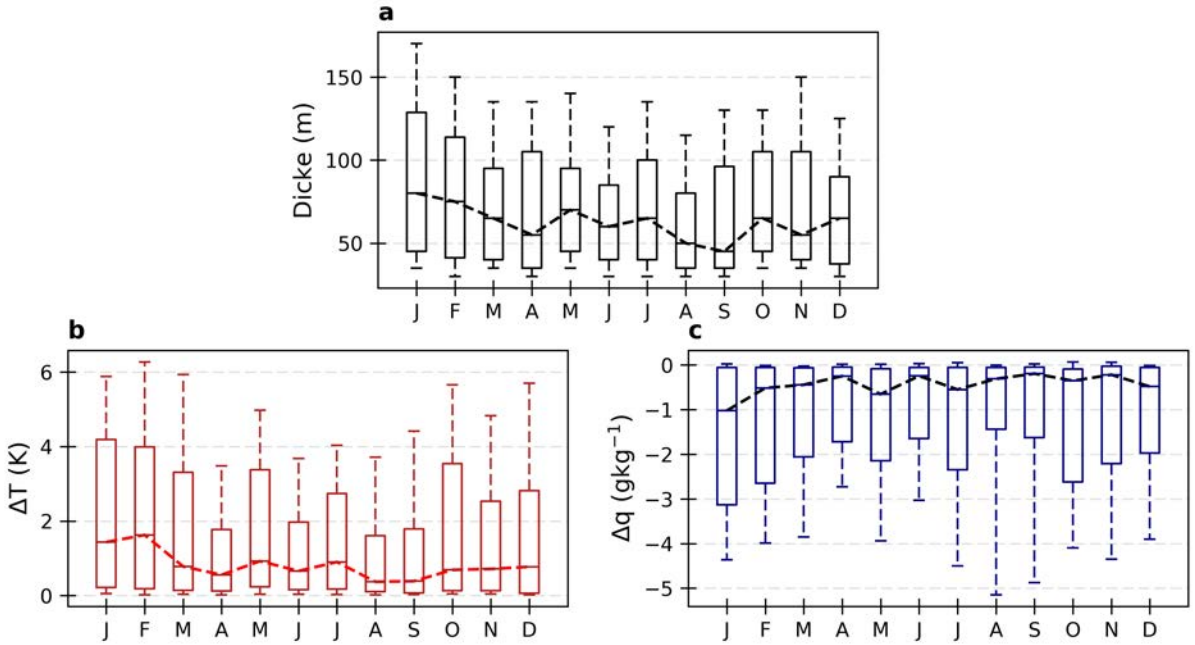

Abbildung 5: Jahresgang der (a) vertikalen Inversionsausdehnung, (b) der Änderung der Temperatur ΔT sowie (c) der Änderung des Mischungsverhältnisses Δq innerhalb der Inversion

Im Jahresgang der Inversionseigenschaften, welcher in Abbildung 5 dargestellt wird, werden Minima der vertikalen Mächtigkeit (a) und des Temperatursprunges (b) an der Inversion im April und im Spätsommer deutlich, wobei im September in mehr als 50% der Fälle eine vertikale Mächtigkeit unter 50 m beobachtet wurde und auch die Temperaturänderung häufig nur wenige Zehntel Kelvin betrug. Das Minimum der vertikalen Mächtigkeit von 30 m wird dagegen durch die Auswertekriterien festgelegt. In Bezug auf die Wolkenhöhen lässt sich ein indirekter Zusammenhang zwischen Wolkenhöhe und Stärke der Inversion feststellen. Dies folgt aus der Stauchung der absinkenden Luftmasse an der Grenzschichtinversion und wird durch die Stabilitätstendenzgleichung beschrieben (vgl. u.a. Petterssen et al., 1947). Demnach wird eine bereits stabile Luftsäule beim Absinken weiter stabilisiert, wodurch sich der Temperaturgradient innerhalb der Inversion weiter verstärkt. Bei flachen Grenzschichten kann die Luftmasse in der freien Troposphäre deutlich weiter absinken als bei höher liegenden Grenzschichten, wodurch der Zusammenhang zum Jahresgang der Temperaturänderungen- und Feuchteänderungen (c) angenommen wird.

In den Wintermonaten zeigen sich vertikal mächtigere Inversionen mit stärkeren Änderungen der Temperatur und des Wasserdampfmischungsverhältnisses. Hier liegt die geringere solare Einstrahlung und damit eine stärkere Abkühlungsrate an der Wolkenobergrenze als Ursache nahe.

5 Fazit

Für die Charakterisierung der Eigenschaften von MSc über der Azoreninsel Graciosa wurden die Messwerte von Radiosonden, einem Ceilometer, einem Distrometer und einem MWR für Zeitraum vom 01. März 2014 bis 31. August 2018 ausgewertet. Dazu wurde eine Methode von Zhang et al. (2010) zur Detektion von Wolkenschichten aus Feuchteprofilen der Radiosonde weiterentwickelt und für die Abgrenzung von MSc zu anderen Wolkenarten angepasst. Eine Evaluation mit den Messungen eines Ka-Band-Wolkenradars und des Ceilometers zeigte, dass die Methode auch zur Detektion von MSc geeignet ist, wobei die verwendeten Schwellwerte der relativen Feuchte offenbar zu niedrig gewählt wurden. Die Abhängigkeit des Fehlers zu einer weiteren Veränderung der Schwellwerte wurde allerdings nicht genauer untersucht. Dagegen konnte ausfallender Niederschlag und mehrschichtige Bewölkung als Ursache zufälliger Abweichungen festgestellt werden.

Auf Basis der weiterentwickelten Methode und unter Einbezug von Messwerten zum Niederschlag und Flüssigwassergehalt wurde der Tages- und Jahresgang der Wolkenhöhe und -dicke, des LWP, des Entkopplungs- und Niederschlagsverhaltens und der Inversionsstärke dargestellt. Der Tagesgang der Eigenschaften fiel im Vergleich zu vorangegangenen Auswertungen durch Rémillard et al. (2012) deutlich schwächer aus, konnte allerdings datenbedingt auch nur zwischen 00 UTC und 12 UTC verglichen werden. Als Ursache für das beobachtete Verhalten wurde der Einfluss der solaren Einstrahlung auf die Wolkendynamik und das Aufbrechen des MSc in der zweiten Tageshälfte angenommen. Für den jährlichen Verlauf wurden die Eigenschaften monatlich zusammengefasst. Die Beobachtungen wurden mit dem Jahresgang der solaren Einstrahlung und der Temperatur sowie der synoptischen Variabilität über den Azoren in Verbindung gebracht. Zum Ausschluss synoptischer Anomalien aus der monatlichen Klimatologie ist jedoch ein noch längerer Auswertezeitraum nötig.

Literatur

ARM (2013a). Atmospheric Radiation Measurement (ARM) user facility. 2013, updated hourly. Balloon-Borne Sounding System (SONDEWNPN). 2014-03-01 to 2018-08-31, Eastern North Atlantic (ENA) Graciosa Island, Azores, Portugal (C1). Compiled by D. Holdridge, J. Kyrouac and R. Coulter. ARM Data Center. Data set accessed 2018-11-09 at http://dx.doi.org/10.5439/1021460.

ARM (2013b). Atmospheric Radiation Measurement (ARM) user facility. Ceilometer (CEIL). 2014-03-01 to 2018-08-31, Eastern North Atlantic (ENA) Graciosa Island, Azores, Portugal (C1). Compiled by B. Ermold and V. Morris. ARM Data Center. Data set accessed 2018-11-09 at http://dx.doi.org/10.5439/1181954.

ARM (2014a). Atmospheric Radiation Measurement (ARM) user facility. 2014, updated hourly. Microwave Radiometer, 3 Channel (MWR3C). 2014-03-01 to 2018-08-31, Eastern North Atlantic (ENA) Graciosa Island, Azores, Portugal (C1). Compiled by M. Cadeddu and V. Ghate. ARM Data Center. Data set accessed 2018-11-09 at http://dx.doi.org/10.5439/1025248.

ARM (2014b). Atmospheric Radiation Measurement (ARM) user facility. Laser Disdrometer (PARS2). 2014-03-01 to 2018-08-31, Eastern North Atlantic (ENA) Graciosa Island, Azores, Portugal (C1). Compiled by J. Delamere, M. Bartholomew and Y. Shi. ARM Data Center. Data set accessed 2018-11-09 at http://dx.doi.org/10.5439/1150252.

ARM (2015). Atmospheric Radiation Measurement (ARM) user facility. 2015, updated hourly. Ka ARM Zenith Radar (KAZRGE). 2017-06-01 to 2017-08-31, Eastern North Atlantic (ENA)

Graciosa Island, Azores, Portugal (C1). Compiled by A. Matthews, B. Isom, D. Nelson, I. Lindenmaier, J. Hardin, K. Johnson and N. Bharadwaj. ARM Data Center. Data set accessed 2018-11-19 at http://dx.doi.org/10.5439/1025214.

Bougeault, P. (1985). A simple parameterization of the large-scale effects of cumulus convection. *Monthly Weather Review*, 113(12):2108–2121.

Dufresne, J.-L. and Bony, S. (2008). An assessment of the primary sources of spread of global warming estimates from coupled atmosphere–ocean models. *Journal of Climate*, 21(19):5135–5144.

Grenzhäuser, J. (2014). Entwicklung neuartiger mess-und auswertungsstrategien für ein scannendes wolkenradar und deren anwendungsbereiche. 55.

Mechem, D. B., Wittman, C. S., Miller, M. A., Yuter, S. E., and de Szoeke, S. P. (2018). Joint synoptic and cloud variability over the northeast atlantic near the azores. *Journal of Applied Meteorology and Climatology*, 57(6):1273–1290.

Nitschke, K. and de Azevedo, E. B. (2015). 3d atmosphere column evaluation and clouds tomography: At eastern north atlantic (ena), graciosa island arm facility. In *Experiment@ International Conference (exp. at'15), 2015 3rd*, pages 91–92. IEEE.

Petterssen, S., Sheppard, P., Priestley, C., and Johannessen, K. (1947). An investigation of subsidence in the free atmosphere. *Quarterly Journal of the Royal Meteorological Society*, 73(315-316):43–64.

Rémillard, J., Kollias, P., Luke, E., and Wood, R. (2012). Marine boundary layer cloud observations in the azores. *Journal of Climate*, 25(21):7381–7398.

Rémillard, J. and Tselioudis, G. (2015). Cloud regime variability over the azores and its application to climate model evaluation. *Journal of Climate*, 28(24):9707–9720.

Wang, J. and Rossow, W. B. (1995). Determination of cloud vertical structure from upper-air observations. *Journal of Applied Meteorology*, 34(10):2243–2258.

Wood, R. (2012). Stratocumulus clouds. *Monthly Weather Review*, 140(8):2373–2423.

Wyant, M. C., Bretherton, C. S., Rand, H. A., and Stevens, D. E. (1997). Numerical simulations and a conceptual model of the stratocumulus to trade cumulus transition. *Journal of the Atmospheric Sciences*, 54(1):168–192.

Yashayaev, I. M. and Zveryaev, I. I. (2001). Climate of the seasonal cycle in the north pacific and the north atlantic oceans. *International Journal of Climatology*, 21(4):401–417.

Zhang, J., Chen, H., Li, Z., Fan, X., Peng, L., Yu, Y., and Cribb, M. (2010). Analysis of cloud layer structure in shouxian, china using rs92 radiosonde aided by 95 ghz cloud radar. *Journal of Geophysical Research: Atmospheres*, 115(D7).

Wissenschaftliche Mitteilungen aus dem Institut für Meteorologie der Universität Leipzig Bd. 57 (2019)

Vertical aerosol distribution in the Southern hemispheric Midlatitudes as observed with lidar at Punta Arenas, Chile (53.2°S and 70.9°W) during ALPACA.

Foth, A.[1,2], Kanitz, T.[1,a], Engelmann, R.[2], Baars, H.[2], Radenz, M.[2] Seifert, P.[2], Barja, B.[3], Fromm, M.[4], Kalesse, H.[1], Ansmann, A.[2]

[1] *Leipzig Institute for Meteorology, University of Leipzig, Leipzig, Germany, E-mail: andreas.foth@uni-leipzig.de*
[2] *Leibniz Institute for Tropospheric Research (TROPOS), Leipzig, Germany*
[3] *Atmospheric Research Laboratory, University of Magallanes, Punta Arenas, Chile*
[4] *U.S. Naval Research Laboratory, Washington, D.C., USA*
[a] *now at: European Space Agency, ESTEC, Noordwijk, the Netherlands*

Summary: This publication gives a brief overview about the main findings of Foth et al. (2019). Within this work, lidar observations of the vertical aerosol distribution above Punta Arenas, Chile (53.2°S and 70.9°W) which have been performed with the Raman lidar Polly^{XT} from December 2009 to April 2010 are presented. Pristine marine aerosol conditions related to the prevailing westerly circulation dominated the measurements. Lofted aerosol layers could only be observed eight times during the whole measurement period. One case study is presented showing long-range transport of smoke from biomass burning in Australia and regionally transported dust from the Patagonian Desert. The aerosol sources are identified by trajectory analyses with HYSPLIT and FLEXPART. However, seven of the eight analysed cases with lofted layers show an aerosol optical thickness (AOT) of less than 0.05. The ground-based lidar observations are supplemented by the AERONET Sun photometers and the space-borne lidar CALIOP on board of CALIPSO. The averaged AOT determined by CALIOP was 0.02 ± 0.01 at Punta Arenas from 2009 to 2010.

Zusammenfassung: Diese Publikation gibt einen kurzen Überblick über ein paar Ergebnisse aus Foth et al. (2019). In dieser Arbeit werden Lidarbeobachtungen der vertikalen aerosolverteilung über Punta Arenas, Chile (53.2°S and 70.9°W) präsentiert, welche mit dem Ramanlidar Polly^{XT} zwischen Dezember 2009 und April 2010 durchgeführt wurden. Die Messungen sind durch reine marine Aerosolbedingungen in Verbindung mit vorherrschenden Westwinden gekennzeichnet. Abgehobene Aerosolschichten können nur acht mal während der gesamten Messperiode beobachtet werden. Einer der hier präsentierten Fälle zeigt weitreichenden Aerosoltransport von Rauch aus Biomasseverbrennung in Australien und regional transportierten Mineralstuab aus der patagonischen Wüste. Die Aerosolquellen wurden durch Trajektorienanalysen mit HYSPLIT und FLEXPART identifiziert. Allerdings zeigen sieben dieser acht Fälle mit abgehobenen Schichten ein optische Dicke des Aerosols (AOT) von weniger als 0,05. Die bodengebundenen Lidabeobachtungen werden durch AERONET Sonnenphotometer und das satellitengetragenge Lidar CALIOP an Bord von CALIPSO ergänzt. Die mittlere AOT, die mittels CALIOP zwischen 2009 und 2010 in Punta Arenas bestimmt wurde, beträgt 0.02 ± 0.01.

1 Introduction

Aerosols might possibly compensate the warming effect of the greenhouse gases in the Earth's radiation budget within the uncertainties of future climate modelling (Boucher et al., 2013). The reason for the high uncertainties in the determination of the general aerosol radiative effect is the aerosols variability in their global occurrence, their radiative properties (size, surface, chemistry), and their effects on cloud microphysics.
Global observations with spaceborne sensors improved the understanding of the seasonal distribution of aerosol layers worldwide, e. g. the seasonal vertical distribution of dust as observed with the Cloud-Aerosol lidar with Orthogonal Polarization (CALIOP, Winker et al., 2007). Nevertheless, extended field campaigns in key environments of the Earth with homogeneous aerosol conditions provided more-detailed information about properties and cloud-interaction of certain aerosol types with multi-sensor approaches, e. g. the Tropospheric Aerosol Radiative Forcing Observational Experiment (TARFOX), the Second Aerosol Characterization Experiment (ACE2), the Saharan Mineral Dust Experiment (SAMUM) or the Saharan Aerosol Long-Range Transport and Aerosol-Cloud-Interaction Experiment (SALTRACE).
Within this publication, lidar observations of the vertical aerosol distribution above Punta Arenas, Chile (53.2°S and 70.9°W) are presented as performed during the Aerosol Lidar measurement at Punta Arenas in the frame of Chilean germAn cooperation (ALPACA) campaign which took place from December 2009 to April 2010. This location at the southern tip of South America yields an excellent opportunity to study almost clean marine aerosol conditions which are characteristic for the Southern Oceans (SO), because of the absence of continental land masses in the latitudinal belt south of 45°S and a constant westerly air flow from the Pacific Ocean (Schneider et al., 2003). The nearest land mass situated towards the prevailing westerlies is New Zealand at a distance of roughly 8000 km and 10° latitude further north. Thus, reported aerosol sources at lower latitudes, like the Amazon rain forest (Baars et al., 2012), the Patagonian desert (Johnson et al., 2010), and the Australian continent (Edwards et al., 2006) are expected to barely affect the aerosol conditions at Punta Arenas.
In the framework of the BACCHUS (Impact of Biogenic versus Anthropogenic emissions on Clouds and Climate: towards a Holistic UnderStanding) project, Carslaw et al. (2017) performed simulations to estimate the aerosol conditions in the year 1750 and their impact on climate. It was found that Punta Arenas is in a region that is still representative for pre-industrial aerosol conditions. A similar notation was already previously reported by Hamilton et al. (2014).

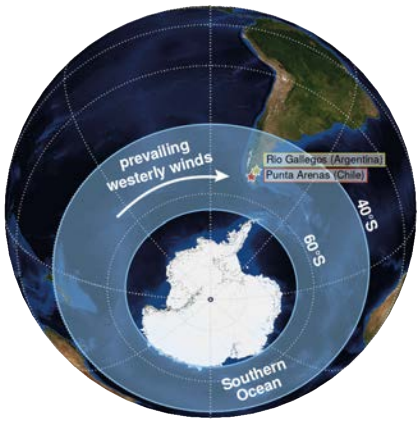

Figure 1: *Map of Antarctica and South America. Punta Arenas and Rio Gallegos are marked by a red and a yellow star, respectively.*

These pristine conditions already motivated the ground-based Aerosol Characterization Experiment (ACE1) in the 1990's (Bates et al., 1998) and were confirmed by Minikin et al. (2003) who contrasted upper-tropospheric in-situ aerosol aircraft observations in the Northern midlatitudes (Scotland) and Southern midlatitudes (Punta Arenas). However, only a few studies of ground-based aerosol and cloud layer profiling were performed in the southern midlatitudes in the following decades (Gouveia et al., 2017), although such measurements would have served as good opportunity to contrast the aerosol radiative effect in the northern and southern midlatitudes with respect to the aerosol sources as well as the influence of aerosols on cloud microphysics (Kanitz et al., 2011; Kanitz et al., 2013).
In the northern midlatitudes, lidar networks like the European Aerosol Lidar Network (EARLINET) (Bösenberg et al., 2000) monitor aerosol and cloud conditions since almost 20 years (Mattis et al., 2008). A comparable network in Latin America, the Latin American Lidar Network (LALINET) was only fully established in 2013 (Guerrero-Rascado et al., 2016). Moreover, the South American Environment Risk Network (SAVER.Net) was established by means of a collaboration between Chile, Argentina and Japan to monitor aerosol, ozone, and UV-radiation since 2012 (Ristori et al., 2018). The Atmospheric Research Laboratory of the Magallanes University in Punta Arenas is participating in this activity with a multiwavelength Raman and polarization lidar since 2016 (Barja et al., 2018). As such, the conducted lidar measurements during ALPACA achieved the most comprehensive data set on aerosol and cloud distribution from ground before the establishment of these networks. Some results of ALPACA are presented in this paper.

2 Experiment

Between the regular shipborne lidar measurements aboard the research vessel Polarstern (Kanitz et al., 2013) in autumn 2009 and spring 2010, the portable lidar Polly^{XT} was deployed at the Magallanes University in Punta Arenas, Chile (53.2°S and 70.9°W) and continuous lidar measurements (24 hours / 7 days a week) were conducted from 4 December 2009 to 4 April 2010, covering a period of four months. Parts of these Polly^{XT} observations have already been evaluated and published by Baars et al. (2016) in the frame of PollyNet.
Figure 1 shows the location of Punta Arenas (red star) in the very south of Chile, at the Strait of Magallanes and between the Pacific and Atlantic Ocean. In this area, the polar front causes a continuous zonal wind band, because of the limited friction of the large ocean surface and the missing structured land masses in contrast to the northern midlatitudes (Cerveny, 1998). Hence, westerly winds prevail the whole year in southern Latin America. Based on the marine

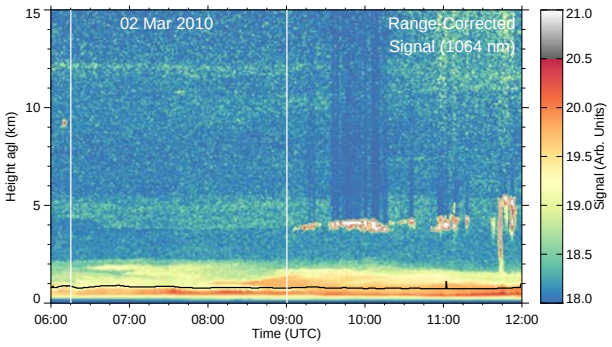

Figure 2: *Height–time display of the range–corrected signal observed at 1064 nm with the Polly^{XT} lidar on 2 March 2010. The analysed period between 06:15 bis 09:00 UTC is framed white. The planetary boundary layer top height is indicated by the black line.*

environment, daily and seasonal variations of the weather are weak (Coronato and Bisigato, 1998). The annual mean temperature is about 6 °C and the annual precipitation amounts to 375 mm. Furthermore, the cyclone passage frequency is very high (3-5 days, Hodges et al., 2011). This Southern Ocean region is characterized by a high cloud fraction (> 80 %, Naud et al., 2014) with a cloud fraction of clouds below 3 km of about 60 % (Haynes et al., 2011). The vegetation is composed by grasslands, tundra, and mixed forest.

3 Instruments

3.1 PollyXT

In the framework of ALPACA the lidar measurements were conducted with the portable multiwavelength Raman and polarization lidar Polly^{XT}_IFT (Althausen et al., 2009), as part of the Polly lidar family (Engelmann et al., 2016) and will be referred to Polly^{XT} in the paper. Technically, the lidar is capable to measure the backscattered light at 355, 532, and 1064 nm wavelength, and Raman scattered light at 387 and 607 nm to determine profiles of the particle backscatter coefficient at three wavelengths and the extinction coefficient at 355 and 532 nm. In fact, below 1500 m the laser beam with the receiver field of view of the bistatic system is incomplete, thus an overlap correction was applied. However, below 400 m the overlap function is less than 0.5 and a reliable overlap correction is not possible. As a consequence, values of the particle backscatter coefficient were set constant below 400 m height, in the lower part of the planetary boundary layer (PBL) under the assumption of well–mixed conditions.
The PBL top height is determined with the wavelet–covariance–transformation that supposes a much higher aerosol load in the PBL than in the free troposphere (Brooks, 2003; Baars et al., 2008).
The rather low aerosol content in the area of Punta Arenas caused low signal–to–noise ratios. Thus, the particle extinction coefficient had to be estimated from the 532 nm and 1064 nm backscatter coefficient by means of appropriate particle lidar ratio (S_P) values.

3.2 Cloud Aerosol Lidar with orthogonal Polarization (CALIOP)

In April 2006, the Cloud Aerosol Lidar Infrared Pathfinder Satellite Observations (CALIPSO) mission started (Winker et al., 2009). Aboard CALIPSO, the two–wavelength backscatter and polarization lidar CALIOP has been operated to achieve a worldwide four dimensional data set of clouds and aerosols. CALIPSO orbits the Earth in a height of nearly 705 km with a velocity of 7 km s^{-1} and overpasses the same location every 16th day.
The CALIPSO data processing provides profiles of backscatter and extinction coefficient at 532 and 1064 nm within the CALIOP level 2 version 4.10 data. In contrast to version 3 data, the version 4.10 data analysis algorithm aims on distinguishing not six but seven tropospheric aerosol subtypes (Omar et al., 2009). In this study, the CALIPSO data is used to determine planetary boundary layer heights, the backscatter-related Ångström exponent, and to retrace the long-range transport of smoke based on total attenuated backscatter profiles at 532 nm (level 1 V4.10) and the aerosol subtype product (level 2 V4.10). Level 3 products of the monthly averaged AOT are still based on version 3.10 because version 4.10 is not yet available.
The CALIOP data processing provides several quality flags. Within the scene classification algorithm, the cloud–aerosol–discrimination (CAD) score is determined (Liu et al., 2009). Aerosol particles are assigned with negative values of −100 to −1 and clouds are assigned with positive values of 1 to 100. The larger or smaller the value the more confident is the discrimination, respectively. Values around zero define an uncertain discrimination.

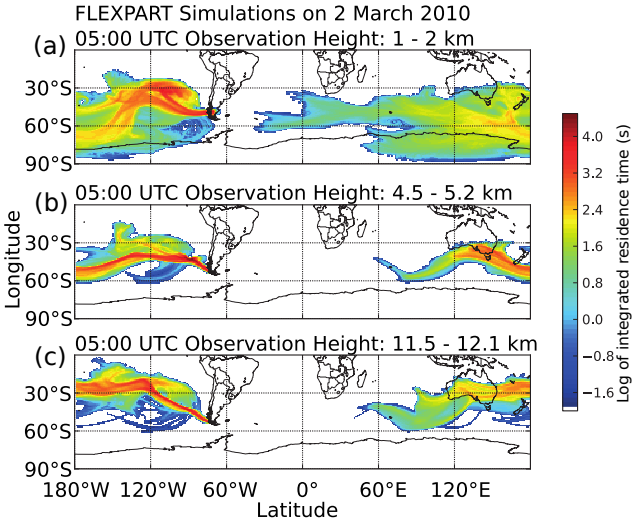

Figure 3: *FLEXPART simulations for the integrated residence time of the particles that traveled in the whole atmospheric column within the last ten days until the observation time on 2 March 2010 for the observed heights between 1 and 2 km (a), 4.5 and 5.2 km (b) and 11.5 and 12.1 km (c). The colors represent the logarithm of the integrated residence time (in seconds) in a grid box for 10–day integration time.*

3.3 Auxiliary data

An AERONET Sun photometer which measures AOT (column-integrated extinction coefficient) from 340 to 1020 nm at 7 channels is located at Rio Gallegos (51.6°S, 69.3°W), Argentina (CEILAP-RG) which is 200 km away from Punta Arenas. Level 2.0 data is used with an AOT uncertainty of 0.01 to 0.02 (Holben et al., 2001).

Two models were used to support the analysis of the air mass transport. HYSPLIT is a model to calculate trajectories of air parcels for simulations of dispersion and deposition at arbitrary locations (Stein et al., 2015). By means of trajectories, aerosol sources are assigned. FLEXPART is a Lagrangian particle dispersion model, which calculates probabilistic trajectories of a large number of air parcels (Stohl et al., 2005). Thereby, the transport and diffusion of aerosol could be described and a coarse assignment of aerosols to their sources is enabled.

In the statistical analysis of the aerosol conditions during ALPACA, we used ensemble backward trajectories combined with a land cover classification for a temporally and vertically resolved airmass source attribution. The 'software for automated trajectory analysis: trace' is used (Radenz and Seifert, 2019). The land cover is a simplified version of the MODIS land cover (Friedl et al., 2002). At first, a 27-member ensemble of 10-day backward trajectories is calculated using HYSPLIT. Meteorological input data for HYSPLIT are taken from the Global Data and Assimilation Service dataset (GDAS1) provided by the Air Resources Laboratory (ARL) of the U.S. National Weather Service's National Centers for Environmental Prediction (NCEP). Each ensemble is generated using a small spatial offset in the trajectory endpoint. Whenever a trajectory is below the PBL height provided in the GDAS1 data ('reception height'), the land cover is categorized using custom defined polygons according to land mass boundaries. Hence, an air parcel is assumed to be influenced by the surface if the trajectory is below the PBL height. The residence time for each category is then the total time an air parcel fulfilled this criterion by land cover category. This calculation is repeated in steps of 3 h in time and 500 m in height to provide a continuous estimate on the airmass source and as a first hint on potential aerosol load. The global aerosol model NAAPS (Navy Aerosol Analysis and Prediction System) and the model results of the Monitoring Atmospheric Composition and Climate (MACC) project are

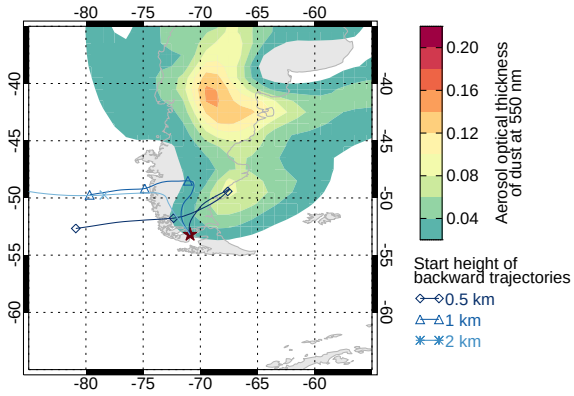

Figure 4: *HYSPLIT 48–hours backward trajectories for heights of 0.5, 1 and 2 km for Punta Arenas on 2 March 2010, 09:00 UTC and modelled dust surface concentrations from the NAAPS aerosol model on 2 March 2010, 06:00 UTC.*

used to obtain the modelled aerosol optical thickness of dust.

4 2 March 2010: Lofted smoke layers and Patagonian dust

In this section, a case is discussed in detail. It shows two lofted smoke layers after intercontinental long-range transport and low level Patagonian dust. On 2 March 2010, the weather at Punta Arenas was dominated by a north–westerly air flow. Between 09:00 UTC and 12:00 UTC, Polly^{XT} observed clouds in the range from 4 to 5 km and a PBL height of about 1 km (Fig. 2). An aerosol layer was situated above the PBL up to a height of 2 km. An increased backscatter was also observed at the height range from 4.5 to 5.2 km (06:00 to 12:00 UTC) and from 11.5 to 12.1 km (06:00 to 09:30 UTC). The source apportionment of the three observed aerosol layers by means of FLEXPART and HYSPLIT analyses is shown in Fig. 3, 4 and 5. In Figure 3a, a FLEXPART analysis for the lower layer (1 to 2 km) reveals that the air masses passed the southern Pacific and southern Patagonia (red colouration in Fig. 3a). HYSPLIT 48–hours backward trajectories for heights of 0.5, 1 and 2 km confirm that the ground–level aerosol on 2 March 2010 was locally affected by an extended residence time above Patagonia (Fig. 4). At this time, modelled aerosol optical thickness (AOT) of dust at 550 nm from the global aerosol model NAAPS regionally peaked at 0.14 and was 0.02 in the area of Punta Arenas (Fig. 4). The AOT of dust at 550 nm from the MACC model reaches values of 0.07 in Southern Patagonia.
The FLEXPART analyses for the layers observed between 4.5 as well as 5.2 km and 11.5 and 12.1 km height reveal a clearly defined region of origin. The observed layers were advected to Punta Arenas from Australia and the southern Pacific (Fig. 3b and c). HYSPLIT 13–days backward trajectories were calculated as well (blue and light blue in Fig. 5). Figure 5 (top) also shows active fire spots (red dots) derived by MODIS (Moderate Resolution Imaging Spectroradiometer, Justice et al., 2011), which were detected between 17 and 25 February 2010. On 18 and 19 February 2010 there were eruptions of pyrocumulonimbus (pyroCb) storms in Western Australia. On 18 February two fires, at approximately 32.6°S, 121.0°E and 33.0°S, 122.1°E, spawned pyroCbs that were active between $\sim$ 04 : 00 – 10 : 00 UTC. The MODIS (Aqua) 11 μm window brightness temperature minimum in the opaque core of the pyroCb anvil was $\sim$ −57°C. According to the nearest radiosonde (Esperance, station number 94638, 33.8°S, 121.9°E, 00:00 UTC 18 February) temperature profile, the brightness-temperature-inferred cloud-top height is $\sim$ 12.3 km. A third fire complex near 32.5°S, 122.8°E produced pyrocumulus convection at that time. Hence smoke was likely emitted at a range of altitudes

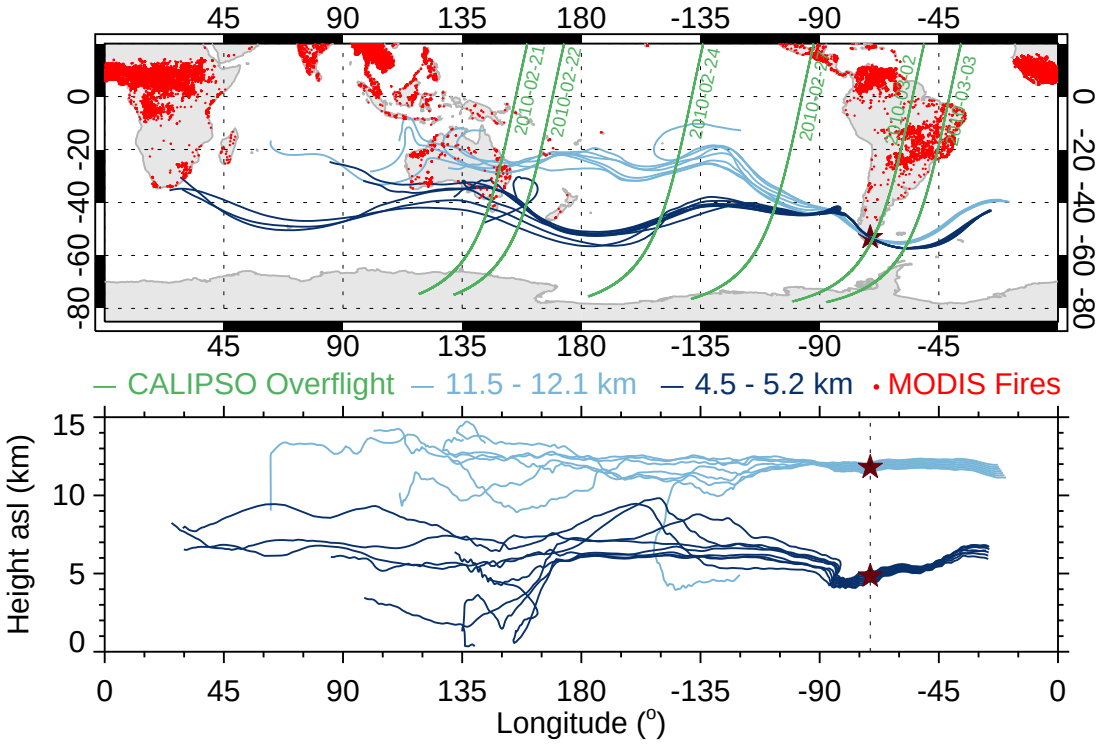

Figure 5: *Top: Map of the HYSPLIT 13–days backward trajectories for heights of 4.5 to 5.2 km (blue) and 11.5 to 12.1 km (light blue) arriving at Punta Arenas (brown star) on 2 March 2010, 09:00 UTC, MODIS fire counts between 17 to 25 February 2010 (red dots) and CALIPSO tracks (green). Bottom: Height of the according trajectories.*

during the various stages of pyroconvection from above the PBL up to ~ 12 km. On 19 February another pyroCb was detected that was likely generated from this third fire. The layer between 4.5 and 5.2 km (blue) as well as the layer between 11.5 and 12.1 km (light blue) crossed these regions with pyroconvection in Western Australia. In summary, the source apportionment study for 2 March 2010 reveals that the surface-near aerosol layer is likely dominated by Patagonian dust, whereas the two observed lofted layers contain long-range transported smoke from Australia.
The Polly^{XT} measurement was analysed for the cloud–free period between 06:15 and 09:00 UTC on 2 March 2010. Figure 6 illustrates the profiles of the optical properties with a smoothing length of 150 m. The particle backscatter coefficients reach their maximum values of up to 1.02 $Mm^{-1}sr^{-1}$ (532 nm) and 0.63 $Mm^{-1}sr^{-1}$ (1064 nm) in the PBL. The observed layers in the height–time display (Fig. 2) are also slightly visible in the profiles of the particle backscatter coefficient in heights of 5 and 12 km. The profile of the particle extinction coefficient (at 532 nm) was reproduced for an assumed constant lidar ratio. According to the origin of the air masses, a lidar ratio of 40 ± 10 sr (Kanitz et al., 2013) was applied to the ground–level layer (up to 2.5 km) and a lidar ratio of 70 ± 10 sr for smoke (Ansmann et al., 2009; Tesche et al., 2011) was used for the lofted layers (Fig. 6c). The AOTs of each single layer result in values of 0.044 ± 0.004 (0 to 2.5 km), 0.004 ± 0.0004 (4.5 to 5.2 km) and 0.002 ± 0.0002 (11.5 to 12.1 km). The backscatter–related Ångström exponent (Fig. 6d) amounts to 0.56 ± 0.21 in the ground–level layer (up to 2 km). Kanitz et al. (2013) determined a Patagonian–dust–related Ångström exponent of 0.4 ± 0.1. In the framework of EARLINET, Saharan–dust–related Ångström exponents of 0.5 ± 0.5 were determined (Müller et al., 2007). In the smoke layer between 4 and 5.5 km, the Ångström exponent was 0.61 ± 0.1. In comparison, biomass–burning–smoke–related Ångström exponents of 1.0 ± 0.4 were determined by lidar observations for long-range transported smoke

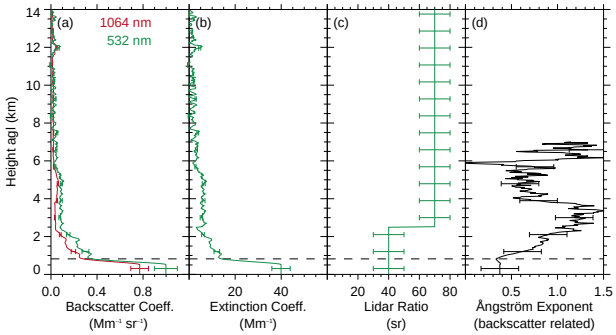

Figure 6: *Vertical profiles of (a) particle backscatter coefficient at 532 nm and 1064 nm with error bars indicating 10 % uncertainty, (b) particle extinction coefficient at 532 nm with error bars resulting from a lidar ratio uncertainty of* ± 10 *sr, (c) particle lidar ratio with error bars of* ± 10 *sr and (d) backscatter related Ångström exponent with propagated error bars, derived by Polly*^{XT} *on 2 March 2010, 06:15 to 09:00 UTC. The planetary boundary layer top height is indicated by the black dashed line.*

from Siberia and Canada (Müller et al., 2007). In Cape Verde, Ångström exponents of smoke originating from the south of western Africa, were 1.06 ± 0.65 (Tesche et al., 2011). Smoke that was transported from Africa to the Amazon rain forest was found to have Ångström exponents of 0.8 (Baars, 2012).

In a next step, CALIPSO lidar observations were used for the characterization of the lofted aerosol layers during long-range transport. Six CALIPSO overpasses were found for the observation of the two lofted layers (see green lines in Fig. 5 top), which provide intersections of the intercontinental transport of the smoke plume. On 21 February 2010, CALIPSO overpassed the region of origin of the smoke in Southern Australia. Figure 7a and b show the height–time display of the attenuated backscatter coefficient and the determined aerosol subtypes (with CAD score < -80) on 21 February 2010. Between heights of 4 and 7 km, a section of increased backscatter can be identified. According to the CALIOP data algorithms, the lofted aerosol layer is a mixture of smoke (black) and continental aerosol (green), which confirms the analysis of their origin discussed above. The AOT of the layer determined by CALIOP amounts to 0.1 (at 532 nm). AERONET Sun photometer measurements show a mean AOT of 0.165 (at 500 nm) in Canberra, Southern Australia, on 21 February 2010. In contrast, a biomass–burning–related AOT of 0.55 (at 532 nm) was determined in the Amazon rain forest during the dry season (Baars, 2012). Additionally, an aerosol layer between 10 and 12 km is identified as clean continental aerosol.

On 22 February 2010, the smoke layer is also visible between heights of 4 and 8 km (Fig. 7c and d). On the following days, CALIOP is not able to determine unambiguously the smoke layer (Fig. 7e,f,g and h). A possible reason might be the decreasing smoke concentration along its transport route caused by dispersion and deposition (Bigg, 1973). The simultaneous occurrence of clouds and aerosol (on 24 February, see Fig. 7e,f at 8 km height and on 27 February at 5 to 11 km height, see Fig. 7g,h), which constrains the detection of the optically thin smoke plume, might be another reason. However, the CAD score of the detected smoke layers is larger than -80 which indicates high discrimination accuracy (Liu et al., 2009). In the region of Punta Arenas (on 2 March 2010 in a height of 4 km), CALIOP is again not able to doubtlessly determine the smoke layer, because all determined aerosol layers are in the vicinity to clouds. On 3 March 2010, the smoke layer was confidently detected by CALIOP (Fig. 7l).

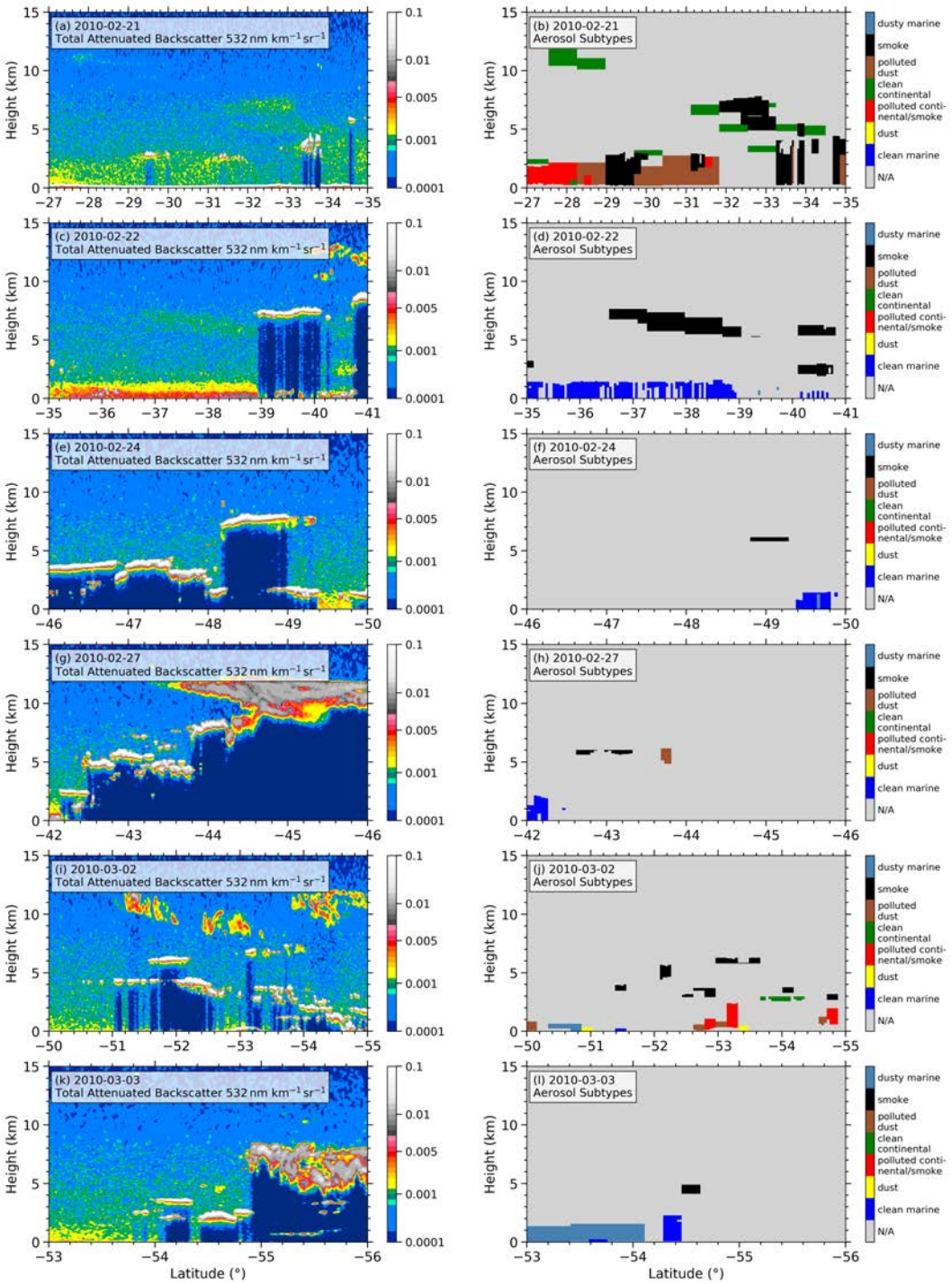

Figure 7: *Height-time display of the total attenuated backscatter at 532 nm (left panel) and corresponding aerosol subtype (right panel) derived by CALIOP from six CALIPSO overpasses on (a,b) 21, (c,d) 22, (e,f) 24, (g,h) 27 February, (i,j) 2 and (k,l) 3 March 2010. The aerosol subtypes are only illustrated if the CAD score is below -80 excluding uncertain classifications.*

5 General aerosol conditions

The general aerosol conditions in Punta Arenas are presented in Fig. 8a in terms of monthly averaged AOT at 532 nm wavelength as determined with CALIOP for the grid cell of Punta Arenas (blue curve) from 1 January 2009 to 31 December 2010. The averaged AOT at Punta Arenas from 2009 to 2010 was 0.02 ± 0.01. The annual course of the monthly averaged AOT indicates the absence of a pronounced seasonal cycle. The large standard deviation may have been caused by the low number of observations, but may also be the result of the CALIOP aerosol typing limitations in coastal regions (Kanitz et al., 2014). For comparison, the AOT as obtained at the AERONET station of Rio Gallegos is shown, too. At Rio Gallegos the mean AOT between 2009 and 2010 (0.02 ± 0.02) is in the same range as at Punta Arenas, although Rio Gallegos is situated closer to the Patagonian desert and 400 km east of the west coast of Latin America. AERONET AOT measurements at Rio Gallegos confirm the very low mean AOT values (2009: 0.02±0.01, 2010: 0.02 ± 0.01) of CALIOP and indicate clean marine conditions at Punta Arenas and Rio Gallegos (Fig. 8b). Such low AOT values were also found in other coastal and remote oceanic areas. During three meridional transatlantic cruises from 50°N to 50°S shipborne lidar measurements revealed AOTs (at 532 nm) of the marine boundary layer of below 0.05 in 78% of the cases (Kanitz et al., 2013). Wilson and Forgan (2002) determined a mean AOT (at 500 nm) of less than 0.04 at Cape Grim, Tasmania from 1986–1999. AERONET Sun photometer measurements in marine areas show AOTs (at 500 nm) of 0.085 ± 0.01 over the Pacific and 0.06 ± 0.02 over the Southern Ocean (Smirnov et al., 2009).
Figure 8 (c) shows the height–time display of the range–corrected signal at 1064 nm wavelength measured by Polly^{XT} for the entire measurement period. As expected, most of the aerosol load is contained within the PBL up to around 1200 m (reddish colors). The free troposphere is characterized by a very low aerosol load but a frequent occurrence of clouds (grey and white colors).
A comprehensive analysis of aerosol source regions based on ensemble HYSPLIT trajectory calculations shows (Fig. 8d) that the influence of the ocean on air parcels (given in accumulated residence time of the backward trajectories within the PBL over the respective surface type) reaching Punta Arenas is a factor of 100 larger in contrast to the continents Africa, Australia and even South America.

6 Conclusions & Outlook

The presented study aimed on providing an overview about the vertical aerosol conditions above Punta Arenas. During the four months of observations of Polly^{XT}, lofted aerosol layers were rarely observed and, when present, were characterised by very low optical thicknesses. Overall, the mean aerosol optical thickness at Punta Arenas was found to be 0.02, which is very low, even for marine conditions. Due to the absence of observations of anthropogenic aerosols, neither local nor long-range transported, our study thus confirms well the conclusions of Hamilton et al. (2014) and Carslaw et al. (2017) that the atmosphere over southern Chile still provides pristine, pre-industrial conditions. CALIPSO observations, which were utilized to track the long-range transport of aerosol from Australia to Punta Arenas, indicate that a considerable fraction of free-tropospheric aerosol is removed by cloud processes and washout taking place over the Pacific Ocean before it reaches South America. The average free-tropospheric aerosol load is thus subject to increase to the west of Punta Arenas. The same can be expected eastward of South America, because, as was found in analyses of NAAPS and MACC aerosol model simulations, substantial amounts of Patagonian dust are frequently emitted into the atmosphere and trans-

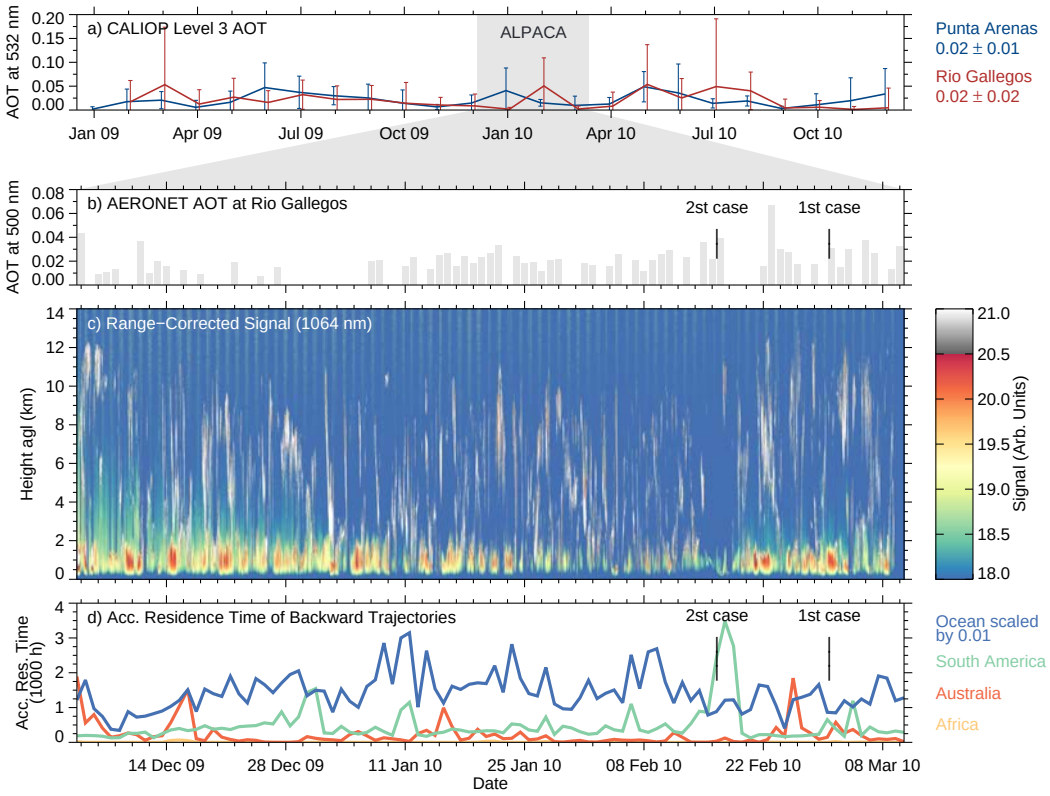

Figure 8: *(a) Monthly average of CALIOP Level 3 AOT (at 532 nm) and their standard deviation at Punta Arenas (blue) and Rio Gallegos (red) in 2009 and 2010. The ALPACA campaign is indicated by the shaded area. (b) Daily average of AERONET Sun photometer AOT (at 500 nm) at Rio Gallegos for the ALPACA campaign. (c) Height-time display of the range–corrected signal (at 1064 nm) measured by Polly^{XT}. Panel d) shows the accumulated residence time of backward trajectories separated by different regions of origin.*

ported lee-ward of South America. We thus conclude from our study that Punta Arenas is one of the few accessible places on Earth with temperate climate where aerosol-cloud-interaction reference studies in the absence of free-tropospheric aerosols can be conducted.

Future studies might enhance the knowledge of the aerosol conditions regarding an aerosol typing (Baars et al., 2017) and separation of aerosol types as well as an estimation of ice nucleating particles and cloud condensation nuclei from multiwavelength Raman and polarization lidar observations (Mamouri and Ansmann, 2015).

In recent years the Southern Ocean, especially the area in the South and South East of Australia, became an increasing focus for atmospheric researchers. Several observation campaigns like MARCUS (Measurements of Aerosols, Radiation, and Clouds over the Southern Ocean), SOCRATES (the Southern Ocean Clouds Radiation Aerosol Transport Experimental Study) and CAPRICORN (Clouds, Aerosols, Precipitation Radiation and atmospherIc Composition Over the southeRN ocean, Protat et al., 2016; Mace and Protat, 2018) provide beneficial data for improving the understanding of aerosol-cloud-interaction in pristine environments.

In the upcoming field experiment organized by TROPOS in collaboration with the Magallanes University, Punta Arenas (UMAG) and the Institute for Meteorology at the University of Leipzig (LIM) an extended version of the Leipzig Aerosol and Cloud Remote Observation System (LACROS, Bühl et al., 2013) will be deployed at UMAG in November 2018 for at least one year to study the seasonal cycle of aerosols and clouds in Punta Arenas. LACROS comprises, amongst others, a Polly^{XT} lidar, a 35 GHz cloud radar, a Doppler lidar, a microwave radiometer,

a distrometer and radiation sensors for direct and diffuse downwelling and upwelling solar and thermal radiation. During this field experiment named DACAPO-PESO (Dynamics, Aerosol, Cloud and Precipitation Observations in the Pristine Environment of the Southern Ocean), the LACROS suite is extended by a 94 GHz frequency-modulated continuous wave cloud radar provided by LIM (LIMRAD94, Küchler et al., 2017) and a 24 GHz micro rain radar (TROPOS) which will allow for multi-frequency polarimetric Doppler radar studies. Complementing instrumentation of UMAG includes radiosondes, radiation observations, in-situ aerosol observations, and multi-wavelength lidar measurements. The latter are performed since 2015 in the frame of LaLiNet (Guerrero-Rascado et al., 2016).
With this extended observational suite, several research questions like the efficiency of liquid-dependent ice formation as well as the influence of aerosol concentration on the frequency of occurrence of mixed-phase cloud processes like aggregation and riming will be addressed. These observations might help to improve the representation of Southern Ocean clouds in global climate models which currently suffer from a strong radiation bias (Bodas-Salcedo et al., 2014) caused by a misrepresentation of cloud phase. Specifically, the amount of ice is overestimated by models while observations show a large amount of clouds with high supercooled-liquid water content at cloud top (Haynes et al., 2011). Since cloud thermodynamics are a strong function of cloud condensation nuclei and ice nucleating particles availability which in turn are related to the aerosol load and type (Mamouri and Ansmann, 2015), the results from the ALPACA campaign, presented here, built a fundamental basis of knowledge about the aerosol conditions, cloud condensation nuclei and ice nucleating particles that can be expected at this site.

References

Althausen, D., Engelmann, R., Baars, H., et al.: Portable Raman lidar PollyXT for automated profiling of aerosol backscatter, extinction, and depolarization, J. Atmos. Oceanic Technol., 26, 2366–2378, doi:10.1175/2009JTECHA1304.1, 2009.

Ansmann, A., Baars, H., Tesche, M., et al.: Dust and smoke transport from Africa to South America: Lidar profiling over Cape Verde and the Amazon rainforest, Geophys. Res. Lett., 36, L11802, doi:10.1029/2009GL037923, 2009.

Baars, H.: Aerosol profiling with lidar in the Amazon Basin during the wet and dry season 2008, Ph.D. thesis, Faculty of Physics and Geoscience, University of Leipzig, 2012.

Baars, H., Ansmann, A., Engelmann, R., and Althausen, D.: Continuous monitoring of the boundary-layer top with lidar, Atmos. Chem. Phys., 8, 7281–7296, doi:10.5194/acp-8-7281-2008, 2008.

Baars, H., Ansmann, A., Althausen, D., et al.: Aerosol profiling with lidar in the Amazon Basin during the wet and dry season, J. Geophys. Res. Atmos., 117, D21201, doi:10.1029/2012JD018338, 2012.

Baars, H., Kanitz, T., Engelmann, R., et al.: An overview of the first decade of PollyNET: an emerging network of automated Raman-polarization lidars for continuous aerosol profiling, Atmos. Chem. Phys., 16, 5111–5137, doi:10.5194/acp-16-5111-2016, 2016.

Baars, H., Seifert, P., Engelmann, R., and Wandinger, U.: Target categorization of aerosol and clouds by continuous multiwavelength-polarization lidar measurements, Atmos. Meas. Tech., 10, 3175–3201, doi:10.5194/amt-10-3175-2017, 2017.

Barja, B., Zamorano, F., Ristori, P., et al.: Aerosols Observations with a new lidar station in Punta Arenas, Chile, EPJ Web Conf., 176, 05 038, doi:10.1051/epjconf/201817605038, 2018.

Bates, T. S., Huebert, B. J., Gras, J. L., Griffiths, F. B., and Durkee, P. A.: International Global Atmospheric Chemistry (IGAC) Project's First Aerosol Characterization Experiment (ACE 1): Overview, J. Geophys. Res., 1031, 16 297–16 318, doi:10.1029/97JD03741, 1998.

Bigg, E.: Ice Nucleus Concentrations in Remote Areas., J. Atmos. Sci., 30, 1153–1157, doi:10.1175/1520-0469(1973)030<1153:INCIRA>2.0.CO;2, 1973.

Bodas-Salcedo, A., Williams, K. D., Ringer, M. A., et al.: Origins of the Solar Radiation Biases over the Southern Ocean in CFMIP2 Models, J. Climate, 27, 41–56, doi:10.1175/JCLI-D-13-00169.1, URL https://doi.org/10.1175/JCLI-D-13-00169.1, 2014.

Bösenberg, J., Ansmann, A., Baldasano, J., et al.: EARLINET: a European aerosol research lidar network, Advances in laser remote sensing, pp. 155–158, 2000.

Boucher, O., Randall, D., Artaxo, P., et al.: Clouds and Aerosols, in: Climate Change 2013: The Physical Science Basis. Contribution of Working Group I to the Fifth Assessment Report of the Intergovernmental Panel on Climate Change, edited by Stocker, T., Qin, D., Plattner, G., et al., Cambridge University Press, Cambridge, United Kingdom and New York, NY, USA, 2013.

Brooks, I. M.: Finding Boundary Layer Top: Application of a Wavelet Covariance Transform to Lidar Backscatter Profiles, J. Atmos. Oceanic Technol., 20, 1092, doi:10.1175/1520-0426(2003)020<1092:FBLTAO>2.0.CO;2, 2003.

Bühl, J., Seifert, P., Wandinger, U., et al.: LACROS: the Leipzig Aerosol and Cloud Remote Observations System, in: Remote Sensing of Clouds and the Atmosphere XVIII; and Optics in Atmospheric Propagation and Adaptive Systems XVI, vol. 8890 of *Proc. SPIE*, p. 889002, doi:10.1117/12.2030911, 2013.

Carslaw, K. S., Gordon, H., Hamilton, D. S., et al.: Aerosols in the Pre-industrial Atmosphere, Current Climate Change Reports, 3, 1–15, doi:10.1007/s40641-017-0061-2, 2017.

Cerveny, R. S.: Present Climates of South America, in: Climates of the Southern Continents: Present, Past and Future, edited by J. E. Hobbs, J. A. L. H. A. B., pp. 107–135, John Wiley, 1998.

Coronato, F. and Bisigato, A.: A temperature pattern classification in Patagonia, Int. J. Climatol., 18, 765–773, doi:10.1002/(SICI)1097-0088(19980615)18:7<765::AID-JOC282>3.0.CO;2-H, 1998.

Edwards, D. P., Emmons, L. K., Gille, J. C., et al.: Satellite-observed pollution from Southern Hemisphere biomass burning, J. Geophys. Res., 111, D14312, doi:10.1029/2005JD006655, 2006.

Engelmann, R., Kanitz, T., Baars, H., et al.: The automated multiwavelength Raman polarization and water-vapor lidar Polly^{XT}: the neXT generation, Atmos. Meas. Tech., 9, 1767–1784, doi:10.5194/amt-9-1767-2016, URL https://www.atmos-meas-tech.net/9/1767/2016/, 2016.

Foth, A., Kanitz, T., Engelmann, R., et al.: Vertical aerosol distribution in the southern hemispheric midlatitudes as observed with lidar in Punta Arenas, Chile (53.2° S and 70.9° W), during ALPACA, Atmospheric Chemistry and Physics, 19, 6217–6233, doi:10.5194/acp-19-6217-2019, URL https://www.atmos-chem-phys.net/19/6217/2019/, 2019.

Friedl, M., McIver, D., Hodges, J., et al.: Global land cover mapping from MODIS: algorithms and early results, Remote Sens. Environ., 83, 287–302, doi:10.1016/S0034-4257(02)00078-0, URL http://www.sciencedirect.com/science/article/pii/S0034425702000780, the Moderate Resolution Imaging Spectroradiometer (MODIS): a new generation of Land Surface Monitoring, 2002.

Gouveia, D. A., Barja, B., Barbosa, H. M. J., et al.: Optical and geometrical properties of cirrus clouds in Amazonia derived from 1 year of ground-based lidar measurements, Atmospheric Chemistry and Physics, 17, 3619–3636, doi:10.5194/acp-17-3619-2017, URL https://www.atmos-chem-phys.net/17/3619/2017/, 2017.

Guerrero-Rascado, J. L., Landulfo, E., Antuña, J. C., et al.: Latin American Lidar Network (LALINET) for aerosol research: Diagnosis on network instrumentation, J. Atmos. Sol.-Terr. Phy., 138-139, 112–120, doi:10.1016/j.jastp.2016.01.001, 2016.

Hamilton, D. S., Lee, L. A., Pringle, K. J., et al.: Occurrence of pristine aerosol environments on a polluted planet, Proceedings of the National Academy of Sciences, 111, 18 466–18 471, doi:10.1073/pnas.1415440111, URL http://www.pnas.org/content/111/52/18466, 2014.

Haynes, J. M., Jakob, C., Rossow, W. B., Tselioudis, G., and Brown, J.: Major Characteristics of Southern Ocean Cloud Regimes and Their Effects on the Energy Budget, J. Climate, 24, 5061–5080, doi:10.1175/2011JCLI4052.1, URL https://doi.org/10.1175/2011JCLI4052.1, 2011.

Hodges, K. I., Lee, R. W., and Bengtsson, L.: A Comparison of Extratropical Cyclones in Recent Reanalyses ERA-Interim, NASA MERRA, NCEP CFSR, and JRA-25, J. Climate, 24, 4888–4906, doi:10.1175/2011JCLI4097.1, URL https://doi.org/10.1175/2011JCLI4097.1, 2011.

Holben, B. N., Tanré, D., Smirnov, A., et al.: An emerging ground-based aerosol climatology: Aerosol optical depth from AERONET, J. Geophys. Res., 106, 12 067–12 098, doi:10.1029/2001JD900014, 2001.

Johnson, M., Meskhidze, N., Solmon, F., et al.: Modeling dust and soluble iron deposition to the South Atlantic Ocean, J. Geophys. Res., 115, D15 202, doi:10.1029/2009JD013311, 2010.

Justice, C. O., Giglio, L., Roy, D., et al.: MODIS-Derived Global Fire Products, in: Land Remote Sensing and Global Environmental Change: NASA's Earth Observing System and the Science of ASTER and MODIS, Remote Sensing and Digital Image Processing, edited by Ramachandran, B., Justice, C. O., and Abrams, M. J., pp. 661–679, Springer, doi:10.1007/978-1-4419-6749-7_29, 2011.

Kanitz, T., Seifert, P., Ansmann, A., et al.: Contrasting the impact of aerosols at northern and southern midlatitudes on heterogeneous ice formation, Geophys. Res. Lett., 38, L17 802, doi:10.1029/2011GL048532, 2011.

Kanitz, T., Ansmann, A., Engelmann, R., and Althausen, D.: North-south cross sections of the vertical aerosol distribution over the Atlantic Ocean from multiwavelength Raman/polarization lidar during Polarstern cruises, J. Geophys. Res. Atmos., 118, 2643–2655, doi:10.1002/jgrd.50273, 2013.

Kanitz, T., Ansmann, A., Foth, A., et al.: Surface matters: limitations of CALIPSO V3 aerosol typ-

ing in coastal regions, Atmos. Meas. Tech., 7, 2061–2072, doi:10.5194/amt-7-2061-2014, URL https://www.atmos-meas-tech.net/7/2061/2014/, 2014.

Küchler, N., Kneifel, S., Löhnert, U., et al.: A W-Band Radar–Radiometer System for Accurate and Continuous Monitoring of Clouds and Precipitation, J. Atmos. Oceanic Technol., 34, 2375–2392, doi:10.1175/JTECH-D-17-0019.1, 2017.

Liu, Z., Vaughan, M., Winker, D., et al.: The CALIPSO Lidar Cloud and Aerosol Discrimination: Version 2 Algorithm and Initial Assessment of Performance, J. Atmos. Oceanic Technol., 26, 1198–1213, doi:10.1175/2009JTECHA1229.1, 2009.

Mace, G. G. and Protat, A.: Clouds over the Southern Ocean as Observed from the R/V Investigator during CAPRICORN. Part I: Cloud Occurrence and Phase Partitioning, J. Appl. Meteorol. and Clim., 57, 1783–1803, doi:10.1175/JAMC-D-17-0194.1, URL https://doi.org/10.1175/JAMC-D-17-0194.1, 2018.

Mamouri, R. E. and Ansmann, A.: Estimated desert-dust ice nuclei profiles from polarization lidar: methodology and case studies, Atmos. Chem. Phys., 15, 3463–3477, doi:10.5194/acp-15-3463-2015, URL https://www.atmos-chem-phys.net/15/3463/2015/, 2015.

Mattis, I., Müller, D., Ansmann, A., et al.: Ten years of multiwavelength Raman lidar observations of free-tropospheric aerosol layers over central Europe: Geometrical properties and annual cycle, J. Geophys. Res., 10.1029/2007JD009636, D009 636, 2008.

Minikin, A., Petzold, A., Ström, J., et al.: Aircraft observations of the upper tropospheric fine particle aerosol in the Northern and Southern Hemispheres at midlatitudes, Geophys. Res. Lett., 30, 1503, doi:10.1029/2002GL016458, 2003.

Müller, D., Ansmann, A., Mattis, I., et al.: Aerosol-type-dependent lidar ratios observed with Raman lidar, J. Geophys. Res., 112, D16 202, doi:10.1029/2006JD008292, 2007.

Naud, C. M., Booth, J. F., and Del Genio, A. D.: Evaluation of ERA-Interim and MERRA Cloudiness in the Southern Ocean, J. Climate, 27, 2109–2124, doi:10.1175/JCLI-D-13-00432.1, URL https://doi.org/10.1175/JCLI-D-13-00432.1, 2014.

Omar, A. H., Winker, D. M., Kittaka, C., et al.: The CALIPSO Automated Aerosol Classification and Lidar Ratio Selection Algorithm, J. Atmos. Oceanic Technol., 26, 1994–2014, doi:10.1175/2009JTECHA1231.1, 2009.

Protat, A., Schulz, E., Rikus, L., et al.: Shipborne observations of the radiative effect of Southern Ocean clouds, J. Geophys. Res. Atmos., 122, 318–328, doi:10.1002/2016JD026061, URL https://agupubs.onlinelibrary.wiley.com/doi/abs/10.1002/2016JD026061, 2016.

Radenz, M. and Seifert, P.: Software for automated trajectory analysis: trace (Version v0.3), doi:10.5281/zenodo.2576558, 2019.

Ristori, P., Otero, L., Jin, Y., et al.: Saver.net lidar network in southern South America, EPJ Web Conf., 176, 09 011, doi:10.1051/epjconf/201817609011, 2018.

Schneider, C., Glaser, M., Kilian, R., et al.: Weather observations across the southern Andes at 53 deg S, Phys. Geogr., 24, 97–119, 2003.

Smirnov, A., Holben, B. N., Slutsker, I., et al.: Maritime Aerosol Network as a component of Aerosol Robotic Network, J. Geophys. Res., 114, D06 204, doi:10.1029/2008JD011257, 2009.

Stein, A. F., Draxler, R. R., Rolph, G. D., et al.: NOAA's HYSPLIT Atmospheric Transport and Dispersion Modeling System, Bull. Amer. Meteorol. Soc., 96, 2059–2077, doi:10.1175/BAMS-D-14-00110.1, 2015.

Stohl, A., Forster, C., Frank, A., Seibert, P., and Wotawa, G.: Technical note: The Lagrangian particle dispersion model FLEXPART version 6.2, Atmos. Chem. Phys., 5, 2461–2474, 2005.

Tesche, M., Müller, D., Gross, S., et al.: Optical and microphysical properties of smoke over Cape Verde inferred from multiwavelength lidar measurements, Tellus B, 63, 677–694, doi:10.1111/j.1600-0889.2011.00549.x, 2011.

Wilson, S. R. and Forgan, B. W.: Aerosol optical depth at Cape Grim, Tasmania, 1986-1999, J. Geophys. Res. Atmos., 107, 4068, doi:10.1029/2001JD000398, 2002.

Winker, D. M., Hunt, W. H., and McGill, M. J.: Initial performance assessment of CALIOP, Geophys. Res. Lett., 34, L19803, doi:10.1029/2007GL030135, 2007.

Winker, D. M., Vaughan, M. A., Omar, A., et al.: Overview of the CALIPSO Mission and CALIOP Data Processing Algorithms, J. Atmos. Oceanic Technol., 26, 2310–2323, doi:10.1175/2009JTECHA1281.1, 2009.

Trends of gravity wave flux over Collm

Ch. Geißler[1], Ch. Jacobi[1], E. Yiğit[2]

[1]*Institute for Meteorology, Universität Leipzig, Stephanstr. 3, 04103 Leipzig*

[2] *George Mason University, Department of Physics and Astronomy, Fairfax, USA*

E-Mail: christoph.geissler@uni-leipzig.de

Summary: With the help of MERRA-2 (Modern-Era Retrospective Analysis for Research and Application, version 2) reanalysis data of the zonal wind, measurements of the mesopause region wind over Collm by low-frequency observations, and data of the Horizontal Wind Model, a height profile for the zonal wind in January and July was created by linear interpolation over altitude. Subsequently, three different 5-year periods (1980-1984, 1994-1998 und 1999-2003) were selected, and the obtained wind profiles and NRLMSISE (Naval Research Labatory Mass Spectrometer Incoherent Scatter, Extended) temperatures (January and July) were averaged over these time intervals. This allowed to run the whole atmosphere nonlinear spectral gravity wave (GW) routine of Yiğit et al. (2008) with these data as background profiles. We obtained a height profile of the GW momentum flux (MF) over these three 5-year periods. Based on this, the long-term tendencies of GW MF are estimated and in this way a statement about the trend of the GW activity in the mesosphere and lower thermosphere can be made. GW MF increases in magnitude in both summer and winter. The results are in qualitative agreement with trends of GW proxies obtained from the meteor radar measurements at Collm.

Zusammenfassung: Mit Hilfe von MERRA-2 - Reanalysedaten des Zonalwindes, Messungen des Meteorradars in Collm und mit Daten des Horizontal Wind Models wurde durch lineare Interpolation ein Höhenprofil für den Zonalwind für die Monate Januar und Juli erstellt. Anschließend wurden aus den gewonnenen Windprofilen und NRLMSISE (Naval Research Labatory Mass Spectrometer Incoherent Scatter, Extended) Temperatur Reanalysen (Januar und Juli) drei verschiedene 5-Jahreszeiträume gewählt (1980-1984, 1994-1998 und 1999-2003) und über diese gemittelt. Diese Daten wurden als Hintergrund für die nichtlineare spektrale Schwerewellenroutine nach Yiğit et al. (2008) verwendet, wodurch der Schwerewellenfluss über die drei 5-Jahreszeiträume bestimmt werden konnte. Aus diesen Analysen ließ sich nun der Trend zwischen den jeweiligen Zeiträumen berechnen und so eine Aussage über den Trend der Schwerewellenaktivität in der Mesosphäre und unteren Thermosphäre ableiten. Die Ergebnisse zeigen gute Übereinstimmungen zu anderen Forschungsergebnissen bzgl. der Trends der GW Proxies von Meteorradarmessungen in Collm.

1. Introduction

Gravity waves (GWs), through their ability to transport energy and momentum from the lower to the upper atmosphere, play an important role for the dynamics of the mesosphere and lower thermosphere (MLT) region. GWs mainly develop in the troposphere and distribute energy and momentum throughout the atmosphere, thus influencing the circulation and the thermal structure of the middle and upper atmosphere. They also allow turbulence and mixing between all vertical layers. GWs emerge mainly through synoptic effects like convection (Tsuda et al., 1994), frontal systems (Plougonven and Zhang, 2014), orography (Smith, 1985; Nastrom and Fritts, 1992) or spontaneous adjustment (Fritts and Alexander, 2003). GWs are able to propagate to the middle and upper atmosphere depending on their horizontal phase speed c and the horizontal background winds. As density decreases exponentially with height in the atmosphere, in turn the GW amplitude increases exponentially with height. According to the linear theory, GW becomes saturated when the phase speed equals the background wind speed, so that they break. This effect is the stronger the closer the phase speed c is to the background wind u. If c and u are equal, a GW reaches its critical level and cannot propagate anymore. Therefore, GWs propagating in the opposite direction than the background wind are usually prevailing in the middle atmosphere. Also, GWs faster than the background wind are able to propagate, but mostly GWs traveling in the same direction than the background are filtered out by the strong mesospheric jet. This is the reason why the wind reverses in the mesosphere due to GW breaking, while GWs deposit their momentum if they travel in the opposite direction to u (Lindzen, 1981; Holton, 1982). The momentum transfer by breaking GWs is also called GW drag.

The background wind and the GWs are in close interaction (Jacobi et al., 2006; Hoffmann et al., 2011). Long-term analyses of mesosphere-lower thermosphere (MLT) winds have shown wind and temperature trends probably due to climate change. The question is, which influence these trends have on the GW activity in the middle atmosphere. Jacobi (2014) examined GW variance trends from low frequency (LF) wind measurements at Collm (reflection point at about 52°N, 15°E), Germany, between 82 km and 90 km altitude. GW variance showed generally positive trends during both summer and winter. Hoffmann et al. (2011), analyzing 22 years of medium frequency (MF) radar wind data over Juliusruh, Germany, showed a long term increase of the mesospheric wind jet and an increase of GW kinetic energy in summer.

In order to check whether the observed GW and mean wind trends at midlatitudes are consistent, and whether MLT GW trends are due to background wind trends in the middle atmosphere, we performed simulations with a state-of-the-art nonlinear whole atmosphere GW parameterization (Yiğit et al., 2008) driven by NRLMSISE (Picone et al., 2002) temperatures and realistic wind profiles based on Modern-Era Retrospective Analysis for Research and Application, version 2 (MERRA-2) reanalyses, Horizontal Wind Model (HWM07) winds (Drob et al., 2008, 2015), and Collm (52°N) MLT winds observed by LF radar (Jacobi et al., 2015). The dataset and analysis method is described in section 2. Section 3 shows the results of the simulations, which are discussed in section 4. Section 5 concludes the paper.

2. Gravity wave parameterization

The GW momentum fluxes are calculated with a GW routine after Yiğit et al. (2008, 2009) and Yiğit and Medvedev (2009) for January and July. The GW parameterization routine calculates GW momentum fluxes and GW dynamical and thermal effects on the circulation of the atmosphere (Yiğit and Medvedev 2015, 2017) for a given set of atmospheric background parameters for 41 vertical levels at a given gridpoint. We use here the location of the Collm meteor radar (52°N, 15°E), where wind data at the mesopause region are available (Jacobi et al., 2015) from 1980 to 2003.

The vertical propagation of GWs in the middle atmosphere is related to nonlinear effects which limit the exponential growth. The GW routine includes a nonlinear parameterization of wave breaking/saturation (Weinstock, 1982, Medvedev and Klaassen, 1995, 2000). Other dissipative mechanisms can occur, like molecular viscosity, thermal conduction and ion drag, and they cannot be neglected. Therefore, the GW routine after Yiğit et al. (2008) allows multiple saturation levels. In the nonlinear saturation scheme that is used in this routine individual waves influence the other harmonics in the spectrum and interact with them. In this case harmonics with shorter vertical wavelengths influences a given wave and cause instabilities on shorter scales than the wavelength of the harmonic. That effect acts as a nonlinear diffusion on the probe wave, when averaging over the scale of the wavelength. Below 80 km the effects of molecular viscosity and thermal conduction on GWs are less important. In the thermosphere molecular diffusion and thermal conduction becomes dominant owing to their exponential growth, so that these dissipative effects have to be taken into account in GW propagation. The ionized atmosphere has an influence on the neutral flow as well. This phenomenon is called ion drag. In the GW routine an approximation from Klostermeyer (1972) is used to describe the ion drag. For the Newtonian cooling, which is a proxy for the radiative damping effect on the subgrid-scale GWs, a parameterization after Holton (1982) is used in the GW routine.

The momentum fluxes in the GW routine are distributed according to a Gaussian function. The maximum of this Gaussian distribution is 0.00025 m^2s^{-2}, the half-width of the distribution is 30 ms^{-1}. The GW spectrum considers 30 waves with phase speeds from -80 ms^{-1} to 80 ms^{-1}. A horizontal wavelength of λ = 300 km is specified.

Important atmospheric background parameters in our case are the vertical profile of zonal wind and temperature. The lowest altitude used is 15 km and the highest one is 100 km. The GW routine calculates the zonal and meridional GW drag, zonal GW flux and the total GW thermal effects (heating and cooling) for 41 vertical levels between 15 km and 100 km.

3. Background wind and temperature profiles

Background fields of zonal wind and temperature are necessary to make calculations with the GW routine up to a height of 100 km. For the zonal wind field MERRA-2 reanalysis data (Gelaro et al., 2017) up to 80 km are used, but only from 1980 to 2003. The reason for this can be seen in Fig. 1 which shows for example the July zonal wind as height-time plot for the years 1980 to 2017 in every pressure level at the gridpoint (51.5°N, 13.1°E) close

to Collm. It can be seen that above 0.4 hPa there is a break in the zonal wind in 2003. This corresponds with a change of used data to the MLS temperature observations from August 2004 to present (Gelaro et al., 2017). The wind value at 91 km is given by the LF measurements at Collm (Jacobi et al., 2015). Between 78 and 91 km, wind values were linearly interpolated. Above 91 km, wind values were taken from HWM07 (Drob et al., 2008, 2015; Emmert et al., 2008) data, with linear weighting of the difference between Collm wind and HWM winds by 100% at 91 km, and zero at 100 km between 91 km and 100km.

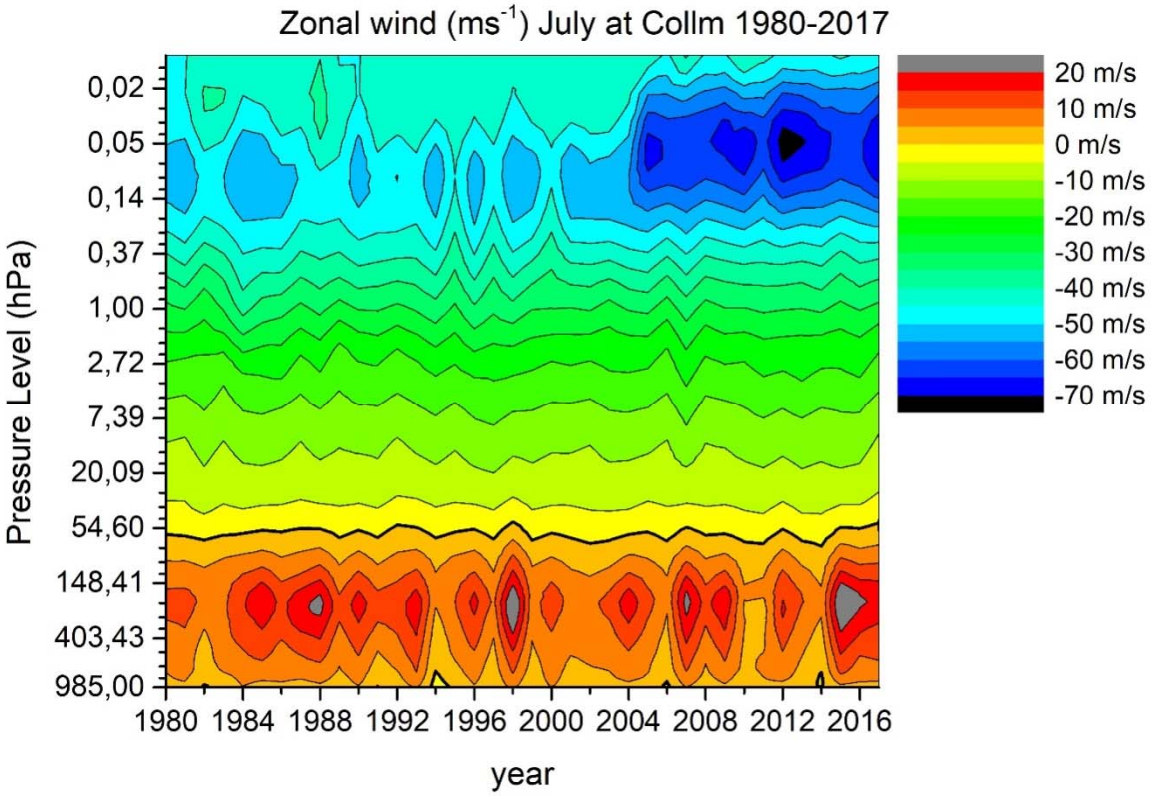

Figure 1: July zonal wind height-time profile over Collm for 1980 to 2017 from MERRA-2 reanalyses.

For the temperature profiles NRLMSISE data are used. NRLMSISE is an empirical, global atmospheric model from surface to space (1000 km) (Picone et al., 2002). The output of the model are temperature and densities of the atmospheric components.

The zonal wind data profiles for January and July at Collm from MERRA-2 reanalyses for different 5-year periods are shown in Fig. 2 (1980-1984 in red, 1994-1998 in blue and 1999-2003 in purple). The three intervals have been chosen because the Collm time series analyses gave indications for a possible trend change in the middle 1990s (Jacobi et al., 2015). The HWM07 wind profile data (black) and the LF measurements at a height of 91 km were added. Fig. 2 (upper row) shows that the profiles of the HWM data differ from the MERRA-2 reanalyses. MERRA-2 data should be preferred to the HWM data for the range up to 75 km. A good match is seen for the LF measurements and the HWM07 data, which is why the interpolation of MERRA-2 reanalyses data at 75 km to the LF measurements is done up to 91 km. The other interpolation is performed between the Collm data at 91 km and the HWM07 data up to 100 km. The result of the linear interpolated zonal wind can be seen in Fig. 2 (lower row) for January and July for three different time

periods. In January there is a trend towards a wind increase in the stratosphere and lower mesosphere between 1980 and 1994. Between 1994 and 2003, however, there is a decent wind decrease, which causes an overall decrease in the zonal wind from 1980 to 2003 up to 60 km. No trend is seen from 60 km to 70 km height. An increase in the west wind over the entire period occurs between 70 km and 95km, which is mainly determined by the period from 1999 to 2003. The trends in July are generally weaker than in January but in the stratosphere and lower mesosphere an increase in the east wind until 1998 can be seen, before there is a decline until 2003. Fig. 2 (lower row) shows a slow increase over the whole considered period above 80km.

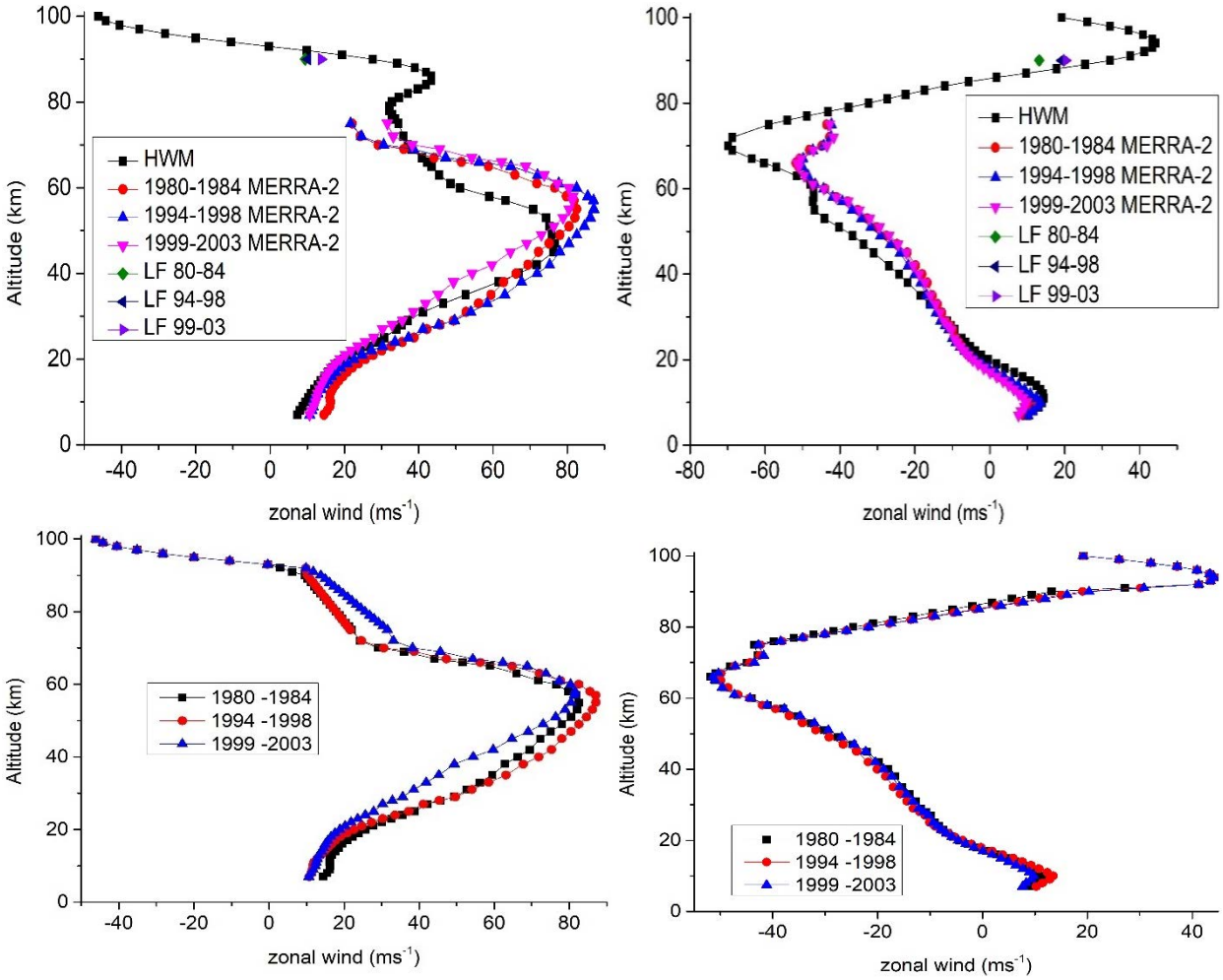

Figure 2: January (left) and July (right) zonal wind height profile at Collm for different 5-year periods from MERRA-2 data, HWM07, and LF measurements at 91 km height in the upper row and linearly interpolated in the lower row.

In Fig. 3 the NRLMSIS temperature profiles for January und July are shown. Obviously, there is no strong trend below 60 km in both months. In January, from 80 km to 91 km the temperature is increasing over the entire period. From 91 km, the temperature increases from 1980 to 1998 and then decreases from 1999 to 2003. This can be observed even more clearly in July from about 70 km to 91 km altitude. Above that, the trend is reversed, so first a decrease and then an increase is recognized. The heights where the greatest trends in temperature and zonal wind are seen, would also suggest the heights with the strongest

trends for GW drag at these height ranges. The profiles from Fig. 2 and Fig. 3 are used as background for the GW routine with the respective 5-year period.

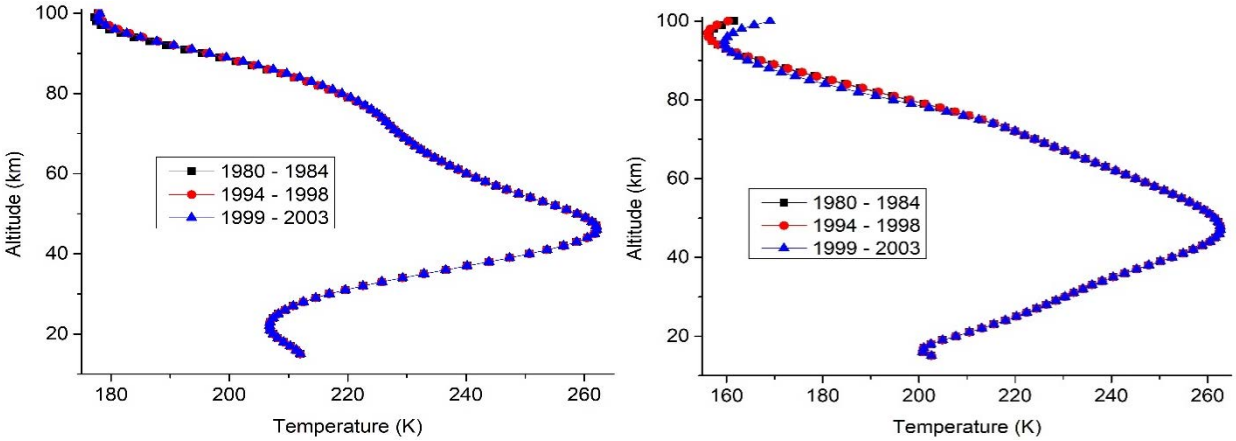

Figure 3: January (left) and July (right) NRLMSISE temperature profile at Collm for different 5-year periods.

4. Results

The results of GW fluxes (left) and trends (right) from the GW routine are shown in Fig. 4 for the different periods for January (upper row) and for July (lower row) above 50 km altitude. In January, the GW flux is negative with a minimum of -10 $m^2 s^{-2}$ in 90 km altitude. On the contrary, the GW flux is positive in July, reaching its maximum of 13 -10 $m^2 s^{-2}$ at about 80 km altitude. A trend can now be calculated from the 5-year periods. The differences between different 5-year periods are shown in Fig. 4 right. The trend between 1980 and 1998 is shown in red. In blue the overall trend from 1980 to 2003 and in green the trend between 1994 and 2003 is shown. For the first trend period (red) in January there is no trend up to about 70 km, up to 80 km it is slightly positive (weaker negative GW flux), then it is small again before it is clearly negative at about 90 km (stronger negative GW flux). Above 95 km, the trend is again approaching zero. For the second period from 1994 to 2003 (green), the trend is mostly negative (stronger negative GW flux). Just between 65 km and 80 km the trend becomes positive (weaker negative GW flux). The trend over the entire period (blue) is mostly negative except for the range between 65 km and 80 km (trend up to +1.0 $m^2 s^{-2}$). A consistently negative trend (weaker positive GW flux) with a maximum of -2.0 $m^2 s^{-2}$ at 80 km altitude results for the period from 1980 to 1998 (red) in July. From 1994 to 2003 (green) in July, there is a positive trend (stronger positive GW flux) up to about 80 km with a maximum of 3.5 $m^2 s^{-2}$. The trend for the entire period from 1980 to 2003 (blue) is positive (stronger positive GW flux) up to 2.0 $m^2 s^{-2}$ in 75 km altitude. Above, the trend will be negative (weaker positive GW flux) with an extremum at 80 km altitude of -4.0 $m^2 s^{-2}$.

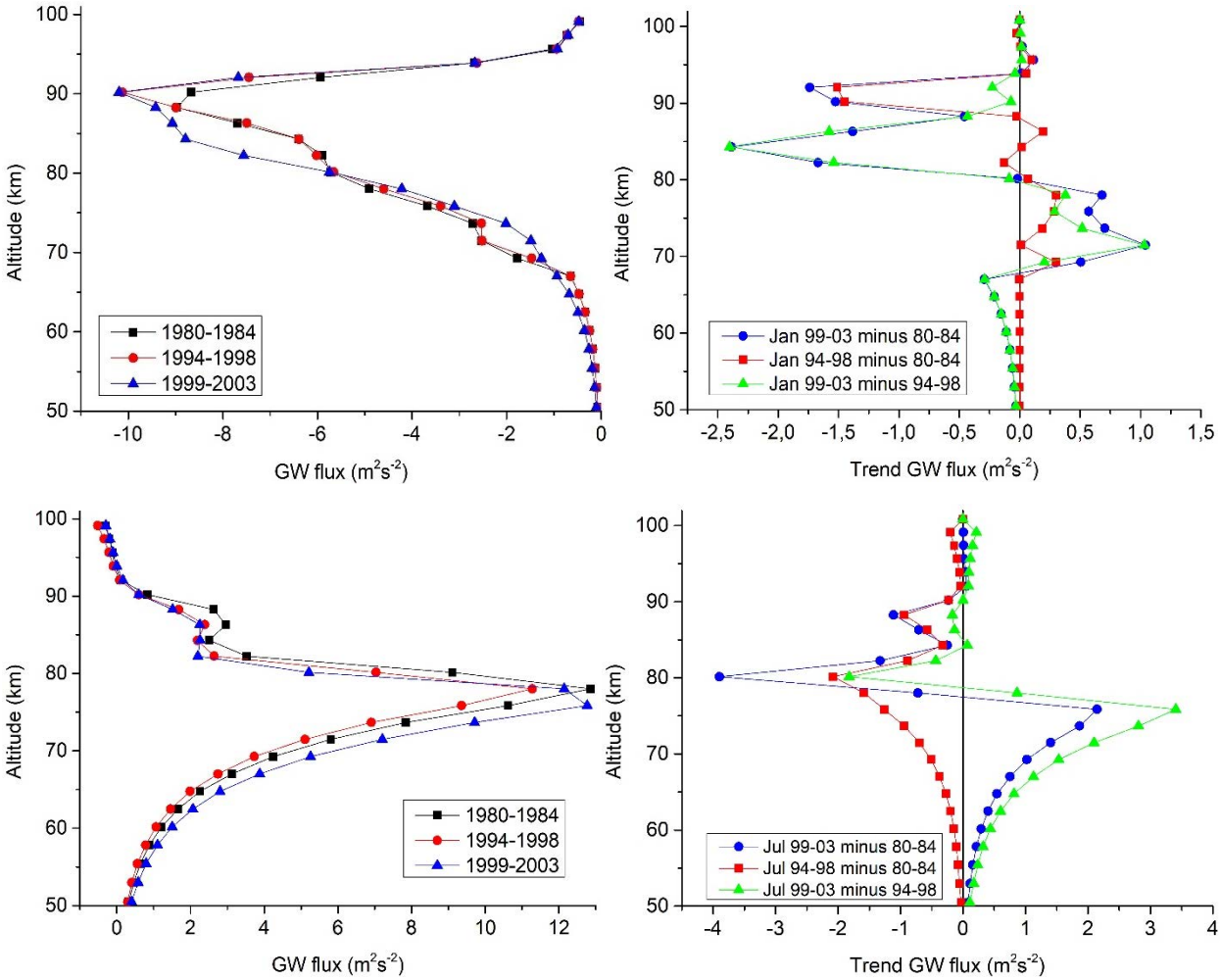

Figure 4: January GW flux (top left) and July (lower left) for different 5-year periods and GW flux trends (right) derived from different 5-year periods of GW flux (left).

4. Discussion

In Fig. 5 the height-time profile of the linear GW variance trend at Collm derived from LF data from 1984 to 2007 is shown. The data are taken from Jacobi (2014), but an extended height range is shown. According to these observations there is a positive trend in January in the altitude range of 84 km to 96 km, which gets stronger above 92 km. However, it should be noted that the data quality of the LF radar observations above 94 km is progressively getting worse. Thus, the positive trend, i.e. the increase in GW variance in the LF data, qualitatively supports the results from the GW routine. For July, the observed GW variance trend in Fig. 5 is negative. The strongest negative trend can be seen between 85 km and 87 km altitude, which roughly matches with the results of the GW routine. The increase in GW flux from the GW routine below 80 km cannot be seen in the radar data. A change in the trend with height, however, is indicated in the observed GW variance, as the negative trend is clearly decreasing below 85 km. Overall, the results of radar data and the GW routine show a qualitative agreement. Li et al. (2010) also noted an increase in GW activity in the summer months, derived from 10.5 years of Lidar temperature measurements.

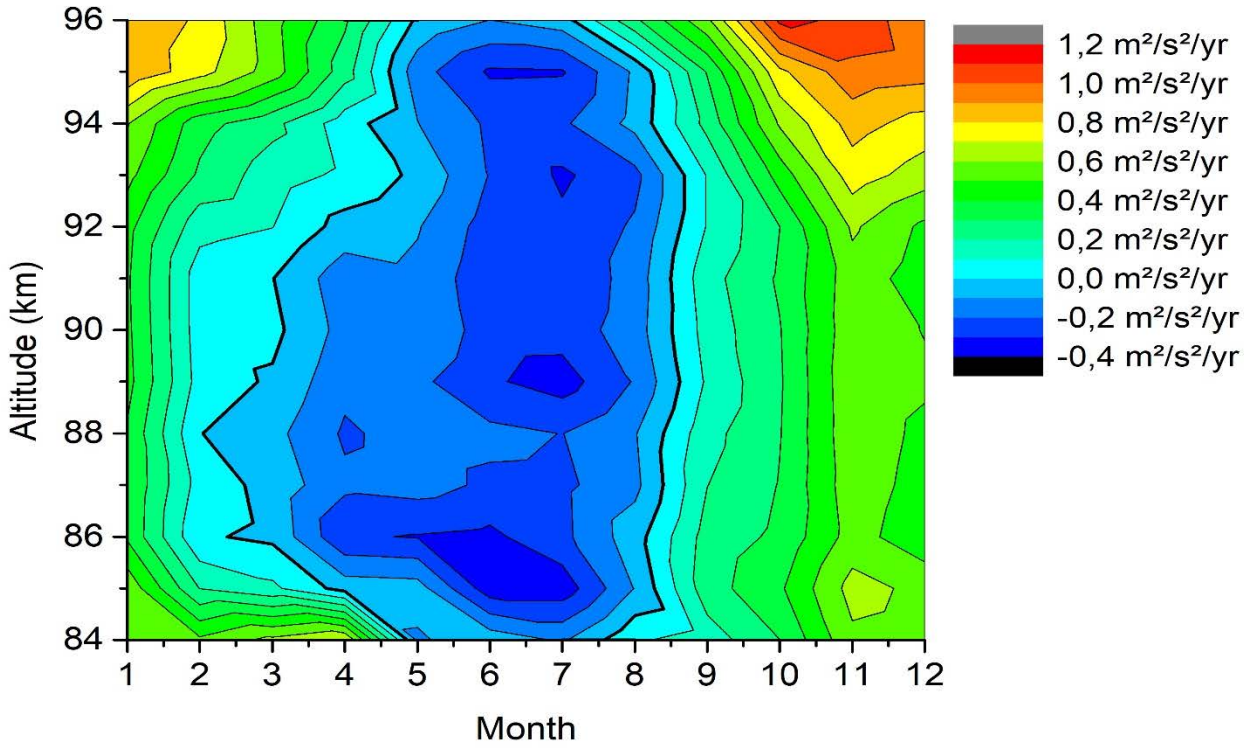

Figure 5: Height-time-profile of linear GW variance trend at Collm from LF radar data (modified from Jacobi, 2014).

This is also in line with the results of Hoffmann et al. (2010), who also showed a stronger GW trend in July. In general it can be said that trends in temperature and wind have a strong influence on GW activity and GW flux in the mesosphere.

5. Conclusions

It could be shown that the GW routine according to Yiğit et al. (2008) could be driven by measurements of the zonal wind at Collm and with reanalysis data for zonal wind and temperature. The results over different 5-year periods allowed the calculation of a trend of GW activity at the gridpoint of Collm. These were in good qualitative agreement with the work of Jacobi (2014), Li et al. (2010) and Hoffmann et al. (2010) with an increase of the GW flux in January above 80 km altitude and a weakening between 65 km and 80 km altitude. In July, GW activity increases with time between 60 km and 75 km altitude, while from 75 km to 90 km altitude the GW flux weakened. In addition, the question arises as to whether the agreement of our results with those of Jacobi (2014), Li et al. (2010) and Hoffmann et al. (2010) is also given for other months except January und July.

Acknowledgements

MERRA-2 and NRLMSISE reanalyses have been provided by NASA through https://gmao.gsfc.nasa.gov/reanalysis/MERRA-2/data_access/ and https://ccmc.gsfc.nasa.gov/modelweb/models/nrlmsise00.php, and have been used in gravity wave routine for assimilation of the wind field. Program code from the Horizontal Wind Model has been provided by CCMS through https://ccmc.gsfc.nasa.gov/modelweb/models_home.html.

References

Drob, D. P., J. T. Emmert G. Crowley et al. (2008): An Empirical Model of the Earth's Horizontal Wind Fields: HWM07, J. Geophys Res., 113, doi:10.1029/2008JA013668.

Drob, D. P., J. T. Emmert, J. W. Meriwether, et al. (2015): An update to the Horizontal Wind Model (HWM): The quiet time thermosphere, Earth Space Sci., 2, 301–319, doi:10.1002/2014EA000089.

Emmert, J. T., D. P. Drob, G. G. Shepherdet al. (2008): DWM07 global empirical model of upper thermospheric storm˜ induced disturbance winds, J. Geophys. Res., 113, A11319, doi:10.1029/2008JA013541

Fritts, D. C. and M. J. Alexander (2003): Gravity wave dynamics and effects in the middle atmosphere, Rev. Geophys., 41, 1003, doi:10.1029/2001RG000106.

Gelaro, R., W. McCarty, M.J. Suárez, et al. (2017): The Modern-Era Retrospective Analysis for Research and Applications, Version 2 (MERRA-2). J. Climate, 30, 5419–5454, doi:10.1175/JCLI-D-16-0758.1.

Hoffmann, P., E. Becker, W. Singer and M. Placke, M. (2010): Seasonal variation of mesospheric waves at northern middle and high latitudes, J. Atmos. Sol.-Terr. Phys. 72, 1068–1079, doi:10.1016/j.jastp.2010.07.002.

Hoffmann, P., M. Rapp, W. Singer and D. Keuer (2011): Trends of mesospheric gravity waves at northern middle latitudes during summer, J. Geophys. Res., 116, D00P08, doi:10.1029/2011JD015717.

Hodges, R. R. (1967): Generation of turbulence in the upper atmosphere by internal gravity waves, J. Geophys. Res., 72, 3455–3458, doi:10.1029/JZ072i013p03455.

Holton, J. R. (1982): The role of gravity wave induced drag and diffusion in the momentum budget of the mesosphere, J. Atmos. Sci., 39, 791–799, doi:10.1175/1520-0469(1982)039<0791:TROGWI>2.0.CO;2.

Jacobi, C., N. M. Gavrilov, D. Kürschner and K. Fröhlich (2006): Gravity wave climatology and trends in the mesosphere/lower thermosphere region deduced from low-frequency drift measurements 1984–2003 (52.1°N, 13.2°E), J. Atmos. Sol.-Terr. Phys., 68, 1913–1923, doi:10.1016/j.jastp.2005.12.007

Jacobi, Ch. (2014): Long-term trends and decadal variability of upper mesosphere/lower thermosphere gravity waves at midlatitudes, J. Atmos. Sol.-Terr. Phys., 118, Part A, 90-95, doi:10.1016/j.jastp.2013.05.009.

Jacobi, Ch., F. Lilienthal, C. Geißler, and A. Krug, 2015: Long-term variability of mid-latitude mesosphere-lower thermosphere winds over Collm (51°N, 13°E), J. Atmos. Sol.-Terr. Phys., 136, B, 174–186, doi:10.1016/j.jastp.2015.05.006.

Klostermeyer, J. (1972): Influence of viscosity, thermal conduction, and ion drag on the propagation of atmospheric gravity waves in the thermosphere, Z. Geophys., 38, 881–890.

Kürschner and Schminder (1986): High-atmosphere wind profiles for altitudes between 90 and 110 km obtained from D1 FL wind measurements over Central Europe in 1983/1984, J. Atmos. Terr. Phys., 48 (1986), pp. 447-453, doi:10.1016/0021-9169(86)90121-2.

Li, T., T. Leblanc, I. S. McDermid, et al. (2010), Seasonal and interannual variability of gravity wave activity revealed by long-term lidar observations over Mauna Loa Observatory, Hawaii, J. Geophys. Res., 115, D13103, doi:10.1029/2009JD013586.

Lindzen, R. S. (1981): Turbulence and stress owing to gravity wave and tidal breakdown, J. Geophys. Res., 86, 9707–9714, doi:10.1029/JC086iC10p09707.

Medvedev, A. S., and G. P. Klaassen (1995): Vertical evolution of gravity wave spectra and the parameterization of associated wave drag, J. Geophys. Res., 100, 25,841–25,853, doi:10.1029/95JD02533.

Medvedev, A. S., and G. P. Klaassen (2000): Parameterization of gravity wave momentum deposition based on nonlinear wave interactions: Basic formulation and sensitivity tests, J. Atmos. Sol. Terr. Phys., 62, 1015–1033, doi:10.1016/S1364-6826(00)00067-5.

Nastrom, G. D. and D. C. Fritts (1992): Sources of Mesoscale Variability of Gravity Waves. Part I: Topographic Excitation, J. Atmos. Sci., 49, 101–110, doi:10.1175/1520-0469(1992)049<0101:SOMVOG>2.0.CO;2, 1992.

Picone, J. M., A. E. Hedin, D. P. Drob, and A. C. Aikin (2002): NRLMSISE˜00 empirical model of the atmosphere: Statistical comparisons and scientific issues, J. Geophys. Res., 107(A12), 1468, doi:10.1029/2002JA009430.

Plougonven, R. and F. Zhang (2014): Internal gravity waves from atmospheric jets and fronts, Rev. Geophys, American Geophysical Union, 52, 33–76, doi:10.1002/2012RG000419.

Smith, R. B. (1985): On Severe Downslope Winds, J. Atmos. Sci., 42, 2597–2603, doi:10.1175/1520-0469(1985)042<2597:OSDW>2.0.CO;2.

Tsuda, T., Y. Muayama, H. Wiryosumarto et al. (1994): Radiosonde observations of equatorial atmosphere dynamics over Indonesia. II: characteristics of gravity waves, J. Geophys. Res., 99, 10.507–10.516, doi:10.1029/94JD00354.

Weinstock, J. (1982): Nonlinear theory of gravity waves: Momentum deposition, generalized Rayleigh friction, and diffusion, J. Atmos. Sci., 39, 1698–1710, doi:10.1175/1520-0469(1982)039<1698:NTOGWM>2.0.CO;2.

Yiğit, E., A. Aylward, and A. S. Medvedev (2008): Parameterization of the effects of vertically propagating gravity waves for thermosphere general circulation models: Sensitivity study, J. Geophys. Res., 113, D19106, doi:10.1029/2008JD010135.

Yiğit, E., and A. S. Medvedev (2009): Heating and cooling of the thermosphere by internal gravity waves, Geophys. Res. Lett., 36, L14807, doi:10.1029/2009GL038507.

Yiğit, E., A. S. Medvedev, A. D. Aylward, et al. (2009): Modeling the effects of gravity wave momentum deposition on the general circulation above the turbopause, J. Geophys. Res., 114, D07101, doi:10.1029/2008JD011132.

Yiğit, E., and A. S. Medvedev (2015): Internal wave coupling processes in Earth's atmosphere, Adv. Space Res., 55, 983-1003, doi:10.1016/j.asr.2014.11.020.

Yiğit, E. and A. S. Medvedev (2017): Influence of parameterized small-scale gravity waves on the migrating diurnal tide in Earth's thermosphere, J. Geophys. Res.: Space Phys., 122, doi:10.1002/2017ja024089.

Implementing a Whole Atmosphere Gravity Wave Parameterization in the Middle and Upper Atmosphere Model: Preliminary Results

F. Lilienthal[(1)], N. Samtleben[(1)], C. Jacobi[(1)], E. Yiğit[(2)]

(1) *Institute for Meteorology, Stephanstr. 3, 04103 Leipzig, Germany*
(2) *Department of Physics and Astronomy, George Mason University, Fairfax, USA*

E-Mail: friederike.lilienthal@uni-leipzig.de

Summary: The Middle and Upper Atmosphere Model (MUAM) is used to implement a modern whole atmosphere gravity wave (GW) parameterization (Yiğit et al., 2008). To adjust the resulting model climatology to observations, we compare two different spectra of GW phase speeds and the related momentum fluxes included in this parameterization. The first spectrum, termed Spectrum1, which is more narrow, covers phase speeds up to $\pm 80\,\mathrm{m\,s^{-1}}$ and the second one, Spectrum2, goes up to $\pm 95\,\mathrm{m\,s^{-1}}$. We analyzed the zonal GW drag, the acceleration of the zonal mean flow owing to breaking GWs, and the resulting background circulation. We also examined zonal wind amplitudes of the diurnal and semidiurnal migrating solar tide. As a result, we find that both GW phase speed spectra have their advantages and disadvantages. For example, Spectrum1 reproduces the zonal wind reversal in the mesosphere correctly, but it does not lead to a reversed zonal GW drag in the lower thermosphere. While the amplitudes of the diurnal tide tend to be more realistic for Spectrum1, those of the semidiurnal tide are more representational for Spectrum2. Overall, the new GW parameterization is a substantial improvement to the MUAM model.

Zusammenfassung: Das Modell für die mittlere und obere Atmosphäre (MUAM) wird für die Implementierung einer neuen Schwerewellenparametrisierung, die für die gesamte Atmosphäre geeignet ist, verwendet (Yiğit et al., 2008). Um die Klimatologie des Modells basierend auf der neuen Parametrisierung an Beobachtungen anzupassen, werden zwei verschiedene Spektren für die Phasengeschwindigkeiten von Schwerewellen und deren Impulsflüsse verglichen. Das erste Spektrum, als Spectrum1 bezeichnet, das einen schmaleren Bereich von Phasengeschwindigkeiten abdeckt, geht bis zu $\pm 80\,\mathrm{m\,s^{-1}}$ und das zweite, Spectrum2, geht bis zu $\pm 95\,\mathrm{m\,s^{-1}}$. Wir analysieren die Beschleunigung des mittleren Zonalwindes durch brechende Schwerewellen und die daraus resultierende Hintergrundzirkulation. Wir untersuchen ebenfalls die Zonalwindamplituden der ganztägigen und halbtätigen migrierenden solaren Gezeiten. Das Ergebnis dieses Experiments zeigt, dass beide Phasengeschwindigkeitsspektren ihre Vor- sowie Nachteile haben. Beispielsweise reproduziert Spectrum1 die Umkehr des Zonalwindes in der Mesosphäre korrekt, jedoch führt es nicht zu einer umgekehrten zonalen Beschleunigung durch Schwerewellen in der Thermosphäre. Während die Amplituden der ganztägigen Gezeit bezüglich Spectrum1 wesentlich realistischer zu sein scheinen, sind jene der halbtägigen Gezeit bezüglich Spectrum2 repräsentativer. Insgesamt ist die neue Parameterisierung eine erhebliche Verbesserung des MUAM Modells.

1 Introduction

The middle atmosphere dynamics are mainly dominated by internal gravity waves (GW), which are mostly generated by orography and convection in the troposphere (Fritts and Alexander, 2003). When they propagate conservatively, the amplitude is exponentially increasing with height due to the decreasing background density. The propagation conditions of GWs strongly depend on their intrinsic phase speed $c - u$, where c is the phase speed of the wave and u is the background zonal wind. When the GW is approaching its critical level, $c = u$, which cannot be penetrated by GWs, the GW is absorbed, reflected back, or starts to dissipate. Thus, c needs to be larger than u, so that the GW can properly propagate. For magnitudes $|c| < |u|$, GWs can only propagate if the zonal mean flow is directed oppositely, i.e. c and u have opposite signs. For typical winter conditions characterized by a strong eastward jet ($u > 0$) in the middle atmosphere, most of the eastward directed GWs ($c > 0$) are filtered out. For this reason we mainly observe GWs with westward phase speeds ($c < 0$) during winter. When these GWs break and deposit their momentum, they decelerate the mean flow, being the main reason for the zonal wind reversal in the mesosphere.
Depending on their characteristics, GWs may also be able to penetrate the thermosphere-ionosphere (Yiğit et al., 2008; Yiğit and Medvedev, 2015). In these altitudes, GWs are additionally influenced by thermospheric dissipation such as molecular viscosity and thermal conduction (Vadas and Fritts, 2005), ion friction and radiative damping (Yiğit et al., 2008).
Among their impact on the zonal mean flow, GWs are able to enhance or damp tidal amplitudes due to GW breaking or momentum deposition (e.g., Forbes et al., 1991; Mayr et al., 1998; Meyer, 1999; Lieberman et al., 2010; Liu et al., 2013; Yiğit and Medvedev, 2017). Usually, solar tides are excited by the absorption of solar radiation in the troposphere and stratosphere. Therefore, they have periods of a solar day (24 h) and its harmonics (e.g., 12 h, 8 h, 6 h, etc.). Additionally, other sources may play an important role for certain harmonics, e.g., Lilienthal et al. (2018) have shown that nonlinear interactions among tides and GW-tide interactions can also excite an 8 h tide, especially in the lower thermosphere, depending on latitude and season. Diurnal (24 h) and semidiurnal (12 h) variations in GW momentum flux have been observed, e.g., by Fritts and Vincent (1987) and Liu et al. (2013). Further modeling studies suggest that interactions between GWs and tides can generate new tides (e.g., Miyahara and Forbes, 1991; Ribstein and Achatz, 2016).
Due to their relatively short horizontal wavelengths (tens to hundreds of km) compared to the grid size of global circulation models, GWs are usually not resolved and require a parameterization. However, most approaches used in middle and upper atmosphere circulation models (e.g., Lindzen, 1981; Hines, 1997; Warner and McIntyre, 2001) do not consider GW propagation into the thermosphere or use simple nonphysical techniques and fudge factors. Yiğit et al. (2008) developed a new GW scheme that extends into the thermosphere and systematically accounts for the realistic dissipation in addition to breaking and saturation. Here, we report on the implementation of this scheme in a mechanistic global circulation model at Leipzig Institute for Meteorology. The results will be presented in the following with special emphasis on the importance of the GW spectrum used.

2 Model Description

The Middle and Upper Atmosphere Model (MUAM) is a 3-dimensional mechanistic primitive equation nonlinear global circulation model. The lower boundary is at 1000 hPa, based on ERA-Interim reanalysis fields (Dee et al., 2011) of zonal mean temperature and geopotential as well as the respective stationary planetary waves with wavenumbers 1-3. These reanalyses are used as decadal (2000 – 2010) and monthly means for solstitial months (January, July) and equinoctial months (April, October). In the vertical domain, the model extends in 56 levels up to a logarithmic pressure height of about 160 km, evenly spaced in log-pressure coordinates with a constant scale height of 7 km. The lower 30 km are nudged to ERA-Interim zonal mean temperature fields to correct the dynamics in the lower atmosphere (Jacobi et al., 2015; Lilienthal et al., 2018).
The model solves the Navier-Stokes equations of motion and includes the first law of thermodynamics, the continuity equation and a hydrostatic assumption (e.g., Jakobs et al., 1986). A Matsuno integration scheme (Matsuno, 1966) is applied. Solar and infrared radiation are parameterized according to Strobel (1978) and Fomichev and Shved (1985), considering absorption due to the most important atmospheric constituents, including H_2O (troposphere), CO_2 and O_3 (stratosphere) as well as absorption bands like the extrem ultra violet (EUV) band in the thermosphere. Further thermospheric processes such as Rayleigh friction, ion drag or Newtonian cooling are also parameterized.
As a major improvement to earlier MUAM versions, we use a whole atmosphere nonlinear gravity wave scheme according to Yiğit et al. (2008). The source level of GWs is defined at 15 km. In the original version of the GW parameterization adapted from Yiğit et al. (2008), the asymmetric spectrum includes a total of 30 harmonics with phase speeds between ±2 and ±80 $\mathrm{m\,s^{-1}}$. The maximum initial momentum flux at the source level is 0.00025 $\mathrm{m^2\,s^{-2}}$ and the full width at half maximum (FWHM) of the spectrum function is located at 35 $\mathrm{m\,s^{-1}}$. This spectrum has been used in a number of publications thereafter (e.g., Yiğit et al., 2009). In the following we refer to this spectrum as Spectrum1. It is shown in Fig. 1a. For comparison, we propose a new modified GW phase speed spectrum (Fig. 1b, Spectrum2) with more harmonics (40 in total) and reaching larger phase speeds up to ±95 $\mathrm{m\,s^{-1}}$. The maximum momentum flux corresponds to that of Spectrum1, but Spectrum2 is broader with a FWHM of 65 $\mathrm{m\,s^{-1}}$. Vertical profiles of the Newtonian cooling coefficient, the eddy diffusion coefficient and electron density are currently not used in the parameterization, i.e. they are zero.
In the first 60 model days, GWs and solar tides are turned off until the simulated global circulation reaches a stable state. During this period, mainly the nudging in the lower atmosphere, zonal mean radiative processes and thermospheric processes such as Rayleigh friction are responsible for controlling the background circulation. Then, GWs start to propagate and build up the typical wind reversal in the mesosphere. After another 120 model days, also solar tides are introduced, i.e. the heating rates in the solar radiation parameterization are allowed to have non-zonal structures. The following 210 model days are necessary to form a stable global circulation, which is in balance with the atmospheric oscillations. The last 30 model days (day 390-420) are used to analyze the monthly mean state of the atmosphere. The results of the two experiments based on the two different GW phase speed spectra are presented below.

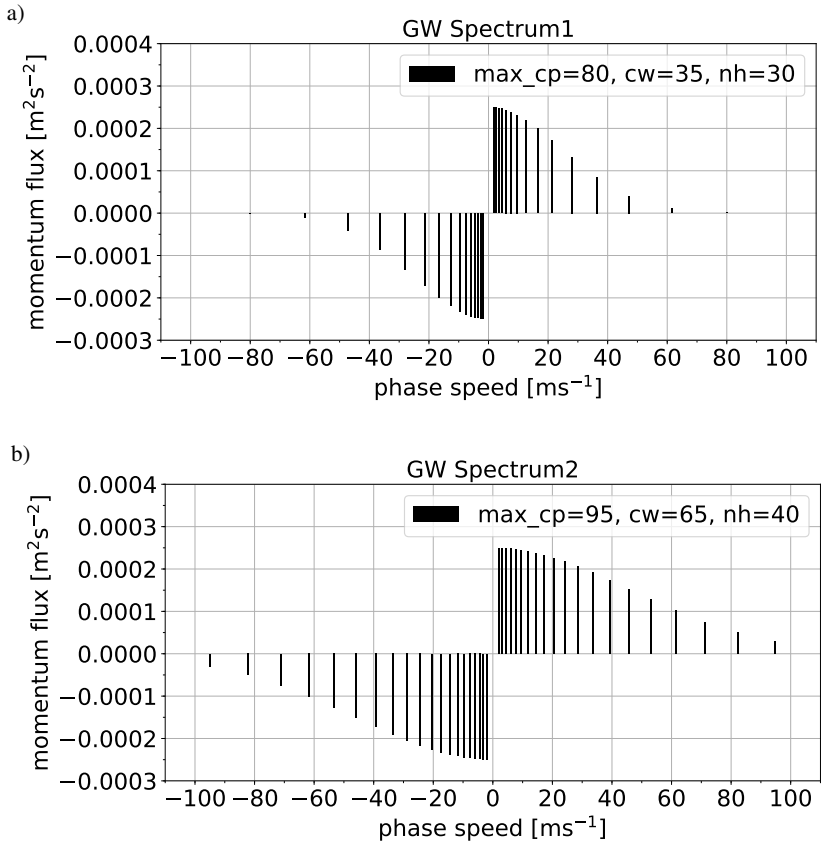

Fig. 1: GW spectra of phase speeds and associated momentum fluxes at the source level of the whole atmosphere GW parameterization. a) Spectrum1: original according to Yiğit et al. (2008, 2009), b) Spectrum2: new modified spectrum.

3 Results

3.1 Zonal wind and zonal GW drag

Figure 2 shows the zonal mean zonal wind (first row) and zonal GW drag (second row) according to Spectrum1 for solstice (January: a, e; July: c, g) and equinox conditions (April: b, f; October: d, h). The same is shown for Spectrum2 in Fig. 3. Spectrum1 leads to relatively strong westerly wind jets up to 80 m s^{-1} in January (Fig. 2a) and 100 m s^{-1} in July (Fig. 2c) in the respective winter hemisphere (WH). Similar results have been obtained in the simulations of Miyoshi and Yiğit (2019). Although Spectrum1 includes slower GWs, the mesospheric jet is just slightly affected by these GWs. This leads to the assumption that the energy and momentum, which is transfered by the slow GWs in the lower part of the atmosphere, is not sufficient. Thus, the number of harmonics needs to be increased to generate more GWs than in Spectrum1. Another interesting feature is the poleward tilt of the westerly jets, which is apparent during all seasons. Based on observations (e.g., Fleming et al., 1990; Swinbank and Ortland, 2003) the mesospheric jet is normally tilted towards the equator with increasing height, but this cannot be reproduced. Note that in July, there is a bridge of positive zonal wind above the equator in the mesosphere/lower thermosphere (MLT; Fig. 2c) connecting the mesospheric and thermospheric jet, which is not seen during January.

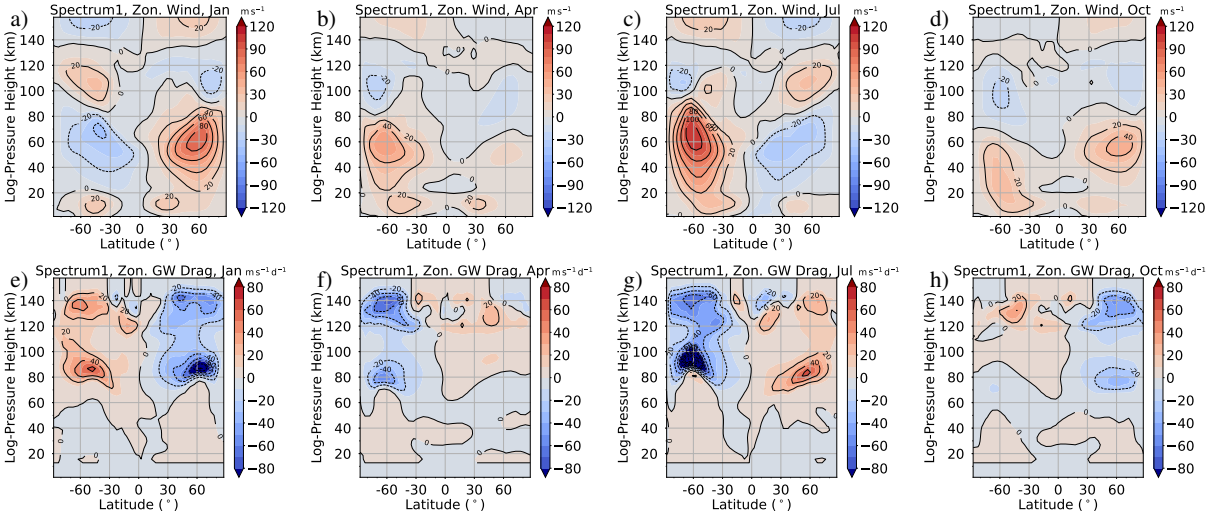

Fig. 2: a)-d): Zonal mean zonal wind based on GW Spectrum1. e)-h): Zonal mean zonal GW drag based on GW Spectrum1. From left to right: January, April, July, October conditions.

The zonal GW drag (Fig. 2e, g) shows a deceleration of more than 80 m s^{-1} day^{-1}, which leads to the wind reversal in the MLT located near 100 km with less than −30 m s^{-1} during winter solstice. Up to 100 km, the distribution of the zonal GW drag is in accordance with other model studies (Yiğit et al., 2008), but above, between 100 and 120 km, the zonal GW drag does not reverse. This may be one indication showing that most of the westward directed GWs are filtered out on their way into the higher atmosphere. The easterly jets in the summer hemisphere (SH) vary between −30 and −40 m s^{-1}. During equinoxes, the zonal wind jets in Fig. 2b and 2d tend to be stronger in the autumn hemisphere, reaching a maximum of 50 m s^{-1} in April. The hemispheres appear more uneven in April than in October. Above 80 km, zonal winds during equinoxes are relatively weak.

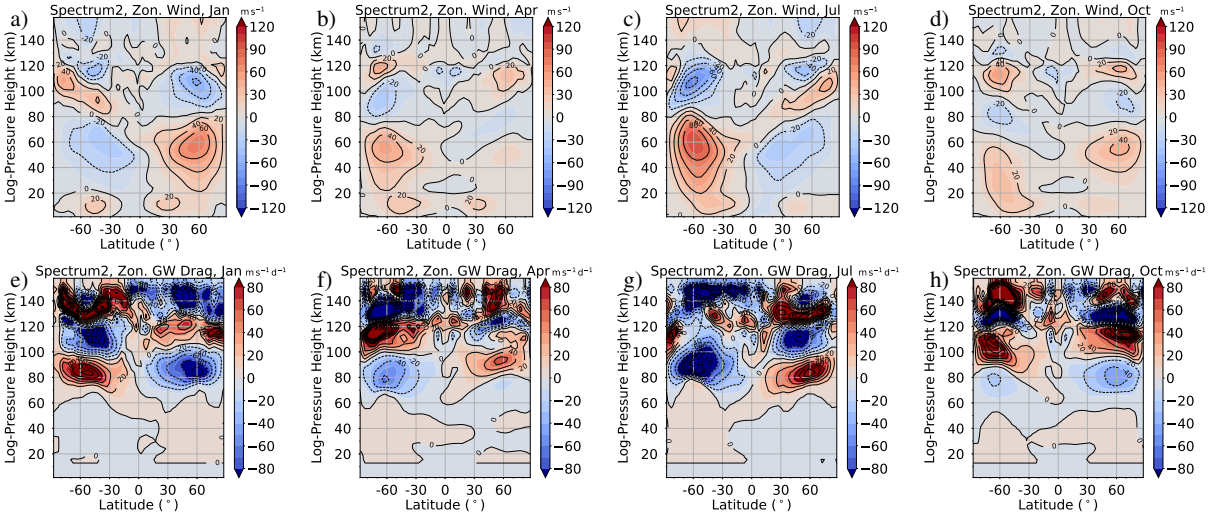

Fig. 3: a)-d): Zonal mean zonal wind based on GW Spectrum2. e)-h): Zonal mean zonal GW drag based on GW Spectrum2. From left to right: January, April, July, October conditions.

Generally, Spectrum2 (Fig. 3) shows similar features, but there are a few different details. The westerly winds in the winter mesosphere are slightly weaker by about $10\,\mathrm{m\,s^{-1}}$, which is an effect of the increased number of harmonics and FWHM of the phase speed distribution in Spectrum2.
There are more slow GWs decelerating the mesospheric jet compared to Spectrum1. This can be also seen in the zonal GW drag, which is much stronger for Spectrum2 (Fig. 3e, g) in comparison to Spectrum1 (Fig. 2e, g). Thus, the resulting wind reversal is more enhanced with a wind speed of more than $-60\,\mathrm{m\,s^{-1}}$. For Spectrum2, the GW forcing originating from the slower GWs with larger amplitudes is dominating the GW forcing induced by the fast GWs with smaller amplitudes. Therefore, the effect of the fast GWs, which usually lead to a higher wind reversal, is weaker for Spectrum2 compared to Spectrum1. In other words, the height of the wind reversal in the mesosphere is mainly determined by the slow GWs, so that the wind reversal of Spectrum2 is found at lower altitudes (near 80 km).
The bridge of positive zonal wind speed above the equator, as before in Fig. 2c, is here seen in January and July (Fig. 3a, c). Furthermore, in contrast to Spectrum1, some fast propagating harmonics can pass the mesospheric jet, without being filtered out. While GW drag in the lower thermosphere does not change sign for Spectrum1, it is strongly reversed between 100-120 km for Spectrum2. Therefore, larger zonal wind speeds are also found in the Spectrum2 simulation in the lower thermosphere, during solstices and equinoxes. Below the MLT, zonal wind during equinoxes is comparable for both spectra.

3.2 Atmospheric Tides

The zonal wind amplitudes of the modeled diurnal tide (DT) and semidiurnal tide (SDT) are shown in Fig. 4 for Spectrum1 and in Fig. 5 for Spectrum2. In general, for Spectrum1 (Fig. 4, first row), the DT maximizes at low latitudes near 110 km with peaks of about 30 to $35\,\mathrm{m\,s^{-1}}$. During equinoxes, both hemispheres have a similar magnitude. During solstices, amplitudes tend to be stronger in the SH. Above 130 km, the DT gradually increases, reaching more than $100\,\mathrm{m\,s^{-1}}$ at the upper boundary of the model. The SDT (Fig. 4, second row) generally shows maxima near 120 km at midlatitudes, whereby the SDT amplitudes are slightly larger during solstices. Below that altitude, amplitudes tend to be larger in the WH with up to $20\,\mathrm{m\,s^{-1}}$, but above, up to 140 km, the amplitudes become larger in the SH, where they can be even larger. Although April has a similar SDT structure like July, the October amplitudes deviate from January by a missing maximum in the northern hemisphere. In contrast to the DT, SDT ampltiudes do not generally increase in the thermosphere but show a maximum in the WH near 160 km that is of similar magnitude like those near 120 km.
DT amplitudes based on Spectrum2 (Fig. 5, first row) reach maxima of more than $40\,\mathrm{m\,s^{-1}}$, raising up to $50\,\mathrm{m\,s^{-1}}$ in July. Again, the SH reveals a stronger DT and during equinoxes, the magnitude is quite uniform for both hemispheres. While Spectrum1 has a relatively homogeneous meridional structure in the thermosphere, the DT maxima at low latitudes are also visible above the MLT (between 120 and 140 km) for Spectrum2. Amplitudes of the SDT are also larger for Spectrum2, but reveal a similar global structure. Moreover, the maxima are reached during equinoxes with about $40\,\mathrm{m\,s^{-1}}$ in the spring hemisphere.

During solstices they reach 20-30 $\mathrm{m\,s^{-1}}$. Similar to the features of the DT, the SDT in the thermosphere has a more distinct structure in the thermosphere for Spectrum2. Even though maxima generally agree with Spectrum1, the amplitudes are much stronger and there is larger meridional fluctuation.

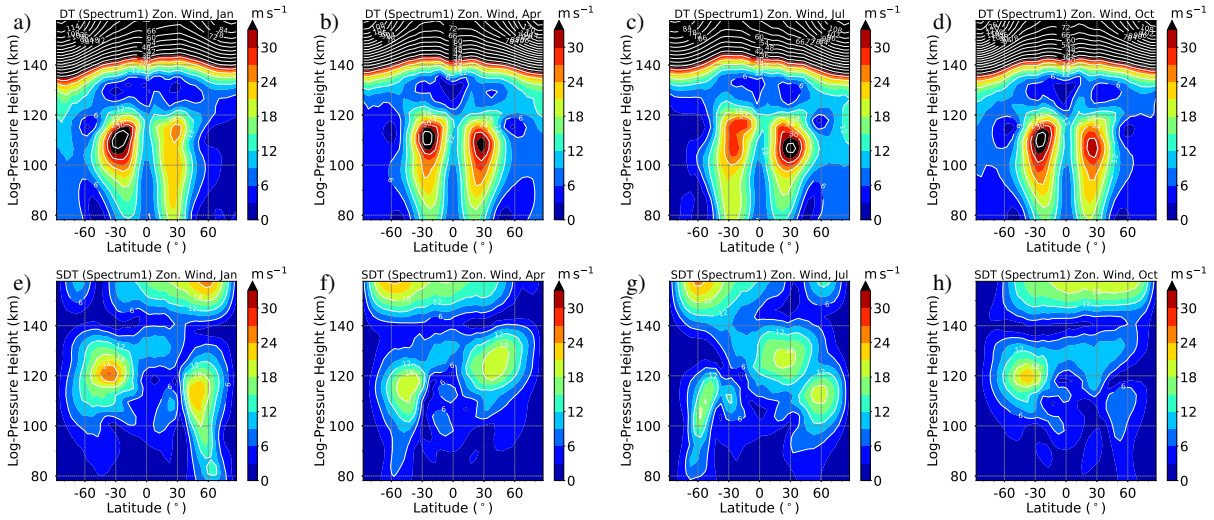

Fig. 4: Zonal mean zonal wind amplitudes of the DT (a-d) and SDT (e-h) based on GW Spectrum1. From left to right: January, April, July, October conditions. Amplitudes that extend the color scale are visualized by additional contour lines.

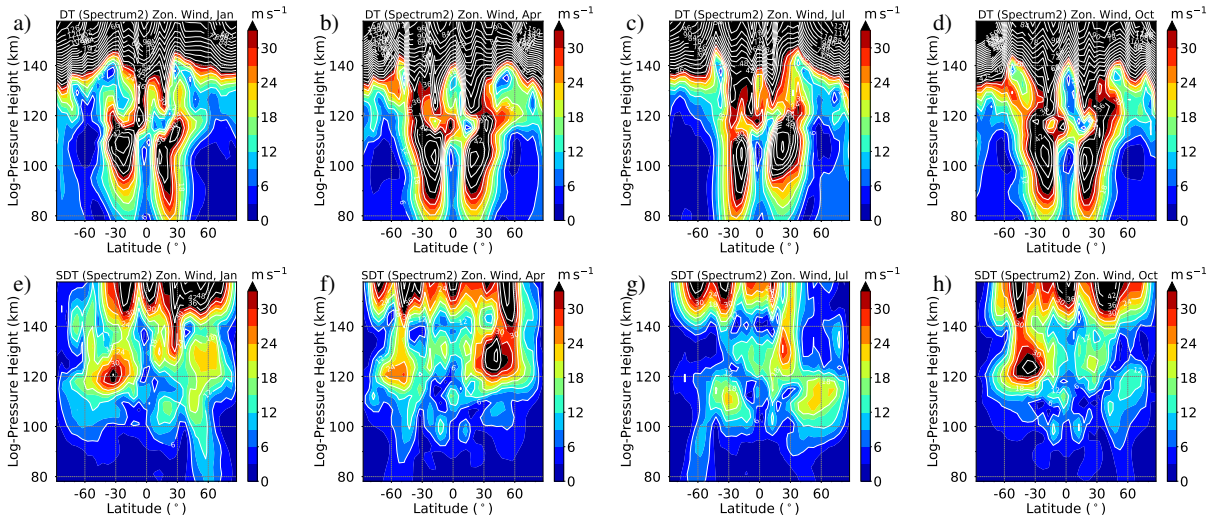

Fig. 5: Zonal mean zonal wind amplitudes of the DT (a-d) and SDT (e-h) based on GW Spectrum2. From left to right: January, April, July, October conditions.Amplitudes that extend the color scale are visualized by additional contour lines.

4 Discussion and Conclusion

Applying a modern parameterization of GWs, suitable for the whole atmosphere, we used a global circulation model to analyze the zonal mean zonal wind and tidal amplitudes. Thereby, we compare two different settings of GW phase speed spectra, defining the source level momentum flux of GWs for a certain range of phase speeds. Spectrum1 is a more narrow spectrum with a strong decay of momentum flux towards faster GWs, while Spectrum2 includes some larger phase speeds and a weaker decline of momentum flux. But the maximum momentum flux remains for both spectra the same. We note that the background circulation as well as atmospheric tides strongly depend on these GW spectra, both showing advantages and disadvantages.
On the one hand, Spectrum1 agrees better with global zonal wind climatologies with respect to the height of the wind reversal in the WH, e.g. the Horizontal Wind Model (HWM; Drob et al., 2008, 2015), the UARS Reference Atmosphere Project (URAP; Swinbank and Ortland, 2003), the Global Empirical Wave Model (GEWM; Portnyagin et al., 2004) and the older COSPAR International Reference Atmosphere (CIRA; Fleming et al., 1990) have a wind reversal near 100 km. On the other hand, the poleward tilt of the jets based on Spectrum1 are not realistic. Spectrum2, however, shows a bridge of westerlies above the equator as it is the case in the climatologies mentioned above. Spectrum1 and Spectrum2 both tend to have rather weak easterly jets in the summer mesosphere. A validation of the neutral wind in the thermosphere is difficult because climatologies for these altitudes are rare. Results from the Coupled Middle Atmosphere-Thermosphere-2 (CMAT2) global circulation model suggest a gradually increasing zonal wind magnitude above 120 km (Yiğit et al., 2009). The associated GW drag in these simulations changes sign in the lower thermosphere as reproduced by our simulation with Spectrum2 but not with Spectrum1. Yiğit et al. (2009) obtain GW drag amplitudes in the WH of about $-80\,\mathrm{m\,s^{-1}\,day^{-1}}$ near 80 km. This is larger than that of Spectrum1 but much smaller than that of Spectrum2. Even if the same spectrum is assumed, the application of the whole atmosphere scheme in two different global circulation models can yield slightly different results, depending on the differences in the dynamical cores of these models. However, the overall structure of the simulated drag demonstrates similarities.
Considering the DT and SDT amplitudes, both simulations generally agree with the global structure from the Global Scale Wave Model (GSWM; e.g., Hagan et al., 2001), although hemispheric differences are more pronounced in our simulations than in GSWM. The amplitudes of Spectrum2 are generally larger than those of Spectrum1 simulation. DT Amplitudes below 120 km are well reproduced by Spectrum1 but they tend to be too large for Spectrum2. The SDT, however, is too weak in Spectrum1 and comes much closer to GSWM amplitudes, when using Spectrum2. It shall also be noted here, that MUAM tidal amplitudes of earlier model version were generally too weak by a factor of 2-3 (e.g., Lilienthal et al., 2018). In fact, similar issues have also been reported for other numerical models (e.g., Smith, 2012; Pokhotelov et al., 2018). Therefore, the new GW parameterization according to Yiğit et al. (2008) is a great step forward to improve the amplitudes of atmospheric tides in MUAM. Similar feature has been reported by Yiğit and Medvedev (2017), suggesting an important influence of thermospheric GWs on the DT. Furthermore, the zonal wind jets in earlier MUAM version were usually very strong,

especially in southern winter (Lilienthal et al., 2017). The use of the new scheme has also helped to resolve this issue.
To conclude, the GW parameterization by Yiğit et al. (2008) can be a substantial improvement to the MUAM model. Here, we have tested an established GW phase speed spectrum (Spectrum1) as well as a variation thereof (Spectrum2) and showed that more realistic distribution of winds and tidal amplitudes can be obtained. Future research will include further tests and validation work concerning atmospheric circulation and solar tides.

Acknowledgements

Monthly mean ECMWF reanalyses data (ERA-Interim) are provided by `https://apps.ecmwf.int/datasets/data/interim-full-moda/levtype=sfc/` and have been used in MUAM for assimilation in the troposphere. The study has been supported by Deutsche Forschungsgemeinschaft under grants JA 836/32-1, JA 836/38-1, and JA 836/43-1. We further acknowledge the work of our student assistant Swetlana Paul who executed the model simulations and analysis tools.

References

Dee, D. P., Uppala, S. M., Simmons, A. J., Berrisford, P., Poli, P., Kobayashi, S., Andrae, U., Balmaseda, M. A., Balsamo, G., Bauer, P., Bechtold, P., Beljaars, A. C. M., van de Berg, L., Bidlot, J., Bormann, N., Delsol, C., Dragani, R., Fuentes, M., Geer, A. J., Haimberger, L., Healy, S. B., Hersbach, H., Hólm, E. V., Isaksen, L., Kallberg, P., Köhler, M., Matricardi, M., McNally, A. P., Monge-Sanz, B. M., Morcrette, J.-J., Park, B.-K., Peubey, C., de Rosnay, P., Tavolato, C., Thépaut, J.-N., and Vitart, F., 2011: The ERA-Interim reanalysis: configuration and performance of the data assimilation system, Quart. J. Roy. Meteor. Soc., 137, 553–597, doi:10.1002/qj.828.

Drob, D. P., Emmert, J. T., Crowley, G., Picone, J. M., Shepherd, G. G., Skinner, W., Hays, P., Niciejewski, R. J., Larsen, M., She, C. Y., Meriwether, J. W., Hernandez, G., Jarvis, M. J., Sipler, D. P., Tepley, C. A., O'Brien, M. S., Bowman, J. R., Wu, Q., Murayama, Y., Kawamura, S., Reid, I. M., and Vincent, R. A., 2008: An empirical model of the Earth's horizontal wind fields: HWM07, J. Geophys. Res.: Space Phys., 113, doi:10.1029/2008JA013668.

Drob, D. P., Emmert, J. T., Meriwether, J. W., Makela, J. J., Doornbos, E., Conde, M., Hernandez, G., Noto, J., Zawdie, K. A., McDonald, S. E., Huba, J. D., and Klenzing, J. H., 2015: An update to the Horizontal Wind Model (HWM): The quiet time thermosphere, Earth Space Sci., 2, 301–319, doi:10.1002/2014EA000089.

Fleming, E. L., Chandra, S., Barnett, J., and Corney, M., 1990: Zonal mean temperature, pressure, zonal wind and geopotential height as functions of latitude, Adv. Space Res., 10, 11–59, doi:10.1016/0273-1177(90)90386-E.

Fomichev, V. and Shved, G., 1985: Parameterization of the radiative flux divergence in the 9.6 μm O_3 band, J. Atmos. Terr. Phys., 47, 1037 – 1049, doi:10.1016/0021-9169(85)90021-2.

Forbes, J. M., Gu, J., and Miyahara, S., 1991: On the interactions between gravity waves and the diurnal propagating tide, Planet. Space Sci., 39, 1249 – 1257, doi: 10.1016/0032-0633(91)90038-C.

Fritts, D. C. and Alexander, M. J., 2003: Gravity wave dynamics and effects in the middle atmosphere, Rev. Geophys., 41, doi:10.1029/2001RG000106.

Fritts, D. C. and Vincent, R. A., 1987: Mesospheric Momentum Flux Studies at Adelaide, Australia: Observations and a Gravity Wave–Tidal Interaction Model, J. Atmos. Sci., 44, 605–619, doi:10.1175/1520-0469(1987)044<0605:MMFSAA>2.0.CO;2.

Hagan, M. E., Roble, R. G., and Hackney, J., 2001: Migrating thermospheric tides, Journal of Geophysical Research: Space Physics, 106, 12 739–12 752, doi:10.1029/2000JA000344.

Hines, C. O., 1997: Doppler-spread parameterization of gravity-wave momentum deposition in the middle atmosphere. Part 2: Broad and quasi monochromatic spectra, and implementation, J. Atmos. Sol.-Terr. Phys., 59, 387 – 400, doi:10.1016/S1364-6826(96)00080-6.

Jacobi, C., Lilienthal, F., Geißler, C., and Krug, A., 2015: Long-term variability of mid-latitude mesosphere-lower thermosphere winds over Collm (51N, 13E), J. Atmos. Sol.-Terr. Phys., 136, 174–186, doi:10.1016/j.jastp.2015.05.006.

Jakobs, H. J., Bischof, M., Ebel, A., and Speth, P., 1986: Simulation of gravity wave effects under solstice conditions using a 3-D circulation model of the middle atmosphere, J. Atmos. Terr. Phys., 48, 1203–1223, doi:10.1016/0021-9169(86)90040-1.

Lieberman, R. S., Ortland, D. A., Riggin, D. M., Wu, Q., and Jacobi, C., 2010: Momentum budget of the migrating diurnal tide in the mesosphere and lower thermosphere, J. Geophys. Res.: Atmos., 115, doi:10.1029/2009JD013684.

Lilienthal, F., Jacobi, C., Schmidt, T., de la Torre, A., and Alexander, P., 2017: On the influence of zonal gravity wave distributions on the Southern Hemisphere winter circulation, Ann. Geophys., 35, 785–798, doi:10.5194/angeo-35-785-2017.

Lilienthal, F., Jacobi, C., and Geißler, C., 2018: Forcing mechanisms of the terdiurnal tide, Atmos. Chem. Phys., 18, 15 725–15 742, doi:10.5194/acp-18-15725-2018.

Lindzen, R. S., 1981: Turbulence and stress owing to gravity wave and tidal breakdown, J. Geophys. Res.: Oceans, 86, 9707–9714, doi:10.1029/JC086iC10p09707.

Liu, A. Z., Lu, X., and Franke, S. J., 2013: Diurnal variation of gravity wave momentum flux and its forcing on the diurnal tide, J. Geophys. Res.: Atmos., 118, 1668–1678, doi:10.1029/2012JD018653.

Matsuno, T., 1966: Numerical integrations of the primitive equations by a simulated backward difference method, J. Meteor. Soc. Jap., 44, 76–84, doi:10.2151/jmsj1965.44.1_76.

Mayr, H. G., Mengel, J. G., Chan, K. L., and Porter, H. S., 1998: Seasonal variations of the diurnal tide induced by gravity wave filtering, Geophys. Res. Lett., 25, 943–946, doi:10.1029/98GL00637.

Meyer, C. K., 1999: Gravity wave interactions with the diurnal propagating tide, J. Geophys. Res.: Atmos., 104, 4223–4239, doi:10.1029/1998JD200089.

Miyahara, S. and Forbes, J. M., 1991: Interactions between Gravity Waves and the Diurnal Tide in the Mesosphere and Lower Thermosphere, J. Met. Soc. Jap. Ser. II, 69, 523–531, doi:10.2151/jmsj1965.69.5_523.

Miyoshi, Y. and Yiğit, E., 2019: Impact of Gravity wave drag on the thermospheric circulation: Implementation of a nonlinear gravity wave parameterization in a whole atmosphere model, Ann. Geophys. Disc., 2019, 1–20, doi:10.5194/angeo-2019-36.

Pokhotelov, D., Becker, E., Stober, G., and Chau, J. L., 2018: Seasonal variability of atmospheric tides in the mesosphere and lower thermosphere: meteor radar data and simulations, Annales Geophysicae, 36, 825–830, doi:10.5194/angeo-36-825-2018.

Portnyagin, Y., Solovjova, T., Merzlyakov, E., Forbes, J., Palo, S., Ortland, D., Hocking, W., MacDougall, J., Thayaparan, T., Manson, A., Meek, C., Hoffmann, P., Singer, W., Mitchell, N., Pancheva, D., Igarashi, K., Murayama, Y., Jacobi, C., Kuerschner, D., Fahrutdinova, A., Korotyshkin, D., Clark, R., Taylor, M., Franke, S., Fritts, D., Tsuda, T., Nakamura, T., Gurubaran, S., Rajaram, R., Vincent, R., Kovalam, S., Batista, P., Poole, G., Malinga, S., Fraser, G., Murphy, D., Riggin, D., Aso, T., and Tsutsumi, M., 2004: Mesosphere/lower thermosphere prevailing wind model, Adv. Space Res., 34, 1755–1762, doi:10.1016/j.asr.2003.04.058.

Ribstein, B. and Achatz, U., 2016: The interaction between gravity waves and solar tides in a linear tidal model with a 4-D ray-tracing gravity-wave parameterization, J. Geophys. Res.: Space Phys., 121, 8936–8950, doi:10.1002/2016JA022478.

Smith, A. K., 2012: Global Dynamics of the MLT, Surveys in Geophysics, 33, 1177–1230, doi:10.1007/s10712-012-9196-9.

Strobel, D. F., 1978: Parameterization of the atmospheric heating rate from 15 to 120 km due to O2 and O3 absorption of solar radiation, J. Geophys. Res.: Oceans, 83, 6225–6230, doi:10.1029/JC083iC12p06225.

Swinbank, R. and Ortland, D. A., 2003: Compilation of wind data for the Upper Atmosphere Research Satellite (UARS) Reference Atmosphere Project, J. Geophys. Res.: Atmos., 108, doi:10.1029/2002JD003135.

Vadas, S. L. and Fritts, D. C., 2005: Thermospheric responses to gravity waves: Influences of increasing viscosity and thermal diffusivity, J. Geophys. Res.: Atmos., 110, doi:10.1029/2004JD005574.

Warner, C. D. and McIntyre, M. E., 2001: An ultrasimple spectral parameterization for nonorographic gravity waves, J. Atmos. Sci., 58, 1837–1857, doi:10.1175/1520-0469(2001)058<1837:AUSPFN>2.0.CO;2.

Yiğit, E. and Medvedev, A. S., 2015: Internal wave coupling processes in Earth's atmosphere, Adv. Space Res., 55, 983 – 1003, doi:10.1016/j.asr.2014.11.020.

Yiğit, E. and Medvedev, A. S., 2017: Influence of parameterized small-scale gravity waves on the migrating diurnal tide in Earth's thermosphere, J. Geophys. Res.: Space Phys., 122, 4846–4864, doi:10.1002/2017JA024089.

Yiğit, E., Aylward, A. D., and Medvedev, A. S., 2008: Parameterization of the effects of vertically propagating gravity waves for thermosphere general circulation models: Sensitivity study, J. Geophys. Res., 113, D19 106, doi:10.1029/2008JD010135.

Yiğit, E., Medvedev, A. S., Aylward, A. D., Hartogh, P., and Harris, M. J., 2009: Modeling the effects of gravity wave momentum deposition on the general circulation above the turbopause, J. Geophys. Res., 114, D07 101, doi:10.1029/2008JD011132.

Trend analyses of solar tides in the middle atmosphere

J. Löffelmann, F. Lilienthal, Ch. Jacobi

Institute for Meteorology, Stephanstr. 3, 04103 Leipzig,
E-Mail: a11849943@unet.univie.ac.at

Summary: Using a mechanistic global circulation model, we analysed the trends of solar tides in the middle atmosphere. Forced by monthly mean assimilation of reanalysis data in the lower atmosphere and monthly adjusted CO_2 and ozone distributions, the simulations represent a time period from January 1980 to May 2019. The time series of monthly mean wind and temperature amplitudes of all tidal components have been extracted from these data. Trend analyses by linear regression show prevailing negative trends in July and October for all tides and for all latitudes in the mesosphere and lower thermosphere. In April and January, however, trends are positive or negative, depending on the tidal component. Furthermore, the data set has been examined on possible trend changes via a statistical trend algorithm. A large part of those break points for the zonal wind amplitudes were found from 1985 to 1988 and from 2012 to 2015 for the investigated months January and April. Therefore, a clear relation between changes in the atmospheric ozone concentration and trends of the amplitudes of solar tides is not evident for the presented variables.

Zusammenfassung: Unter Verwendung eines mechanistischen globalen Zirkulationsmodells wurden Trends von solaren Gezeiten in der mittleren Atmosphäre analysiert. Die Simulationen, die in den unteren Atmosphärenschichten mit monatlich gemittelten Reanalysedaten angetrieben wurden sowie mit angepassten CO_2 und Ozonverteilungen, decken einen Zeitraum von Januar 1980 bis Mai 2018 ab. Aus diesen Daten wurden Zeitreihen für Monatsmittel in den Amplituden des Windes und der Temperatur für alle vier Gezeiten herausgefiltert. Die über lineare Regression gewonnen Trends ergeben - global betrachtet in der Mesosphäre und unteren Thermosphäre - vorwiegend negativ-signifikante Trends im Juli und Oktober. Im April und Januar können jedoch je nach Gezeit und Parameter positive wie auch negative Trends vorkommen. Weiterhin wurden die Datenreihen auf mögliche Trendänderungen mit Hilfe eines statistischen Algorithmus untersucht. Ein Großteil dieser Trend-Wendepunkte in den Zonalwindamplituden liegen für die untersuchten Monate Januar und April in den Jahren von 1985 bis 1988 und von 2012 bis 2015. Eine direkte Verbindung zwischen Änderungen in der atmosphärischen Ozonkonzentration und Trends in den Amplituden solarer Gezeiten lassen sich in den hier behandelten Größen daher nicht ableiten.

1 Introduction

Solar atmospheric tides are inertio-gravity waves which propagate from their source region into the MLT-region (mesosphere/ lower thermosphere) where they are one of the essential driving mechanism for the dynamics in the middle and upper atmosphere

(Pokhotelov et al., 2018). They can be divided into periods of a solar day (24 h) and its harmonics (12 h, 8 h, 6 h, ...). Because of the low density, amplitudes of atmospheric tides reach their maximum in the MLT-region where they can become comparable to the background flow (Jacobi et al., 2017).
It is generally accepted that the semidiurnal tide (SDT) is mainly excited by absorption of solar radiation in the deep ozone heating region in the stratosphere (e.g., Andrews et al., 1987). Due to its short vertical wavelength, the diurnal tide (DT), however, experiences destructive interferences in this region and therefore, it is more efficiently excited by the water vapour in the troposphere (Andrews et al., 1987). The mechanisms for higher harmonics, such as the terdiurnal or quarterdiurnal tide (TDT/QDT) are less well known. Generally, the DT and SDT have larger amplitudes than the higher harmonics (e.g., Jacobi et al., 2017; Lilienthal et al., 2018).
Changes in the atmospheric ozone content might be linked to the observed trends of tidal amplitudes (e.g., Keuer et al., 2007; Merzlyakov et al., 2009; Jacobi et al., 2012). In the early nineties the concentration of ozone reached its minimum due to large emissions of chlorofluorocarbons. After those chemicals have been banned by the Montreal Protocol in 1987 and its amendments, the ozone concentration increased and has a more or less constant level over the last twenty years (e.g., Geißler, 2016). A decrease in the ozone concentration may lead to weaker thermal forcing and, as a result, to smaller tidal amplitudes (e.g., Ross and Walterscheid, 1991).
Global trend investigations of the atmospheric solar tides using satellite or model data are rare. Most of previous trend determinations are based on radar measurements and concentrate on the DT and SDT amplitudes. Bremer (1997), for instance, found solely negative trends in the DT and SDT wind amplitudes for six different locations on both hemispheres between 1964 and 1995. Also Jacobi et al. (2005) determined negative trends for DT amplitudes over Collm (52° N, 15° E) and Obninsk (55° N, 37° E). Ratnam et al. (2014), however, detected mostly positive trends for the DT, increasing with height. Since they used ERA-Interim reanalysis data, they could only examine the upper troposphere and stratosphere. Further positive trends in the DT and SDT have been described by Baumgärtner et al. (2005) over Antarctica from 1987 and 2004 and by Sridharan et al. (2010) at 13° N from 1993 and 2007. Both of them suggested a possible connection to the ozone increase between 1996 and 2003. Other positive trends have been found by Keuer et al. (2007) who analysed wind amplitudes for SDT at mid-latitudes. They suggested a reversal of the trend line with a negative trend before 1995 and a positive afterwards. Jacobi et al. (2012) investigated radar data for three different stations at the northern hemisphere on trend changes for SDT amplitudes. In the winter months they found similar breakpoints before 1992 for all stations, in summer a linear trend dominated especially over Collm. Similar analyses have been made by Merzlyakov et al. (2009). They determined trend changes in 1982, from 1989 to 1993 and in 1995, the latter one being associated with ozone changes. In the QDT amplitudes for Collm and Obninsk Jacobi et al. (2017) found breakpoints in 1990 and 2017 using a statistical trend algorithm after Liu et al. (2010). To summarize, MLT tide trends have been observed mainly using local radar observations. To extend these studies to a global scale, we will use a global circulation model (GCM) and apply both linear trends analysis and piecewise regression with breakpoints according to Liu et al. (2010).
The paper is structured as follows: In section 2 the model as well as the statistical trend

algorithm for determination of possible break points are shortly described. Section 3 contains a comprehensive overview on the linear trends of all tidal components during the equinox and solticial seasons. The second part presents possible trend break points of DT and SDT, exemplary for January and April zonal wind amplitudes. Section 4 concludes and discusses the results.

2 Model description and data analyses

2.1 MUAM

The Middle and Upper Atmosphere Model (MUAM; e.g., Pogoreltsev et al., 2007; Lilienthal et al., 2018) is a three-dimensional, non-linear, mechanistic grid point model with a horizontal resolution of 5° in latitude and 5.625° in longitude. The vertical resolution is defined by a log-pressure height $z = -H \ln(p/p_0)$ with a constant scale height $H = 7\,\mathrm{km}$ and the reference pressure of the ground level $p_0 = 1000\,\mathrm{hPa}$. The default 56 vertical layers result together with the vertical grid resolution of 2.842 km in a total model height of about 160 km.
In the beginning of each run the model is initialized with zero wind and a standard atmosphere temperature profile. In the first 120 model day phase, the mean wind field is simulated. Because of longitudinal averaging of solar heating rates, tides will not develop during this phase. In the second 90-day phase, tides are forced due to the allowed longitudinal dependence of solar heating. The last 30 days of the second model phase are used for further analysis to receive the tidal amplitudes for each month.
Furthermore, zonal mean temperature fields are assimilated in the lowest 30 km from 1980 to 2018 using monthly mean ERA-Interim reanalysis data (ECMWF, 2018; Dee et al., 2011). Inserting a nudging term into the prognostic equation for temperature adjusts the zonal mean temperature of the model to the reanalysis data (see Lilienthal et al., 2018).
In addition, zonal mean temperature and geopotential fields are included as boundary conditions at 1000 hPa. In contrast to other versions of the model (e.g. Pogoreltsev et al., 2007; Jacobi et al., 2015; Lilienthal et al., 2017) there is no forcing of stationary planetary waves at the lower boundaries of this version.
For basic modelling of solar tides, atmospheric heating and absorption processes of ozone and molecular oxygen are parameterised according to Strobel (1978) and Mlynczak and Solomon (1993). Heating rates of CO_2 are included after Liou (1992) as well as heating rates of water vapour after Freidenreich and Ramaswamy (1999). Furthermore, zonal and monthly mean ozone values are implemented using MERRA-2 reanalysis (NASA, 2018; Gelaro et al., 2017). CO_2 monthly means, measured by Mauna Loa Observatory (ESRL, 2018; Thoning et al., 1989), are also applied in the model where the CO_2 distribution is assumed to be globally constant with an exponential decline above roughly 80 km. While Ermakova et al. (2017) applied a 3-dimensional water vapour distribution into MUAM, the present version uses an analytical profile, based on zonal mean mixing ratios at the lower boundary.
For the present study, we use the MUAM time series of monthly mean tidal amplitudes (1980-2018) where each month is considered independently for trend analysis. Hence, the length of each time series is 39, according to the number of years.

2.2 Statistical trend algorithm

Long-term trends have been calculated from the monthly tidal data of each year using least-squares regression. A statistical model after Liu et al. (2010) is used to investigate possible breakpoints (BP) in the trends based on the time series of tidal amplitudes obtained from MUAM. As a result, the model provides the most likely number of breakpoints of a time series, and, for an arbitrary number of breakpoints, their respective positions.
The mathematical principle of the model is partly based on an algorithm of Tomé and Miranda (2004) and is described in detail by Liu et al. (2010). For a priori unknown number and position of BP the algorithm investigates a time series for piecewise linear trends. The model analyses a data set separately for each number of BP. Each analysis must meet some predefined conditions regarding the minimal distance between two consecutive BP, the minimal length between starting (ending) point of the time series and the first (last) BP as well as a minimum trend change at each BP. To achieve this, the model uses the least squares method (Tomé and Miranda, 2004; Liu et al., 2010). In the case of zero BP the linear fit is estimated by a simple linear regression (Schönwiese, 2000; Liu et al., 2010). Thereafter, the trend estimations are extended by first- and second-order autoregressive components (AR(1) and AR(2)) (e.g. Seidel and Lanzante, 2004). Here, the value of a parameter is not independent from its previous value and therefore there is a connection of the values among each other. Additionally, the model provides all trend assessments without auto regression (AR(0)).
Furthermore, the residuals of the trend results are tested whether they are normally distributed to detect white noise. By applying and minimizing the Schwarz Bayesian Information Criterion (BIC, e.g. Ng and Perron, 2005; Portnyagin et al., 2006) to the data the first and second choice model results are selected with regard to the auto regression and number of BP. Using the Monte Carlo simulation approach, for which the repetition rate can also be predefined in the model, the uncertainty of the model parameters is assessed.
We set the maximum number of BP to 5. The minimal distance between two BP and between one BP and beginning or end of the time series is five years. Also, the minimum trend change is determined with 0.01 $ms^{-1}year^{-1}$ or 0.01 $K\,year^{-1}$, respectively.

3 Results

In the following, the climatologies for DT and SDT as well as the results of the linear trend analysis for all tides will be shown. Furthermore, some investigations of possible BP computed by the statistical model which is described in the previous section will be presented also for DT and SDT.

3.1 Linear Trends

At first, climatologies from January 1980 to May 2019 are created to get a general overview of the global distribution of maxima and minima along with seasonal changes. Here, the mean amplitudes of the zonal wind can be seen in Fig. 1 for DT and in Fig. 2 for SDT (upper row) for January and April, respectively. In accordance with observations (e.g., Manson et al., 2002; Wu et al., 2008), the modeled DT reveals maxima at low

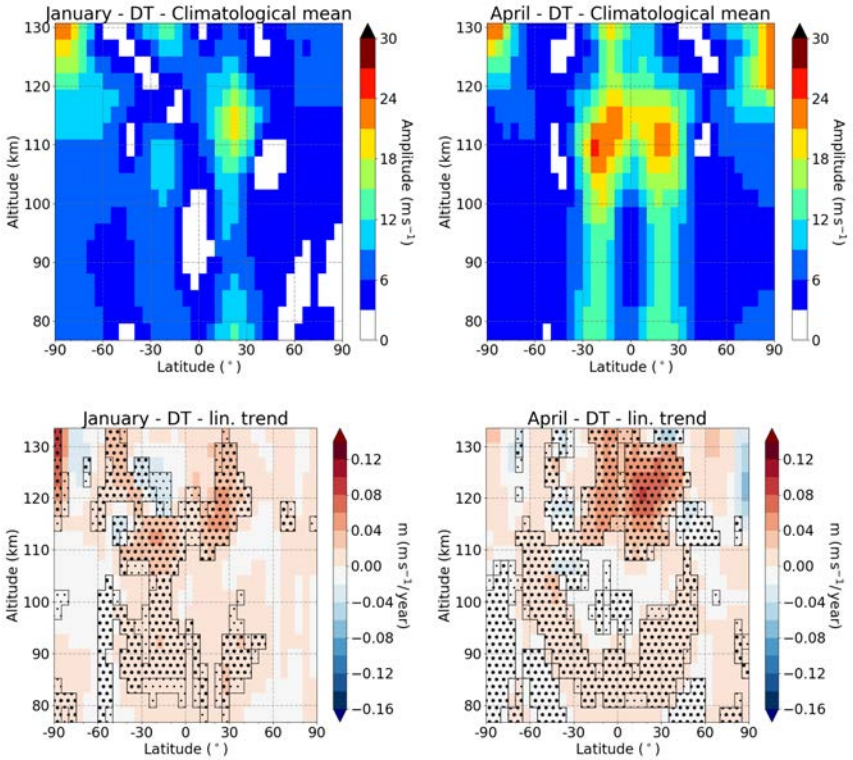

Fig. 1: Upper row: Climatological means of the DT zonal wind amplitudes for January (left) and April (right) from 1980 to 2018. Lower row: Slope (m) of the linear fit for DT zonal wind for January (left) and April (right). The framed areas with smaller dots represent A_{sig} *with a significance level of 90 %, the bigger dots stand for a significance level of 95 %.*

latitudes with larger amplitudes during April than during January. Amplitudes of the SDT are generally larger than those of the DT. In the MLT, SDT amplitudes maximise at middle latitudes of the winter hemisphere and they are almost symmetric with respect to the equator during equinoxes. This agrees well with baseline numerical models like the Global Scale Wave Model (GSWM, Hagan et al., 1995), but further above, the SDT is larger in the summer hemisphere. Large summer amplitudes have also been shown by Pancheva et al. (2009). Generally, MUAM underestimates tidal amplitudes up to a factor of 2, compared to observations (e.g., Jacobi, 2012; Davis et al., 2013).

In order to visualise global trend distributions, a linear regression is applied to the MUAM time series of tidal amplitudes (1980-2018) at each latitude/altitude of the model, and for each month individually. Figure 1 shows the slopes (m) of the linear fits for DT zonal wind amplitudes, while Figure 2 shows those of the SDT. Positive (negative) values indicate positive (negative) trends. Dotted areas indicate a high significance (90/95 % significance level for small/big dots). Note that the level of significance does not provide information about the strength of the trend.

In Fig. 1 there are significant trends in January with large m in the area where amplitudes of the DT in the respective panel above maximise. In April significant values with a large m can be found only above 110 km, slightly higher than the amplitude maximum. Below, the amplitudes and the trends are rather small. For the SDT zonal amplitudes in January (Fig. 2), primarily positive trends can be found but almost all of them are not significant.

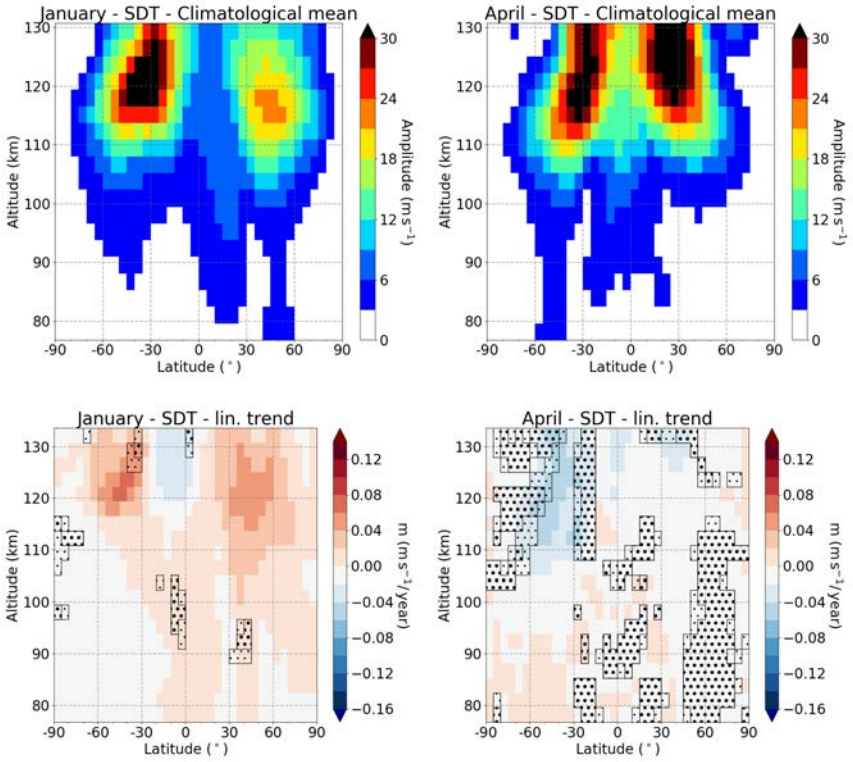

Fig. 2: Analogous to Fig. 1 for SDT.

However, in April there are more significant trends but again the values of *m* are small. To analyse a global trend behaviour of the tidal amplitudes, the number of grid points with significant trends on a 90 % level has been divided by the total number of grid points of the presented height window in Fig. 1 and 2. The percentage of significant trends (A_{sig}) is shown in table 1 for all tides and all three parameters for January, April, July and October. Different months have been chosen to point out possible seasonal behaviour of trends. The positive significance ratio shown in the last row of the tables specify the percentage of positive trends within A_{sig}. If this ratio is greater than 50 % more trends are positive than negative and a ratio of 100 % indicates only positive trends. The same is valid for negative trends whereas the ratio has to be smaller than 50 % and 0 % indicates solely negative trends. This procedure has been applied to the temperature (tem), zonal wind (zon) and meridional wind component (mer).

For the DT, table 1 shows more positive trends in January for all three parameters and clearly negative trends for the months July and October. In April no clear trend behaviour can be found because the values of the ratio are close to 50 %. However, A_{sig} is largest in April compared to the other months shown here.

For the SDT amplitudes negative trends also dominate, except for January. However, the amount of significant trends is rather small in January and the positive significant ratio of A_{sig} is close to 50 %. Therefore, we cannot draw a clear conclusion for the SDT trends in January.

The TDT shows a negative trend behaviour for January, July and October where again A_{sig} is smallest in January and largest in April. In April positive trends dominate for the meridional wind. For zonal wind and temperature the values are close to 50 % and therefore again no clear statement concerning the trend behaviour can be made for April

Table 1: Percentages of significant trends (black) and the positive significant ratio of the same (primarily positive/ negative trends are marked red/ blue).

		Jan			Apr			Jul			Oct		
		zon	mer	tem	zon	mer	tem	zon	mer	tem	zon	mer	tem
DT	A_{sig} [%]	36	33	33	53	52	52	23	31	31	36	48	34
	pos. sig. ratio [%]	84	88	77	64	41	48	0	0	0	1	0	1
SDT	A_{sig} [%]	5	7	10	35	33	36	51	39	37	36	31	31
	pos. sig. ratio [%]	57	70	60	2	9	18	0	0	0	0	0	3
TDT	A_{sig} [%]	21	15	16	49	49	52	36	27	33	26	18	24
	pos. sig. ratio [%]	13	27	22	65	74	51	0	1	2	5	2	1
QDT	A_{sig} [%]	36	25	33	53	62	52	23	33	31	36	10	34
	pos. sig. ratio [%]	63	80	49	62	85	66	20	3	14	10	0	2

conditions.
The QDT has the largest percentage of positive trends in January and April compared to the previously mentioned tides. Largest values can be seen in January and April for the meridional wind. For zonal wind and temperature the values are smaller but still greater than 50 % (except the temperature in January). In the second half of the year, trends tend to be negative.

3.2 Trends with breakpoints for DT and SDT

To investigate possible trend changes in the tidal amplitudes, the statistical trend algorithm described above has been used. Therefore, again the MUAM time series from January 1980 to May 2018 has been analysed for all latitudes and for a height range from 80 km to 110 km. Due to the long computing time of the algorithm only DT and SDT amplitudes of the zonal wind for January and April have been analysed with regard to possible BP. Figure 3 shows an exemplary time series for the DT zonal wind amplitudes as well as the trend development given by the algorithm for the assumption of zero to five BP. The trend line for zero BP is the same as the linear regression line used in the previous subsection. The more BP the better the trend lines represent the actual time series. But instead of always choosing the solution with the most BP, the algorithm uses the BIC to weight the variance of the residuals and, as a consequence, to determine a first choice solution (solid red line) and a second choice solution (dashed blue line). In this case only the results for one BP (first choice) will be analysed.
The left column of Fig. 4 shows the number of BP (first choice) for all latitudes and the defined height range for January and April for DT zonal wind amplitudes. For January most of the area has a solution without any BP as a first choice. Only in the tropics above 90 km are larger parts for a one BP solution. In April, solutions with one BP are more common, also in lower altitudes and higher latitudes. Occasionally, trends with two to four BP appear but they are usually found where the DT amplitude is small (see Fig. 1). The right column presents the year of the trend change under the assumption of exactly one BP. The cross-hatched areas highlight the position where exactly one BP is also first choice. In January a lot of trend changes are most likely in the years between 2003 and

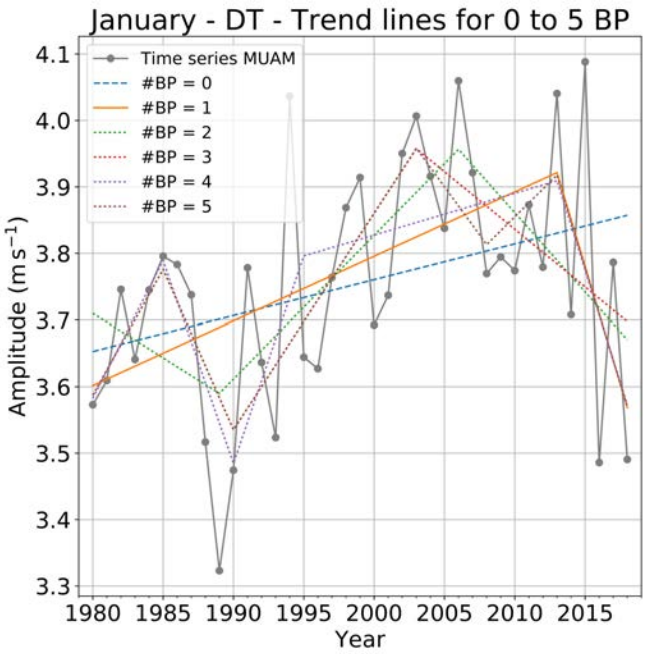

Fig. 3: Time series of MUAM for DT zonal wind amplitudes for January, 52, 5° N and 92 km from 1980 to 2018. Additionally the trend developments are shown for 0 to 5 BP and AR(0) in different colours.

2006. But only a small part above 100 km on the southern hemisphere near the equator are first choice. The main trend changes for solutions where one BP is most likely and where the DT maximises can be found between 2012 and 2015. In general, there are few BP in the nineties. In contrast to January, there are large areas in the tropics on both hemispheres in April with BP between 1997 and 2000 which are first choice. In addition, many trend changes at the equator as well as around 60° S appear from 1985 to 1988.
For the SDT zonal wind amplitudes in January, even less trends with one BP as first choice can be seen (Fig. 5). Almost all BP of the continuous area between 30° S and 60° S are located between 1985 and 1988. For BP which are not first choice also the years 2012 to 2015 are common. In April the solution with one BP appears more often on both hemispheres and between 60° N and 90° N a lager area with two breakpoints as first choice can be seen, where the SDT amplitude is rather small (see Fig. 2). For areas of larger amplitudes, 0 and 1 BP dominate. But again, there are not many events in the nineties. Most of the trend changes occur between 1995 and 1998 as well as between 2009 and 2012.
For the TDT and QDT (not shown here) the results look similar to the DT and SDT with even less events where one BP is first choice. Large areas with a linear trend dominate here. Also, the prevailing time ranges are 1995 to 1998 and 2012 to 2015.

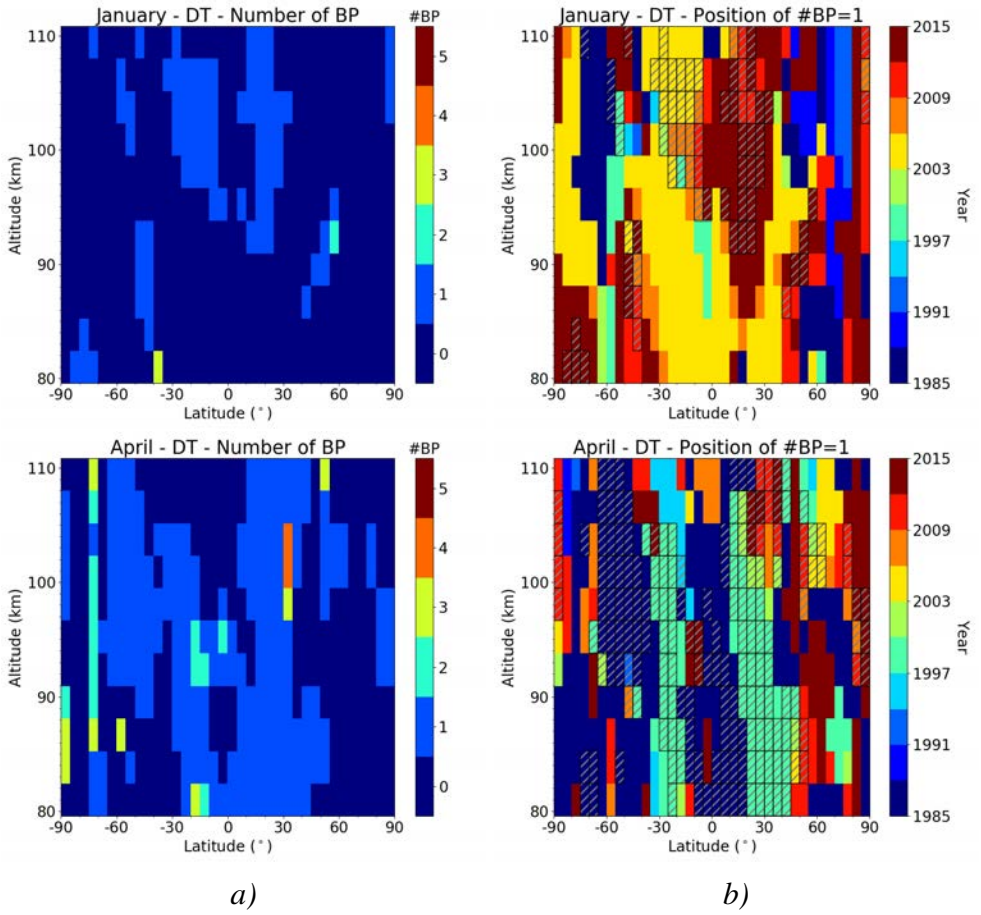

Fig. 4: a) Number of BP for DT zonal wind amplitudes for January and April (first choice). b) Position of BP also for January and April for one BP. The cross-hatched areas show all grid points where exactly one BP is the first choice. The colour scales's spacing is three years.

4 Discussion and Conclusion

By using data of the MUAM, a trend analysis for DT, SDT, TDT and QDT zonal and meridional wind amplitudes as well as temperature amplitudes has been performed. With a linear regression, the global trend behaviour has been examined. Furthermore, a statistical algorithm has been applied to the zonal amplitudes to investigate possible changes in the trend developments.

Trends obtained by linear regression primarily show negative trends for all four tides in July and October with the DT and SDT having the highest percentages of negative significant trends. In January the DT and SDT amplitudes show prevailing positive but, especially for the SDT, mostly insignificant trends. In April the same is valid for the TDT and QDT but with a slightly larger significance. The QDT has the highest percentages of positive trends compared to the other tides. Furthermore, the three parameters are acting similar in their trend behaviour. However, all the linear trend results must be seen in relation to the general ratio of significant trends which ranges from 5 % to 62 % of the designated area.

Comparing the results with measurements, the simulations of MUAM agree well with

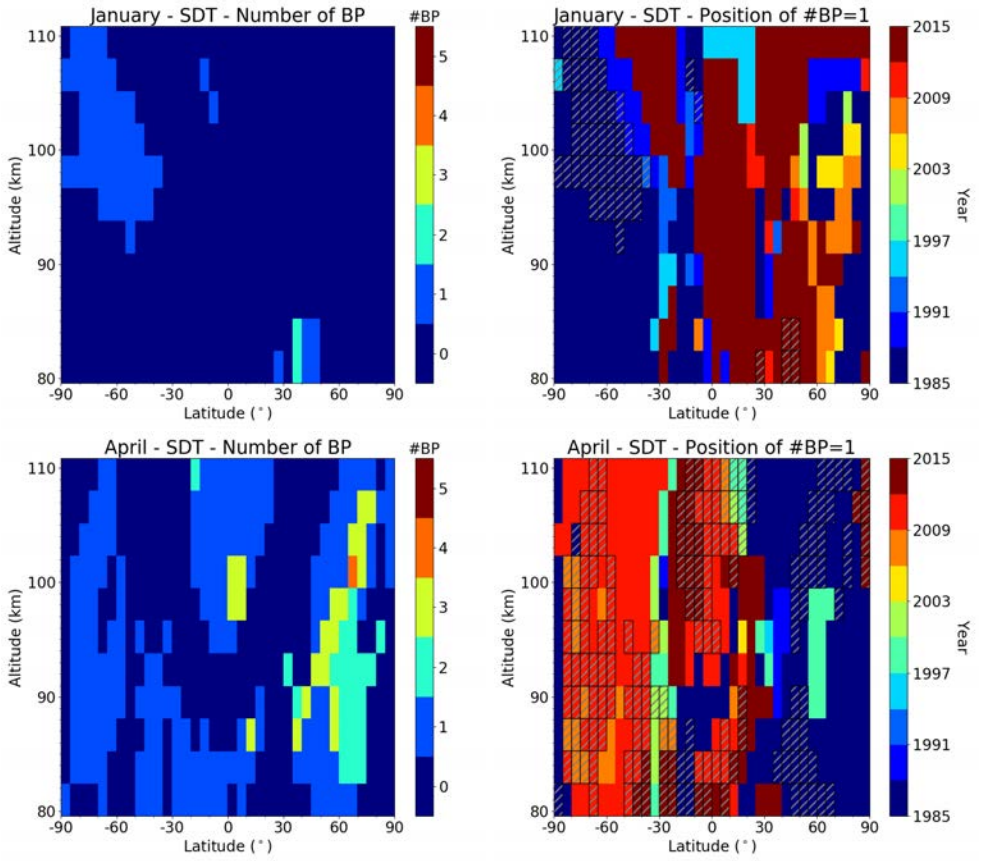

Fig. 5: Analogous to Fig. 4 for SDT.

observations by Bremer (1997) and Jacobi et al. (2005) who also found negative trends over different places on both hemispheres for the DT and SDT. Jacobi et al. (2012) could determine a negative linear trend only for summer months. Though, Ratnam et al. (2014), Sridharan et al. (2010) and Baumgärtner et al. (2005) could find a positive trend behaviour for lower latitudes as well as over the Antarctica. A connection between rising ozone values since 1995 and positive trends in tidal amplitudes, which was suggested by Sridharan et al. (2010) and Ratnam et al. (2014), can not be confirmed by this work. Nevertheless it must be said that a direct comparison of the results of different datasets, measurement techniques and methods is always connected with large uncertainties.
The trend analysis by the statistical algorithm shows similar behaviour for the DT and SDT. Especially, areas with one BP can be found where the amplitudes maximize in the presented height window. In general, there are less events in January where one BP is first choice than in April. For the DT zonal amplitudes the majority of first choice trend changes can be seen in the late nineties. For the SDT, however, the years from 1985 to 1988 and 2009 to 2012 dominate. In contrast to Keuer et al. (2007) and Merzlyakov et al. (2009) who both identify trend changes in 1995 for the SDT and see a possible connection to the ozone concentration, this relation can not be confirmed here. However, further analyses for other months as well as meridional wind and temperature amplitudes have to be made to get more reliable results with regard to the connection to ozone changes.

Acknowledgements

The authors are thankful to ECMWF for providing free ERA-Interim reanalysis data, to NOAA for the carbon dioxide measurements at Mauna Loa as well as to NASA for the MERRA-2 reanalysis data. Ch. Jacobi and F. Lilienthal acknowledge support by Deutsche Forschungsgemeinschaft under grants JA836/34-1, JA836/38-1, and JA836/43-1.

References

Andrews, D. G., Leovy, C. B., and Holton, J. R., 1987: Middle atmosphere dynamics, vol. 40, Academic press, Orlando, Fla., P. 157 f.

Baumgärtner, A., McDonald, A., Fraser, G., and Plank, G., 2005: Long-term observations of mean winds and tides in the upper mesosphere and lower thermosphere above Scott Base, Antarctica, Journal of Atmospheric and Solar-Terrestrial Physics, 67, 1480–1496, https://doi.org/10.1016/j.jastp.2005.07.018.

Bremer, J., 1997: Long-term trends in the meso-and thermosphere, Advances in Space Research, 20, 2075–2083, https://doi.org/10.1016/S0273-1177(97)00598-X.

Davis, R., Du, J., Smith, A., Ward, W., and Mitchell, N., 2013: The diurnal and semidiurnal tides over Ascension Island (8° S, 14° W) and their interaction with the stratospheric quasi-biennial oscillation: studies with meteor radar, eCMAM and WACCM, Atmospheric Chemistry and Physics, 13, 9543–9564, https://doi.org/10.5194/acp-13-9543-2013.

Dee, D. P., Uppala, S. M., Simmons, A., Berrisford, P., Poli, P., Kobayashi, S., Andrae, U., Balmaseda, M., Balsamo, G., Bauer, d. P., et al., 2011: The ERA-Interim reanalysis: Configuration and performance of the data assimilation system, Quarterly Journal of the Royal Meteorological Society, 137, 553–597, https://doi.org/10.1002/qj.828.

ECMWF, 2018: http://apps.ecmwf.int/datasets/data/interim-full-moda/levtype=pl, Last access: 13.08.2018.

Ermakova, T., Statnaya, I., Fedulina, I., Suvorova, E., and Pogoreltsev, A., 2017: Three-dimensional semi-empirical climate model of water vapor distribution and its implementation to the radiation module of the middle and upper atmosphere model, Russian Meteorology and Hydrology, 42, 594–600, https://doi.org/10.3103/S1068373917090060.

ESRL, 2018: https://www.esrl.noaa.gov/gmd/ccgg/trends/data.html, Last access: 13.08.2018.

Freidenreich, S. and Ramaswamy, V., 1999: A new multiple-band solar radiative parameterization for general circulation models, Journal of Geophysical Research: Atmospheres, 104, 31 389–31 409, https://doi.org/10.1029/1999JD900456.

Geißler, C.: Trends der Temperatur und des Windes in der Mesosphäre, Master's thesis, Faculty for Physcs and Earth Sciences at the University of Leipzig, 2016.

Gelaro, R., McCarty, W., SuÃ¡rez, M. J., Todling, R., Molod, A., Takacs, L., Randles, C. A., Darmenov, A., Bosilovich, M. G., Reichle, R., Wargan, K., Coy, L., Cullather, R., Draper, C., Akella, S., Buchard, V., Conaty, A., da Silva, A. M., Gu, W., Kim, G.-K., Koster, R., Lucchesi, R., Merkova, D., Nielsen, J. E., Partyka, G., Pawson, S., Putman, W., Rienecker, M., Schubert, S. D., Sienkiewicz, M., and Zhao, B., 2017: The Modern-Era Retrospective Analysis for Research and Applications, Version 2 (MERRA-2), Journal of Climate, 30, 5419–5454, https://doi.org/10.1175/JCLI-D-16-0758.1.

Hagan, M., Forbes, J., and Vial, F., 1995: On modeling migrating solar tides, Geophysical Research Letters, 22, 893–896, https://doi.org/10.1029/95GL00783.

Jacobi, C., 2012: 6 year mean prevailing winds and tides measured by VHF meteor radar over Collm (51° N, 13° E), Journal of Atmospheric and Solar-Terrestrial Physics, 78, 8–18, https://doi.org/10.1016/j.jastp.2011.04.010.

Jacobi, C., Portnyagin, Y. I., Merzlyakov, E., Solovjova, T., Makarov, N., and Kürschner, D., 2005: A long-term comparison of mesopause region wind measurements over Eastern and Central Europe, Journal of atmospheric and solar-terrestrial physics, 67, 229–240, https://doi.org/10.1016/j.jastp.2004.10.002.

Jacobi, C., Hoffmann, P., Liu, R., Merzlyakov, E., Portnyagin, Y. I., Manson, A., and Meek, C., 2012: Long-term trends, their changes, and interannual variability of Northern Hemisphere midlatitude MLT winds, Journal of Atmospheric and Solar-Terrestrial Physics, 75, 81–91, https://doi.org/10.1016/j.jastp.2011.03.016.

Jacobi, C., Lilienthal, F., Geißler, C., and Krug, A., 2015: Long-term variability of mid-latitude mesosphere-lower thermosphere winds over Collm (51° N, 13° E), Journal of Atmospheric and Solar-Terrestrial Physics, 136, 174–186, https://doi.org/10.1016/j.jastp.2015.05.006.

Jacobi, C., Krug, A., and Merzlyakov, E., 2017: Radar observations of the quarterdiurnal tide at midlatitudes: Seasonal and long-term variations, Journal of Atmospheric and Solar-Terrestrial Physics, 163, 70–77, https://dx.doi.org/10.1016/j.jastp.2017.05.014.

Keuer, D., Hoffmann, P., Singer, W., and Bremer, J., 2007: Long-term variations of the mesospheric wind field at mid-latitudes, 25, 1779–1790, https://doi.org/10.5194/angeo-25-1779-2007.

Lilienthal, F., Jacobi, C., Schmidt, T., Torre, A. d. l., and Alexander, P., 2017: On the influence of zonal gravity wave distributions on the Southern Hemisphere winter circulation, 35, 785–798, https://doi.org/10.5194/angeo-35-785-2017.

Lilienthal, F., Jacobi, C., and Geißler, C., 2018: Forcing mechanisms of the terdiurnal tide, Atmospheric Chemistry and Physics, 18, 15 725–15 742, https://doi.org/10.5194/acp-18-15725-2018.

Liou, K.-N., 1992: Radiation and cloud processes in the atmosphere. Theory, observation, and modeling.

Liu, R., Jacobi, C., Hoffmann, P., Stober, G., and Merzlyakov, E., 2010: A piecewise linear model for detecting climatic trends and their structural changes with application to mesosphere/lower thermosphere winds over Collm, Germany, Journal of Geophysical Research: Atmospheres, 115, https://doi.org/10.1029/2010JD014080.

Manson, A., Luo, Y., and Meek, C., 2002: Global distributions of diurnal and semi-diurnal tides: observations from HRDI-UARS of the MLT region, 20, 1877–1890, https://hal.archives-ouvertes.fr/hal-00317410.

Merzlyakov, E., Jacobi, C., Portnyagin, Y. I., and Solovjova, T., 2009: Structural changes in trend parameters of the MLT winds based on wind measurements at Obninsk (55° N, 37° E) and Collm (52° N, 15° E), Journal of Atmospheric and Solar-Terrestrial Physics, 71, 1547–1557, https://doi.org/10.1016/j.jastp.2009.05.013.

Mlynczak, M. G. and Solomon, S., 1993: A detailed evaluation of the heating efficiency in the middle atmosphere, Journal of Geophysical Research: Atmospheres, 98, 10 517–10 541, https://doi.org/10.1029/93JD00315.

NASA, 2018: https://disc.gsfc.nasa.gov/datasets?keywords=%22MERRA-2%22&page=1&source=Models%2FAnalyses%20MERRA-2, Last access: 13.08.2018.

Ng, S. and Perron, P., 2005: A note on the selection of time series models, oxford Bulletin of Economics and statistics, 67, 115–134, https://doi.org/10.1111/j.1468-0084.2005.00113.x.

Pancheva, D., Mukhtarov, P., and Andonov, B., 2009: Global structure, seasonal and interannual variability of the migrating semidiurnal tide seen in the SABER/TIMED temperatures (2002–2007), 27, 687–703, https://doi.org/10.5194/angeo-27-687-2009s.

Pogoreltsev, A., Vlasov, A., Fröhlich, K., and Jacobi, C., 2007: Planetary waves in coupling the lower and upper atmosphere, Journal of Atmospheric and Solar-Terrestrial Physics, 69, 2083–2101, https://doi.org/10.1016/j.jastp.2007.05.014.

Pokhotelov, D., Becker, E., Stober, G., and Chau, J. L., 2018: Seasonal variability of atmospheric tides in the mesosphere and lower thermosphere: meteor radar data and simulations, 36, 825–830, https://doi.org/10.5194/angeo-36-825-2018.

Portnyagin, Y. I., Merzlyakov, E., Solovjova, T., Jacobi, C., Kürschner, D., Manson, A., and Meek, C., 2006: Long-term trends and year-to-year variability of mid-latitude mesosphere/lower thermosphere winds, Journal of Atmospheric and Solar-Terrestrial Physics, 68, 1890–1901, https://doi.org/10.1016/j.jastp.2006.04.004.

Ratnam, M. V., Rao, N. V., Vedavathi, C., Murthy, B. K., and Rao, S. V. B., 2014: Diurnal tide in the low-latitude troposphere and stratosphere: Long-term trends and role of the extended solar minimum, Journal of Atmospheric and Solar-Terrestrial Physics, 121, 168–176, https://dx.doi.org/10.1016/j.jastp.2014.06.004.

Ross, M. N. and Walterscheid, R. L., 1991: Changes in the solar forced tides caused by stratospheric ozone depletion, Geophysical Research Letters, 18, 420–423, https://doi.org/10.1029/90GL02786.

Schönwiese, C.-D., 2000: Praktische Statistik für Meteorologen und Geowissenschaftler, Schweizerbart Science Publishers, Stuttgart, Germany, 3. verb. und erw. Ed., P. 163 ff.

Seidel, D. J. and Lanzante, J. R., 2004: An assessment of three alternatives to linear trends for characterizing global atmospheric temperature changes, Journal of Geophysical Research: Atmospheres, 109, https://doi.org/10.1029/2003JD004414.

Sridharan, S., Tsuda, T., and Gurubaran, S., 2010: Long-term tendencies in the mesosphere/lower thermosphere mean winds and tides as observed by medium-frequency radar at Tirunelveli (8.7° N, 77.8° E), Journal of Geophysical Research: Atmospheres, 115, https://doi.org/10.1029/2008JD011609.

Strobel, D. F., 1978: Parameterization of the atmospheric heating rate from 15 to 120 km due to O2 and O3 absorption of solar radiation, Journal of Geophysical Research: Oceans, 83, 6225–6230, https://doi.org/10.1029/JC083iC12p06225.

Thoning, K. W., Tans, P. P., and Komhyr, W. D., 1989: Atmospheric carbon dioxide at Mauna Loa Observatory: 2. Analysis of the NOAA GMCC data, 1974–1985, Journal of Geophysical Research: Atmospheres, 94, 8549–8565, https://doi.org/10.1029/JD094iD06p08549.

Tomé, A. and Miranda, P., 2004: Piecewise linear fitting and trend changing points of climate parameters, Geophysical Research Letters, L02207, 31, https://doi.org/10.1029/2003GL019100.

Wu, Q., Ortland, D., Killeen, T. L., Roble, R., Hagan, M., Liu, H.-L., Solomon, S., Xu, J., Skinner, W., and Niciejewski, R., 2008: Global distribution and interannual variations of mesospheric and lower thermospheric neutral wind diurnal tide: 1. Migrating tide, Journal of Geophysical Research: Space Physics, 113, https://doi.org/10.1029/2007JA012542.

Heat flux classification of CMIP5 model results using self-organizing maps

D. Mewes, Ch. Jacobi

Universität Leipzig, Institute for Meteorology, Stephanstr. 3, 04103 Leipzig,
E-Mail: daniel.mewes@uni-leipzig.de

Summary: We used the self-organizing maps (SOMs) method on eight models that participated in the Coupled model intercomparison project phase 5 (CMIP5) and two different greenhouse gases (GHG) concentration experiments. The SOMs were created from the winter 500 hPa horizontal temperature flux for each model. The clustering by the SOM revealed that in addition to the three flux pathways found in reanalyses (Pacific, Atlantic and Siberian/continental pathway), superpositions of these occur for the free running climate models, which develop their dynamic more freely than the reanalyses. It was found that the general structure of fluxes is indirectly dependent on the GHG concentrations, as the derived results from SOM patterns are different between the two GHG concentrations. It is suggested that flux patterns change from stable cyclonic motion over the north pole to flux pathways that feature more meridional fluxes through the North Atlantic and North Pacific into the Arctic.

Zusammenfassung: Die Methode der Self-Organizing Maps (SOMs) wurde auf acht CMIP5-Modelle mit jeweils zwei verschiedenen Treibhausgasszenarien angwendet. Die SOMs wurden für jedes Modell und jede der beiden Modelläufe für den horizontalen Temperaturfluss in 500 hPa im Winter erstellt. Zusätzlich zu den aus der Analyse von Reanalyse-Daten erwarteten drei Transportwegen (pazifisch, atlantisch und sibirisch/kontinental) wurden Überlagerungen dieser gefunden. Es konnte gezeigt werden, dass die grundsätzliche Struktur der Transporte indirekt abhängig von der Treibhausgaskonzentration ist. Die Ergebnisse deuten darauf hin, dass sich die generelle Struktur des atmosphärischen Transports von einer stabilen zyklonalen Bewegung über dem Nordpol sich zu Transporten verschiebt, welche meridionale Transporte über den Nortdatlantik und den Nordpazifik in die Arktis führen.

1 Introduction

The change in surface air temperature in the Arctic is by a factor of two stronger compared to the rest of the Earth (Stroeve et al., 2012; Wendisch et al., 2017). This rapid change is influencing the atmospheric transports and circulation (Mewes and Jacobi, 2019). Climate change is driven by increased greenhouse gases (GHG) concentrations (Crowley, 2000), especially CO_2. Within the Climate Model Intercomparison Project 5 (CMIP5, Taylor et al., 2012) multiple models were used to calculate the state of the atmosphere for different GHG scenarios. This includes, e.g., GHG concentrations of the pre-industrial era

and different projections of GHG concentrations based on the development of technology and society. As an example of those results from the CMIP5, Ceppi et al. (2018) found that poleward shifts of extra tropical circulation is a typical response to the increased CO_2 in climate models.
To analyse climatic patterns and their variability, self-organizing maps (SOMs) have proved to be an effective tool (Cassano et al., 2006; Liu et al., 2006; Skific et al., 2009; Liu and Weisberg, 2011; Lynch et al., 2016; Mewes and Jacobi, 2019). In comparison with measurements, Loikith and Broccoli (2015) could show using SOMs, that the CMIP5 multimodel ensemble of the 500 hPa geopotential fits well with observations over North America.
In this report we, analyze the horizontal temperature flux using SOMs on CMIP5 historical and Representative Concentration Pathway 8.5 (RCP85) data. We want to test how applicable the SOM method is across different CMIP5 models and different GHG concentration realizations. In Section 2, we explain the data and methods that have been used. Section 3 will show the results of the analyses. The last section 4 will shortly summarize and discuss the results.

2 Data and Method

For this study, we used CMIP5 winter data of eight models that participated at CMIP5 (Taylor et al., 2012) see Table 1. Based on previous experiments, we decided to use

Table 1: List of used CMIP5 models and their respective resolution at the equator (res.)

CMIP5 Model ID	Institute, country of origin	Horizontal res. (°)	Latitude res. (km)	Longitude res. (km)	Vertical levels
MRI-CGCM3	MRI, Japan	1.1×1.1	120	120	48
MPI-ESM-MR	MPI-M, Germany	1.9×1.9	210	210	95
MPI-ESM-LR	MPI-M, Germany	1.9×1.9	210	210	47
MIROC-ESM	JAMSTEC, Japan	2.8×2.8	310	310	80
HadGEM2-CC	MOHC, UK	1.9×1.2	210	130	38
GFDL-CM3	NOAA, GDFL, USA	2.5×2.0	275	220	48
CMCC-CMS	CMCC, Italy	1.9×1.9	210	210	95
CMCC-CESM	CMCC, Italy	3.7×3.7	410	410	39

the horizontal temperature flux at 500 hPa (F) as a proxy for the total stratospheric horizontal moist static energy transport. F was calculated from daily CMIP5 data for two time periods. The first period is for the winters from 1950 to 2005. For this period, the historical greenhouse gas concentrations described in the CMIP5 setup (Taylor et al., 2012) is used. The second period uses the RCP85 greenhouse gas concentrations and contains the winters from 2006-2061. The RCP85 describes a greenhouse gas concentration development, and the number means that a radiative forcing of 8.5 W m^{-2} is reached in the year 2100.
The daily 500 hPa horizontal temperature fluxes for each of the eight CMIP5 models were used to extract intrinsic flux patterns by using the SOM method. The general principle

and related formulas of the SOM method are summarized in Mewes and Jacobi (2017). Similar to Mewes and Jacobi (2019), the SOM for each CMIP5 model was created using a 3×4 size SOM. This results in a total of eight SOMs, each of these SOMs were manually inspected as in Mewes and Jacobi (2019) to distinguish between an Atlantic pathway, continental pathway or Pacific pathway. The manual grouping is based on the visual inspection and comparison of the general direction and rotations of the two-dimensional vector field of F. As described in Mewes and Jacobi (2019) the Atlantic (Pacific) pathway represents mostly horizontal fluxes into the Arctic that originate from the North Atlantic (North Pacific). In comparison to Mewes and Jacobi (2019), we are not considering only a so-called Siberian pathway. During the analysis of the CMIP5 model SOM results, it was necessary to extend the Siberian pathway definition to fluxes into the Arctic that originates either from the North American continent or from the Eurasian land-mass. These fluxes were further called continental pathways. Additionally, an undefined type was introduced where none of the pathways above is applicable to the resulting horizontal temperature flux pattern. These unassigned patterns are always superpositions of the pathways mentioned above. To do not misinterpret these superpositions we decided to group them as miscellaneous. Generally speaking, eventually each pathway type is composed out of specific fluxes depicted by the SOM's patterns. As the CMIP5 models are climate models compared to the ERA-Interim reanalysis (Dee et al., 2011) the general variation and fluxes were expected to be different.
However, concerning the changes due to the different greenhouse gas concentrations between the historical and the RCP85 experiment, we conducted two different analysis. First as described above, we used the SOM method to create the SOMs for each model for the historical time frame. This we define as a baseline for our comparison. For the RCP85 time frame, we used a) the SOM based on the historical frame for each model respectively and used b) the SOM derived from the RCP85 time frame for each model respectively to project the RCP85 data for each model onto the respective SOM. This will help to understand if there might be substantial shifts in the temperature flux patterns between the historical and the RCP85 experiments. If the results between these two approaches would differ strongly, it might be possible to state that the circulation between the analyzed two time frames differs enough so that in the RCP85 experiment the general structure of the circulation might have changed drastically compared to the historical time frame.

3 Results

Figures 1 to 8 show the SOM for each analyzed model for the historical time frame. The Figures show how the manual grouping described in the previous section looks like. The Pacific pathway is defined by vectors that originates in the North Pacific and go through the Bering Strait, or over Alaska or east Siberia into the Arctic ocean. The Atlantic pathway is defined as transports or fluxes that originates from the North Atlantic and passing into the Arctic ocean via Svalbard and the Fram Strait. The continental pathway is described by neither clear transports from one of the oceans, but more focussed transports and fluxes from the Eurasian and North American continent, as well as transports and fluxes originating from Greenland.
Generally, the models differ in only a few specific temperature flux patterns. All SOMs

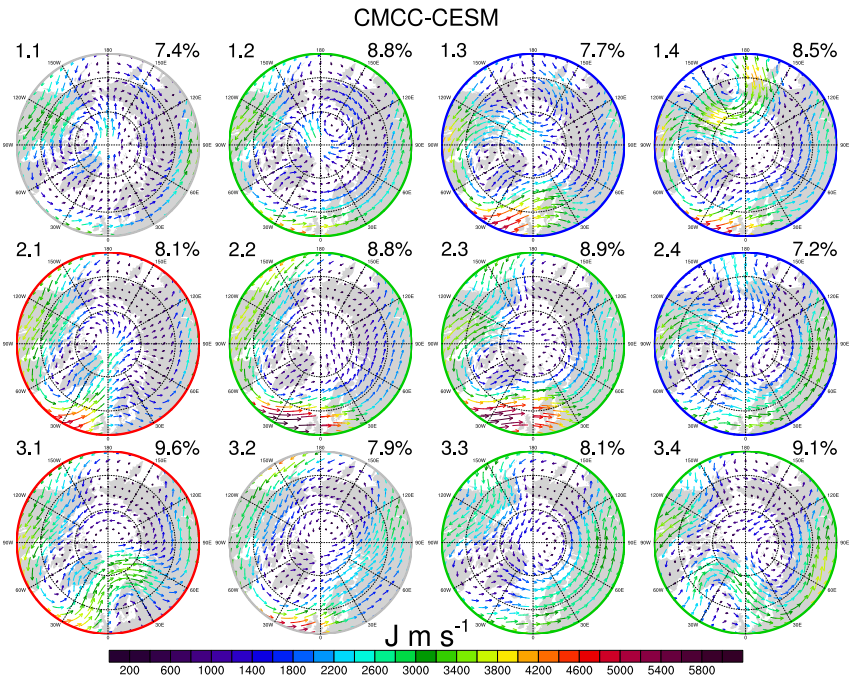

Fig. 1: SOM with 4 columns and 3 rows of the 500 hPa horizontal temperature flux, derived from the historical run winter data from 1860-1915 of the CMCC-CESM. Numbers in the top left are used for naming each specific pattern within a SOM, numbers in the top right denotes the relative occurrence frequency during the historical run this pattern was present. Colored frames denote grouping to the respective pathway: red Atlantic pathway, green continental pathway, blue Pacific pathway, and grey miscellaneous pathway.

contain at least two patterns that describe an Atlantic pathway type flux (e.g., MRI-CGCM3 pattern 2.4, MPI-ESM-MR pattern 2.3, or CMCC-CMS pattern 2.4), at least two patterns that describe an Pacific pathway type flux (e.g., MRI-CGCM3 pattern 3.1, MPI-ESM-LR pattern 1.1, or HadGEM2-CC pattern 3.2), at least two patterns that describe an continental pathway type flux (e.g., MRI-CGCM3 pattern 2.2, MIROC-ESM pattern 1.2, or GFDL-CM pattern 1.3) and at least one pattern that cannot be connected to one pathway type alone (e.g., MRI-CGCM3 pattern 3.4, or CMCC-CESM pattern 1.1).
The general amplitude of these temperature fluxes differs between the models. While the MRI-CGCM3 and the HadGEM2-CC provide the strongest flux amplitudes of all the models, the CMCC-CMS and the GFDL-CM3 provides relatively low amplitudes, especially over the north pole region.
The relative frequencies of occurrences of the described pathways are shown in Table 2 for the historical time frame and greenhouse gas concentrations. It can be seen in the mean relative frequencies that all three major pathways are differing slightly (about 3%). The Pacific pathway is the most frequent one with 28,8%, followed by the Pacific pathway with 26,4%, the Atlantic pathway with 25,1% and the states of superposition of different pathways with 19,7%. The miscellaneous patterns mainly feature superpositions of the continental pathway with either the Atlantic or the Pacific pathway (not shown).
Looking at the specific models, the results are not as clear. The MRI-CGCM3 favors mainly the Pacific pathway while the CMCC-CESM mainly produces very structured continental pathways that are usually connected with strong cyclonal circulation with

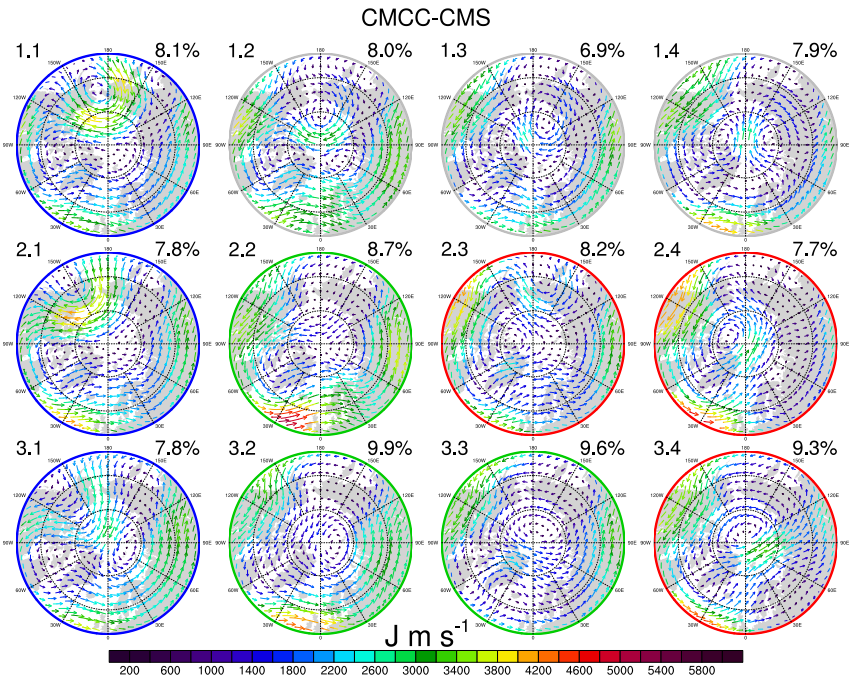

Fig. 2: Same as Fig.1 but for CMCC-CMS.

Table 2: Relative frequencies of occurrence (in %) for each of the analyzed CMIP5 models, historical runs.

Model	Pacific pathway	Continental pathway	Atlantic pathway	misc.
MRI-CGCM3	43,04	16,64	31,24	9,08
MPI-ESM-MR	32,69	25,23	33,16	8,92
MPI-ESM-LR	21,21	35,65	25,72	17,41
MIROC-ESM	25,07	41,69	16,68	16,56
HadGEM2-CC	16,85	24,92	24,35	33,89
GFDL-CM3	25,17	14,70	26,28	33,85
CMCC-CMS	23,66	28,25	25,23	22,85
CMCC-CESM	24,43	43,65	17,71	15,22
Mean	26,39	28,84	25,05	19,72

centres near the north pole. For other models, the fluxes pathways are relatively close to the mean (e.g. CMCC-CMS, MPI-ESM-MR).

As described in Section 2, the comparison between the historical and the RCP85 time frame was separated. First, we look into the change of frequencies of occurrence of the pathways in dependence of the historical SOM. This was done by projecting the RCP85 data onto the historical SOMs and observe the resulting frequencies of occurrences for each model. The assumption here is that the general strength and systematics are transferable from the historical to the RCP85 runs. Generally, it is a viable guess to assume that the general structure is similar. The results of this comparison are shown in Table 3. The differences between historical and the RCP85 runs are not very strong. Comparing the mean values across all models, the largest change occurs for the Atlantic pathway that it is getting less frequent by about 1,5%. The Pacific pathway occurrence frequency is getting larger by 0,9%, the continental pathway is more frequent by 0,1% and the miscellaneous patterns increasing in frequency by 0,5% compared to the historical

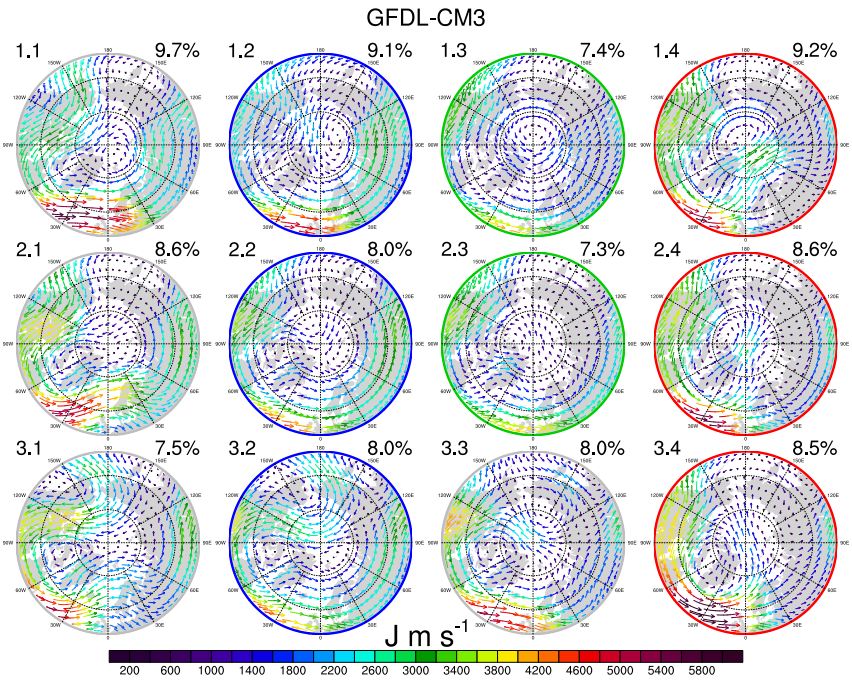

Fig. 3: Same as Fig.1 but for GFDL-CM3.

Table 3: Difference of Relative frequencies of occurrence (in %) for each of the analyzed CMIP5 models, RCP85 frequencies based on historical patterns minus historical frequencies.

Model	Pacific pathway	Continental pathway	Atlantic pathway	misc.
MRI-CGCM3	6,55	-3,66	-5,28	2,39
MPI-ESM-MR	0,83	-4,25	2,73	0,69
MPI-ESM-LR	2,37	6,96	-2,39	-6,94
MIROC-ESM	-5,52	7,87	0,63	-2,99
HadGEM2-CC	1,24	-2,75	-0,10	1,61
GFDL-CM3	5,40	-2,83	-5,14	2,57
CMCC-CMS	-0,81	1,98	-2,28	1,11
CMCC-CESM	-2,83	-2,55	-0,44	5,82
Mean	0,90	0,10	-1,53	0,53

experiment. The individual models show different results. The largest difference between the models occurs for the superpositions of the pathways, with a maximum difference of about 13% between the MPI-ESM-LR(-7%) and the CMCC-CESM (6%). The Atlantic pathway shows the least difference between the models with about 8% between the MPI-ESM-MR (3%) and the GFDL-CM3 (-5%).

The results for the occurrence frequencies of the pathways in dependence of the separated SOM of the historical and RCP85 runs are shown in Table 4. It has to be noted that the respective RCP85 SOMs are not shown. This approach accounts for shifts in the circulation that might have occurred due to the GHG increase and makes sure that the constraints of the historical SOMs are not limiting the interpretation. Based on this comparison, changes in the circulation can be detected and specifically grouped into the pathways, whereas with the former approach comparing to the historical run the RCP85 fluxes might be mismatched to certain historical patterns. The mean values

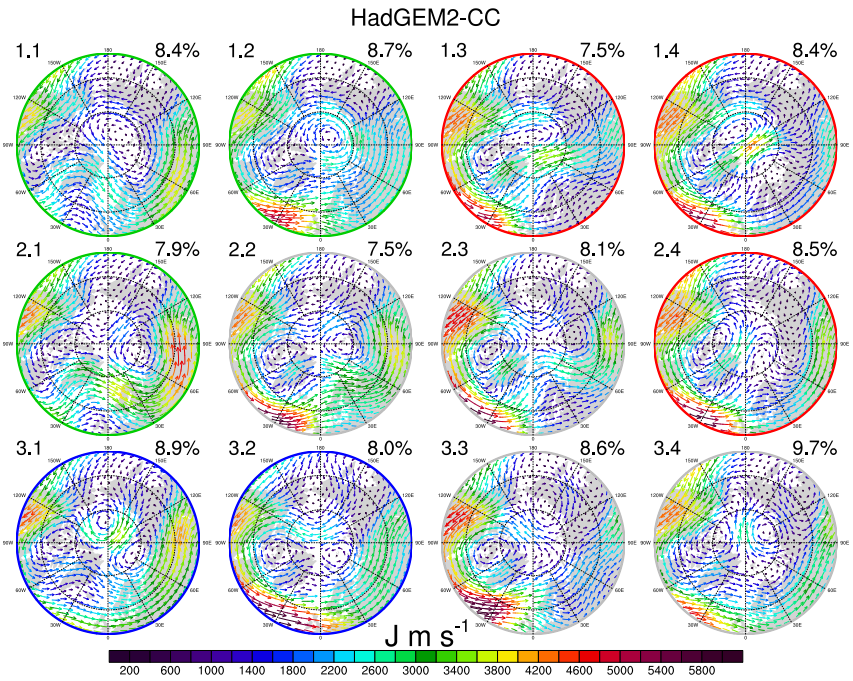

Fig. 4: Same as Fig.1 but for HadGEM-CC.

Table 4: Difference of Relative frequencies of occurrence (in %) for each of the analyzed CMIP5 models, RCP85 frequencies based on RCP85 patterns minus historical frequencies.

Model	Pacific pathway	Continental pathway	Atlantic pathway	misc.
MRI-CGCM3	-17,39	16,66	-6,47	7,20
MPI-ESM-MR	5,64	0,61	-6,09	-0,16
MPI-ESM-LR	19,55	-17,41	6,49	-8,63
MIROC-ESM	-0,95	-15,85	15,75	1,05
HadGEM2-CC	8,38	-0,82	17,37	-24,93
GFDL-CM3	15,83	12,82	-3,19	-25,46
CMCC-CMS	5,32	-0,32	1,29	-6,29
CMCC-CESM	9,26	-25,72	23,05	-6,59
Mean	5,70	-3,75	6,02	-7,98

differ substantially compared to the results of Table 3. The biggest change occurs for the miscellaneous patterns that occur about -8,0% less often. The continental pathway reduces its occurrence frequency by about -3,8%. Both pathways with fluxes pathways over the oceans are getting more frequent. The Atlantic pathway is occurring more frequently by about 6,0% and the Pacific pathway by about 5,7%. The intermodel comparison similarly shows that the biggest spread between the models occur for the continental pathway, with about 42 % difference in the occurrence frequency between MRI-CGCM3 (17%) and CMCC-CESM (-26%) The smallest difference between the models is shown for the Atlantic pathway (about 29%) between the models MRI-CGCM3 (6%) and CMCC-CESM (23%).

Comparing Tables 3 and 4 shows that the mean amplitudes of change are up to an order of magnitude larger for the second table. Also, the differences for the respective pathways differ. While both results show an increase for the Pacific pathway's occurrence frequency,

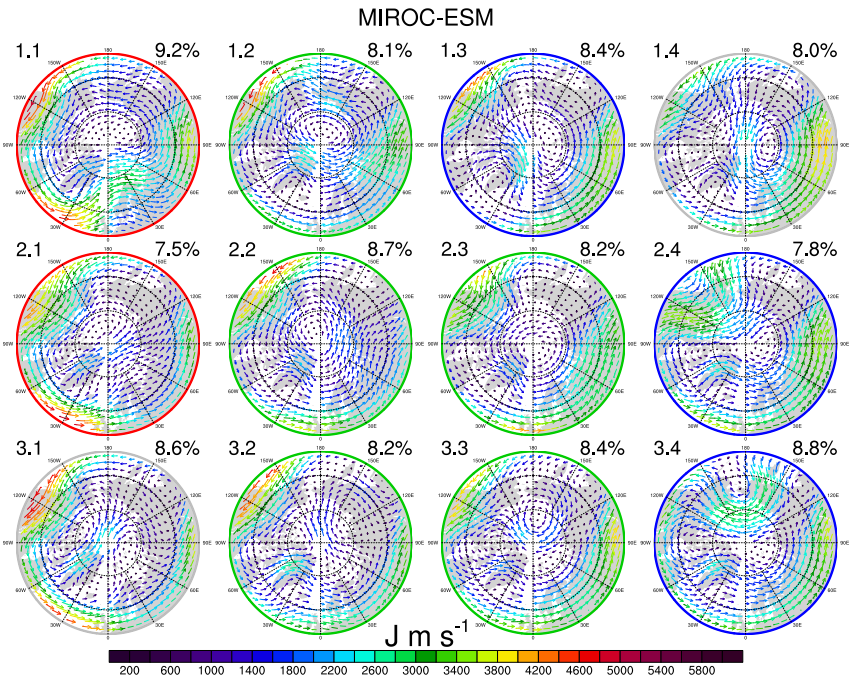

Fig. 5: Same as Fig.1 but for MIROC-ESM.

in the other three cases, the two results are the opposite.

4 Discussion and Summary

Eight different models from the CMIP5 experiment were used to analyze the horizontal temperature flux at 500 hPa. This was used as a surrogate for the vertically integrated measure of energy fluxes (as in Mewes and Jacobi (2019)). The winter season was analyzed for two different time periods. Each period features different greenhouse gas (GHG) concentrations as prescribed by the CMIP5 (Taylor et al., 2012). The first period named historical contains mostly pre-industrial GHG concentrations while the second period named RCP85 contains GHG concentrations from the projected future.
These winter fluxes were then used to drive an unsupervised learning method, called SOM, to cluster the data into intrinsic fluxes patterns. The emerging patterns were then further manually grouped in dependence on the respective direction and rotation of the flux vector field into either Atlantic pathway, Pacific pathway, continental pathway or miscellaneous pathways. After this grouping, the relative occurrence frequencies of each pathway were calculated. For the historical runs, the relative frequencies were calculated based on the historical SOMs only. On the contrary, the RCP85 runs were compared to the patterns derived from the historical SOMs and additionally compared to the patterns derived from the RCP85 SOMs (not shown). This gave the advantage to investigate if there are distinct differences in the fluxes between the historical and the RCP85 cases.
Concerning the SOM patterns, it has been found that the general description of the three major pathways is in agreement with Mewes and Jacobi (2019), who showed the Atlantic pathway, the Pacific pathway and the Siberian/continental pathway in ERA-Interim (Dee et al., 2011). In addition, the CMIP5 models also showed superposition of those three pathways, which were classified as miscellaneous pathways. This was the case for both the historical SOMs (Figures 1 to 8) and the RCP85 SOMs (not shown). The general

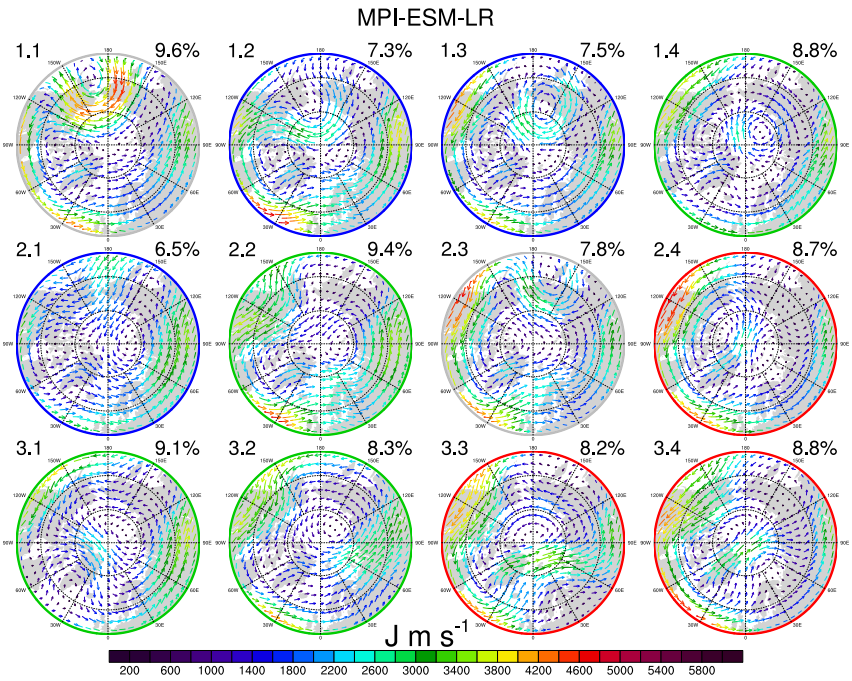

Fig. 6: Same as Fig.1 but for MPI-ESM-LR.

superposition of the pathways was expected as the CMIP5 models are free running models, where the dynamics are not constrained.

Specifically, for the different models, Franzke et al. (2017) showed that for some CMIP5 models, the large-scale atmospheric circulation is related to Arctic warming. Thus, an influence of GHG concentration on the large-scale circulation is also partly dependent on the model mean state. This might explain the large differences in the occurrence frequencies between the models.

Comparing the differences in occurrence frequencies between the historical based and the RCP85 based changes in occurrences showed interesting results. RCP85 frequencies based on RCP85 SOMs show much stronger response compared to the RCP85 frequencies based on historical SOMs. This suggests that due to the change in GHG concentrations the general circulation has changed in a way that the specific flux types (patterns) of the historical case are not directly comparable to the specific flux types (patterns) of the RCP85 case. These changes presented by the RCP85 frequencies based on the RCP85 SOMs show changes that are partly comparable to the results of Mewes and Jacobi (2019). For ERA-Interim, they showed an likely increase in occurrence frequency for the Atlantic pathway, but no increase for the Pacific Pathway like it could be found here. However, in Mewes and Jacobi (2019) no superposition have been identified.

Generally, the comparison between the RCP85 and the historical pathway frequencies shows that with a increase of the GHG concentrations the continental pathway is getting less frequent. As described above the continental pathway is connected with a stable cyclonic motion centered above the north pole. This stable state is getting less frequent in favour of increasingly meridional fluxes either through the North Atlantic or the North Pacific. The two oceanic pathways are occurring more frequent in the RCP85-based runs, with the continental pathway and the superpositions occurring less frequent. This suggests that there is a change to a different kind of stable state of the fluxes. While in the

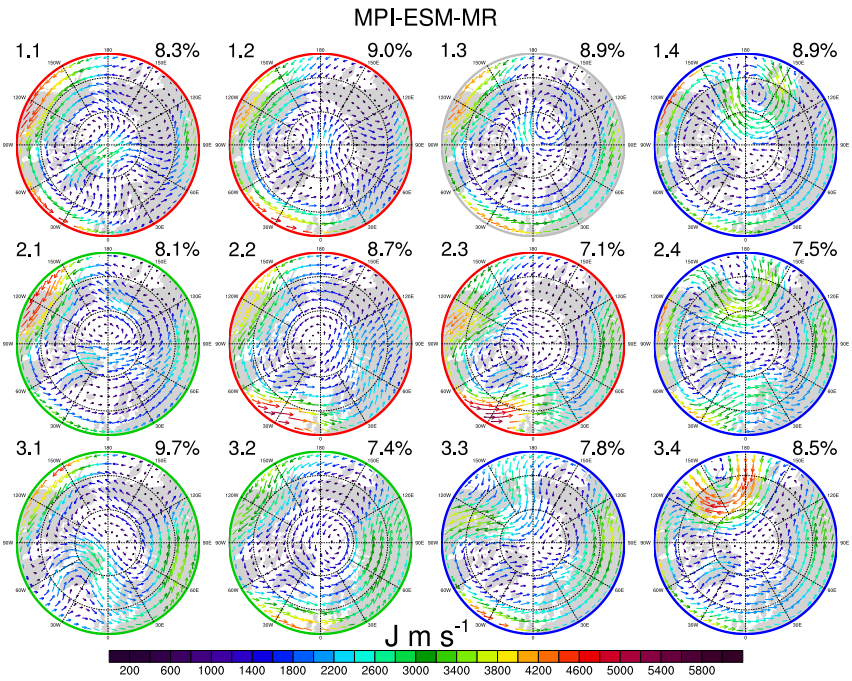

Fig. 7: Same as Fig.1 but for MPI-ESM-MR.

ERA-Interim data, the Pacific pathway was the most frequent and the continental was the least frequent pathway, within the historical runs of the CMIP5 models, the most frequent is the continental pathway. Further, in the RCP85 data the continental pathway is getting less important, and also the Pacific Pathway is most frequent. This leads to the suggestion that the RCP85 frequencies are similar to the results for the ERA-Interim data.
The suggested reasoning would be that due to the increased GHG concentrations the temperature increases. The Arctic warming intensifies (Arctic amplification). This increased warming in the Arctic region weakens the meridional temperature gradient and thus the general driver of the planetary circulation. Due to weaker circulation, the polar jet might be easier to perturb, which results on the long term to an increased meandering and increased meridional flux of energy. Following this, stable states with a strong cyclonic flux around the Northern Hemisphere change to more meandering fluxes.

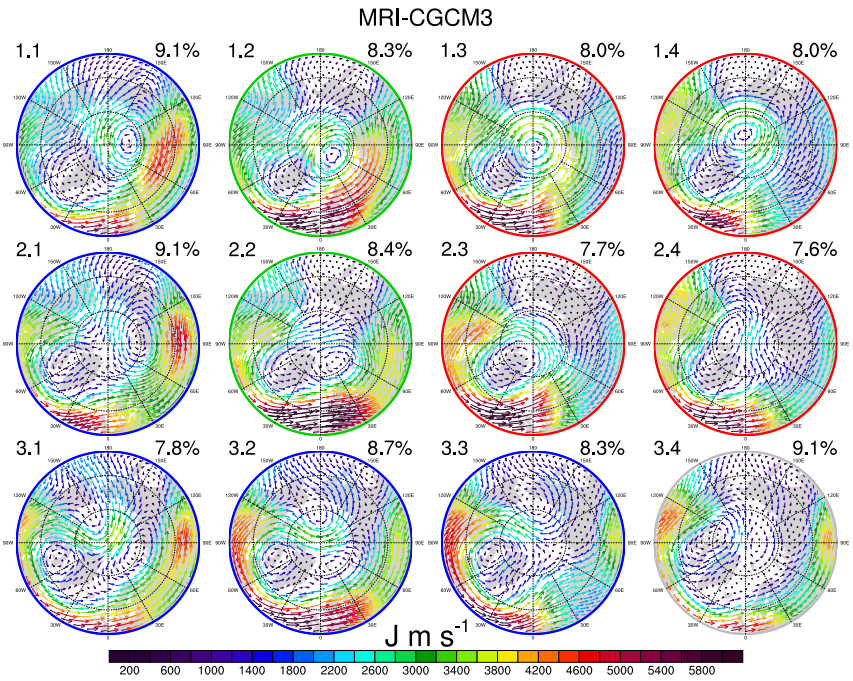

Fig. 8: Same as Fig.1 but for MRI-CGCM3.

Acknowledgements

We gratefully acknowledge the support from the German Research Foundation (Deutsche Forschungsgemeinschaft) within the Transregional Collaborative Research Center (TR 172) “Arctic Amplification: Climate Relevant Atmospheric and Surface Processes, and Feedback Mechanisms (AC)^3.”

References

Cassano, J. J., Petteri, U., and Amanda, L., 2006: Changes in synoptic weather patterns in the polar regions in the twentieth and twenty-first centuries, part 1: Arctic, Int. J. Climatol., 26, 1027–1049, doi:10.1002/joc.1306.

Ceppi, P., Zappa, G., Shepherd, T. G., and Gregory, J. M., 2018: Fast and Slow Components of the Extratropical Atmospheric Circulation Response to CO2 Forcing, Journal of Climate, 31, 1091–1105, doi:10.1175/JCLI-D-17-0323.1.

Crowley, T. J., 2000: Causes of climate change over the past 1000 years, Science, 289, 270–277, doi:10.1126/science.289.5477.270.

Dee, D. P., Uppala, S. M., Simmons, A. J., Berrisford, P., Poli, P., Kobayashi, S., Andrae, U., Balmaseda, M. A., Balsamo, G., Bauer, P., Bechtold, P., Beljaars, A. C. M., van de Berg, L., Bidlot, J., Bormann, N., Delsol, C., Dragani, R., Fuentes, M., Geer, A. J., Haimberger, L., Healy, S. B., Hersbach, H., Hólm, E. V., Isaksen, L., Kållberg, P., Köhler, M., Matricardi, M., McNally, A. P., Monge-Sanz, B. M., Morcrette, J.-J., Park, B.-K., Peubey, C., de Rosnay, P., Tavolato, C., Thépaut, J.-N., and Vitart, F., 2011: The ERA-Interim reanalysis: configuration and performance of the data assimilation system, Quart. J. Roy. Meteor. Soc., 137, 553–597, doi:10.1002/qj.828.

Franzke, C. L. E., Lee, S., and Feldstein, S. B., 2017: Evaluating Arctic warming mechanisms in CMIP5 models, Climate Dynamics, 48, 3247–3260, doi:10.1007/s00382-016-3262-9.

Liu, Y. and Weisberg, R. H., 2011: A review of Self-Organizing Map applications in meteorology and oceanography, InTech, doi:10.5772/13146.

Liu, Y., Weisberg, R. H., and Mooers, C. N. K., 2006: Performance evaluation of the self-organizing map for feature extraction, J. Geophys. Res. Oceans, 111, C05 018, doi:10.1029/2005JC003117.

Loikith, P. C. and Broccoli, A. J., 2015: Comparison between Observed and Model-Simulated Atmospheric Circulation Patterns Associated with Extreme Temperature Days over North America Using CMIP5 Historical Simulations, Journal of Climate, 28, 2063–2079, doi:10.1175/JCLI-D-13-00544.1.

Lynch, A. H., Serreze, M. C., Cassano, E. N., Crawford, A. D., and Stroeve, J., 2016: Linkages between Arctic summer circulation regimes and regional sea ice anomalies, J. Geophys. Res. Atmos., 121, 7868–7880, doi:10.1002/2016JD025164.

Mewes, D. and Jacobi, C., 2017: Variability of horizontal temperature fluxes over the Arctic, Wiss. Mitteil. aus dem Instit. f. Meteorol. der Univ. Leipzig, 55, 51–60, URL http://nbn-resolving.de/urn:nbn:de:bsz:15-qucosa2-167700.

Mewes, D. and Jacobi, C., 2019: Heat transport pathways into the Arctic and their connections to surface air temperatures, Atmospheric Chemistry and Physics, 19, 3927–3937, doi:10.5194/acp-19-3927-2019.

Skific, N., Francis, J. A., and Cassano, J. J., 2009: Attribution of projected changes in atmospheric moisture transport in the Arctic: A self-organizing map perspective, J. Climate, 22, 4135–4153, doi:10.1175/2009JCLI2645.1.

Stroeve, J. C., Serreze, M. C., Holland, M. M., Kay, J. E., Malanik, J., and Barrett, A. P., 2012: The Arctic's rapidly shrinking sea ice cover: a research synthesis, Climatic Change, 110, 1005–1027, doi:10.1007/s10584-011-0101-1.

Taylor, K. E., Stouffer, R. J., and Meehl, G. A., 2012: An overview of CMIP5 and the experiment design, B. Am. Meteorol. Soc., 93, 485–498.

Wendisch, M., Brückner, M., Burrows, J., Crewell, S., Dethloff, K., Ebell, K., Lüpkes, C., Macke, A., Notholt, J., Quaas, J., Rinke, A., and Tegen, I., 2017: Understanding causes and effects of rapid warming in the Arctic, EOS, 98, 22–26, doi:10.1029/2017EO064803.

Ionospheric response to solar variability during solar cycles 23 and 24

Vaishnav, R.[1], Jacobi, Ch.[1], Berdermann, J.[2], Schmölter, E.[2], Codrescu, M.[3]

[1]*Leipzig Institute for Meteorology, Universität Leipzig, Stephanstr. 3, 04103 Leipzig, Germany, E-Mail: rajesh_ishwardas.vaishnav@uni-leipzig.de*
[2]*German Aerospace Center, Kalkhorstweg 53, 17235 Neustrelitz, Germany*
[3]*Space Weather Prediction Centre, National Oceanic and Atmospheric Administration, Boulder, Colorado, USA.*

Summary: The ionospheric variability and its complexity is strongly dependent on continuous varying intense solar extreme ultraviolet (EUV) and UV radiations. We investigate the ionospheric response to the solar activity variations during the solar cycle (SC) 23 (1999-2008) and 24 (2009-2017) by using the F10.7 index, and Total Electron Content (TEC) maps provided by the international GNSS service (IGS). Wavelet cross-correlation method is used to evaluate the correlation between F10.7 and the global mean TEC. The maximum correlation is observed at the solar rotation time scale (16-32 days). There is a significant difference in the correlation at the time scale of 32-64 days. During SC 23, the correlation is stronger than during SC 24. This is probably due to the longer lifetime of active regions during SC 23. The wavelet variance estimation method suggests that the variance during SC 23 is more significant than during SC 24. Furthermore, the Coupled Thermosphere Ionosphere Plasmasphere Electrodynamics (CTIPe) model was used to reproduce the ionospheric delay of about 1-2 days observed in the IGS TEC observations. A strong correlation was modelled as well as observed during a high solar activity year (2013) as compared to low a solar activity year (2008).

Zusammenfassung: Die ionosphärische Variabilität ist stark abhängig von der kontinuierlich variierenden intensiven solaren extrem ultravioletten (EUV) und UV-Strahlung. Wir untersuchen die ionosphärische Reaktion auf Variationen der Sonnenaktivität während der Sonnenzyklen (SC) 23 (1999-2008) und 24 (2009-2017) mit Hilfe des F10.7-Radioflussindexes und TEC (Gesamtelektronengehalt, Total Electron Content) -Karten, die vom internationalen GNSS-Dienst (IGS) bereitgestellt werden. Wavelet-Kreuzkorrelation wird verwendet, um die Korrelation zwischen F10.7 und global gemitteltem TEC zu bestimmen. Die maximale Korrelation wird auf der Zeitskala der Sonnenrotation (16-32 Tage) beobachtet. Es gibt einen signifikanten Unterschied in der Korrelation auf der Zeitskala von 32 bis 64 Tagen. Während des SC 23 ist die Korrelation stärker als während SC 24. Dies ist auf die längere Lebensdauer der aktiven Regionen zurückzuführen. Das Wavelet-Varianz-Schätzverfahren legt nahe, dass die Varianz beim SC 23 mehr von Bedeutung ist, als während SC 24. Des Weiteren wurde das gekoppelte Thermosphäre-Ionosphäre-Plasmasphäre-Elektrodynamik (CTIPe) Modell verwendet, um die ionosphärische Verzögerung von 1-2 Tagen zu reproduzieren. Eine starke Korrelation wurde bei hoher Sonnenaktivität (2013) im Gegensatz zu geringer Sonnenaktivität (2008) simuliert und auch beobachtet.

1. Introduction

It has been well established that solar activity plays a vital role in the formation of the ionosphere. Changes in thermospheric and ionospheric structure through photoionization and photodissociation of the major species O, O_2, and N_2 depend on the intensity of the incoming solar EUV and UV radiation at different time scales, including the well understood quasi solar rotation (SR) period and the 11 years solar cycle (SC) (e.g., Jakowski et al., 1991; Afraimovich et al., 2008; Liu and Chen, 2009; Chen et al., 2015). Solar radiation variations can be easily observed in the ionosphere, which significantly shows an impact on Global Navigation Satellite System (GNSS) and satellite communication. Hence, it is crucial to characterize the influence of solar radiation in the thermosphere-ionosphere regime. EUV can vary during solar minimum to maximum by more than a factor of 2. Various numerical, empirical, and physics-based models have been developed, which includes solar EUV effects. Several ionospheric parameters have been used to characterize the ionosphere such as total electron content (TEC, given in TEC unit, 1 TECU=10^{16} electrons m^{-2}) and peak electron density of F2 region (NmF2, unit m^{-3}). As long term direct EUV observations are not reliable due to satellite degradation (BenMoussa et al., 2013), solar EUV proxies, e.g., the F10.7 solar radio flux at 10.7 cm, given in solar flux units (sfu), 1 sfu = 10^{-22}Wm^{-2} Hz^{-1} (Tapping, 2013), are used to represent solar activity.

The correlation of solar flux and the ionosphere has been investigated by various researchers to understand the behavior of the ionosphere at different time scales (e.g., Jakowski et al., 1991; Afraimovich et al., 2008; Min et al., 2009; Lee et al., 2012; Jacobi et al., 2016; Vaishnav et al., 2019). Solar proxies are well correlated with ionospheric parameters at a longer time scales (e.g. SC), and weaker correlated at short time scales like the SR. In particular, ionospheric TEC gets delayed by ~1-2 days in comparison to solar radiations at the SR period (Jakowski et al., 1991; Forbes et al., 2000; Afraimovich et al., 2008; Lee et al., 2012; Jacobi et al., 2016; Vaishnav et al., 2018a, b; Schmölter et al., 2018; Vaishnav et al., 2019, see also references therein).

To shed more light on the ionospheric response to solar variability at the SR period, Vaishnav et al. (2018a) used the Coupled Thermosphere Ionosphere Plasmasphere Electrodynamics **(**CTIPe) model and reproduced delay about one day. The observed delay could be due to vertical transport processes (Vaishnav et al., 2018a) or slow diffusion of atomic oxygen at 180 km (Jakowski et al., 1991) or due to photochemical, electrodynamic processes in the thermosphere-ionosphere system (Ren et al., 2018). Vaishnav et al. (2018b) studied the ionospheric response with solar EUV proxies and showed significant differences in correlation during low and high solar activity years. The ionospheric behavior also varies with the solar cycles. The overall solar activity during SC 23 was reported to be more intense followed by the extended solar minimum during the years 2007-2009, where the solar activity was reported extremely low, followed by an overall decrease in the solar activity of SC 24. Vaishnav et al. (2019) used multiple solar proxies and TEC observations to explore long term variations using wavelet analysis. They investigated the ionospheric variance by using the wavelet method and reported higher variance during solar maxima of SC 23 (2002-2004) as compared to SC 24 (2012-2014).

To analyze the SC effect on the solar flux-ionosphere coupling in more detail, in this study, we aim to reproduce the delay observed in the TEC observations using CTIPe model simulations during the low and high solar activity years 2008 and 2013 using realistic atmospheric conditions. Furthermore, we will estimate the solar flux-ionosphere correlation using the wavelet cross-correlation by the sequence method at different time scales (4-8 days, 8-16 days, 16-32 days and 32-64 days), and wavelet variance by scale using TEC observations along with F10.7 for SCs 23 and 24.

2. Data and model description

2.1. Data sources

The International GNSS Service (IGS, Hernandez-Pajares et al., 2009) provides global ionospheric TEC maps by NASA's data archive service (CDDIS, 2017) with a time resolution of 2 hours and a lat/lon grid of 2.5°/ 5°. Global TEC datasets can be used to understand the temporal and spatial variations of the ionosphere. We have computed daily GTEC values. The daily F10.7 index is taken from the LISIRD (DeWolfe et al., 2010) database to represent to solar activity.

2.2. Coupled Thermosphere Ionosphere Plasmasphere Electrodynamics (CTIPe)

The CTIPe model is a first principal, time-dependent, global, three dimensional, nonlinear, physics-based numerical model of the coupled thermosphere-ionosphere region which includes a neutral thermosphere model (Fuller-Rowell and Rees, 1980), a mid- and high-latitude ionosphere convection model (Quegan et al., 1982), a plasmasphere and low latitude ionosphere model (Millward et al., 1996), and a self-consistent electrodynamics model (Richmond et al., 1992), which runs simultaneously and are fully coupled. The CTIPe model solves the equations of composition, momentum, and energy of the neutral gas, to output global temperature, density, wind components, and atmospheric neutral and plasma composition. The horizontal resolution used in this study is 2° × 18°, and there are 15 pressure surfaces from 80 to ~450 km, with a vertical resolution of one scale height. The corresponding geometric heights are variable depending on temperature and therefore on altitude and the solar and magnetic activity. The numerical solution of the composition equation with the energy and momentum equations describes transport, turbulence, and diffusion of atomic oxygen, molecular oxygen, and nitrogen (Fuller-Rowell and Rees, 1983). The model includes various external drivers like Weimer electric field, TIROS/NOAA auroral precipitation, and tidal forcing. Solar EUV and UV radiation specified by a reference solar spectrum based on the EUV flux model for Aeronomic Calculations (EUVAC, Richards et al., 1994) driven by the modified F10.7 index (F10.7A: average of daily F10.7 and previous 41 days average F10.7) is used in the model to calculate ionization rates, heating rates, and oxygen dissociation rates. The lower boundary is characterized by the output of the Whole Atmospheric model (WAM, Akmaev, 2011). More description of CTIPe is available in Codrescu et al. (2008, 2012).

3. Results and discussion

3.1. Spatial distribution of TEC

The temporal and spatial distribution of TEC is highly depended on the absorption of solar EUV radiation by ionizing the neutrals in the ionosphere, and thermospheric dynamics during quite space weather conditions. To represent the spatial distribution, we have computed long-term averaged IGS TEC data for each grid point at a resolution of 2.5°/ 5°. Figure 1 shows the spatial variation of TEC for (a) SC 23 (1999-2008) and (b) SC 24 (2009-2017), and the superimposed white contour lines show the standard deviation calculated from daily TEC datasets. The Figure shows maximum distribution of TEC along the both sides of magnetic equator around ±20^{o}, which is due to the well-known fountain effect (Appleton, 1946), and smaller TEC at high latitudes. Maximum values of the standard deviation are observed in the low latitude region with about 17 and 13 TECU in SC 23 and SC 24 respectively.

The spatial distribution of TEC depends on the ionisation of neutrals, transport processes, and recombination rates, which varies latitudinally and longitudinally. As compared to SC 24, SC 23 was stronger, and it shows more TEC distribution. Maximum TEC observed during SC 23 as 35 TECU, and 30 TECU during SC 23.

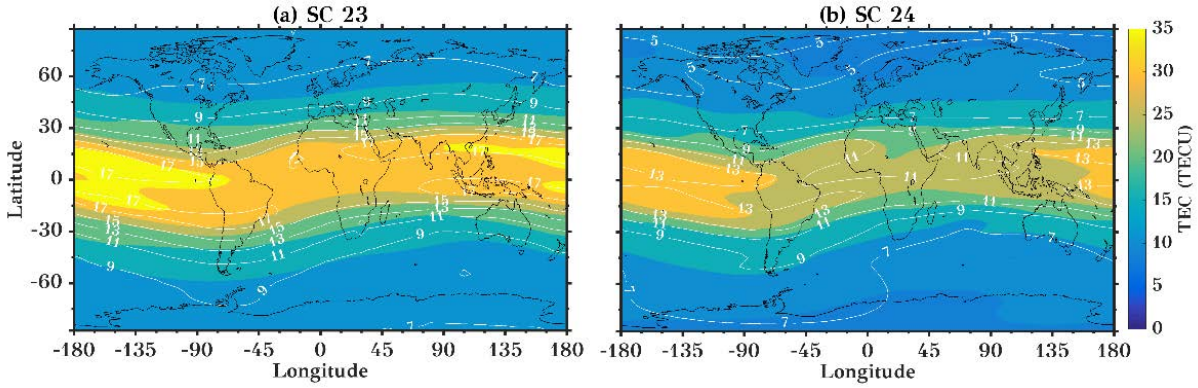

Fig. 1. Spatial distribution of averaged TEC during the (a) SC 23 and (b) SC 24. The white contour lines indicate the standard deviation based on daily data.

3.2. Influence of the solar activity on ionosphere at different time scales

The thermosphere-ionosphere system is strongly influenced by the solar activity at different time scales, as solar activity varies from short time scales (e.g. minutes) to longer time scales (e.g. SC). Hence, a better understanding is required in order to explore the key features of the thermosphere-ionosphere system. The wavelet analysis method is a well-established tool to analyze the datasets at different time scales. We have used the maximal overlap discrete wavelet transforms (MODWT) technique (Percival and Walden, 2000), which is a modified version of the discrete wavelet transform (Mallat, 1989; Whitcher et al., 2000) to filter the time series at different time scales. This method filters the time series at different time scales. In order to investigate the correlation between GTEC and F10.7, we have used the wavelet cross-correlation sequence method with a Fejer-Korovkin filter (Percival and Walden, 2000). This method

is used to calculate the cross-correlation at different time scales with standard deviation. Figure 2 shows the cross-correlation by sequence method for (a) SC 23 and (b) SC 24. There is the strongest positive correlation at the time scale representing 16-32 days cycles, followed by 32-64 days during SC 23 and 24. This is not surprising as the SR period of about 27 days is the most dominating period. During SC 23, the correlation at time scales of 16-32 days is about 0.7, which is also observed during SC 24.

At the time scales of 32-64 days, the correlation is lower during SC 24 as compared to SC 23. The SC 23 was more intense as compared to SC 24, and the mean SR period was extended due to the longer lifetime of active regions on the solar surface. Hence, during SC 23, the mean SR period was longer than 27 days, which results in a stronger correlation about 0.7 at 32-64 days. However, as compared to SC 23, SC 24 shows lower correlation coefficients of about 0.65 at 32-64 days period.

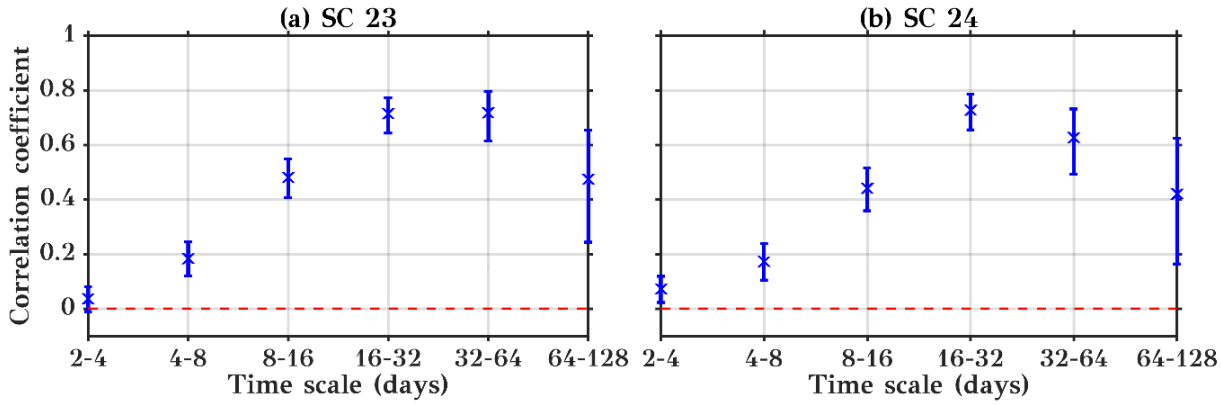

Fig. 2. Correlation coefficients at different time scales using wavelet coefficients for (a) SC 23 and (b) SC 24 between GTEC and F10.7. Error bars show the standard deviation.

Furthermore, we examine the wavelet cross-correlation at different time scales representing 4-8 days to 32-64 days for SC 23 (blue) and SC 24 (red), as shown in Figure 3. The Figure shows the cross-correlation along with the 95% confidence intervals up to lag 20. Red and blue dashed lines show the 95% confidence bands. Poor correlation is observed at the time scale of 4-8 days with a correlation coefficient of about 0.25 (0.18) with a delay of about one day during SC 23 (24). The maximum correlation of about 0.8 is observed at the 16-32 days time scale during both the SCs 23 and 24 with a delay of about two days, shows that the behavior of ionosphere is similar during SCs 23 and 24 at the time scales of 16-32 days.

A similar result with a correlation coefficient about 0.7 is observed at the timescale of 32-64 days, see also Figure 2, during SC 23. As compared to SC 23, there is a weaker correlation at the time scales of 32-64 days observed during SC 24, with a correlation coefficient of about 0.6 with the ionospheric delay about one day. The differences observed in the correlation between SCs 23 and 24 suggest that during SC 23, the lifetime of solar active regions was longer than during SC 24.

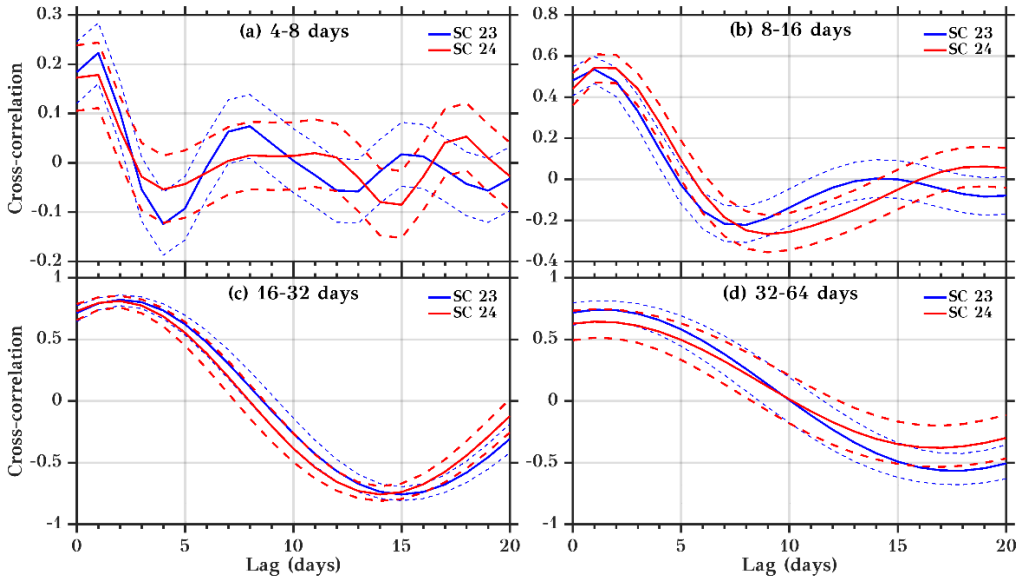

Fig. 3. Wavelet cross-correlation sequences between GTEC and F10.7 during SC 23(blue) and SC 24 (red) for different time scales 4-8, 8-16, 16-32 and 32-64 days. Red and blue dashed lines show the 95% confidence bands.

3.3. Wavelet variance estimation

Figure 4 shows the wavelet variance estimated for GTEC and F10.7 index using Daubechies 2 (db2) wavelets. To calculate the variance, we first calculated the wavelet coefficient using MODWT. Wavelet variance (Cornish et al., 2006) is calculated from the wavelet coefficient for different time scales starting from 2-4 days to 64-128 days. The red/black color in the plot represents the SCs 23/24, respectively. For GTEC, maximum variance appears in the 64-128 days period (quasi-three-monthly oscillations) during SC 23. The second strongest variance is observed at the timescale of 16-32 days. Stronger variance is observed in SC 23 as compared to SC 24 at all the timescales. In contrast to GTEC, F10.7 shows maximum variance at the 16-32 days period, which indicates that the variance is more predominant at the SR period. Again, the variance observed during SC 23 is stronger than the one during SC 24. As the solar activity was more intense during SC 23 as compared to SC 24, the stronger variance is expected during SC 23.

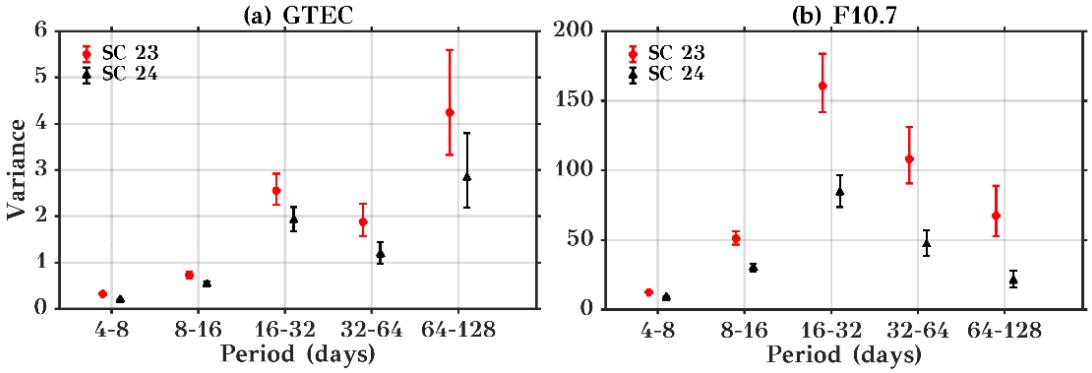

Fig. 4. Wavelet variances for the SC 23 (red) and 24 (black) for (a) GTEC and (b) F10.7. Error bars show the 95% coverage probability of the confidence interval obtained from the 'Chi2Eta3' confidence method.

3.4. Delay and variance estimation using model simulations and IGS TEC

Figure 5 shows the average cross-correlation along with the standard errors, represented by the error bars. The cross-correlation and delay have been calculated for nine sets of 27 days IGS GTEC observations for (a) 2008 and (b) 2013. The time series of the year 2008 and 2013 have been filtered by using a 25 to 33 days bandpass filter. The maximum correlation is observed to be about 0.7 (0.8) with a delay of about one day in GTEC observations with the F10.7 index during low (high) solar activity conditions. Stronger correlation is observed during high solar activity as compared to low solar activity.

We ran CTIPe model to simulate the ionospheric behavior. We performed ensemble runs of each 27 days using real atmospheric conditions in the WAM model for the low solar activity (Figure 5c) year 2008 and the high solar activity (Figure 5d) year 2013. Datasets have been filtered as in the same manner mentioned above. The averaged cross-correlations between CTIPe simulated GTEC and F10.7A for the years 2008 and 2013 were calculated. The maximum correlation observed is about 0.49 (0.6) during low (high) solar activity conditions with a delay of about one day. The CTIPe simulated results are thus capable to reproduce the delay observed in the GTEC observations. Figure 5 also shows the lower correlation during low solar activity as compared to high solar activity, similar to the observations. This may be explained that, although the solar activity is the main drivers to control the ionospheric plasma density, the ionosphere is also influenced by various other factors which include lower atmospheric forcing like planetary waves (Forbes et al., 2000) and by the solar wind, in particular from coronal holes. This is the case especially for low solar activity, and that is why we observe and simulate lower correlation during lower solar activity conditions. In contrast, for strong solar forcing, the meteorological influences are weaker than solar ones.

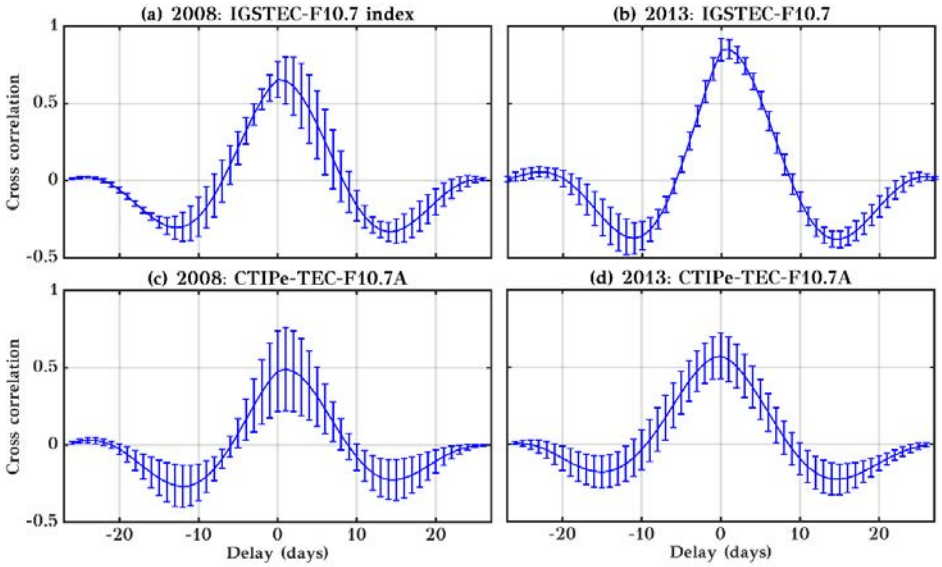

Fig. 5. Averaged cross-correlation and delay using nine sets of ensemble runs for 27 days using IGSTEC-F10.7 (upper panel) and CTIPe simulated TEC-F10.7A (lower panel) for low (2008) and high (2013) solar activity. Error bars represent standard errors.

4. Summary and conclusion

This paper investigates the influence of solar activity variations on the GTEC during the SCs 23 (1999-2008) and 24 (2009-2017). The wavelet cross-correlation by sequence method is used to evaluate the correlation between the wavelet coefficients of F10.7 and GTEC calculated by the MODWT method at different timescales. The maximum correlation is observed at the solar rotation time scale (16-32 days). There is a significant difference in the correlation at the timescale of 32-64 days. During SC 23 the correlation is stronger than during SC 24, probably due to longer lifetime of active regions on the solar surface. Further, the wavelet variance estimation method is used to find the variance of the SCs 23 and 24. Variance during SC 23 is stronger than during SC 24. CTIPe simulations were used to reproduce the variance and delay observed in the GTEC observation.

A strong correlation was observed during a high solar activity year (2013) as compared to a low solar activity year (2008) in the model simulated TEC, as well as in the observed TEC with a delay about 1-2 days.

An attempt was made by Jakowski et al. (1991) to understand the delay reported in TEC against the solar activity, and they suggested that slow diffusion of atomic oxygen could be a possible reason. Vaishnav et al. (2018) show that the vertical transport processes as one of the possible reasons for the delay observed in GTEC using CTIPe simulations. In addition to this, dynamics and electrodynamics also play an essential role in the delay mechanism, as suggested by Ren et al. (2018). Further numerical modeling is required to explore the major processes which cause and contribute to the ionospheric delay.

Acknowledgements

IGS TEC maps have been provided via NASA through ftp://cddis.gsfc.nasa.gov/gnss/products/ionex/. Daily F10.7 indices have been provided by LASP at http://lasp.colorado.edu/lisird/noaa_radio_flux. The study has been supported by Deutsche Forschungsgemeinschaft (DFG) through grant No. JA 836/33-1.

References

Afraimovich, E. L., Astafyeva, E. I., Oinats, A. V., Yasukevich, Yu. V., Zhivetiev, I. V., 2008: Global electron content: a new conception to track solar activity, Ann. Geophys., 26, 335–344, https://doi.org/10.5194/angeo-26-335-2008.

Akmaev, R. A., 2011: Whole atmosphere modeling: Connecting terrestrial and space weather, Rev. Geophys., 49, RG4004, https://doi.org/10.1029/2011RG000364.

Appleton, E. V., 1946: Two anomalies in the ionosphere, Nature, 157, 691. https://doi.org/10.1038/157691a0.

BenMoussa, A., S. Gissot, U. Schühle, G. Del Zanna, F. Auchère, et al., 2013: On-orbit degradation of solar instruments, Sol. Phys., 288, 389–434, https://doi.org/10.1007/s11207-013-0290-z.

CDDIS: GNSS Atmospheric Products, available at: http://cddis.nasa.gov/Data_and_Derived_Products/GNSS/atmospheric_products.html, last access: 15 April 2019.

Cornish, C. R., Bretherton, C. S., Percival, D. B., 2006: Maximal overlap wavelet statistical analysis with application to atmospheric turbulence, Boundary-Layer Meteorology, 119(2), 339-374, https://doi.org/10.1007/s10546-005-9011-y.

Chen, Y., Liu, L., Le, H., Zhang, H., 2015: Discrepant responses of the global electron content to the solar cycle and solar rotation variations of EUV irradiance, Earth, Planets and Space, 67(1), 80, https://doi.org/10.1186/s40623-015-0251-x.

Codrescu, M. V., Fuller-Rowell, T. J., Munteanu, V., Minter, C. F., Millward G. H., 2008: Validation of the coupled thermosphere ionosphere plasmasphere electrodynamics model: CTIPe-Mass Spectrometer Incoherent Scatter temperature comparison, Space Weather, 6, S09005, doi:10.1029/2007SW000364.

Codrescu, M. V., Negrea, C., Fedrizzi, M., Fuller-Rowell, T. J., Dobin, A., Jakowsky, N., Khalsa, H., Matsuo, T., Maruyama, N., 2012: A real-time run of the Coupled Thermosphere Ionosphere Plasmasphere Electrodynamics (CTIPe) model, Space Weather, 10, S02001, https://doi.org/10.1029/2011SW000736.

DeWolfe, A. W., Wilson, A., Lindholm, D. M., Pankratz, C. K., Snow, M. A., Woods, T. N., 2010: Solar Irradiance Data Products at the LASP Interactive Solar Irradiance Datacenter (LISIRD), In AGU Fall255 Meeting 2010, Abstract GC21B-0881.

Forbes, J. M., Palo, S. E., Zhang, X., 2000: Variability of the ionosphere, J. Atmos. Sol-Terr. Phys., 62(8), 685-693, https://doi.org/10.1016/S1364-6826(00)00029-8.

Fuller-Rowell, T. J., Rees, D., 1980: A three-dimensional time-dependent global model of the thermosphere. J. Atmos. Sci., 37, 2545–2567, https://doi.org/10.1175/1520-0469(1980)037<2545:ATDTDG>2.0.CO;2.

Fuller-Rowell, T. J., Rees, D., 1983: Derivation of a conservation equation for mean molecular weight for a two-constituent gas within a three-dimensional, time-dependent model of the thermosphere, Planet. Space Sci., 31(10), 1209-1222, https://doi.org/10.1016/0032-0633(83)90112-5.

Hernandez-Pajares, M., Juan, J. M., Sanz, J., Orus, R., Garcia-Rigo, A., Feltens, J., Komjathy, A., Schaer, S. C., Krankowski, A., 2009: The IGS VTEC maps: a reliable source of ionospheric information since 1998, J. Geod., 83, 263–275, https://doi.org/10.1007/s00190-008-0266-1.

Jacobi, C., Jakowski, N., Schmidtke, G., Woods, T. N., 2016: Delayed response of the global total electron content to solar EUV variations, Adv. Radio Sci., 14, 175, https://doi.org/10.5194/ars-14-175-2016.

Jakowski, N., Fichtelmann, B., Jungstand, A., 1991: Solar activity control of Ionospheric and thermospheric processes, J. Atmos. Terr. Phys., 53, 1125–1130, https://doi.org/10.1016/0021-9169(91)90061-B.

LASP (2019). LASP Interactive Solar Irradiance Data Center, http://lasp.colorado.edu/lisird, last access: 30 April 2019.

Lee, C. K., Han, S. C., Bilitza, D., Seo, K. W., 2012: Global characteristics of the correlation and time lag between solar and ionospheric parameters in the 27-day period, J. Atmos. Sol-Terr. Phys., 77, 219-224, https://doi.org/10.1016/j.jastp.2012.01.010.

Liu, L., Chen, Y., 2009: Statistical analysis of solar activity variations of total electron content derived at Jet Propulsion Laboratory from GPS observations, J. Geophys. Res., 114, A10311, https://doi.org/10.1029/2009JA014533.

Mallat, S., 1989: A theory of multiresolution signal decomposition: The wavelet representation, IEEE Trans. on Pattern Analysis and Machine Intelligence 11, 647-693, https://doi.org/10.1109/34.192463.

Millward, G. H., Moffett, R. J., Quegan, S., Fuller-Rowell, T. J., 1996: A coupled thermosphere-ionosphere-plasmasphere model (CTIP), in Solar-Terrestrial Energy Program: Handbook of Ionospheric Models, ed. R. W. Schunk. 239–279, Cent. for Atmos. and Space Sci., Utah State Univ., Logan, Utah.

Min, K., Park, J., Kim, H., Kim, V., Kil, H., Lee, J., Rentz, S., Lühr, H., Paxton, L., 2009: The 27-day modulation of the low-latitude ionosphere during a solar maximum, J. Geophys. Res., 114, A04317, https://doi.org/10.1029/2008JA013881.

Percival, D. B., Walden, A. T., 2000: Wavelet Methods for Time Series Analysis. Cambridge, U.K: Cambridge University Press.

Quegan, S., Bailey, G. J., Moffett, R. J., Heelis, R. A., Fuller- Rowell, T. J., Rees, D., Spiro, R. W., 1982: A theoretical study of the distribution of ionization in the high-latitude ionosphere and the plasmasphere: First results on the mid-latitude trough and the light-ion trough, J. Atmos. Terr. Phys., 44, 619–640, https://doi.org/10.1016/0021-9169(82)90073-3.

Ren, D., Lei, J., Wang, W., Burns, A., Luan, X., Dou, X., 2018: Does the peak response of the ionospheric F2 region plasma lag the peak of 27-day solar flux variation by multiple days? J. Geophys. Res., 123. https://doi.org/10.1029/2018JA025835.

Richards, P. C., Fennelly, J. A., Torr, D. G. 1994: EUVAC: A solar EUV flux model for aeronomic calculations, J. Geophys. Res., 99, 8981–8992, https://doi.org/10.1029/94JA00518.

Richmond, A. D., Ridley, E. C., Roble, R. G., 1992: A thermosphere/ionosphere general circulation model with coupled electrodynamics, Geophys. Res. Lett., 19, 601–604, https://doi.org/10.1029/92GL00401.

Schmölter, E., Berdermann, J., Jakowski, N., Jacobi, C., Vaishnav, R., 2018: Delayed response of the ionosphere to solar EUV variability, Adv. Radio Sci., 16, 149-155, https://doi.org/10.5194/ars-16-157-2018.

Tapping, K. F., 2013: The 10.7 cm solar radio flux (F10.7), Space Weather, 11, 394–406, https://doi.org/10.1002/swe.20064.

Vaishnav, R., Jacobi, C., Berdermann, J., 2019: Long-term trends in the ionospheric response to solar EUV variations, Ann. Geophys. Discuss., https://doi.org/10.5194/angeo-2019-34, in review.

Vaishnav, R., Jacobi, C., Berdermann, J., Schmölter, E., Codrescu, M., 2018a: Ionospheric response to solar EUV variations: Preliminary results, Adv. Radio Sci., 16, 157-165, https://doi.org/10.5194/ars-16-149-2018.

Vaishnav, R., Jacobi, C., Berdermann, J., Schmölter, E., Codrescu, M., 2018b: Ionospheric response during low and high solar activity, Rep. Inst. Meteorol. Univ. Leipzig 56, 1-10, ISBN: 978-3-9814401-6-4, http://nbn-resolving.de/urn:nbn:de:bsz:15-qucosa2-317670.

Whitcher, B., Guttorp, P., Percival, D. B., 2000: Wavelet analysis of covariance with application to atmospheric time series, J. Geophys. Res., 105 (D11), 14941-14962, https://doi.org/10.1029/2000JD900110.

Einfluss der Erhöhung der Oberflächenalbedo in Sibirien auf die Zirkulation in der mittleren Atmosphäre

A. Adler, D. Mewes, Ch. Jacobi

Institute for Meteorology, Stephanstr. 3 04103 Leipzig
E-Mail: aa58vudu@studserv.uni-leipzig.de

Summary: The Northern hemisphere circulation is supposed to change due to changed sea-ice cover in the Arctic and the increase of Siberian surface albedo. The latter is tested using the state of the art atmospheric circulation model ICON. We artificially increased the albedo of Siberia to values comparable to the Greenland ice sheet to investigate the change of vertical wave propagation and the general change of the background circulation. It was found for the winter season that the increased albedo results in increased vertical wave propagation for December and January. This is accompanied by a warming of the stratosphere that was found for the whole winter.

Zusammenfassung: Es wird angenommen, dass die Zirkulation der Nordhemisphäre durch den Rückgang von Meereis in der Arktis und der Zunahme der Oberflächenalbedo in Sibirien beeinflusst wird. Letzteres wurde mit dem aktuellen atmosphärischen Zirkulationsmodell ICON getestet. Die Albedo über Sibirien wurde innerhalb eines Experimentes erhöht, und zwar auf Werte welche vergleichbar mit denen über dem grönländischen Eisschild sind. Es wurde festgestellt, dass in den Wintermonaten Dezember und Januar die vertikale Wellenausbreitung stärker in die Stratosphäre reicht; dem folgt auch die in der Theorie erwartete Erwärmung in der Stratosphäre.

1. Einleitung

Die Dynamik der mittleren Atmosphäre der nördlichen Hemisphäre wird wesentlich durch planetare Wellen geprägt. Die damit verbundene Lage des Polarjets bestimmt sowohl die Entwicklung des Polarwirbels als auch die Druckgebilde in der Troposphäre. Einhergehend mit der Ausprägung des Polarwirbels sind langanhaltende stratosphärische Prozesse. Bestimmt werden diese unter anderem durch die Meereis-Bedeckung sowie die polare Albedo (abnehmende Meereisbedeckung und zunehmende Albedo durch wachsende Schneeflächen). Die Auswirkungen der einflussnehmenden Faktoren, die durchaus für zukünftige Szenarien realistisch sind, zu kennen und die damit verbundenen Folgen für die troposphärischen Prozesse in den hohen und mittleren Breiten abzuschätzen stellt einen wesentlichen Baustein zum Verständnis dar. Mit Hilfe des ICON-Modells soll im vorliegenden Fall jedoch zunächst einzig die Erhöhung der Albedo in Sibirien simuliert werden.

Für den Zusammenhang zwischen der atmosphärischen Zirkulation in der Arktis und den mittleren Breiten gibt es drei wichtige dynamische Antriebe: die Änderungen der Tiefdruckbahnen, die Position und Struktur des Jetstreams und die Aktivität der

planetaren Wellen. Unter arktischer Verstärkung versteht man die schnellere Erwärmung der arktischen Regionen im Vergleich zum globalen Mittel (Stroeve et al. 2012, Wendisch et al. 2017), wobei die Erwärmung bis in die Stratosphäre reicht (Cohen et al. 2014). Diese ändert direkt und indirekt die planetare Wellenaktivität in der Troposphäre und den Jetstream in den mittleren und hohen Breiten. Weitere steuernde Prozesse sind die natürliche Variabilität und der Klimawandel. Die arktische Verstärkung und damit direkt bzw. indirekt die Änderungen der Tiefdruckzugbahnen, des Jetstreams und der planetaren Wellen wird beeinflusst durch Verringerung des Meereises und zunehmende Schneebedeckung der nördlichen Hemisphäre.

Durch die schnellere Erwärmung der Arktis kommt es zu einem deutlichen Verlust von Meereis, zur Abnahme der Albedo und damit zu mehr Absorption von Sonnenlicht. Im Herbst, wenn die Luft kälter ist als der Ozean geht überschüssige Wärmeenergie in die Atmosphäre über und die untere Troposphäre der Arktis erwärmt sich. Eisbildung im Winter wird dementsprechend geringer, womit sich im nächsten Jahr die Erwärmung und der Meereisverlust noch mehr ausprägt. Der meridionale Temperaturgradient zwischen Arktis und Tropen wird geringer und es kommt zu einer Abschwächung des polaren Jetstreams, der dann größere Mäander ausbildet (Cohen et. al 2014). Dies hat zur Folge, dass sich ostwärts ziehende Systeme verlangsamen und länger anhaltende Wetterereignisse auftreten.

Nach den Modellvorstellungen nach Cohen et al. (2014) kommt es im September/Oktober zu der Abnahme des Meereises. Dadurch erfährt die atmosphärische Grenzschicht der Arktis eine Erwärmung und Zunahme der Feuchtigkeit. Über der „Wärmequelle“ sinken Luftmassen ab, die das Hoch verstärken (über Barent- und Karasee), wodurch der Jet blockiert wird. Dieser mäandriert weiter nach Süden, ein Trog entwickelt sich und kalte Luft strömt äquatorwärts nach Süden. Feuchte Luftmassen über Eurasien sorgen für intensive Schneefälle und die Schneebedeckung nimmt zu. Die Zunahme der Schneebedeckung bewirkt eine Abkühlung der atmosphärischen Grenzschicht, wodurch sich das Hoch in der mittleren Troposphäre abschwächt, der Trog verstärkt sich und es kommt zu einer Rückenbildung im Bereich der Barent- und Karasee. Die Mäander des polaren Jetstreams werden stärker, die Rossby-Wellen verstärken sich also und reichen bis in die Stratosphäre.

Somit führen diese beiden zusammenhängende Prozesse zu einer Verstärkung der vertikalen Ausbreitung der planetaren Wellen bis in die Stratosphäre. Als Folge gelangt der stratosphärische Jetstream in Schwingung, der Stratosphärenjet schwächt sich ab und wird instabil. Dadurch wird der Polarwirbel geschwächt und Warmluft dringt in Wirbel ein. Die Stratosphärenerwärmung kann den Zusammenbruch des Polarwirbels bewirken, der Polarwirbel kann sich sogar teilen. Dieser Einfluss von Schneebedeckung und damit der Änderung der Albedo, wurde bereits von Fletcher et al. (2007) in Modellen gezeigt. Sie konnten zeigen, dass bei erhöhter Schneebedeckung die Stratosphären- und Troposphären-Interaktion zunimmt.

Im 2. Kapitel beschreiben wir das verwendete Modell sowie die Methoden und die geänderten Parameter innerhalb des Modells. Im folgenden 3. Kapitel werden die Resultate präsentiert, welche in Kapitel 4 zusammengefasst werden.

2. Daten und Methoden

Das ICON (Icosahedral nonhydrostatic atmospheric general circulation model) – Modell ist an das ECHAM-Modell angelehnt, hat die Modellphysik von ECHAM übernommen, um die gleichen Antriebsfaktoren zu haben. Der Unterschied zwischen ECHAM und ICON ist, dass ECHAM hydrostatisch und ICON nicht-hydrostatisch modelliert.

Das Modell arbeitet im Ikosaeder-Gitter, wobei die Ikosaeder auf eine Kugel projiziert werden. Der Vorteil dieser Methode ist, dass Pole nicht überpräsentiert werden. Das Modell läuft mit 47 vertikalen Niveaus (16 in Stratosphäre, 8 in Mesosphäre), vergleichbar mit dem ECHAM6-LR. Beide haben 47 Level und beide in 80 km das höchste Level, ECHAM hat jedoch bei dem letzten Level eine unendliche Schichtdicke. Für das Experiment mit ICON wurde eine Auflösung von R2B4 gewählt, was eine effektive Maschenweite von 13 km bedeutet, die mittlere Fläche der Gitterelemente ist 173 km^2.

Die Ausbreitung der Rossby-Wellen in vertikaler Ausrichtung wird bestimmt durch den zonalen Wind. Ab einer kritischen Geschwindigkeit bzw. dem Vorliegen einer östlichen Strömung kommt die Wellenausbreitung zum Erliegen. Diese Begrenzung wird definiert durch das Charney-Drazin-Kriterium. Dem Charney-Drazin-Kriterium folgend, haben Wellen mit unterschiedlichen Wellenzahlen (WZ) unterschiedliche Auswirkungen und können unter Umständen auch eine Spaltung des Polarwirbels zur Folge haben. Für die Betrachtungen sind vor allem Wellen mit den WZ 1 und 2 von Interesse. Höhere WZ haben im Vergleich zu den WZ 1 und 2 eine vernachlässigbare Auswirkung, sodass sie hier nicht betrachtet werden.

Zur Charakterisierung der Wellenausbreitung in der Stratosphäre und ihrer Auswirkungen auf den Grundstrom dienen die Eliassen-Palm-Flüsse (EP-Flüsse) und ihre Divergenz. Der EP-Fluss $\boldsymbol{F}$ ist definiert als

$$F = \begin{pmatrix} F_y \\ F_z \end{pmatrix} = \begin{pmatrix} -\rho\,\overline{u^* v^*} \\ \rho f_0 \dfrac{\overline{v^* \theta^*}}{\dfrac{\partial \theta_0}{\partial z}} \end{pmatrix} \tag{1}$$

mit den Komponenten F_y und F_z nach Osten bzw. oben, ρ als Dichte, $\overline{v^* \theta^*}$ als zonal gemittelter meridionaler Wärmefluss, $\overline{v^* u^*}$ als Impulsfluss und f_0 als dem Coriolisparameter (Bleßmann 2010). $\boldsymbol{F}$ beschreibt den Einfluss von atmosphärischen Störungen auf den Grundstrom, die durch die Wellen verursachten Wärme- und Impulsflüsse. Er besteht aus zwei Vektorkomponenten, anschaulich betrachtet aus der vertikalen und der meridionalen Ausbreitung der Wellen. Die Divergenz des EP-Flusses steht somit für das Entstehen und Brechen von Wellen. Der EP-Fluss in 100 hPa gilt als Maß für die vertikale Ausbreitung von troposphärischen planetaren Wellen in der Stratosphäre (Bleßmann 2010).

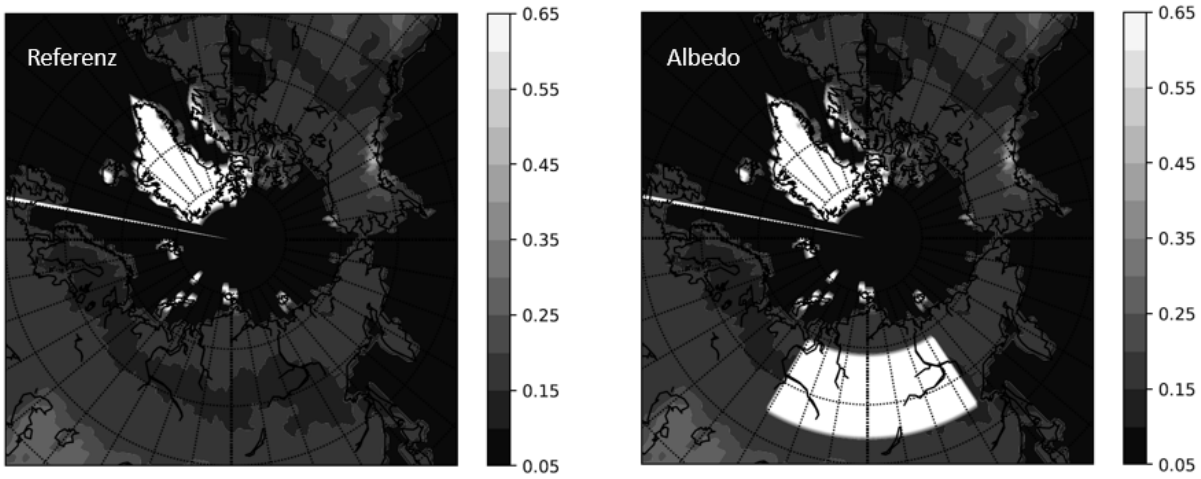

Abb. 1 Darstellung der Albedo im Referenzlauf (links) und im Albedolauf (rechts).

In diesem Versuchslauf wurde die Albedo im Bereich Sibiriens auf 0.80 erhöht (Abb. 1), wodurch eine zugenommene Schneebedeckung angenommen wird. Die Änderung erfolgte von 70° bis 133° östliche Länge und von 55° bis 68° nördliche Breite. Die Modellierung lief über den Zeitraum 01.01.1979 bis 01.01.1985, wobei das Jahr 1979 zum Start und als Spin-up des Modells dient. Für die Auswertung wurden die Jahre 1980-1984 betrachtet.

Aus diesen Vorbetrachtungen ergeben sich nun folgende Thesen, die durch den Experimentierlauf überprüft werden sollen:

1. Die EP-Flüsse müssten durch den höheren Temperaturgradienten in den Wintermonaten Dezember, Januar, Februar (DJF) weiter in die Stratosphäre reichen.
2. Dementsprechend nehmen die Wellenamplituden in der Stratosphäre zu.
3. Da sich durch die planetaren Wellen wärmere Luftmassen nach Norden strömen, kann es zu einer leichten Erwärmung der Stratosphäre kommen.
4. Damit sich die Wellen weiter in Stratosphäre ausbreiten, müsste der zonale Wind wiederum abnehmen (Charney-Drazin-Kriterium).

3. Ergebnisse

Die EP-Flüsse in Abb. 2 zeigen für das Dezembermittel, dass im Referenzlauf die Ausbreitung der Wellen mit der WZ 1 vertikal weit reichender ist als im Versuchslauf. Zudem zeigt sich in dem Diagramm eine stärkere Ablenkung äquatorwärts im Versuchslauf, wohingegen die Pfeile im Referenzlauf senkrecht nach oben gehen bzw. leichte Tendenz polwärts haben. Die Färbung der Pfeile spiegelt die Amplituden wieder, die in diesem Fall nahezu gleich sind. Hinsichtlich der WZ 2 zeigt sich ein ähnliches Bild in den beiden Läufen, wobei im Versuchslauf eine leicht stärke Wellenaktivität gesehen werden kann. Hinsichtlich des EP-Flusses an der Tropopause ist zu beobachten, dass Wellen mit der WZ 1 in beiden Fällen bis in die Stratosphäre und der WZ 2 bis in die Troposphäre reichen. Insgesamt lässt sich anhand der Amplituden eine leicht höhere Aktivität durch die Albedo-Änderung feststellen.

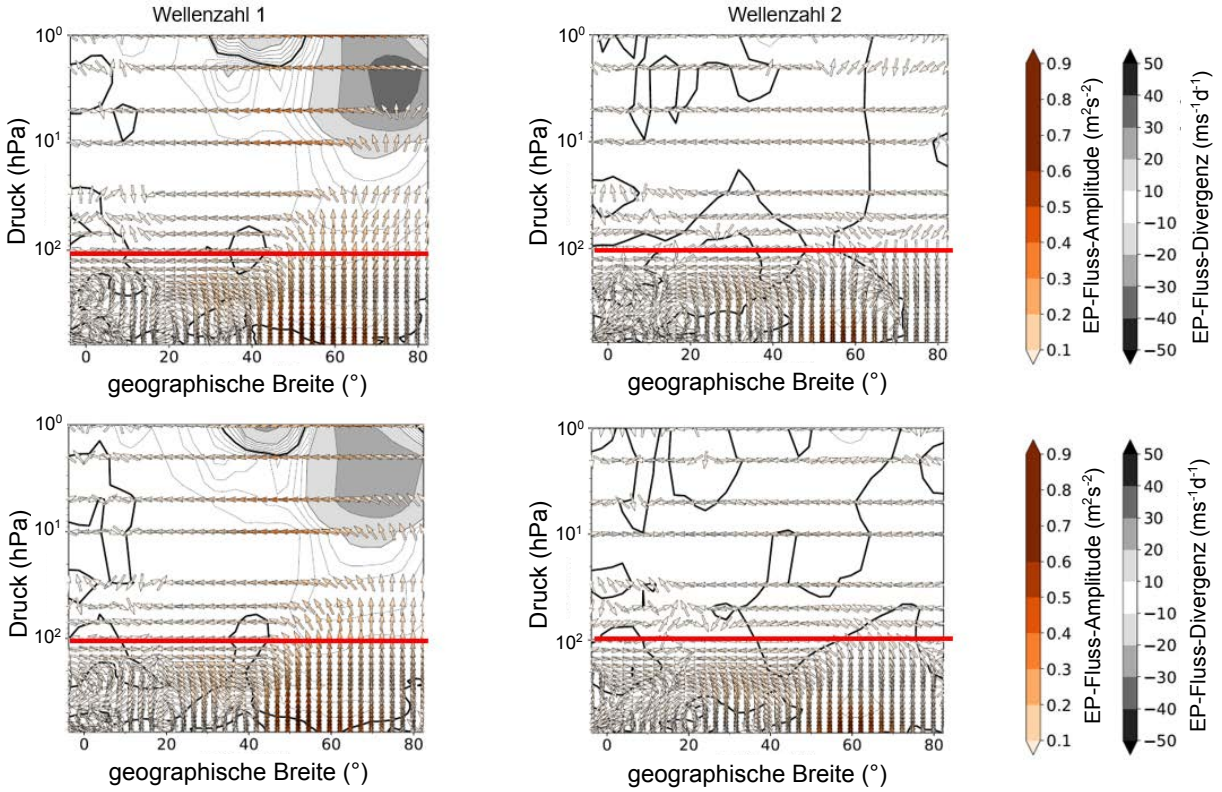

Abb. 2 EP-Flüsse im Referenzlauf (oben) und Versuchslauf (unten) im Dezember über alle Jahre für WZ eins (links) und WZ zwei (rechts). Die rote Linie markiert das 100 hPa Höhenniveau. Orange Farben markieren die EP-Flussamplitude und Schattierungen die EP-Flussdivergenz.

Im Januar ist ein anderer Zustand vorliegend (Abb. 3). Die Ausbreitung der Wellen mit der WZ 1 reichen im Versuchslauf zwar weiter in die Stratosphäre, jedoch sind die Amplituden deutlich geringer. Es zeigt sich zudem im Versuch eine leichte Ablenkung polwärts, während die Ausbreitung im Referenzlauf konsequent äquatorwärts ist. Insgesamt kann so für den Januar eine deutlich geringere Wellenaktivität durch die Albedoerhöhung festgestellt werden.

Das Gegenteil ist im Februar zu beobachten (Abb. 4). Im Versuchslauf ist die Wellenausbreitung weiter in die Stratosphäre reichend und äquatorwärts abgelenkt. Die Amplituden sind ebenfalls deutlich höher. Hier ist auch bei Wellen der WZ 2 eine stärkere Aktivität durch den Versuch zu beobachten, wobei hier eine Ausbreitung bis in die Stratosphäre zu erkennen ist. Somit liegt im Februar eine deutlich höhere Wellenaktivität vor.

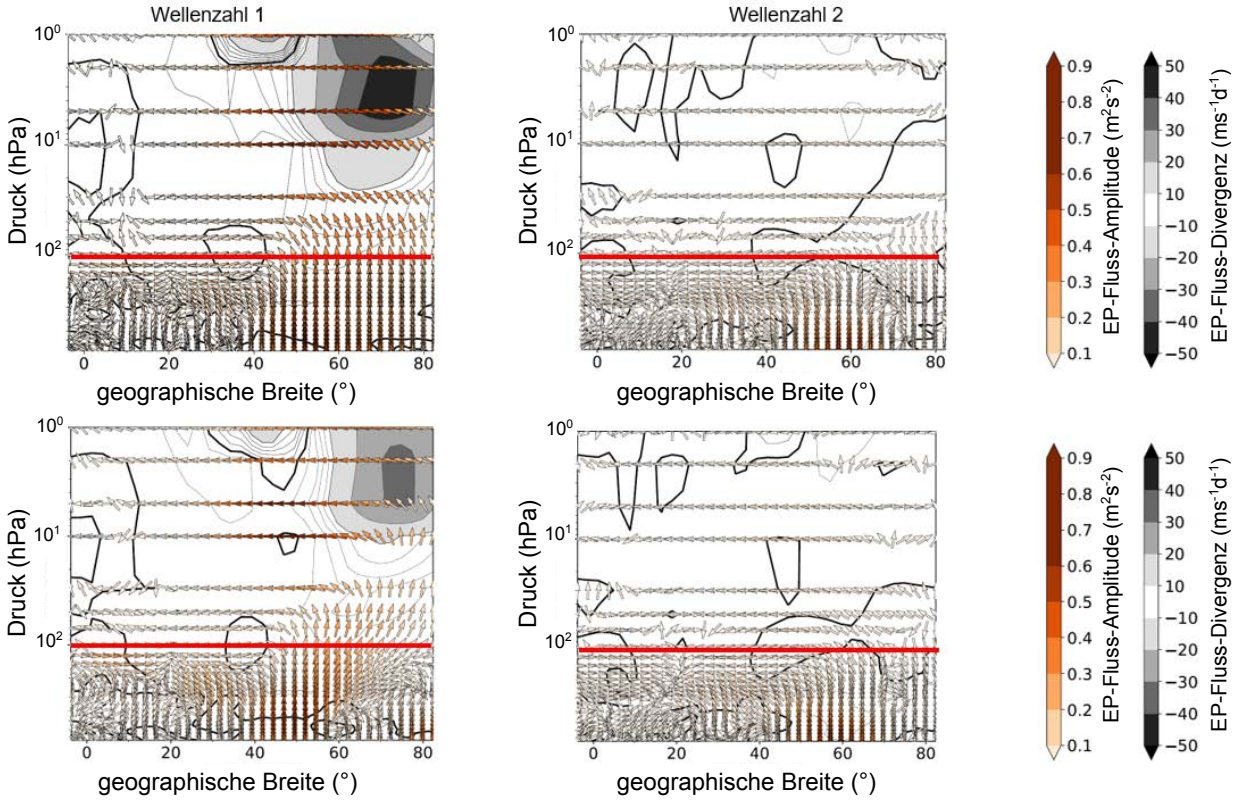

Abb. 3 EP-Flüsse im Referenzlauf (oben) und Versuchslauf (unten) im Januar über alle Jahre für WZ eins (links) und WZ zwei (rechts). Die rote Linie markiert das 100 hPa Höhenniveau. Orange Farben markieren die EP-Flussamplitude und Schattierungen die EP-Flussdivergenz.

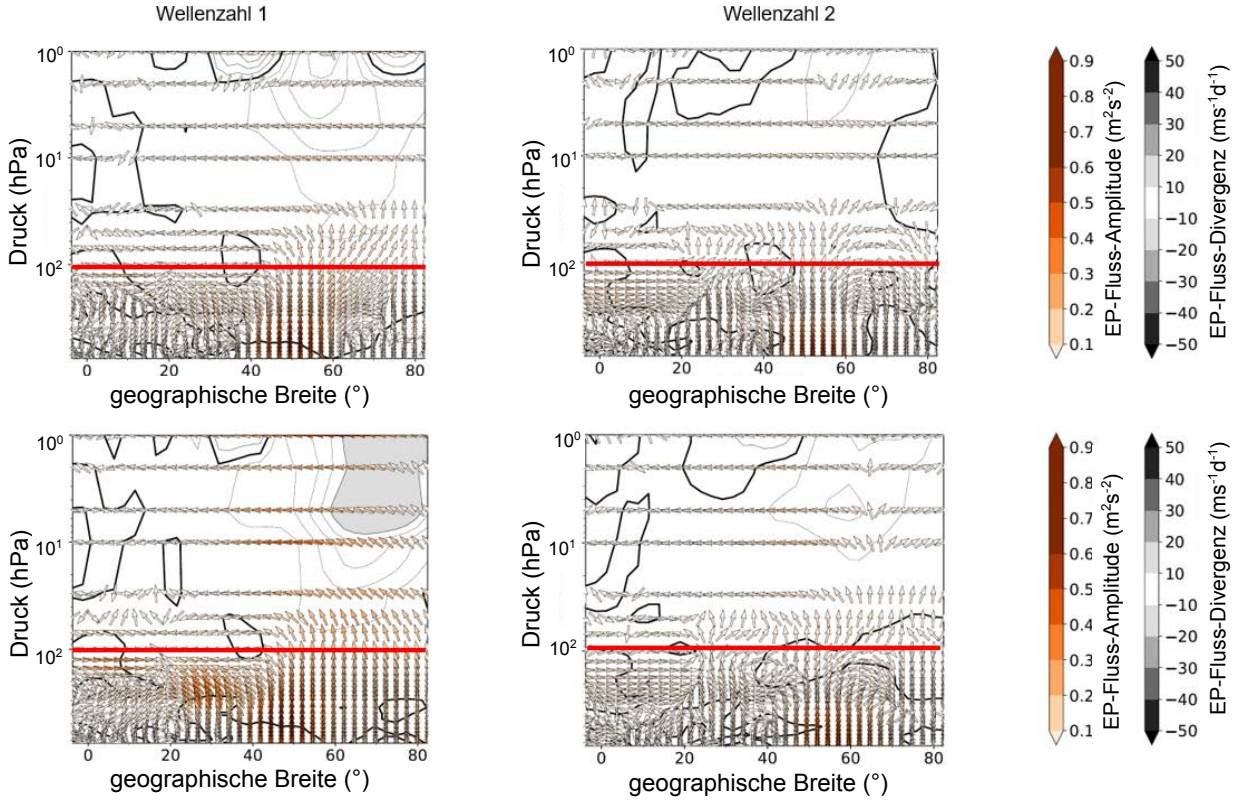

Abb. 4 EP-Flüsse im Referenzlauf (oben) und Versuchslauf (unten) im Februar über alle Jahre für WZ eins (links) und WZ zwei (rechts). Rote Linie und Farben wie Abb.3

Betrachtet man nun mit diesen Erkenntnissen die Amplituden im zonalen Wind und der Temperatur so lassen sich die gleichen Ergebnisse feststellen (Abb. 5). Im Dezember sind die Amplituden vergleichbar. Es zeigen sich im Bereich des Pols lediglich minimal höhere Aktivitäten (2 – 4 m/s) im Versuchslauf beim zonalen Wind. Vergleicht man dazu den reinen zonalen Wind aus den Hintergrundwerten ist dieser im Versuchslauf leicht erhöht. Im Januar ist deutlich eine Abnahme (10 – 12 m/s) durch die erhöhte Albedo in den Wellenamplituden bei beiden Parametern zu beobachten, was für die bereits festgestellte geringere Wellenaktivität spricht. Der zonale Wind nimmt gleichzeitig deutlich zu, was konform mit dem Charney-Drazin-Kriterium ist. Durch den erhöhten zonalen Wind können sich die Wellen nicht mehr so stark ausprägen. Im Februar ist wie zu erwarten das Gegenteil der Fall. Am Pol haben wir eine konsequente Abnahme des zonalen Windes (4 – 6 m/s) im Versuchslauf, wodurch sich die Wellen vertikal weiter ausbreiten können. Dementsprechend sind die Wellenamplituden auch deutlich höher.

4. Zusammenfassung und Diskussion

Die Thesen von Beginn aufgreifend ergeben sich nun folgende Ergebnisse:

1. Die EP-Flüsse müssten durch den höheren Temperaturgradienten in den Wintermonaten Dezember, Januar, Februar (DJF) weiter in die Stratosphäre reichen. Da sich in den Wintermonaten nun deutliche Unterschiede ergeben haben, zeigt sich nun eine Bestätigung für Dezember und Februar. Dahingegen ist die vertikale Ausbreitung im Januar durch die Erhöhung der Albedo nicht erhöht.
2. Dementsprechend nehmen die Wellenamplituden in der Stratosphäre zu. Hier hat sich das gleiche Bild wie unter 1. gezeigt. Im Dezember und Februar sind die Amplituden in der Stratosphäre erhöht (im Februar deutlich höher als im Dezember). Im Januar sind die Amplituden im Versuch geringer.
3. Da sich durch die planetaren Wellen wärmere Luftmassen nach Norden strömen, kann es zu einer leichten Erwärmung der Stratosphäre kommen. In allen drei Wintermonaten konnte dies bestätigt werden. Die Temperatur in der Stratosphäre nimmt minimal zu, wohingegen der Polarwirbel sich weiter abkühlt.
4. Damit sich die Wellen weiter in Stratosphäre ausbreiten, müsste der zonale Wind wiederum abnehmen (Charney-Drazin-Kriterium). Für Januar und Februar trifft das Charney-Drazin-Kriterium zu. Geringere Wellenaktivität im Januar geht einher mit einer Erhöhung des zonalen Windes und anders herum im Februar. Im Dezember liegt eine minimale Zunahme des zonalen Windes vor, wobei die Ausbreitung der Wellen vermindert, dahingegen aber die Amplituden erhöht sind.

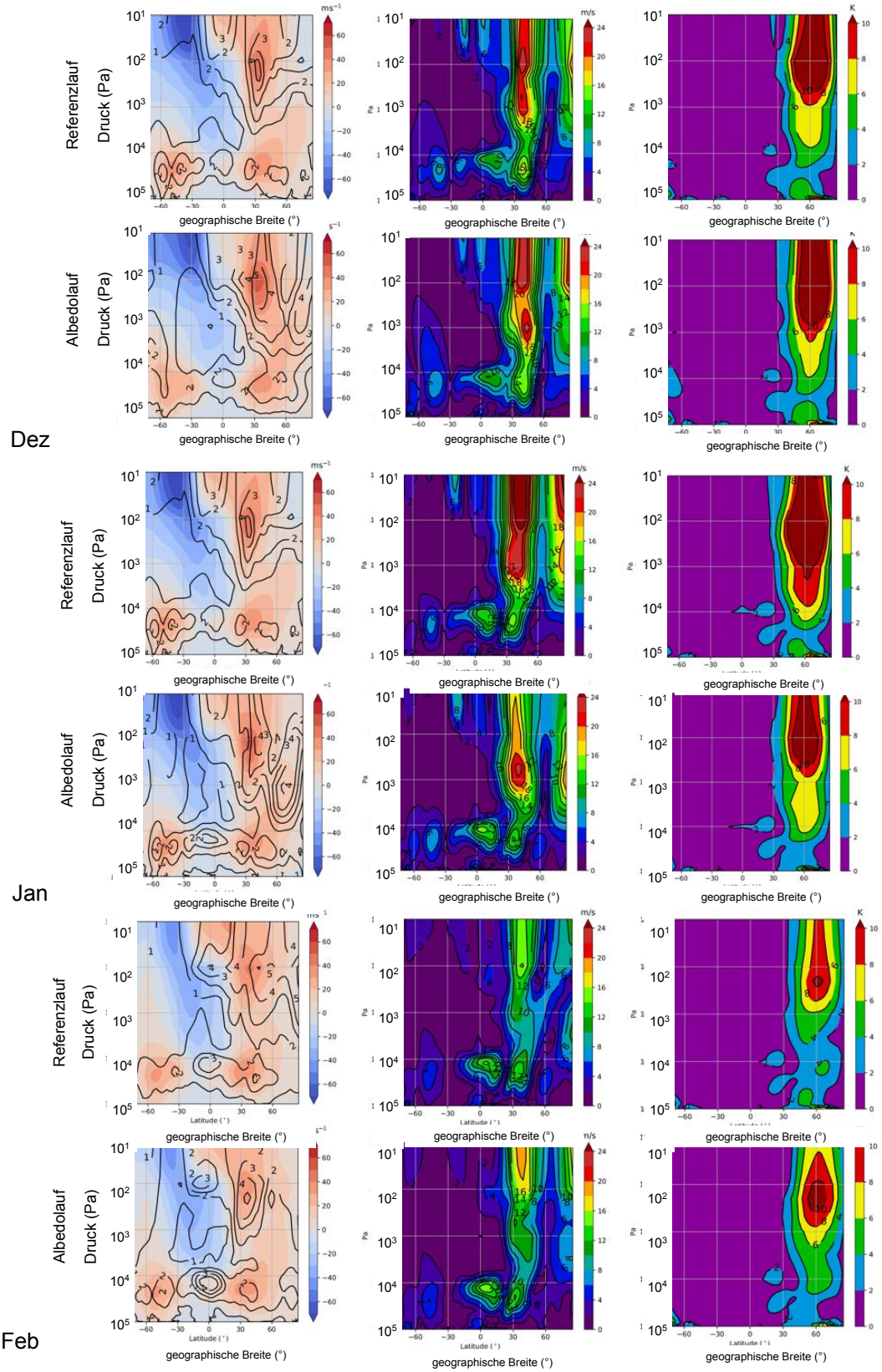

Abb. 5 Mittleren Wellenamplituden des Zonalwindes (Mitte, in m/s) und der Temperatur (rechts, in K), und zeitlich und zonal gemittelten Zonalwind (links, in m/s) für die Monate Dezember, Februar und Januar (von oben nach unten).

Generell lässt sich feststellen, dass die Ablenkung äquatorwärts grundlegend zu gering ist (Abb. 2, 3, 4). Die Auslenkung sollte sich mehr Richtung Äquator ausbilden, da dort der Hintergrundwind geringer ist und somit eine bessere Ausbreitung möglich ist. Eine direkt senkrechte Ausbreitung bzw. polwärts gerichtete Ausbreitung sollte nicht auftreten, da wie durch das Charney-Drazin-Kriterium bereits ausgesagt, der zonale Wind bei entsprechender Stärke eine Ausbreitung verhindert. Weiterhin ist der bei 10 hPa befindliche Polarnachtjet nicht in den Diagrammen des Zonalwindes abgebildet. Dieser müsste sein Maximum bei etwa 10 hPa und mindestens 20 m/s haben. Damit ist auch die fälschlicherweise senkrechte Ausbreitung der Wellen zu erklären.

Betrachtet man die Temperaturen, so kann man im Allgemeinen sagen, dass der Polarwirbel zu warm dargestellt ist (Abb. 6). Er sollte bei 10 hPa etwa 195 K haben, die Stratosphäre im Modell ist allerdings allgemein zu warm. Das Minimum an der Tropopause am Äquator und auch die folgende Temperaturzunahme in der vertikalen Betrachtung entsprechen dem tatsächlichen Verlauf. Am Pol allerdings sollte es über der Tropopause nicht direkt wärmer werden. Dadurch ist um den Nordpol der Polarwirbel nicht stark genug dargestellt, woraus sich auch Fehler in der Modellierung ergeben können. Außerdem kann man bei dem Versuch davon ausgehen, dass Unterschiede zwischen den Jahren durch interne Variabilität des Modells oder vielleicht solaren Zyklen auftreten. Auch wenn die Standardabweichung nur geringe Schwankungen suggeriert, kann in vereinzelten Jahren sich ein anderes Bild ergeben. Daher wäre es sinnvoll auch die einzelnen Jahre zu betrachten.

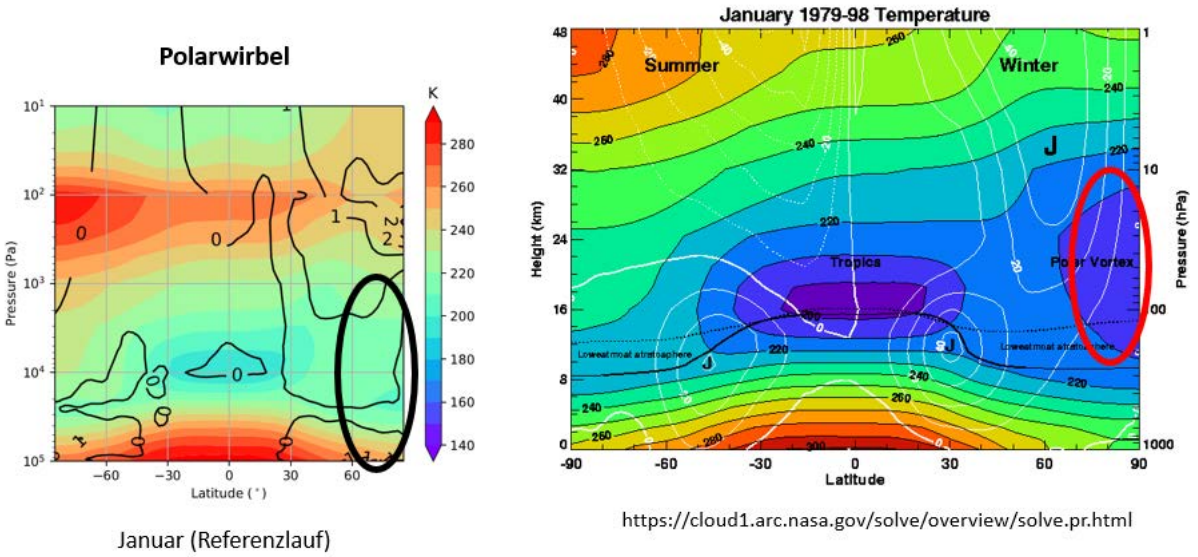

Abb. 6 Vergleich des Temperaturverlaufes im Referenzexperiment und der in Realität vorzufindenden Temperatur im Bereich des Polarwirbels.

Insgesamt lässt sich der Versuch mit dem ICON gut darstellen, jedoch sind vereinzelt Fehlerquelle erkannt worden, die schon an den Ausgangsbedingungen des Modells liegen.

Die verstärkte Kopplung zwischen Troposphäre und Stratosphäre bei erhöhter Schneebedeckung konnte auch in Sensitivitätsstudien mit dem ARPEGE-Climate Modell bestätigt werden (Peings et al., 2012).

Literatur

Bleßmann, D. 2010: Der Einfluss der Dynamik auf die stratosphärische Ozonvariabilität über der Arktis im Frühwinter, Diss., Universität Potsdam, https://publishup.uni-potsdam.de/opus4-ubp/frontdoor/deliver/index/docId/4934/file/ blessmann_diss.pdf (13.05.2019)

Cohen, J., Screen, J. A., Furtado, J. C., Barlow, M., Whittleston, D., Coumou, D., Francis, J., Dethlo, K., Entekhabi, D., Overland, J. and Jones, J., 2014: Recent Arctic amplication and extreme mid-latitude weather, Nature Geoscience, 7, 627, https://doi:10.1038/ngeo223410.1038/ngeo2234

Crueger, T., Giorgetta, M. A., Brokopf, R., Esch, M., Fiedler, S., Hohenegger, C., Kornblueh, L., Mauritsen, T., Nam, C., Naumann, A. K., Peters, K., Rast, S., Roeckner, E., Sakradzija, M., Schmidt, H., Vial, J., Vogel, R., and Stevens, B., 2018: ICON-A, The Atmosphere Component of the ICON Earth System Model: II. Model Evaluation, Journal of Advances in Modeling Earth Systems, 10, 1638-1662, https:// doi: 10.1029/2017MS001233

Giorgetta, M. A., Brokopf, R., Crueger, T., Esch, M., Fiedler, S., Helmert, J., Hohenegger, C., Kornblueh, L., Köhler, M., Manzini, E., Mauritsen, T., Nam, C., Raddatz, T., Rast, S., Reinert, D., Sakradzija, M., Schmidt, H., Schneck, R., Schnur, R., Silvers, L., Wan, H., Zangl, G., and Stevens, B., 2018: ICON-A, the Atmosphere Component of the ICON Earth System Model: I. Model Description, Journal of Advances in Modeling Earth Systems, 10, 1613-1637, https://doi.org/10.1029/ 2017MS001242, 2018

Peings, Y., D. Saint-Martin, and H. Douville, 2012: A Numerical Sensitivity Study of the Influence of Siberian Snow on the Northern Annular Mode. J. Climate, 25, 592–607, https://doi.org/10.1175/JCLI-D-11-00038.1

SAGE III Ozone Loss and Validation Experiment, SOLVE; NASA, https://cloud1.arc.nasa.gov/solve/overview/solve.pr.html, zuletzt aufgerufen: 24.05.2019.

Stroeve, J. C., Serreze, M. C., Holland, M. M., Kay, J. E., Malanik, J., and Barrett, A. P., 2012: The Arctic's rapidly shrinking sea ice cover: a research synthesis, Climatic Change, 110, 1005–1027, https://doi.org/10.1007/s10584-011-0101-1.

Wendisch, M., Brückner, M., Burrows, J. P., Crewell, S., Dethloff, K., Ebell, K., Lüpkes, Ch., Macke, A., Notholt, J., Quaas, J., Rinke, A., und Tegen, I., 2017: Understanding causes and effects of rapid warming in the Arctic, Eos, 98, https://doi.org/10.1029/2017EO064803

Forschungsbericht 2018
Bearbeitete Forschungsprojekte

Institut für Meteorologie

Direktor Prof. Dr. M. Wendisch

Allgemeine Meteorologie; Manfred Wendisch
AG Atmosphärische Strahlung

Koordination des Schwerpunktprogramms 1294 "Atmosphären- und Erdsystemforschung mit dem Forschungsflugzeug HALO (High Altitude and Long Range Research Aircraft)"
HALO coordination project

Schlagworte: flugzeuggetragene Forschung

Projektleiter: M. Wendisch (m.wendisch@uni-leipzig.de)
Professor Dr. Joachim Curtius, Goethe-Universität Frankfurt am Main, Institut für Atmosphäre und Umwelt
Dr.-Ing. Mirko Scheinert, Technische Universität Dresden, Institut für Planetare Geodäsie

Projektmitarbeiter: Gunda Nitzsche, Anja Schwarz, Jörg Schmidt

Projektbeginn: 2010
Projektende: 2019

Beschreibung
Das Projekt dient vornehmlich der Kooperation und der Kommunikation unter den Einzelprojekten des Schwerpunktprogramms. Im Rahmen des Projekts werden ein jährliches Statusseminar sowie jährliche Themen-Workshops geplant und durchgeführt. Die drei Koordinatoren vertreten den SPP gegenüber der DFG, dem Wissenschaftlichen Lenkungsausschuss von HALO (WLA), dem HALO Projektteam des Deutschen Zentrums für Luft- und Raumfahrt (DLR) und nach außen. Das Koordinatoren-Team betreibt Maßnahmen zur Nachwuchs- und Gleichstellungsförderung. Zentrale Initiativen wie gemeinsame Sammelveröffentlichungen in einem Sonderband oder die Durchführung von Sitzungen zu Themenschwerpunkten ("special sessions") bei internationalen Konferenzen sowie der Internetauftritt des SPP werden im Rahmen dieses Projekts koordiniert und durchgeführt.

Description
Funds for the central coordination of SPP 1294 HALO are requested within this proposal. The project serves most of all the promotion of cooperation and communication among the individual scientific projects of the SPP. An annual status seminar as well as topical workshops are organized and conducted within this project. The coordinators represent the SPP via the DFG, the scientific steering committee of HALO (WLA), the HALO project team of the German Aerospace Center (DLR) and the public. The funds for measures to promote gender equality are managed and measures for training of young researchers are coordinated. Within the project special sessions at international conferences or publication of special issues are initiated. An SPP web page is set up and maintained. To support the coordinators in conducting these tasks, staffing for a half-time position of a scientific administrator is applied for.

Mittelgeber: DFG WE 1900/24-1
****

EUFAR2 - European Facility for Airborne Research in Environmental and Geo-sciences

Schlagworte: flugzeuggetragene Forschung

Projektleiter: M. Wendisch (m.wendisch@uni-leipzig.de)
Projektmitarbeiter:

Projektbeginn: 2014
Projektende: 2018

Beschreibung (Deutsch- Pflicht; <2000 Zeichen)
Im Rahmen dieses Projektes werden die Expert Working Groups koordiniert. Workshops werden organisiert, und ein Buch wurde geschrieben:
Wendisch, M., and J.-L. Brenguier (Eds.), 2013: Airborne Measurements for Environmental Research: Methods and Instruments. Wiley-VCH Verlag GmbH & Co. KGaA, Weinheim, Germany. ISBN: 978-3-527-40996-9. 655 pp., doi:10.1002/9783527653218.

Description
Within the project Expert Working Groups were coordinated. Workshops were organized with the aim to publish a book reviewing airborne atmospheric measurement methods.
Weiterführung: nein

Mittelgeber: EU

Flugzeuggetragene spektrale solare Strahlungsmessungen während ACRIDICON zur Untersuchung hochreichender Konvektion und Validierung satellitengetragener Fernerkundungssysteme.
Airborne spectral solar radiation measurements during ACRIDICON to investigate deep convection and validate space borne remote sensing.

Schlagworte: flugzeuggetragene Fernerkundung, Satellitenvalidierung, hochreichende Konvektion.

Projektleiter: M. Wendisch (m.wendisch@uni-leipzig.de)

Projektmitarbeiter: Trismono Candra Krisna

Projektbeginn: 2014
Projektende: 2018

Beschreibung
Innerhalb des ACRIDICON Projektes wurden flugzeuggetragene solare Strahlungsmessungen an Bord des Forschungsflugzeuges HALO durchgeführt. Die Messungen fanden in Brasilien im tropischen Regenwald statt und hatten das Ziel hochreichende konvektive Bewölkung zu

untersuchen. Die spektralen Messungen sollen für zwei Ziele verwendet werden. In einem ersten Schritt sollen kalibrierte Strahldichtemessungen des SMART-Albedometers genutzt werden, um die Genauigkeit von Satellitenmessungen zu quantifizieren. Im zweiten Schritt werden die Daten verwendet, um Wolkeneigenschaften abzuleiten. Ein Vergleich der Ergebnisse mit den vom Satelliten abgeleiteten Wolkenparametern soll dazu dienen, die Unsicherheiten in den Satellitenmessungen zu bestimmen. Die Möglichkeiten zur Verbesserung der Ableitungsalgorithmen durch die Nutzung der vollen spektralen Information soll untersucht werden. Die abgeleiteten Wolkenparameter sollen über statistische Verfahren genutzt werden, um den Strahlungseinfluss der Wolken im Verlaufe ihres Lebenszyklus zu verfolgen.

Mittelgeber: DAAD

Einfluss der Eisphase auf den Strahlungsantrieb von Wolken: Messungen und Representation in numerischen Wettervorhersagemodellen
Influence of ice phase on radiative forcing of clouds: Observations and representation in numerical weather prediction models

Schlagworte: flugzeuggetragene Messungen, Wolken, Strahlungsantrieb, Eisphase

Projektleiter: M. Wendisch (m.wendisch@uni-leipzig.de)

Projektmitarbeiter: Kevin Wolf

Projektbeginn: 2016
Projektende: 2019

Beschreibung
Methoden der flugzeuggetragenen passiven Fernerkundung mit Hilfe spektraler, solarer und reflektierter Strahldichten werden zur Ableitung der thermodynamischen Phase, der optischen Dicke und des Partikeleffektivradius von Wolken während der HALO Missionen NARVAL-II und NAWDEX angewendet. Insbesondere werden die horizontalen und vertikalen Verteilungen der thermodynamischen Phasen in unterschiedlichen Wolkentypen untersucht. Die Kombination mit anderen HALO-Fernerkundungsinstrumenten einschließlich Radar und Mikrowellensensoren ist geplant. Gleichzeitige Messungen der Wolkenalbedo werden durchgeführt und zur Analyse der Abhängigkeit des Strahlungsantriebs von Wolken-makrophysikalischen und mikrophysikalischen Eigenschaften verwendet. Auf der Basis von breitbandigen und spektralen Strahlungsgrößen dient die gemessene spektrale Wolkenalbedo zur Bewertung von Ergebnissen des ECMWF Integrated Forecast System (IFS). In mehreren Schritten werden 1D und 3D Strahlungstransfermodelle zusammen mit Beobachtungen verwendet, um die Unsicherheiten in der ECMWF-Vorhersage zu identifizieren. Unsicherheiten in Bezug auf das Strahlungsschema und die simulierten Wolkeneigenschaften werden separiert.

Description
The airborne passive solar remote sensing of spectral reflected radiance will be applied to derive cloud thermodynamic phase, optical thickness, and particle effective radius during the HALO Missions NARVAL-II and NAWDEX. In particular, cloud thermodynamic phase and its horizontal and vertical distribution in different cloud types will be investigated. Combination with other remote sensing instruments of HALO including active radar and passive microwave sensors is

planned. Simultaneous measurements of cloud top albedo will be derived and used to analyse the dependence of cloud radiative forcing on cloud macrophysical and microphysical properties. Measured spectral cloud top albedo will be employed to evaluate the ECMWF Integrated Forecast System (IFS) on the basis of broadband and spectral radiative quantities. In different steps, 1D and 3D radiative transfer models will be utilized in combination with the observations to identify and quantify uncertainties in IFS forecasts and analysis fields. Uncertainties due to the radiations scheme and simulated cloud properties will be separated.

Mittelgeber: DFG, SPP 1294

Hochaufgelöste Messungen von Turbulenz, Wolkenmikrophysik, und Strahlungsabkühlungsraten in der Einmischungszwischenschicht von marinen Stratocumulus-Wolken.
High resolved measurements of turbulence, cloud microphysical properties and radiative cooling rates in the entrainment zone of marine strato cumulus.

Schlagworte: hubschraubergetragene Messungen, Stratocumulus, Energiebilanz, Strahlungsabkühlung.

Projektleiter: M. Wendisch (m.wendisch@uni-leipzig.de)
Dr. Holger Siebert, Leibniz-Institut für Troposphärenforschung e.V. (TROPOS)

Projektmitarbeiter: Felix Lauermann

Projektbeginn: 2015
Projektende: 2018

Beschreibung
Obwohl bisher schon viele Fortschritte im allgemeinen Verständnis von Mischungs- und Strahlungsprozessen in Stratocumulus (Sc) gemacht wurden, verursachen wolkenbedingte Rückkopplungseffekte von Sc Wolken erhebliche Unsicherheiten in Klimaprojektionen. Diese Probleme werden teilweise verursacht durch eine unrealistische Beschreibung der feinskaligen Mischungsprozesse, die hauptsächlich am Oberrand der Wolken stattfinden. Die Strahlungs-Abkühlung am Wolkenoberrand ist eng mit dynamischen und turbulenten Wolkenprozessen verbunden. Abkühlung am Oberrand der Wolken verursacht ein Absinken. Diese Vertikalbewegungen bedingen Turbulenzen wodurch trockene und warme Umgebungsluft in die Wolke eingemischt wird, so dass sich die damit verbundene Verdunstungsabkühlung erhöht. Zur Untersuchung dieser Vorgänge schlagen wir folgende wesentlichen Projektziele vor: (a) die Verbesserung des Verständnisses der feinskaligen Struktur der Einmischungsinversionszwischenschicht (entrainment interface layer, EIL), (b) die Quantifizierung des Einflusses der EIL auf die Einmischung trockener und warmer Umgebungsluft in Sc Wolken, (c) die Bewertung der Rolle von Strahlungserwärmungs- und Abkühlungsraten bei Einmischungsprozessen in Sc Wolken. Um diese Ziele erreichen zu können, werden Beobachtungen mit den zwei kombinierten, hubschraubergetragenen Messsystemen ACTOS (Airborne Cloud Turbulence Observation System) und SMART--HELIOS (Spectral Modular Airborne Radiation measurement sysTem) vorgeschlagen. Die Messungen finden auf den Azoren statt. Beide Messsysteme werden durch einen langsam fliegenden Hubschrauber getragen. Das kombinierte Messsysteme-Paket ermöglicht in-situ Messungen von dynamischen,

thermodynamischen, Wolken-mikrophysikalischen und Strahlungsparametern mit hoher örtlicher Auflösung (überwiegend im cm-Bereich). Kein anderes Messsystem weltweit erreicht diese hohe Auflösung, die allerdings unabdingbar ist für die Erreichung der Projektziele ist. Dies trifft insbesondere auf die Vermessung der Vorgänge in der EIL zu, welche meist eine vertikale Dicke von nur 10 m aufweist.

Mittelgeber: DFG, WE 1900/33-1

STRATOCLIM - Stratospheric and upper tropospheric processes for better climate predictions

Schlagworte: flugzeuggetragene Forschung

Projektleiter: M. Wendisch (m.wendisch@uni-leipzig.de)
Projektmitarbeiter: Tim Carlsen

Projektbeginn: 2013
Projektende: 2018

Beschreibung (Deutsch- Pflicht; <2000 Zeichen)
STRATOCLIM wird verlässlichere Vorhersagen von Klimaänderungen und stratosphärischer Ozonverteilung erreichen, durch eine Verbesserung des Systemverständnisses von wichtigen Prozessen in der oberen Troposphäre und unteren Stratosphäre. Unsere Gruppe ist mit Modellberechnungen zur Bestimmung von Erwärmungs- und Abkühlungsraten in der Tropopausenregion beteiligt.

Description
StratoClim will produce more reliable projections of climate change and stratospheric ozone by a better understanding and improved representation of key processes in the Upper Troposphere and Stratosphere (UTS). This will be achieved by an integrated approach bridging observations from dedicated field activities, process modelling on all scales, and global modelling with a suite of chemistry climate models (CCMs) and Earth system models (ESMs). At present, complex interactions and feedbacks are inadequately represented in global models with respect to natural and anthropogenic emissions of greenhouse gases, aerosol precursors and other important trace gases, the atmospheric dynamics affecting transport into and through the UTS, and chemical and microphysical processes governing the chemistry and the radiative properties of the UTS. StratoClim will (a) improve the understanding of the microphysical, chemical and dynamical processes that determine the composition of the UTS, such as the formation, loss and redistribution of aerosol, ozone and water vapour, and how these processes will be affected by climate change; (b) implement these processes and fully include the interactive feedback from UTS ozone and aerosol on surface climate in CCMs and ESMs. Through StratoClim new measurements will be obtained in key regions:

(1) in a tropical campaign with a high altitude research aircraft carrying an innovative and comprehensive payload,
(2) by a new tropical station for unprecedented ground and sonde measurements, and
(3) through newly developed satellite data products.

The improved climate models will be used to make more robust and accurate predictions of surface climate and stratospheric ozone, both with a view to the protection of life on Earth. Socioeconomic implications will be assessed and policy relevant information will be communicated to policy makers and the public through a dedicated office for communication, stakeholder contact and international co-operation.

Mittelgeber: EU

SFB/Transregio 172 „Arktische Verstärkung“
Zentrale Dienstleistungen, Verwaltung und Koordinierung (Z01)
Central services, administration and coordination (Z01)

Schlagworte: Arktis.

Projektleiter:
M. Wendisch (m.wendisch@uni-leipzig.de)
Prof. Dr. Susanne Crewell, Universität zu Köln, Institut für Geophysik und Meteorologie
Prof. Dr. Justus Notholt, Universität Bremen, Institut für Umweltphysik

Projektmitarbeiter: Dr. Marlen Brückner, Dr. Christa Engler

Projektbeginn: 2016
Projektende: 2019

Beschreibung (Deutsch- Pflicht; <2000 Zeichen)
Innerhalb des TR 172 Antrages werden Mittel für die zentrale Koordinierung beantragt. Dieses Teilprojekt dient dazu, die Kooperationen und Kommunikation im Verbund unter den einzelnen wissenschaftlichen Projekten und Clustern zu fördern. Aus diesem Grund werden monatliche Videokonferenzen, halbjährliche Meetings, jährliche wissenschaftliche Konferenzen, als auch spezielle Workshops organisiert und durchgeführt. Die Mittel für Gleichstellungsmaßnahmen werden dazu verwendet um junge Wissenschaftler/innen in Zusammenarbeit mit lokalen Graduiertenschulen zu trainieren. Die internationale Präsenz des TR 172 wird etabliert. Eine Internetseite wird erstellt und implementiert. Die logistische Organisation und wissenschaftliche Planung von intensiven Messkampagnen innerhalb des TR 172 werden durch das Projekt Z01 unterstützt. Öffentlichkeitsarbeit zwischen den verschiedenen Partnern wird organisiert und koordiniert.

Description
Funds for the central coordination of TR 172 are requested within this proposal. The project serves the promotion of cooperation and communication among the individual scientific projects and clusters. Monthly video conferences, biannual general assemblies, annual scientific conferences, as well as topical workshops will be organized and conducted. The funds for measures to promote gender equality are managed the training of young researchers is coordinated, in collaboration with local graduate schools. The international visibility of TR 172 will be fostered. A web page will be set up and maintained. The logistic organization and scientific planning of the extensive observational campaigns within TR 172 will be supported by project Z01. Public outreach activities will be organized and coordinated between the different partners.

Mittelgeber: DFG, TRR 172

SFB/Transregio 172 „Arktische Verstärkung“
Fesselballongetragene Messungen des Energiebudgets in der wolkenbedeckten Zentralarktis (A02)
Tethered balloon-borne energy budget measurements in the cloudy central Arctic (A02)

Schlagworte: Arktis, ballongetragene Messungen, Energiebilanz, Strahlungsabkühlung.

Projektleiter: M. Wendisch (m.wendisch@uni-leipzig.de)
Dr. Holger Siebert, Leibniz-Institut für Troposphärenforschung e.V. (TROPOS)

Projektmitarbeiter: Matthias Gottschalk

Projektbeginn: 2016
Projektende: 2019

Beschreibung
Während der Forschungsfahrt von FS Polarstern im Frühsommer (Mai bis Juni) 2017 werden Fesselballon-getragene Messungen von einer Eisschollenstation analysiert. Atmosphärische Vertikalprofile (bis zu einem Kilometer Höhe) der turbulenten Energieflüsse (sensible und latente Wärme), Strahlungsenergieflüsse und turbulente Impulserhaltung werden gemessen. Die Beobachtungen werden den Einfluss von makrophysikalischen (Wolkenbasishöhe, Temperatur, geometrische Dicke, Wolkenbedeckung) und mikrophysikalischen (effektiver Tropfenradius) Eigenschaften von arktischen tiefen Wolken auf (i) die Profile der Flüsse, (ii) den entsprechenden Strahlungsantrieb und (iii) die damit verbundenen netto Erwärmung/Abkühlung der bodennahen Lufttemperatur untersuchen.

Description
Tethered balloon-borne measurements from an ice-floe camp during the cruise of RV Polarstern in early summer (May to June) 2017 will be analysed. Atmospheric vertical profiles (up to one-kilometer altitude) of turbulent energy fluxes (sensible and latent heat), radiative energy fluxes, and turbulent fluxes of momentum will be measured. The observations will investigate the influence of macrophysical (cloud base height and temperature and geometric thickness, cloud cover) and microphysical (effective radius) properties of Arctic low--level clouds on (i) the profiles of fluxes, (ii) the respective radiative forcing, and (iii) the related net warming/cooling of the near-surface air temperature.

Mittelgeber: DFG, TRR 172

SFB/Transregio 172 „Arktische Verstärkung“
Einfluss von tiefen Wolken auf die arktische atmosphärische Grenzschichtturbulenz und -Strahlung (A03)
Impact of low-level clouds on Arctic atmospheric boundary layer turbulence and radiation (A03)

Schlagworte: Arktis, flugzeuggetragene Messungen, Energiebilanz, Strahlungsabkühlung.

Projektleiter: M. Wendisch (m.wendisch@uni-leipzig.de)

Dr. Christof Lüpkes, Alfred-Wegener-Institut Helmholtz-Zentrum für Polar- und Meeresforschung

Projektmitarbeiter: Johannes Stapf

Projektbeginn: 2016
Projektende: 2019

Beschreibung (Deutsch- Pflicht; <2000 Zeichen)
Vertikalprofile von Strahlungsenergie- und Turbulenzenergieflüssen sowie Impulserhaltung werden untersucht durch (i) Verwendung vorheriger Schiffs- und Flugzeugkampagnen und (ii) durch die Analyse neuer Messungen von zwei geplanten Flugzeugkampagnen über dem Arktischen Ozean. Die beiden neuen Kampagnen beziehen die AWI Forschungsflugzeuge Polar 5 & 6 ein, um die vertikalen Flussprofile als Funktion von Wolken- und Meereisbedeckung unter verschiedenen synoptischen Bedingungen zu messen. Die Flugzeugbeobachtungen sind für Mai/Juni 2017 und März 2019 geplant und decken somit Zeiträume starker (Spätwinter) und schwacher (Frühsommer) arktischer Verstärkung ab.

Description
Tethered balloon-borne measurements from an ice-floe camp during the cruise of RV Polarstern in early summer (May to June) 2017 will be analysed. Atmospheric vertical profiles (up to one-kilometer altitude) of turbulent energy fluxes (sensible and latent heat), radiative energy fluxes, and turbulent fluxes of momentum will be measured. The observations will investigate the influence of macrophysical (cloud base height and temperature and geometric thickness, cloud cover) and microphysical (effective radius) properties of Arctic low--level clouds on (i) the profiles of fluxes, (ii) the respective radiative forcing, and (iii) the related net warming/cooling of the near-surface air temperature.

Mittelgeber: DFG, TRR 172

SFB/Transregio 172 „Arktische Verstärkung“
Einfluss von Bodenheterogenität auf den Strahlungsantrieb und Ableitung von Aerosol- und Wolkeneigenschaften in der Arktis (C01)
Influence of surface heterogeneity on radiative forcing and retrieval of aerosol and cloud properties in the Arctic (C01)

Schlagworte: Arktis, flugzeuggetragene Messungen, Eis- und Schneealbedo, BRDF

Projektleiter: M. Wendisch (m.wendisch@uni-leipzig.de)
Dr. Georg Heygster , Universität Bremen, Institut für Umweltphysik (IUP)

Projektmitarbeiter: Dr. Evelyn Jäkel
Projektbeginn: 2016
Projektende: 2019

Beschreibung
Für die Arktis ist ein diskontinuierlicher Albedo Unterschied zwischen hoch reflektierenden Schnee/Eisoberfächen und meist stark absorbierenden Meeresoberflächen typisch. In diesem Teilprojekt wird quantifiziert, inwiefern diese Heterogenität der Reflektionseigenschaften der

Erdoberfläche (i) den Strahlungsantrieb von Wolken (Erwärmung/Abkühlung) und (ii) die Fernerkundungsprodukte von Wolken und Aerosolpartikeln beeinflussen. Aus diesem Grund werden flugzeuggetragene Messungen und Strahlungstransfermodellierungen vorgeschlagen.

Description
In the Arctic, a discontinuous albedo contrast between highly reflecting snow/ice and mostly absorbing sea surfaces is typical. In this project it will be quantified how these affect (i) the radiative forcing of clouds (warming/cooling), and (ii) the remote sensing products of clouds and aerosol particles. For this purpose, airborne measurements and Radiative Transfer modelling studies are proposed.

Mittelgeber: DFG, TRR 172

SFB/Transregio 172 „Arktische Verstärkung“
Charakterisierung von arktischen Mischphasenwolken durch flugzeuggetragene in-situ Messungen und Fernerkundung (B03)
Characterization of Arctic mixed-phase clouds by airborne in-situ measurements and remote sensing (B03)

Schlagworte: Arktis, flugzeuggetragene Messungen, Mischphasenwolken.

Projektleiter: Dr. André Ehrlich (a.ehrlich@uni-leipzig.de)
Professor Dr. Susanne Crewell, Universität zu Köln, Institut für Geophysik und Meteorologie
Professor Dr. Andreas Macke, Leibniz-Institut für Troposphärenforschung e.V. (TROPOS)

Projektmitarbeiter: Elena Ruiz
Projektbeginn: 2016

Projektende: 2019

Beschreibung
Dieses Teilprojekt schlägt neuartige Beobachtungsstrategien für arktische Wolken vor durch Kombination von flugzeuggetragenen Fernerkundungsmethoden mit in-situ mikrophysikalischen Messungen von Wolken- und Aerosoleigenschaften. Unter der Verwendung von zwei nebeneinanderfliegenden Flugzeugen (Polar 5 & 6) wird es möglich sein die mikrophysikalischen Partikeleigenschaften innerhalb von Wolken gleichzeitig durch in-situ Sensoren zu messen. Ebenfalls werden die vertikale Säule und deren Strahlungseinfluss mittels Fernerkundungsmessungen oberhalb von Wolken gemessen. Beide Kampagnen werden im Sommer 2017 (ACLOUD, Svalbard) und Frühling 2019 (AFLUX, Svalbard und Grönland) durchgeführt, um typische arktische Grenzschichtwolken als Teil der hauptsächlichen experimentellen Aktivitäten innerhalb des TR 172 zu untersuchen.

Description
The project proposes novel observation strategies for Arctic clouds by combining airborne remote sensing with in-situ microphysical measurements of cloud and aerosol properties. Using two identical collocated aircraft, Polar 5 and 6, it will be possible to simultaneously measure the microphysical particle characteristics within clouds by in-situ sensors and probe the vertical column and radiative impact from remote sensing measurements above clouds. Two campaigns

will be performed in summer 2017 (ACLOUD, Svalbard) and spring 2019 (AFLUX, Svalbard and Greenland) to investigate typical Arctic boundary layer clouds as part of the major experimental activities of the TR 172.

Mittelgeber: DFG, TRR 172

SFB/Transregio 172 „Arktische Verstärkung“
Wechselwirkungen von Schnee auf Meereis mit atmosphärischen Bestandteilen inklusive Ruß (C02)
Interactions of snow on sea ice with atmospheric constituents including black carbon (C02)

Schlagworte: Arktis, flugzeuggetragene Messungen, Black Carbon, Eis und Schneealbedo

Projektleiter: Dr. André Ehrlich (a.ehrlich@uni-leipzig.de)
Dr. Rüdiger Gerdes, Alfred-Wegener-Institut Helmholtz-Zentrum für Polar- und Meeresforschung

Projektmitarbeiter: Tobias Donth

Projektbeginn: 2016
Projektende: 2019

Beschreibung
Gleichzeitige Beobachtungen von atmosphärischem Ruß und Rußpartikeln in Schnee- und Bodeneigenschaften sind selten. Daher wird dieses Teilprojekt flugzeug- und bodengebundene Beobachtungen von Aerosolen und Rußkonzentrationen kombinieren, sowie optische Schneeeigenschaften und deren Rückkopplungsmechanismen in der arktischen Region untersuchen. In-situ Messungen von atmosphärischen Rußpartikeln (boden- und flugzeuggetragen) in Verbindung mit Rußpartikeln in Schneeproben und Fernerkundungsbeobachtungen von Schneeeigenschaften werden zusammengefügt.

Description
Concurrent observations of atmospheric Black Carbon (BC), and BC in snow and surface properties are rare. Hence, this project will combine airborne and ground-based observations of aerosols and BC concentrations and snow optical properties to investigate their feedback mechanisms in Arctic regions. In-situ measurements of atmospheric BC (ground-based and airborne) along with sampling of BC in snow and remote sensing observations of snow properties will be merged.

Mittelgeber: DFG, TRR 172

Entwicklung von tropischer hochreichender Konvektion abgeleitet aus bodengebundenen abbildenden Spektroradiometermessungen
Evolution of tropical deep-convective clouds derived from ground-based imaging spectroradiometer measurements

Schlagworte: Konvektive Wolken, atmosphärische Strahlung, bodengebundene Fernerkundung

Projektleiter: M. Wendisch (m.wendisch@uni-leipzig.de)

Projektmitarbeiter: Kátia Mendes de Barros (katia.mendes_de_barros@uni-leipzig.de)

Projektbeginn: 2017
Projektende: 2020

Beschreibung
Im Rahmen des Projekts soll aus bodengebundenen Wolkenseitenmessungen der reflektierten Strahlung mittels eines abbildenden Spektrometersystems von tropischer hochreichender Konvektion auf das Vertikalprofil der mikrophysikalischen Eigenschaften der Wolke geschlossen werden. Damit soll die vertikale Entwicklung von hochreichender Konvektion, die eine wesentliche klimarelevante Rolle spielt, unter Berücksichtigung des Einflusses von Aerosolpartikeln und von thermodynamischen Bedingungen auf das Tropfenwachstum charakterisiert werden. Die geplanten Messungen sollen auf einem 320 m hohen Messturm (ATTO: Amazonian Tall Tower Observatory), der kürzlich im brasilianischen Regenwald errichtet wurde, stattfinden. ATTO ist mit Messgeräten ausgestattet, die meteorologische, chemische und Aerosolparameter liefern. Die Messregion bietet ideale Beobachtungsbedingungen mit klar definierten Jahreszeiten (Regen- und Trockenzeit), täglicher Konvektion und variablen Aerosolbedingungen. Aus den Messungen eines neuen abbildenden Spektrometersystems, SPIRAS (SPectral Imaging Radiation System) sollen Vertikalprofile der thermodynamischen Phase und der Partikelgröße mit hoher zeitlicher und räumlicher Auflösung und mit Hilfe von adaptierten Verfahren unter Verwendung von dreidimensionalen Strahlungstransportsimulationen abgeleitet werden. Damit sollen vertikale Bereiche, die das Tropfenwachstum beschreiben (Diffusion, Koaleszenz, Mischphasenbereich und Vereisung), identifiziert werden. Zusätzliche Messungen einer Infrarotkamera und eines scannenden Depolarisations-Lidars werden für die Höhen- und Temperaturbestimmung der beobachteten Wolkenelemente herangezogen. Zusätzlich werden die Polarisationsmessungen des Lidars zur Bestimmung der thermodynamischen Phase verwendet, um den wichtigen Phasenübergang zu identifizieren. Mit Hilfe der gewonnenen Daten werden außerdem Annahmen (Effektivradius als konservative Wolkeneigenschaft) wie sie von Ableitungsverfahren zur Bestimmung von mikrophysikalischen Wolkenprofilen aus Satellitenmessungen gemacht werden, überprüft.

Description
Specifically the project will derive the vertical profile of microphysical properties of tropical deep-convective clouds (DCC) from ground-based measurements of reflected radiation from cloud sides by an imaging spectroradiometer system. This general objective is to characterize the vertical evolution of DCCs, which play an important role in the Earths climate system. The evolution will be studied with respect to the impact of aerosol and thermodynamic conditions on the cloud particle growth. The planned measurements will be performed on the new Amazonian Tall Tower Observatory (ATTO), of 320 m height situated in the Amazon Basin near the equator. ATTO is equipped with instruments to measure micrometeorological and atmospheric chemical variables, as well as aerosol properties. It provides ideal observation conditions with clear seasons (wet and dry season), and daily occurrence of DCCs in a highly variable environment with respect to concentrations and types of aerosol particles. The new imaging spectroradiometer system, SPIRAS (SPectral Imaging Radiation System), will be used to derive vertical profiles of thermodynamic phase and cloud effective radius with high temporal and spatial resolution by means of adapted methods based on three-dimensional radiative transfer simulations. In this way vertical zones characterizing the droplet growth (diffusion, coalescence, mixed-phase, and glaciation) will be identified. Auxiliary measurements by an infrared camera and a scanning depolarization Lidar will

be used to estimate the height and the temperature of the observed cloud element. Additionally, polarization measurements by Lidar will support the retrieval of the thermodynamic phase which is important to identify the phase transition. By means of the data obtained we will validate assumptions (effective particle radius as conservative cloud property) of retrieval methods for satellite-based observations to derive microphysical profiles.

Mittelgeber: DFG WE 1900/34-1

Theoretische Meteorologie; Johannes Quaas

AG Wolken und globales Klima

Wolken und Niederschlag im Klimasystem
High Definition Clouds and Precipitation for Climate Prediction (HD(CP)²)

Projektleiter: Johannes Quaas
Projektmitarbeiter: Christine Nam, Ordran Sourdeval, Andreas Foth
Projektbeginn: 01.01.2011
Projektende: 31.12.2019

Beschreibung (Deutsch)
Es werden die Teilprojekte: HD(CP)² - O2 Full-domain observations HD(CP)² - S1 Diagnostics HD(CP)² - S6 PDF cloud schemes bearbeitet. Ziel von HD(CP)² ist es, Parametrisierungen von Wolken- und Niederschlagsprozessen in Klimamodellen zu verbessern, und die Verbesserung der simulierten Wolken-Klima-Feedbacks nachzuweisen. Dazu wird in den Teilprojekten zur Modellierung eine hochaufgelöste (100 m horizontal) Simulation für mehrere Monate über Mitteleuropa vorbereitet, die als Referenz dienen kann. In den Teilprojekten zur Beobachtung werden Datensätze erstellt, die der Evaluierung dieses Modells und der Erstellung oder Verbesserung und Evaluierung von Klimamodellparametrisierungen dienen. In O2 werden konkret Messnetze (Niederschlagsradar, GPS, Ceilometer) und Satellitendaten für flächige Informationen über dem gesamten HD(CP)²-Gebiet aufgearbeitet. In den Teilprojekten zur Synthese wird darauf hingearbeitet, die sehr großen Datenmengen der geplanten Simulation sinnvoll zu verarbeiten. Konkret werden in Teilprojekt S1 Diagnostiken entwickelt, die relevante Metriken online während der Simulation berechnen, so dass kein Herausschreiben von sehr großen Datensätzen und Postprocessing nötig ist. Im Beitrag der Universität Leipzig werden hier Joint-PDFs konstruiert, die für Wolkenparametrisierungen relevant sind. In Teilprojekt S6 wird die Nutzung dieser PDFs für die Evaluierung von Wolkenparametrisierungen in Klimamodellen, die auf Wahrscheinlichkeitsdichtefunktionen (probability density functions, PDFs) der subskaligen Verteilung von der Gesamtwasser-spezifischen Feuchte und ggf. anderen Größen basieren, vorbereitet. Dazu werden Sensitivitätssimulationen mit ECHAM6 mit verschiedenen Wolkenparametrisierungen durchgeführt, und eine Evaluierung auf der Basis der HD(CP)²-Beobachtungen vorgenommen.

Beschreibung (Englisch)
The aim of the project is to improve the understanding of, above all, high definition cloud and precipitation processes and their role in climate change.

Mittelgeber: BMBF Bundesministerium für Bildung und Forschung

Marine Startocumulus Wolkenbedeckung und Klima
Marine Stratocumulus Cloud Cover and Climate

Schlagworte: Stratokumulus, Aerosol-Wolken-Wechselwirkungen

Projektleiter: Koordinator: Tom Goren (tom.goren@uni-leipzig.de)

Projektmitarbeiter: Dr. Tom Goren (tom.goren@uni-leipzig.de)

Projektbeginn: 2016
Projektende: 2018

Beschreibung
Das Projekt untersucht anhand von Satellitendaten und globalen Modellen den Einfluss anthropogener Aerosol-Emissionen auf marine Grenzschichtwolken. Dabei soll insbesondere untersucht werden, ob das Aufbrechen der geschlossenen Wolkendecken in verschmutzten Luftmassen später erfolgt als ohne anthropogenes Aerosol.

Weiterführung: nein

Mittelgeber: EU Horizon 2020 Marie Skłodowska-Curie Individual Fellowship.

****

Learning about cloud brightening under risk and uncertainty: Investigation of feasibility, traceability, Incentives and de-centralised governance of limited-area climate engineering (LEAC-II)

Schlagworte: Klima-Engineering, Klimawandel, Wolken impfen

Projektleiter:
Koordinator: Johannes Quaas, Universität Leipzig (johannes.quaas@uni-leipzig.de)

Projektmitarbeiter: Dr. Dipu Sudhakar (dipu.sudhakar@uni-leipzig.de)

Projektbeginn: 2016
Projektende: 2019

Beschreibung
Im Rahmen des Schwerpunktprojekts „Climate engineering – risks, challenges, opportunitites?“ der Deutschen Forschungsgemeinschaft untersucht das Projekt „LEAC-II“ in Zusammenarbeit mit dem Fachbereich Umweltökonomie an der Universität Kiel, inwiefern eine Beeinflussung des Klimas auf regionaler Skala machbar wäre. Dabei wird untersucht, ob etwa durch technische Änderung von Wolkeneigenschaften lokal Hitzewellen abgemildert werden könnten und inwiefern die Änderung des Klimas in einer Region Auswirkungen auf benachbarte Regionen hat.

Weiterführung: ja

Mittelgeber: Deutsche Forschungsgemeinschaft (DFG) SPP 1689

****

Forcing im langwelligen Spektrum aufgrund von Aerosol-Wolken-Wechselwirkungen: Satellit und Klimamodellierung vs. HALO (FLASH)
Forcing in the long-wave spectrum due to aerosol-cloud interactions: satellite and climate modelling vs. HALO (FLASH)

Schlagworte: Eiswolken, Eiswolken-Aerosol-Wechselwirkungen, Strahlungsantrieb, HALO

Projektleiter:
Koordinator: Johannes Quaas, Universität Leipzig (johannes.quaas@uni-leipzig.de)

Projektmitarbeiter:
Dr. Johannes Mülmenstädt (johannes.muelmenstaedt@uni-leipzig.de)

Projektbeginn: 2016
Projektende: 2019

Beschreibung
In der Arbeitsgruppe wurden neue Satellitendaten für die Eiskristallkonzentration entwickelt. Diese sollen im Projekt FLASH mit Hilfe von HALO-In-situ-Beobachtungen evaluiert werden. Dabei soll unter anderem zusammen mit dem DLR-Institut für Physik der Atmosphäre das Satellitenprodukt für kombinierte Radar-Lidar-Retrieval mit Daten der luftgetragenen Instrumente verglichen werden; daneben sollen die Satellitenprodukte mit in-situ-Beobachtungen evaluiert werden.

Weiterführung: ja

Mittelgeber: Deutsche Forschungsgemeinschaft (DFG) SPP 1294

****

Copernicus Atmospheric Monitoring Service 74 - Radiative Forcings

Schlagworte: Aerosol-Strahlungsantrieb, Reanalyse, Aerosol-Wolken-Wechselwirkungen

Projektleiter:
Koordinator: Nicolas Bellouin, Universität Reading (n.bellouin@reading.ac.uk)
J. Quaas (johannes.quaas@uni-leipzig.de)

Projektmitarbeiter: Dr. Johannes Mülmenstädt (johannes.muelmenstaedt@uni-leipzig.de)

Projektbeginn: 2016
Projektende: 2019

Beschreibung

Ziel dieses Services des COPERNICUS Atmospheric Monitoring Service ist die Bereitstellung einer Diagnostik für den anthropogenen Strahlungsantrieb durch verschiedene Mechanismen auf Basis der Reanalyse der Atmosphärenzusammensetzung. Beitrag der Uni Leipzig ist hierbei der Strahlungsantrieb durch Aerosol-Wolken-Wechselwirkungen.

Weiterführung: ja

Mittelgeber: Europäische Union, COPERNICUS-Programm, COPERNICUS Atmospheric Monitoring Service (Subcontractor der Uni Reading)

****

Modellierung von Aerosolen und Aerosol-Wolken-Wechselwirkungen in der Arctis (D02)
Modelling aerosols and aerosol-cloud interactions in the Arctic (D02)

Schlagworte: Arktischer Klimawandel, Aerosol-Wolken-Wechselwirkungen, Modellierung

Projektleiter:
Koordinator: Johannes Quaas, Universität Leipzig (johannes.quaas@uni-leipzig.de)

Projektmitarbeiter:
Jan Kretzschmar (jan.kretzschmar@uni-leipzig.de)

Projektbeginn: 2016
Projektende: 2019

Beschreibung
In diesem Beitrag zum SFB/Transregio (AC)³ soll mit Hilfe von globaler Modellierung in Kombination mit verschiedenen Beobachtungen der Einfluss anthropogener Aerosole auf den arktischen Klimawandel untersucht werden. In Kooperation mit dem Leibniz-Institut für Troposphärenforschung liegt hierbei der Schwerpunkt auf dem Meridionaltransport der Aerosole (TROPOS) und der Wechselwirkung von Aerosol mit Wolken (LIM).

Weiterführung: ja

Mittelgeber: Deutsche Forschungsgemeinschaft (DFG) TRR 172 (AC)³
****

Arktische Rückkopplungsprozesse in Klimamodellen (E01)
Assessment of Arctic feedback processes in climate models (E01)

Schlagworte: Arktischer Klimawandel, Feedbacks, Modellierung

Projektleiter:
Koordinator: Johannes Quaas, Universität Leipzig (johannes.quaas@uni-leipzig.de)

Projektmitarbeiterin:
Karoline Block (karoline.block@uni-leipzig.de)

Projektbeginn: 2016
Projektende: 2019

Beschreibung
In diesem Beitrag zum SFB/Transregio (AC)³ sollen mit Hilfe von globaler Modellierung in Kombination mit verschiedenen Beobachtungen die verschiedenen Klima-Feedback-Mechanismen quantifiziert und in den Klimamodellen evaluiert werden. Spezielles Augenmerk ist hierbei in Kooperation mit der Uni Köln auf dem Wolken-Feedback.

Weiterführung: ja

Mittelgeber: Deutsche Forschungsgemeinschaft (DFG) TRR 172 (AC)³

****

Aerosol-Wolke-Niederschlag-Wechselwirkungen über Gebieten von Emissionsquellen
Aerosol-cloud-rainfall interactions over emission source regions

Schlagworte: Aerosol-Wolken-Niederschlagswechselwirkungen, Solar dimming

Projektleiter:
Koordinator: Dr. Ribu Cherian, Universität Leipzig (ribu.cherian@uni-leipzig.de)

Projektmitarbeiter: Dr. Ribu Cherian (ribu.cherian@uni-leipzig.de)

Projektbeginn: 2017
Projektende: 2020

Beschreibung
Aerosol-Wolken-Wechselwirkungen stellen einen der wesentlichen Unsicherheitsfaktoren bei Verständnis und Quantifizierung der geographischen Verteilung von Wolken- und Niederschlagseigenschaften, aber auch des Strahlungsantriebs des globalen Klimawandels dar. Die grundlegende Idee des Projekts ist es, regional unterschiedliche Trends in anthropogenenen Emissionen von Aerosolen zu nutzen, um deren Einfluss auf Trends in Wolken-, Niederschlags- und Strahlungsgrößen zu bestimmen. Hierzu sollen verschiedene Szenarien in Multi-Klimamodell-Ensembles ("historische" Simulationen mit allen Strahlungsantrieben und "Aerosol"-Simulationen mit allen Antrieben außer anthropogenem Aerosol) analysiert werden und mit Beobachtungsdaten verglichen werden. Konkret werden vier Fragen untersucht:
(i) Welche Beziehung besteht zwischen regionalen Trends in Aerosolemissionen und Wolken-Strahlungs-Effekten? - Diese Studien analysieren Simulationen aus dem Multi-Modell-Ensemble.
(ii) Wie erfolgreich reproduzieren die Modelle beobachtete Trends? Hier werden die Klimamodelle mit Beobachtungsdaten verglichen.
(iii) Welchen Einfluss haben Emissionstrends für Aerosole und resultierende Strahlungsantriebe auf die atmosphärische Zirkulation? Simulationen mit dem Aerosol-Klima-Modell ECHAM6-HAM2 sollen für drei Zeitscheiben durchgeführt und analysiert werden.
(iv) Welche Rolle spielen Emissionstrends für Änderungen in Extremniederschlägen in Südost-Asien? - Mit speziellen Simulationen sollen die verschiedenen Hypothesen getestet werden.

Weiterführung: ja

Mittelgeber: Deutsche Forschungsgemeinschaft (DFG) (Eigene Stelle)
****

Hochatmosphäre, Christoph Jacobi
Upper Atmosphere

Untersuchung der Anregungsmechanismen der 8-stündigen solaren Gezeiten in der mittleren Atmosphäre
Analysis of forcing mechanisms of the terdiurnal tide in the middle atmosphere

Schlagworte: Mittlere Atmosphäre, Gezeiten, Wellen

Projektleiter:
Prof. Dr. Christoph Jacobi (jacobi @ rz.uni-leipzig.de)

Projektmitarbeiterin:
F. Lilienthal

Projektbeginn: 1.1.2014
Projektende: 31.8.2018

Beschreibung
Ein nichtlineares mechanistisches Zirkulationsmodell der mittleren Atmosphäre wird verwendet, um die Anregungsmechanismen der 8-stündigen Gezeiten in der mittleren Atmosphäre zu untersuchen. Das verwendete Modell MUAM (Middle and Upper Atmosphere Model) verfügt über Strahlungsroutinen zur selbstkonsistenten Anregung von Gezeiten. Zur Analyse der Gezeitenanregung werden im Modell die potenziellen Anregungsmechanismen einzeln und gemeinsam abgeschaltet. Die zu untersuchenden Anregungsmechanismen sind einerseits die direkte Anregung durch die 8-stündige Komponente im Strahlungsantrieb und andererseits die nichtlineare Wechselwirkung der ganz- und halbtägigen Gezeiten, repräsentiert in den Advektionstermen der Bewegungsgleichungen. Durch Vergleich mit Referenzläufen mit vollständiger Gezeitenanregung wird es möglich sein, die Anteile der jeweiligen Anregungsmechanismen am gesamten Wellenantrieb zu bestimmen. Die Arbeiten werden komplettiert durch Analyse von Radar- und Satellitendaten.

Mittelgeber: Deutsche Forschungsgemeinschaft (DFG JA 836/30-1)
****

Dynamik der mittleren Atmosphäre (RSHU)
Dynamics of the middle atmosphere (RSHU)

Schlagworte: Mittlere Atmosphäre, Reanalyse, empirische Modelle

Projektleiter:
Prof. Dr. Christoph Jacobi (jacobi @ rz.uni-leipzig.de)

Projektmitarbeiter:
-

Projektbeginn: 1.9.2017
Projektende: 31.8.2018

Beschreibung
Innerhalb des Projekts sollen globale Daten empirischer Modelle und meteorologischer Reanalysen, als auch regionale Radardaten umfassend untersucht werden. Dabei sollen globale Reanalyse-Datensätze verwendet werden, um empirische Modelle des Windes der mittleren Atmosphäre zu validieren. Die Arbeiten werden innerhalb einer Masterarbeit an der Russischen Staatlichen Hydrometeorogischen Universität (RSHU), Abteilung Meteorologische Vorhersagen, St. Petersburg, durchgeführt. Das Projekt umfasst weiterhin einen einmonatigen Besuch einer Stipendiatin in Leipzig.

Mittelgeber: DAAD (Leonhard Euler, 57375423)
****

Large-scale dynamical impacts on regional Arctic climate change
Der Einfluss großräumiger Dynamik auf regionale arktische Klimaänderungen

Schlagworte: Arktische Verstärkung, Klimavariabilität

Projektleiter:
Prof. Dr. Christoph Jacobi (jacobi @ rz.uni-leipzig.de), Prof. Dr. Johannes Quaas (johannes.quaas @ uni-leipzig.de)

Projektmitarbeiter: Daniel Mewes

Projektbeginn: 1.1.2016
Projektende: 31.12.2019

Beschreibung
Das Projekt umfasst die Wechselwirkung zwischen der variablen großskaligen Zirkulation und regionalen arktischen Klimaänderungen und der Diagnose der arktischen Verstärkung auf regionaler Skala als Reaktion auf Variationen großskaliger Zirkulation in der Vergangenheit sowie in Klimaszenarien zukünftigen Klimwandels. Es werden hierzu Reanalysedaten und CMIP5-Modellergebnisse herangezogen. Die Kopplung von Troposphäre und Stratosphäre als wichtiger Bestandteil der Variabilität der polaren Atmosphäre wird auch mit numerischen Simulationen untersucht.

Mittelgeber: Deutsche Forschungsgemeinschaft, SFB-Transregio 172

Effeke lokalen Schwerewellenantriebs auf die mittlere Atmosphäre
Middle atmosphere effects of localized gravity wave forcing (MATELO)

Schlagworte: Schwerewellen, mittlere Atmosphäre, residuelle Zirkulation, Globale Navigationssatellitensysteme, planetare Wellen

Projektleiter:
Prof. Dr. Christoph Jacobi (jacobi @ rz.uni-leipzig.de)

Projektmitarbeiter:
N. Samtleben

Projektbeginn: 1.1.2017
Projektende: 31.12.2019

Beschreibung
Das Projekt beinhaltet eine Studie der Auswirkungen einer begrenzten Region erhöhter atmosphärischer interner Schwerewellenaktivität und Schwerewellenrechens auf die mittlere Atmosphäre. Die Charakteristik solch einer Region, ihre räumlich und zeitliche Variabilität und Verbindung zu anderen Klimaparametern wird anhand von GPS Radiookkultationsanalysen untersucht. Es werden Algorithmen zur dreidimensionalen Analyse der Wellenreibung und der Brewer-Dobson-Zirkulation (BDC) verwendet; als Datengrundlage dienen Simulationen mit einem mechanistischen Zirkulationsmodell der mittleren Atmosphäre und Reanalysedaten. Die dreidimensionaler Variabilität der BDC und die Rolle lokalisierter erhöhte Schwerewellenaktivität wird so untersucht. Weiterhin wird die Anregung und folgende Ausbreitung planetarer Wellen durch eine Region erhöhter Schwerewellenaktivität untersucht. Die Auswirkungen auf die Polarregionen (mittlere Zirkulation, Präkonditionierung, winterliche Stratosphärenerwärmungen) und auf die äquatoriale Stratosphäre (Einfluss auf Tropopausenbrüche und Stratosphäre-Troposphäre-Austausch) werden untersucht. Weiterhin wird der Einfluss lokalisierten Schwerewellenbrechens auf die mittlere Zirkulation der Mesosphäre analysiert, insbesondere im Hinblick auf stationäre Wellen, und ihre Variabilität. Das Projekt ist eine Kooperation zwischen dem LIM und dem Department Atmosphärenphysik, Karls-Universität Prag.

Mittelgeber: Deutsche Forschungsgemeinschaft (DFG JA 836/32-1)

6-stündige Gezeiten in den mittleren Atmosphäre (QuarTA)
Quarterdiurnal tide in the middle atmosphere (QuarTA)

Schlagworte: mittlere Atmosphäre; Gezeiten; Ionosphäre

Projektleiter:
Prof. Dr. Christoph Jacobi (jacobi @ rz.uni-leipzig.de)

Projektmitarbeiter:
C. Geißler

Projektbeginn: 1.2.2017
Projektende: 31.1.2020

Beschreibung

Die Dynamik der Mesosphäre und unteren Thermosphäre wird zu großen Teilen von solaren Gezeiten dominiert. Eine davon ist die 6-stündige Gezeit (quarterdiurnal tide, QDT), die unter anderem in sporadischen E-Schichten und mit Hilfe von Radar- und Satellitenmessungen beobachtet wurde. Während allerdings die ganztägigen, halbtägigen, und auch 8-stündigen Gezeiten vergleichsweise gut dokumentiert und untersucht sind, sind Beobachtungen und Analysen der - weniger starken aber nichtsdestoweniger als ein Bestandteil der dynamischen Prozesse in ihrer Gesamtheit zu sehenden - 6-stündigen Komponente bislang selten. Um diese Lücke zu schließen, werden innerhalb des QuarTA-Projekts die 6-stündigen Gezeiten und ihre Antriebsmechanismen im Detail untersucht. Die Klimatologie der Gezeiten wir mit Hilfe von Meteorradarwindmessungen, vor allem der Langzeitreihe in Collm, ergänzt durch weitere Radarmessungen, erstellt. Die globale Verteilung der Gezeitenamplituden wird mit Hilfe von Ionosonden- und GPS-Radiookkultationsmessungen sporadischer E-Schichten untersucht, und die Beobachtungen in Verbindung mit Windscherungen aus Radarmessungen und numerischen Simulationen interpretiert. Um Einblick in die hauptsächlichen Anregungsmechanismen der 6-stündigen Gezeiten zu erhalten, wird ein nichtlineares mechanistisches Zirkulationsmodell, welches auch die Anregung durch Absorption solarer Strahlung enthält, verwendet. Hierbei wird, einzeln und in Kombination, die Anregung der 6-stündigen Gezeit durch Absorption solarer Strahlung und durch nichtlineare Wechselwirkung von Gezeiten in den Simulationen ausgeschaltet, so dass die Hauptantriebsquelle erkennbar wird. Innerhalb des QuarTA-Projekts wird daher, durch die Kombination von Beobachtungen und Modellsimulationen, ein vertiefter Einblick in die Klimatologie und die Anregung der 6-stündigen Gezeiten ermöglicht, der bislang noch nicht in ausreichendem Maße gegeben ist.

Mittelgeber: Deutsche Forschungsgemeinschaft (DFG JA 836/34-1)

Verzögerte Antwort der Ionosphäre auf Variationen des solaren EUV (DRIVAR)
Delayed response of the ionosphere to solar EUV variability (DRIVAR)

Schlagworte: Ionosphäre, solare Variabilität

Projektleiter:
Prof. Dr. Christoph Jacobi (jacobi @ rz.uni-leipzig.de)

Projektmitarbeiter:
R. Vaishnav

Projektbeginn: 1.5.2017
Projektende: 30.4.2020

Beschreibung

Mittelgeber: Deutsche Forschungsgemeinschaft (DFG JA 836/33-1)

Nicht-zonale Strukturen der Dynamik der Mesosphäre/unteren Thermosphäre in mittleren Breiten (NOSTHEM)
Non-zonal Structures of Mesosphere/lower Thermosphere Dynamics at Middle Latitudes (NOSTHEM)

Schlagworte: mittlere Atmosphäre; Radarmessungen

Projektleiter:
Prof. Dr. Christoph Jacobi (jacobi @ rz.uni-leipzig.de)

Projektmitarbeiter:
F. Lilienthal

Projektbeginn: 1.9.2018
Projektende: 31.8.2021

Beschreibung
In NOSTHEM sollen zonale Unterschiede des mittleren Windes, Gezeitenparameter, planetarer Wellen und Schwerewellen in der Mesosphäre und unteren Thermosphäre untersucht und erklärt werden. Ihr Einfluss auf die Repräsentativität einzelner Messungen für ein zonales Mittel von mittlerem Wind und Wellen wird bestimmt werden. Dies soll eine quantitative Einschätzung der Unsicherheiten von mittlerer Klimatologie, Langzeittrends und Maßen für die Variabilität auf der Basis einzelner Messungen ermöglichen. Der Beitrag nicht-zonaler Strukturen auf die mittlere Zirkulation und ihre Variabilität wird bestimmt. Hemisphärische Analysen von Wellen und Zirkulation in der unteren und mittleren Atmosphäre werden verwendet, um deren Rolle bei der Bildung longitudinaler Unterschiede zu klären. Dies wird auch die Frage beantworten, ob die schon seit langem beobachteten Unterschiede des mesosphärischen Windes über Mittel- und Osteuropa signifikant sind und wenn ja, welche Prozesse zu deren Auftreten beitragen.
In NOSTHEM werden Beobachtungen zweier praktisch identischer VHF-Meteorradare auf ähnlicher geographischer Breite, aber mit 36° Längenunterschied herangezogen. Daher kann daraus der Beitrag nicht-zonaler Strukturen zur lokalen Klimatologie und Variabilität ermittelt werden. Um ein umfassendes hemisphärisches Bild zu erhalten, werden die lokalen Radarmessungen durch Satellitenbeobachtungen und Reanalysedaten ergänzt, sowie numerische Simulationen mit einem Zirkulationsmodell der mittleren Atmosphäre durchgeführt.
Die Hauptziele von NOSTHEM sind (1) eine quantitative Darstellung von Ähnlichkeiten und Unterschieden der mesosphärischen/thermosphärischen Zirkulation an zwei Längengraden, (2) eine Erweiterung dieser Analyse durch hemisphärische Daten und (3) eine Quantifizierung der Rolle von Wellen bei der Ausprägung der Zirkulation an einzelnen Orten. Als Endziel werden nicht-zonale Strukturen und ihre Gründe und die zu ihnen führenden Prozesse geklärt, und auch Hinweise für die Interpretation von Klimatologie und Variabilität an einzelnen Orten in Bezug auf die gesamthemisphärische Dynamik gegeben.
NOSTHEM wird als Kooperation des Instituts für Meteorologie, Universität Leipzig und des radiophysikalischen Departments, Universität Kasan gemeinsam durchgeführt.

Mittelgeber: Deutsche Forschungsgemeinschaft (DFG JA 836/38-1)

Fernerkundung; Heike Kalesse
AG Fernerkundung der Atmosphäre und das Arktische Klimasystem

Bodengebundene Fernerkundung der Atmosphäre zur Verbesserung der Charakterisierung mikrophysikalischer Wolkeneigenschaften sowie der Leistungsprognose erneuerbarer Energien

Ground-based remote sensing of the atmosphere for improving the characterization of microphysical cloud properties and for improving the load prediction of renewable energies

Schlagworte: bodengebundene Fernerkundung, erneuerbare Energien, Wolkenretrieval, DACAPO-PESO

Projektleiter: H. Kalesse (heike.kalesse@uni-leipzig.de), A. Ehrlich (a.ehrlich@uni-leipzig.de), M. Schäfer (michael.schaefer@uni-leipzig.de), M. Wendisch (m.wendisch@uni-leipzig.de)
Projektmitarbeiter:
AP1: M. Lochmann (moritz.lochmann@uni-leipzig.de),
AP2: W. Schimmel (willi.schimmel@uni-leipzig.de),
AP3: A. Emmanouilidis (alexandros.emmanouilidis@uni-leipzig.de)

Projektbeginn: 1.9.2018
Projektende: 31.8.2021

Beschreibung
Die bodengebundene Fernerkundung der Atmosphäre dient sowohl der Grundlagenforschung von Wolken und Niederschlag, als auch im operationellen Dienst der Wettervorhersage als ein wichtiger Baustein für die Leistungsprognose erneuerbarer Energien. Innerhalb dieses Projekts gibt es zwei Hauptzielstellungen: Zum einen wird analysiert werden, wie künstliche neuronale Netze (KNN) zur Leistungsprognose von Photovoltaik- und Windkraftanlagen optimiert werden können, wenn zusätzliche Daten von Wetterstationen und bodengebundenen Fernerkundungsmessungen implementiert werden. Zum anderen sollen in zwei weiteren Teilprojekten für Wolkenbeobachtungen Ableitungsalgorithmen (Retrievals) weiterentwickelt werden, um die Bestimmung von Wolkeneigenschaften zu verbessern und zu erweitern. Dabei stehen Messgerätesynergien zur Ableitung der Wolkentröpfchenkonzentration sowie die Entwicklung anwendungsspezifischer KNN zur Charakterisierung der Verteilung von Flüssigwasser in Mischphasenwolken im Vordergrund.

Das Projekt ist in drei Arbeitspakete unterteilt:
AP1: Test des Einflusses zusätzlicher Messdaten von Wetterstationen und aus der bodengebundenen Fernerkundung auf die Leistungsprognose von PV- und Windkraft-Anlagen mittels künstlicher Neuronaler Netze (KNN)

AP2: Entwicklung eines auf Wolkenradar- und Lidar basierendem KNN zur Detektion von Flüssigwasser in Wolken

AP3: Entwicklung einer auf synergistischen Fernerkundungsmessungen basierenden Methode zur Ableitung der Wolkentröpfchenkonzentration

Description
Ground-based remote sensing of the atmosphere serves both, the basic research of clouds and precipitation, and in the operational service of weather forecasting as an important building block for the power prognosis of renewable energies. Within this project there are two main objectives: Firstly, it will be analysed how artificial neural networks (ANN) can be optimized for power forecasting of Photovoltaics (PV) and wind turbines, if additional data from weather stations and ground-based remote sensing measurements are implemented. On the other hand, in two further subprojects for cloud observations, retrieval algorithms will be developed to improve and extend the determination of cloud properties. The focus will be on instrument synergies for the

derivation of cloud droplet concentrations and the development of application-specific ANN for the characterization of the distribution of liquid water in mixed-phase clouds.

The project is divided into three work packages:
AP1: Testing the influence of additional measurement data from weather stations and ground-based remote sensing on the power prognosis of PV and wind power plants using artificial neural networks (ANN)
AP2: Development of a cloud radar and lidar based ANN for detection of liquid water in clouds
AP3: Development of a cloud droplet concentration retrieval based on synergistic remote sensing observations

Mittelgeber: ESF - Sächsische Aufbaubank (SAB), Antragsnummer : 100339509

PICNICC - Durch CCN und INP beeinflusste Polarimetrie in Zypern und Chile – Abschätzung von hemisphärischen Kontrasten in radarpolarimetrischen Größen und deren Beziehung zu Unterschieden in der Aerosolbelastung
Polarimetry Influenced by CCN aNd INP in Cyprus and Chile (PICNICC):
An assessment of hemispheric cloud polarimetric contrasts and its relation to differences in aerosol load

Schlagworte: Radarpolarimetrie, DACAPO-PESO, Wolkenmikrophysik, Aerosol-Wolken-Wechselwirkung

Projektleiter: H. Kalesse (heike.kalesse@uni-leipzig.de)
Dr. P. Seifert, Leibniz Institut für Troposphärenforschung (TROPOS)
Projektmitarbeiter:
Prof. J. Quaas (johannes.quaas@uni-leipzig.de)
Teresa Vogl (teresa.vogl@uni-leipzig.de), A. Teissiere (TROPOS)

Projektbeginn: 1.11.2018
Projektende: 31.12.2021

Beschreibung
Das Verständnis von mikrophysikalischen Wachstumsprozessen in Mischphasenwolken wie Aggregation und Bereifung beruht auf einer gründlichen Charakterisierung der in der Wolke vorhandenen Flüssigphase. In dieser Studie wird eine einzigartige Messmöglichkeit mit einer erweiterten Fernerkundungsinstrumentensuite genutzt, die polarimetrische Radarbeobachtungen bei mehreren Wellenlängen auf der Nord- und Südhalbkugel beinhaltet, um die Millimeterwellenlängen-Radarpolarimetrieforschung für mikrophysikalische Prozessstudien voranzubringen. Die übergeordnete Hypothese, die in diesem Projekt untersucht wird, ist, dass Mischphasen-Wolkenprozesse anfällig für Aerosolstörungen sind. Wir postulieren, dass:
A) Die Aggregation wird bei hohen Aerosolbelastungen und damit verbundenen höheren INP (Ice Nucleating Particle)-Konzentrationen häufiger erfolgen, da höhere Eiskristallkonzentrationen die Aggregation begünstigen.
B) Bereifung von Eiskristallen wird häufiger auftreten, wenn aufgrund einer Knappheit von INP anhaltende unterkühlte Flüssigkeitsschichten auftreten.
Um diese Hypothesen anzugehen, wird die Häufigkeit des Auftretens von Aggregation und Bereifung in mehrjährigen Datensätzen charakterisiert, die bei Feldexperimenten in der Aerosol-

Lasten-Atmosphäre über Limassol, Zypern und der unberührten Region Punta Arenas, Chile, erhalten wurden und werden. Die beobachtete Reaktion von Mischphasen-Wolkenprozessen auf Aerosolstörungen wird im Zusammenhang mit einer Modellsensitivitätsstudie von Simulationen mit einer wolkensystemauflösenden (1 km) Version des ICON-NWP für die gesamten Beobachtungszeiträume für regionale Bereiche um die Beobachtungsstandorte in Zypern und Chile gestellt, die von Radar-Fortsimulationen begleitet werden.

Description

Understanding mixed-phase cloud processes such as aggregation and riming relies on a thorough characterization of the liquid phase present in the cloud. For this study we propose to use a unique measurement opportunity with an extended remote-sensing instrument suite including triple-frequency polarimetric radar observations on the Northern and Southern hemisphere to bring forward millimeter wavelength radar polarimetry research for microphysical process studies. The overarching hypothesis that we would like to study within this project is that mixed-phase cloud processes are susceptible to aerosol perturbations. We postulate that

A) Aggregation will be more frequent for high aerosol loads and associated higher ice nucleating particle (INP) concentrations because higher ice crystal concentrations favor aggregation.

B) Riming will be more frequent where sustained supercooled liquid layers occur due to a scarcity of INP.

To address these hypotheses, we will characterize the frequency of occurrence of aggregation and riming in multi-year datasets obtained during institutional-funded field experiments in the aerosol-burden atmosphere above Limassol, Cyprus and the pristine region of Punta Arenas, Chile. For that purpose, we will make slanted linear depolarization (SLDR) polarimetric observations with a Ka-band radar a versatile technique for classification of hydrometeors in mixed-phase clouds. The observed response of mixed-phase cloud processes to aerosol perturbations will be put in context to a model sensitivity study of simulations with a cloud-system-resolving (1 km) version of the ICON-NWP for the entire observation periods for regional domains around the observations sites in Cyprus and Chile that are accompanied by radar forward simulations.

Mittelgeber: DFG KA 4162/2-1 innerhalb SPP-PROM (SPP-2115)

Allgemeine Meteorologie
AG Akustik
Acoustics

Lärm- und Feldlagerschutz der Bundeswehr
Noise protection of Bundeswehr

Schlagworte: Lärmschutz, Schallklima

Projektleiter:
Dr. A. Raabe (raabe@uni-leipzig.de)

Projektmitarbeiter:
Dipl. Met. Michael Wilsdorf (mwils@uni-leipzig.de)

Projektbeginn: 01.06.2017

Projektende: 31.05.2018

Beschreibung

Die Bewertung von Schallimmissionen, deren Quellen sich in großen Entfernungen (bis zu 15km), aber auch in der näheren Umgebung (weniger als 5km) von Truppenübungsplätzen, oder auch Feldlagern der Bundeswehr befinden, ist ohne Berücksichtigung der aktuellen Wettersituation nicht möglich. Das heißt, dass die Ausbreitung akustischer Signale über mehrere Kilometer Entfernung wesentlich von der Temperatur- und Windvektorverteilung in dem Teil der Atmosphäre abhängen, durch den sich die Schallwellen ausbreiten. Die bisherige Vorgehensweise bei der Beachtung atmosphärischer Verhältnisse im Zusammenhang mit Schallimmissionen basiert im Wesentlichen auf der Verwendung von Radiosondendaten. Ihr Nachteil besteht darin, dass meist nur wenige Radiosondenaufstiege am Tag (meist 2x) durchgeführt werden und (weltweit) sich nur wenige Stationen über ein riesiges Gebiet verteilen. Deshalb wird der Frage nachgegangen ob Wetter-Modelldaten die Radiosondendaten auf eine solche Weise ersetzen können, dass die auf Basis der Modelldaten abgeleiteten Aussagen bezogen auf die Schallimmissionsverhältnisse weitgehend identisch bleiben.

Mittelgeber: BMVg,AGeoBw; M/U2CD/CA277/CA647

Forschungsbericht 2018
GREMIUM MITGLIEDSCHAFT

Prof. Dr. Manfred Wendisch:
-Ordentliches Mitglied der Sächsischen Akademie der Wissenschaften
-Mitglied des Präsidiums der Sächsischen Akademie der Wissenschaften
-Mitglied im Vorstand der Meteorologischen Gesellschaft, Sektion Mitteldeutschland
-Gewähltes Mitglied im IRC (Internationale Strahlungskommission) innerhalb von IAMAS
-Koordinator Expert Working Groups innerhalb von EUFAR (European Facility for Airborne Research)
-Mitglied des „User Group Selection Panel“ (UGSP) innerhalb von EUFAR
-Koordinator des DFG-SPP (Schwerpunktprogramm) 1294 zu HALO (High Altitude and Long Range Research Aircraft), gemeinsam mit Prof. J. Curtius (Uni Frankfurt am Main) und Mirko Scheinert (TU Dresden)
-Vize-Sprecher der „Leibniz-Graduate School on Clouds, Aerosols, and Radiation (LGS-CAR)“
-Mitglied des Gutachtergremiums für Atmosphärenwissenschaften der Finnländischen Akademie der Wissenschaften
-Mitglied des Wissenschaftlichen Beirats des Deutschen Wetterdienstes (DWD)
-Mitglied des Programmrates „Hans-Ertel-Zentrum für Wetterforschung (HErZ)“ des DWD
-Stellvertretender Vorsitzender des wissenschaftlichen Lenkungsausschusses (WLA) für HALO (High Altitude and -Long Range Research Aircraft)
-Sprecher des Sonderforschungsbereiches SFB-Transregio 172: “Arktische Verstärkung: Klimarelevante Atmosphären- und Oberflächenprozesse, und Rückkopplungsmechanismen (AC)^3”
-Koordinator des YOPP (Year of Polar Prediction) Task Teams zu Flugzeuggetragenen Messplattformen
-Mitglied des Steuerungskommittees für MOSAiC (**M**ultidisciplinary drifting **O**bservatory for the **S**tudy of **A**rct**i**c **C**limate), Team Koordinator für Flugzeugoperation
-Mitglied DFG-Senatskommission für Erdsystemforschung

Prof. Dr. Johannes Quaas:
- Lead author 6th assessment report, Intergovernmental Panel on Climate Change (WG I, Chapter 2 ”Changing state of the climate system”)
- Co-chair, Aerosols, Clouds, Precipitation and Climate (gemeinsame Aktivität des IGBP/iLEAPS und WCRP/GEWEX; Mitglied des wissenschaftlichen Lenkungsausschusses seit 2010; Co-Chair seit 2013)
- Mitglied des Leibniz-Instituts für Troposphärenforschung e.V. (TROPOS)
- Mitglied des Wissenschaftlichen Beirats des Leibniz-Instituts für Troposphärenforschung (TROPOS)

Prof. Dr. Christoph Jacobi:
Mitglied im Vorstand der Meteorologischen Gesellschaft, Sektion Mitteldeutschland
Stellv. Leiter der Division II „Aeronomic Phenomena“ der IAGA
Leiter der Arbeitsgruppe II-D der IAGA: „External Forcing of the Middle Atmosphere“
Vorsitzender der Mitgliederversammlung des TROPOS

Dr. A. Raabe:
- Vorsitzender der Deutschen Meteorologischen Gesellschaft e.V., Sektion Mitteldeutschland
- Mitglied Sektorkomitee Erneuerbare Energien bei Deutsche Akkreditierungsstelle (DAkkS) des BMWiuT,

Forschungsbericht 2018
Mitgliedschaften in Redaktionskollegien, Herausgebergremien

Prof. Dr. Manfred Wendisch:
Atmos. Meas. Tech. Co-Editor
Meteorologische Zeitschrift Co-Editor
Herausgeber: Wiss. Mitt. Inst. f. Meteorol. Univ. Leipzig

Prof. Dr. Johannes Quaas
Atmos. Chem. Phys. Co-Editor
Prof. Dr. Christoph Jacobi:
Annales Geophysicae Editor-in-Chief
Mitteilungen der DMG Mitglied Redaktionsteam

Dr. A. Raabe:
Koordinator Meteorologische Zeitschrift DMG eV
Herausgeber: Wiss. Mitt. Inst. f. Meteorol. Univ. Leipzig

Dr. M. Salzmann
Annales Geophysicae Co-Editor

Publikationen LIM 2018				
Autor_Name	Vorname	weitere Autoren	Titel	ID, DOI Publikationsort
Andreae	M. O.	Afchine, A., Albrecht, R., Holanda, B. A., Artaxo, P., Barbosa, H. M. J., Bormann, S., Cecchini, M. A., Costa, A., Dollner, M., Fütterer, D., Järvinen, E., Jurkat, T., Klimach, T., Konemann, T., Knote, C., Krämer, M., **Krisna, T.,** Machado, L. A. T., Mertes, S., Minikin, A., Pöhlker, C., Pöhlker, M. L., Pöschl, U., Rosenfeld, D., Sauer, D., Schlager, H., Schnaiter, M., Schneider, J., Schulz, C., Spanu, A., Sperling, V. B., Voigt, C., Walser, A., Wang, J., Weinzierl, B., **Wendisch, M.,** and Ziereis, H.	Aerosol characteristics and particle production in the upper troposphere over the Amazon Basin	doi:10.5194/acp-18-921-2018 Atmos. Chem. Phys., 18 (2018), 921-961
Li	Li	Li, Z., Li, K., Sun, B., Wu, Y., Xu, H., Xie, Y., Goloub, P., and **Wendisch, M.**	Uncertainties of atmospheric polarimetric measurements with sun-sky radiometers induced by errors of relative orientations of polarizers	doi:10.1016/j.jqsrt.2018.01.013 J. Quant. Spectrosc. Radiat. Transfer, 209 (2018), 10-18
Emde	Claudia	V. Barlakas, C. Cornet, F. Evans, Z. Wang, L. C.-Labonotte, A. Macke, B. Mayer, and **M. Wendisch**	IPRT polarized radiative transfer model intercomparison project - Three-dimensional test cases (phase B)	doi:10.1016/j.jqsrt.2018.01.024 J. Quant. Spectrosc. Radiat. Transfer, 209 (2018), 19-44
Krisna	**Trismono. C.**	**Wendisch, M., Ehrlich, A., Jäkel, E., Werner, F**., Weigel, R., Borrmann, S., Mahnke, C., Pöschl, U., Andreae, M. O., Voigt, C., and Machado, L. A. T.	Comparing airborne and satellite retrievals of cloud optical thickness and particle effective radius using a spectral radiance ratio technique: two case studies for cirrus and deep convective clouds	doi:10.5194/acp-18-4439-2018 Atmos. Chem. Phys., 18 (2018), 4439-4462
Grosvenor	D.P.	**O. Souderval**, P. Zuidema, A.S. Ackerman, M.D. Alexandrov, R. Bennartz, R. Boers, B. Cairns, J.C. Chiu, M. Christensen, H. Deneke, M. Diamond, G. Feingold, A. Fridlind, A. Hünerbein, C. Knist, P. Kollias, A. Marshak, D. McCoy, D. Merk, D. Painemal, J. Rausch, D. Rosenfeld, H. Russchenberg, P. Seifert, K.	Remote sensing of cloud droplet number concentration: Review of current and perspectives for new approaches	doi:10.1029/2017RG000593 Rev. Geophys., 56 (2018), 409-453

		Sinclair, P. Stier, B. van Diedenhoven, **Wendisch, M.**, F. Werner, R. Wood, Z. Zhang, and **J. Quaas**		
Machado	L. A. T.	Calheiros, A. J. P., Biscaro, T., Giangrande, S., Silva Dias, M. A. F., Cecchini, M. A., Albrecht, R., Andreae, M. O., Araujo, W. F., Arttaxo, P., Borrmann, S., Braga, R., Burleyson, C., Eichholz, C. W., Fan, J., Feng, Z., Fisch, G. F., Jensen, M. P., Martin, S. T., Pöschl, U., Pöhlker, C., Pöhlker, M. L., Ribaud, J.-F., Rosenfeld, D., Saraiva, J. M. B., Schumacher, C., Thalman, R., Walter, D., and **Wendisch, M.**	Overview: Precipitation characteristics and sensitivities to the environmental conditions during GoAmazon2014/5 and ACRIDICON-CHUVA	doi:10.5194/acp-18-6461-2018 Atmos. Chem. Phys., 18 (2018), 6461-6482
Saturno	J.	Ditas, F., Penning de Vries, M., Holanda, B. A., Pöhlker, M. L., Carbone, S., Walter, D., Bobrowski, N., Brito, J., Chi, X., Gutmann, A., Hrabe de Angelis, I., Machado, L. A. T., Moran-Zuloaga, D., Rüdiger, J., Schneider, J., Schulz, C., Wang, Q., **Wendisch, M.**, Artaxo, P., Wagner, T., Pöschl, U., Andreae, M. O., and Pöhlker, C.	African volcanic emissions influencing atmospheric aerosols over the Amazon rain forest	doi:10.5194/acp-18-10391-2018 Atmos. Chem. Phys., 18 (2018), 10391-10405
Schäfer	**Michael**	Loewe, K., **Ehrlich, A.**, Hoose, C., and **Wendisch, M.**	Simulated and observed horizontal inhomogeneities of optical thickness of Arctic stratus	doi:10.5194/acp-18-13115-2018 Atmos. Chem. Phys., 18 (2018), 13115-13133
Schäfler	Andreas	G. Craig, H. Wernli, P. Arbogast, J.D. Doyle, R. McTaggart-Cowan, J. Methven, G. Rivière, F. Ament, M. Boettcher, M. Bramberger, Q. Cazenave, R. Cotton, S. Crewell, J. Delanoë, A. Dörnbrack, **A. Ehrlich**, F. Ewald, A. Fix, C.M. Grams, S.L. Gray, H. Grob, S. Groß, M. Hagen, B. Harvey, L. Hirsch, M. Jacob, T. Kölling, H. Konow, C. Lemmerz, O. Lux, L. Magnusson, B. Mayer, M. Mech, R. Moore, J. Pelon, J. Quinting, S. Rahm, M. Rapp, M. Rautenhaus, O. Reitebuch, C.A. Reynolds, H. Sodemann, T. Spengler, G. Vaughan, **M.**	The North Atlantic Waveguide and Downstream Impact Experiment	doi:10.1175/BAMS-D-17-0003.1 Bull. Am. Meteorol. Soc., 8 (2018), 1607-1637

		Wendisch, M. Wirth, B. Witschas, **K. Wolf**, and T. Zinner		
Schulz	Christine	Schneider, J., Amorim Holanda, B., Appel, O., Costa, A., de Sá, S. S., Dreiling, V., Fütterer, D., Jurkat-Witschas, T., Klimach, T., Krämer, M., Martin, S. T., Mertes, S., Pöhlker, M. L., Sauer, D., Voigt, C., Walser, A., Weinzierl, B., Ziereis, H., Zöger, M., Andreae, M. O., Artaxo, P., Machado, L. A. T., Pöschl, U., **Wendisch, M.**, and Borrmann, S.	Aircraft-based observations of isoprene-epoxydiol-derived secondary organic aerosol (IEPOX-SOA) in the tropical upper troposphere over the Amazon region	doi:10.5194/acp-18-14979-2018 Atmos. Chem. Phys., 18 (2018), 14979-15001
Järvinen	Emma	Jourdan, O., Neubauer, D., Yao, B., Liu, C., Andreae, M. O., Lohmann, U., **Wendisch, M.**, McFarquhar, G. M., Leisner, T., and Schnaiter, M.	Additional Global Climate Cooling by Clouds due to Ice Crystal Complexity	doi:10.5194/acp-18-15767-2018 Atmos. Chem. Phys., 18 (2018), 15767-15781
Pithan	Felix	Svensson, G., Caballero, R., Chechin, D., Cronin, T. W., Ekman, A. M. L., Neggers, R., Shupe, M. D., Solomon, A., Tjernström, M., and **Wendisch, M.**	Role of air-mass transformations in exchange between the Arctic and mid-latitudes	doi:10.1038/s41561-018-0234-1 Nat. Geosci., 11 (2018), 805-812
Li	Li	Li, Z., Li, Q., Hua, X., and **Wendisch, M.**	Retrieval of the polarized phase function of aerosol particles based on multi-angle multi-spectral measurements of Stokes parameters Q and U	doi:10.3964/j.issn.1000-0593(2018)12-3699-09 Spectrosc. Spect. Anal., 38(12) (2018), 3699-3707
Knudsen	E. M.	Heinold, B., Dahlke, S., Bozem, H., Crewell, S., Gorodetskaya, I. V., Heygster, G., Kunkel, D., Maturilli, M., Mech, M., Viceto, C., Rinke, A., Schmithüsen, H., **Ehrlich, A.**, Macke, A., Lüpkes, C., and **Wendisch, M.**	Meteorological conditions during the ACLOUD/PASCAL field campaign near Svalbard in early summer 2017	doi:10.5194/acp-18-17995-2018 Atmos. Chem. Phys., 18 (2018), 17995-18022
Baran	Anthony J.	H. Ishimoto, **O. Sourdeval**, E. Hesse, and C. Harlow	The applicability of physical optics in the millimetre and sub-millimetre spectral region. Part II: Application to a three-component model of ice cloud and its evaluation against the bulk single-scattering properties of various other aggregate models	10.1016/j.jqsrt.2017.10.027 J. Quant. Spectrosc. Radiat. Transf., 206 (2018), 83-100

Crueger	Traute	M.A. Giorgetta, R. Brokopf, M. Esch, S. Fiedler, C. Hohenegger, L. Kornblueh, T. Mauritsen, **C. Nam**, A.K. Naumann, K. Peters, S. Rast, E. Roeckner, M. Sakradzija, H. Schmidt, J. Vial, R. Vogel, and B. Stevens	ICON-A, the atmospheric component of the ICON Earth System Model. Part II: Model Evaluation	doi:10.1029/2017MS001233 J. Adv. Model. Earth Syst., 10 (2018), 1638-1662
Fauchez	Thomas	S. Platnick , **O. Sourdeval,** C. Wang, K. Meyer , C. Cornet , F. Szczap	Effects on cloud optical Property retrievals from MODIS near to thermal infrared channels as a function of spatial resolution	doi: 10.1029/2018JD028726 J. Geophys. Res. Atmos., 19 (2018), 11141-11153
Giorgetta	Marco A.	R. Brokopf, T. Crueger, M. Esch, S. Fiedler, J. Helmert, C. Hohenegger, L. Kornblueh, M. Koehler, E. Manzini, T. Mauritsen, **C. Nam**, S. Rast, C. Reick, D. Reinert, M. Sakradzija, H. Schmidt, R. Schnur, L. Silvers, H. Wan, G. Zaengl, and B. Stevens	ICON-A, the atmospheric component of the ICON Earth System Model. Part I: Model Description	doi:10.1029/2017MS001242 J. Adv. Model. Earth Syst., 10 (2018), 1613-1637
Goren	Tom	D. Rosenfeld, **O. Sourdeval**, and **J. Quaas**	Satellite observations of precipitating marine stratocumulus show greater cloud fraction for decoupled clouds in comparison to coupled clouds	doi:10.1029/2018GL078122 Gephys. Res. Lett., 45 (2108), 5126-5134
Grosvenor	Daniel P.	**O. Sourdeval**, and R. Wood	Parameterizing cloud top effective radii from satellite retrieved values, accounting for vertical photon transport: quantification and correction of the resulting bias in droplet concentration and liquid water path retrievals	doi: 10.5194/amt-11-4273-2018 Atmos. Meas. Tech., 11 (2018), 4273-4289
Grosvenor	Daniel P.	**O. Sourdeval**, P. Zuidema, A. Ackerman, M. D. Alexandrov, R. Bennartz, R. Boers, B. Cairns, C. Chiu, Matthew Christensen, H. Deneke, M. Diamond, G. Feingold, A. Fridlind, A. Hünerbein, C. Knist, P. Kollias, A. Marshak, D. McCoy, D. Merk, D. Painemal, J. Rausch, D. Rosenfeld, H. Russchenberg, Patrick Seifert, K. Sinclair, P. Stier, B. Van Diedenhoven, **Manfred Wendisch**, F. Werner, R. Wood, Z. Zhang, and **J. Quaas**	Remote sensing of cloud droplet number concentration in warm clouds: A review of the current state of knowledge and perspectives	doi:10.1029/2017RG000593 Rev. Geophys., 56 (2018), 409-453

Gryspeerdt	Edward	**J. Quaas**, **T. Goren**, D. Klocke, and **M. Brueck**	An automated cirrus classification	doi:10.5194/acp-18-6157-2018 Atmos. Chem. Phys., 18 (2018), 6157-6169
Gryspeerdt	Edward	**O. Sourdeval**, **J. Quaas**, J. Delanoë, and **P. Kühne**	Ice crystal number concentration estimates from lidar-radar satellite retrievals. Part 2: Controls on the ice crystal number concentration	doi:10.5194/acp-18-14351-2018 Atmos. Chem. Phys., 18 (2018), 14351-14370,
Ma	Xiaoyan	H. Jia, F. Yu, and **J. Quaas**	Opposite aerosol index-cloud droplet effective radius correlations over major industrial regions and their adjacent oceans	doi:10.1029/2018GL077562 Geophys. Res. Lett., 45 (2018), 5771-5778
Mülmenstädt	**Johannes**	G. Feingold	The radiative forcing of aerosol-cloud interactions in liquid clouds: Wrestling and embracing uncertainty	doi:10.1007/s40641-018-0089-y Curr. Clim. Change Rep., 4 (2018), 23-40
Mülmenstädt	**Johannes**	**O. Sourdeval**, D. S. Henderson, T. S. L'Ecuyer, **C. Unglaub**, L. Jungandreas, C. Böhm, L. M. Russell, and **J. Quaas**	Using CALIOP to estimate cloud-field base height and its uncertainty: The Cloud Base Altitude Spatial Extrapolator (CBASE) algorithm and dataset	doi:10.5194/essd-10-2279-2018 Earth Syst. Sci. Data, 10 (2018), 2279-2293
Nam	**Christine**	**P. Kühne**, **M. Salzmann**, and **J. Quaas**	A prospectus for constraining rapid adjustments in general circulation models	doi:10.1029/2017MS001153 J. Adv. Model. Earth Syst., 10 (2018), 2080-2094
Petersik	**Paul**	**M. Salzmann**, **Jan Kretzschmar**, **R. Cherian**, D. Mewes, and **J. Quaas**	Subgrid-scale variability of clear-sky relative humidity and forcing by aerosol-radiation interactions in an atmosphere model	doi:10.5194/acp-18-8589-2018 Atmos. Chem. Phys., 18 (2018), 8589-8599
Sourdeval	**Odran**	E. Gryspeerdt, M. Krämer, **T. Goren**, J. Delanoë, A. Afchine, F. Hemmer, and **J. Quaas**	Ice crystal number concentration estimates from lidar-radar satellite remote sensing. Part 1: Method and evaluation	doi:10.5194/acp-18-14327-2018 Atmos. Chem. Phys., 18 (2018), 14327-14350
Wendisch	Manfred	A. Macke, A. Ehrlich, C. Lüpkes, M. Mech, D. Chechin, C. Barrientos, H. Bozem, M. Brückner, H.-C. Clemen, S. Crewell, T. Donth, R. Dupuy, K. Ebell, U. Egerer, R. Engelmann, C. Engler, O. Eppers, M. Gehrmann, X. Gong, M. Gottschalk, C. Gourbeyre, H. Griesche, J.	The Arctic cloud puzzle: Using ACLOUD/PASCAL multi-platform observations to unravel the role of clouds and aerosol particles in Arctic Amplification	doi:10.1175/BAMS-D-18-0072.1 Bull. Amer. Meteorol. Soc, in press

		Hartmann, M. Hartmann, A. Herber, H. Herrmann, G. Heygster, P. Hoor, S. Jafariserajehlou, E. Jäkel, E. Järvinen, O. Jourdan, U. Kästner, S. Kecorius, E. M. Knudsen, F. Köllner, **J. Kretzschmar**, L. Lelli, D. Leroy, M. Maturilli, L. Mei, S. Mertes, G. Mioche, R. Neuber, M. Nicolaus, T. Nomokonova, J. Notholt, M. Palm, M. Pinxteren, **J. Quaas**, P. Richter, E. Ruiz-Donoso, M. Schäfer, K. Schmieder, M. Schnaiter, J. Schneider, A. Schwarzenböck, P. Seifert, M. D. Shupe, H. Siebert, G. Spreen, J. Stapf, F. Stratmann, T. Vogl, A. Welti, H. Wex, A. Wiedensohler, M. Zanatta, S. Zeppenfeld, K. Dethloff, and B. Heinold		
Smith	C. J.	R. J. Kramer, G. Myhre, P. M. Forster, B. J. Soden, T. Andrews, O. Boucher, G. Faluvegi, D. Fläschner, O. Hodnebrog, M. Kasoar, V. Kharin, A. Kirkevag, J.-F. Lamarque, **J. Mülmenstädt**, D. Olivié, T. Richardson, B. H. Samset, D. Shindell, P. Stier, T. Takemura, A. Voulgarakis, D. Watson-Parris	Understanding rapid adjustments to diverse forcing agents	10.1029/2018GL079826 Geophys. Res. Lett., 45, 12023-12031
Jacobi	Christoph	Ermolenko, S.I., Shved, G.M.	Detecting atmospheric normal modes with periods less than 6 h by barometric observations	https://doi.org/10.1016/j.jastp.2017.12.007 J. Atmos. Sol.-Terr. Phys., 169, 1-5
Jacobi	Christoph	Wüst, S., Offenwanger, T, Schmidt, C., Bittner, M., Stober, G. , Yee, J.-H., Mlynczak, M.G., Russell III, J.M.	Derivation of horizontal and vertical wavelengths using a scanning OH(3-1) airglow spectrometer	https://doi.org/10.5194/amt-2017-350. Atmos. Meas. Tech., 11, 2937-2947
Jacobi	Christoph	Stober, G., Chau, J.L., Vierinen, J., Wilhelm, S.	Retrieving horizontally resolved wind fields using multi-static meteor radar observations	https://doi.org/10.5194/amt-11-4891-2018 Atmos. Meas. Tech., 11, 4891-4907
Jacobi	Christoph	C. Geißler, Lilienthal, F., Krug, A.	Forcing mechanisms of the 6-hour tide in the mesosphere/lower thermosphere	https://doi.org/10.5194/ars-16-141-2018 Adv. Radio Sci.,16, 141-147

Jacobi	Christoph	Schmölter, E., Berdermann, J., Jakowski, N., Vaishnav, R. I.	Delayed response of the ionosphere to solar EUV variabilities	https://doi.org/10.5194/ars-16-149-2018 Adv. Radio Sci., 6, 149–155
Jacobi	Christoph	Vaishnav, R., Berdermann, J., Schmölter, E., Codrescu, M.	Ionospheric response to solar EUV variations: Preliminary results	https://doi.org/10.5194/ars-16-157-2018 Adv. Radio Sci., 16, 157-165
Jacobi	Christoph	Lilienthal, F., Geißler, C.	Forcing mechanisms of the terdiurnal tide	https://doi.org/10.5194/acp-18-15725-2018 Atmos. Chem. Phys., 18, 15725-15742
Jacobi	Christoph	Kaifler, N., Kaifler, B., Wilms, H. Rapp, M., Stober, G.	Mesospheric temperature during the extreme mid-latitude noctilucent cloud event on 18/19 July 2016	https://doi.org/10.1029/2018JD029717 J. Geophys. Res.: Atmospheres, 123, 13775-13789
Foth	Andreas	Kanitz, T., Engelmann, R., Baars, H., Radenz, M., Seifert, P., Barja, B., **Kalesse, H.,** and Ansmann, A.	Vertical aerosol distribution in the Southern hemispheric Midlatitudes as observed with lidar at Punta Arenas, Chile (53.2° S and 70.9° W) during ALPACA	https://doi.org/10.5194/acp-2018-1124 Atmos. Chem. Phys. Discuss.,
Kalesse	Heike	Luke, E., and Seifert, P.	Phase-partitioning in mixed-phase clouds – An approach to characterize the entire vertical column	AMS 15th Conference on Cloud Physics, 9-13 July, 2018 Vancouver, Canada https://ams.confex.com/ams/15CLOUD15ATRAD/webprogram/Paper344134.html
Seifert	Patric	**Kalesse, H.,** Bühl, J., Radenz, M., Ansmann, A., Baars, H., Engelmann, R., Barja, B., and Zamorano, F.	The DACAPO-PESO Field Experiment: Filling an Observational White Spot on the Globe By Longterm Ground-Based Remote Sensing Observations of Clouds and Aerosols in the Midlatitudes of South America	AMS 15th Conference on Cloud Physics, 9-13 July, 2018 Vancouver, Canada https://ams.confex.com/ams/15CLOUD15ATRAD/webprogram/Paper347227.html
Atlas	Rachel	A. M. Fridlind, D. H. Rind, J. A. Jonas, A. S. Ackerman, **H. Kalesse**, and D. Barahona	Evaluating the Influence of Gravity Waves on Synoptic Cirrus in the ModelE3 Climate Model	AMS 15th Conference on Cloud Physics, 9-13 July, 2018 Vancouver, Canada

				https://ams.confex.com/ams/15CLOUD15ATRAD/webprogram/Paper347232.html
Gatzsche	Katrin	Babel, W., Falge, E., Pyles, R. D., Paw U, K. T., Raabe, A., and Foken, T.	Footprint-weighted tile approach for a spruce forest and a nearby patchy clearing using the ACASA model	Biogeosciences, 15, 2945-2960, https://doi.org/10.5194/bg-15-2945-2018, 2018.
Lochmann	Moritz	Raabe, A.	Dynamik der atmosphärischen Grenzschicht über der Stadt – erste Ergebnisse der Wind-LIDAR-Messungen am Leipziger Institut für Meteorologie,	Mitteil. Inst. f. Meteorol., 56, S. 91-102, 2018 http://nbn-resolving.de/urn:nbn:de:bsz:15-qucosa2-317999

Mitarbeiter am LIM 2018

Name	E-Mail-Adresse
Can, Özge	oezge.can@tropos.de
Carlsen, Tim	tim.carlsen@uni-leipzig.de
Cherian, Ribu	ribu.cherian@uni-leipzig.de
Donth, Tobias	tobias.donth@uni-leipzig.de
Engler, Christa	christa.engler@uni-leipzig.de
Ehrlich, André	a.ehrlich@uni-leipzig.de
Feck-Yao, Wolfgang	feckyao@uni-leipzig.de
Foth, Andreas	andreas.foth@uni-leipzig.de
Geißler, Christoph	christoph.geissler@uni-leipzig.de
Goren, Tom	tom.goren@uni-leipzig.de
Gottschalk, Matthias	matthias.gottschalk@uni-leipzig.de
Jacobi, Christoph	jacobi@rz.uni-leipzig.de
Jäkel, Evelyn	evi.jaekel@uni-leipzig.de
Kaiser, Falk	fkaiser@rz.uni-leipzig.de
Kalesse, Heike	heike.kalesse@uni-leipzig.de
Krisna, Trismono Candra	trismono_candra.krisna@uni-leipzig.de
Kretzschmar, Jan	jan.kretzschmar@uni-leipzig.de
Lauermann, Felix	felix.lauermann@uni-leipzig.de
Lindemann, Simone	simone.lindemann@uni-leipzig.de
Lilienthal, Friederike	friederike.lilienthal@uni-leipzig.de
Lochmann, Moritz	moritz.lochmann@uni-leipzig.de
Mendes de Barros, Kátia	katia.mendes_de_barros@uni-leipzig.de
Mewes, Daniel	daniel.mewes@uni-leipzig.de
Mülmenstädt, Johannes	johannes.muelmenstaedt@uni-leipzig.de
Quaas, Johannes	johannes.quaas@uni-leipzig.de
Raabe, Armin	raabe@uni-leipzig.de
Rehnert, Jutta	rehnert@uni-leipzig.de
Ruiz Donoso, Elena	elena.ruiz_donoso@uni-leipzig.de
Salzmann, Marc	marc.salzmann@uni-leipzig.de
Samtleben, Nadja	nadja.samtleben@uni-leipzig.de
Schandert, Katrin	schandrt@rz.uni-leipzig.de
Schäfer, Michael	michael.schaefer@uni-leipzig.de
Schmidt, Jörg	joerg.schmidt@uni-leipzig.de
Schwarz, Anja	anja.schwarz@uni-leipzig.de
Seydel, Birgit	birgit.seydel@uni-leipzig.de
Sourdeval, Odran	odran.sourdeval@uni-leipzig.de
Sudhakar, Dipu	dipu.sudhakar@uni-leipzig.de
Sun, Bin	bin.sun@uni-leipzig.de
Stapf, Johannes	johannes.stapf@uni-leipzig.de
Vaishnav, Rajesh Ishwardas	rajesh_ishwardas.vaishnav@uni-leipzig.de
Weiße, Frank	weisse@uni-leipzig.de
Wendisch, Manfred	m.wendisch@uni-leipzig.de
Wilsdorf, Michael	mwils@uni-leipzig.de
Wolf, Kevin	kevin.wolf@uni-leipzig.de

Immatrikulationen am Institut f. Meteorologie

BSC Meteorologie

Datum	Semester	1.FS	2. FS	3.FS	4.FS	5.FS	6. FS	7.FS	8.FS	9. FS	10.FS	>10.FS	Meteo_BSC
Datum	Semester	BSC_FS1	BSC_FS2	BSC_FS3	BSC_FS4	BSC_FS5	BSC_FS6	BSC_FS7	BSC_FS8	BSC_FS9			Meteo_BSC
15.10.2018	WS 18/19	48		14		9		5					76
15.10.2017	WS 17/18	37		17		7		5					66
15.10.2016	WS 16/17	48		7		5		3					63
15.10.2015	WS 15/16	35		5		9		3					52
15.10.2014	WS 14/15	35		14		15		3		3		1	71
15.10.2013	WS 13/14	39		23		21		13		4			100
15.10.2012	WS 12/13	60		29	1	22	2	16	1	2			133
15.10.2011	WS 11/12	60		27		26	1	19		1			134
15.10.2010	WS 10/11	64		34		20							118
15.10.2009	WS 09/10	67	0	21	0	20	0						108
15.10.2008	WS 08/09	71	0	28	0	12							111
15.10.2007	WS 07/08	98	0	15									113
13.12.2006	WS 06/07	31											31

MSC Meteorologie

Datum	Semester	1.FS	2. FS	3.FS	4.FS	5.FS	6. FS
Datum	Semester	MSC_FS1	MSC_FS2	MSC_FS3	MSC_FS4	>MSC_FS5	Meteo_MSC
15.10.2018	WS18/19	5		5		9	19
15.10.2017	WS 17/18	5		9		10	24
15.10.2016	WS 16/17	9		13		17	39
15.10.2015	WS 15/16	13		19		18	50
15.10.2014	WS 14/15	19		18		16	53
15.10.2013	Ws 13/14	18		16		20	54
15.10.2012	WS 12/13	18		20	1	15	54
15.10.2011	WS 11/12	21		17		10	48
15.10.2010	WS 10/11	20		9		5	34
15.10.2009	WS 09/10	11					11

Ausbildung Diplom-Meteorologie beendet

Diplom Meteorologie

Datum	Semester	1.FS	2. FS	3.FS	4.FS	5.FS	6. FS	7.FS	8.FS	9. FS	10.FS	>10.FS	Meteo_Diplom
15.10.2013	WS 13/14											2	2
17.10.2012	WS 12/13											3	3
16.10.2011	WS 11/12											3	3
15.10.2010	WS 10/11											14	14
15.10.2009	WS 09/10								0	14	0	7	21
15.10.2008	WS 08/09						0	14	0	23	1	25	63
15.10.2007	WS 07/08				0	22	0	26	1	18	2	19	88
13.12.2006	WS 06/07		0	40	0	36	0	24	2	14	1	17	175
15.10.2005	WS 05/06	109	0	49	0	30	2	16	1	17	1	13	237
08.12.2004	WS 04/05	97	0	35	1	20	0	19	0	12	1	15	200
03.12.2003	WS 03/04	68	1	25	0	20	1	13	1	12	1	13	155
14.10.2002	WS 02/03	45	0	19	0	16	0	15	1	12	1	9	118
06.12.2001	WS 01/02	43	0	21	0	16	0	13	0	7	0	5	105
07.12.2000	WS 00/01	41	1	27	0	22	0	8	0	6	1	6	112
01.12.1999	WS 99/00	40	0	24	0	9	0	9	0	6	1	6	95
16.12.1998	WS 98/99	36	0	11	0	17	1	9	1	5	0	8	88
10.11.1997	WS 97/98	29	0	17	0	10	1	8	0	7	0	4	76

Abschlussarbeiten Institut für Meteorologie 2018

Bachelorarbeiten 2018

Löffelmann, Jana: Analyse von Trends solarer Gezeiten in der mittleren Atmosphäre

Mohr, Max: Trends in Windzeitreihen: Terrestrial Stilling oder Konsequenz steigender Windenergieausnutzung

Masterarbeiten 2018

Lemme, Annceline: Der Vergleich von beobachteten und simulierten Wolkeneigenschaften tropischer Konvektion über dem Atlantik unter Einfluss von Saharaluft

Chevalier Santos Bulhoes, Karine: Aerosol prozesses in the marine boundary layer and free troposphere over the Eastern North Atlantic Ocean during July 2017

Lochmann, Moritz: Dynamik der atmosphärischen Grenzschicht über der Stadt

Löffler, Mareike: Ice Nucleating Particles in the Atlantic Boundary Layer and around Antarctica

Lubitz, Jasmin: Untersuchungen zur Immersionsgefriereffizienz verschiedener Flugaschepartikel

Metzner, Enrico: Role of 'Atlantification' in the Eurasian Basin of the Arctic Ocean on Arctic Amplification

Mewes, Silke: Characterization of aerosol properties by lidar measurements at Haifa, Israel

Mohamdeen, Abdelrhman: Patterns Identification in Micrometeorological Simulations usind EOFs Analysis

Stammer, Peter: Water vapor Retrieval in the upper troposphere and lower stratosphere using airborne spectral solar measuresments of Spectral Solar Irradiance

Strehl, Pit: Ist ein Einfluss auf Wolkeneigenschaften im Luv und Lee von großen urbanen Gebieten in Satellitendaten erkennbar?

Urbanneck, Claudia: Retrieval of aerosol optical and microphxsical properties in Cyprus during A-LIFE and CyCARE by lidar-towards aerosol-cloud interaction investigation (CCNIIN)

Vogl, Teresa: Mix state of the artic sub aerosol

Weger, Michael: The impact of Saharan desert dust on cloud formation: A regional modelling study

Wenke, Marius: Veränderung der klimatischen Bedingungen auf der Grundlage phänologischer Jahreszeiten

Promotionen 2018

Finger, Fanny
Spectral Optical Layer Properties of Cirrus - Collocated Airborne Measurements and Radiative Transfer Simulations

Nair, Aswathy Vijayan
Learning about marine cloud brightening: detectability of field experiments, benefits and risks of implementation

Unglaub, Claudia
Cloud regime based analysis of adjustments to aerosol-cloud interactions using spaceborne measurements

Block, Karoline
Aerosol-Cloud-Radiation interactions in regimes of liquid water clouds

Carlsen, Tim
Influence of snow properties on directional surface reflectance in Antarctica

Schmeißner, Tina
Exploring Mechanisms of Large Droplet Production in Trade Wind Cumuli

Ying, Chen
Abschluss: 10.07.2017
Evaluation and Improvement of Particle Number/Mass Size Distribution Modelling in WRF-Chem over Europe

Foth, Andreas
Abschluss: 10.07.2017
Optimal Estimation of Water Vapour Profiles using a Combination of Raman Lidar and Microwave Radiometer

Merk, Daniel
Abschluss: 24.04.2017
Uncertainties in the Quantification of Aerosol-Cloud Interactions

Bauditz, Stefanie
Abschluss: 27.11.2017
Immersion freezing experiments of biological, mineral dust and dust-bio-mixed particles with the Leipzig Aerosol Cloud Interaction Simulator

Bley, Sebastian
Abschluss: 23.10.2017
Investigation of warm convective cloud fields with Meteosat observations and high resolution models

Wissenschaftliche Mitteilungen aus dem Institut für Meteorologie der Universität Leipzig

Band 1	*A. Raabe, G. Tetzlaff* und *W. Metz* (Edn.), 1995: Meteorologische Arbeiten aus Leipzig I
Band 2	*R. Devantier*, 1995: Wolkenbildungsprozesse über der südwestlichen Ostsee - Anwendungen eines neuen Wolkenschemas in einem mesoskaligen Modell
Band 3	*J. Laubach*, 1996: Charakterisierung des turbulenten Austausches von Wärme, Wasserdampf und Kohlendioxid über niedriger Vegetation anhand von Eddy-Korrelations-Messungen
Band 4	*A. Raabe* und *J. Heintzenberg* (Edn.), 1996: Meteorologische Arbeiten aus Leipzig II
Band 5	Wind- und Seegangsatlas für das Gebiet um Darß und Zingst *D. Hinneburg, A. Raabe* und *G. Tetzlaff*, 1997: Teil I: Windatlas
Band 6	*W. von Hoyningen-Huene* und *G. Tetzlaff* (Edn.), 1997: Sediment and Aerosol Teil I: Beiträge zur Alfred-Wegener-Konferenz, Leipzig 1997 Teil II: Aktuelle Beiträge aus dem Institut für Meteorologie
Band 7	*B.-R. Beckmann*, 1997: Veränderungen in der Windklimatologie und in der Häufigkeit von Sturmhochwassern an der Ostseeküste Mecklenburg-Vorpommerns
Band 8	*P. Posse*, 1997: Bestimmung klimarelevanter Parameter des maritimen Aerosols unter besonderer Berücksichtigung der Nichtkugelform realer Aerosolteilchen
Band 9	*A. Raabe, K. Arnold* und *J. Heintzenberg* (Edn.),1998: Meteorologische Arbeiten aus Leipzig III
Band 10	Wind- und Seegangsatlas für das Gebiet um Darß und Zingst, Teil II, 1998: *D. Hinneburg, A. Raabe* und *G. Tetzlaff*: Vergleich Windatlas –Beobachtungsdaten; *M. Börngen, H.-J. Schönfeldt, F. Riechmann, G. Panin* und *G. Tetzlaff:* Seegangsatlas; *M. Stephan* und *H.-J. Schönfeldt*: Sedimenttransportatlas
Band 11	*J. Rissmann, 1998*: Der Einfluss langwelliger Strahlungsprozesse auf das bodennahe Temperaturprofil
Band 12	*A. Raabe, K. Arnold* und *J. Heintzenberg* (Edn.), 1999:Meteorologische Arbeiten aus Leipzig IV
Band 13	*U. Müller, W. Kuttler und G. Tetzlaff (Edn.)*, 1999: Workshop Stadtklima 17. / 18. 02. 1999 in Leipzig
Band 14	*R. Surkow, 1999*: Optimierung der Leistungsverfügbarkeit von Windenergie durch ihre Integration in Wind-Biogas-Hybridanlagen
Band 15	*N. Mölders,* 1999: Einfache und akkumulierte Landnutzungsänderungen und ihre Auswirkungen auf Evapotranspiration, Wolken- und Niederschlagsbildung
Band 16	G. Tetzlaff und U. Grünewald (Edn.), 1999:2. Tagung des Fachausschusses Hydrometeorologie 15./16. 11. 1999 in Leipzig
Band 17	A. Raabe und K. Arnold (Edn.), 2000: Meteorologische Arbeiten aus Leipzig V
Band 18	K. Arnold, 2000: Ein experimentelles Verfahren zur Akustischen Tomographie im Bereich der atmosphärischen Grenzschicht
Band 19	*A. Ziemann*, 2000: Eine theoretische Studie zur akustischen Tomographie in der atmosphärischen Grenzschicht
Band 20	*Ch. Jacobi*, 2000: Midlatitude mesopause region dynamics and its coupling with lower and middle atmospheric processes
Band 21	*M. Klingspohn*, 2000: Interdekadische Klimavariabilität über dem Nordatlantik – Statistische Analysen und Modellstudien –
Band 22	*A. Raabe* und *K. Arnold* (Edn.), 2001: Meteorologische Arbeiten aus Leipzig VI
Band 23	*K. Arnold, A. Ziemann, G. Tetzlaff, V. Mellert* und *A. Raabe* (Edn.), 2001: International Workshop Tomography and Acoustics: Recent developments and methods 06. - 07.03.2001 in Leipzig
Band 24	*O. Fanenbruck*, 2001: Ein thermophysiologisches Bewertungsmodell mit Anwendung auf das Leipziger Stadtgebiet
Band 25	*M. Lange*, 2001: Modellstudien zum CO_2-Anstieg und O_3-Abbau in der mittleren Atmosphäre und Einfluss des Polarwirbels auf die zonale Symmetrie des Windfeldes in der Mesopausenregion
Band 26	*A. Raabe* und *K. Arnold* (Edn.), 2002: Meteorologische Arbeiten aus Leipzig VII
Band 27	*M. Simmel*, 2002: Ein Modul zur spektralen Beschreibung von Wolken und Niederschlag in einem Mesoskalenmodell zur Verwendung auf Parallelrechnern
Band 28	*H. Siebert*, 2002: Tethered-Balloon Borne Turbulence Measurements in the Cloudy Boundary Layer
Sonderband	*G. Tetzlaff* (Hrsg.), 2002:- Atmosphäre - Aktuelle Beiträge zu Luft, Ozon, Sturm, Starkregen und Klima
Band 29	*U. Harlander*, 2003: On Rossby wave propagation in atmosphere and ocean
Band 30	*A. Raabe* und *K. Arnold* (Edn.), 2003: Meteorologische Arbeiten aus Leipzig VIII
Band 31	*M. Wendisch*, 2003: Absorption of Solar Radiation in the Cloudless and Cloudy Atmosphere
Band 32	*U. Schlink*, 2003: Longitudinal Models in Biometeorology: Effect Assessment and Forecasting of Ground-level Ozone
Band 33	*H. Heinrich*, 2004: Finite barotrope Instabilität unter synoptischem Antrieb
Band 34	*A. Raabe* und *K. Arnold* (Edn.), 2004: Meteorologische Arbeiten aus Leipzig IX

Band 35 *C. Stolle*, 2004: Three-dimensional imaging of ionospheric electron density fields using GPS observations at the ground and on board the CHAMP satellite

Band 36 *A. Raabe* und *K. Arnold* (Edn.), 2005: Meteorologische Arbeiten (X) und Jahresbericht 2004 des Institutes für Meteorologie der Universität Leipzig

Band 37 *A. Raabe* und *K. Arnold* (Edn.), 2006: Meteorologische Arbeiten (XI) und Jahresbericht 2005 des Institutes für Meteorologie der Universität Leipzig

Band 38 *K. Fröhlich,* 2006: The Quasi Two-Day Wave – its impact on zonal mean circulation and wave-wave interactions in the middle atmosphere

Band 39 *K. Radtke*, 2006: Zur Sensitivität von Starkwindfeldern gegenüber verschiedenen meteorologischen Parametern im Mesoskalenmodell LM

Band 40 *K. Hungershöfer,* 2007: Optical Properties of Aerosol Particles and Radiative Transfer in Connection with Biomass Burning

Band 41 *A. Raabe* (Hrsg.), 2007: Meteorologische Arbeiten (XII) und Jahresbericht 2006 des Institutes für Meteorologie der Universität Leipzig

Band 42 *A. Raabe* (Hrsg.), 2008: Meteorologische Arbeiten (XIII) und Jahresbericht 2007 des Institutes für Meteorologie der Universität Leipzig

Band 43 *A. Kniffka, 2008*: Einfluss der Inhomogenitäten von Aerosol, Bodenalbedo und Wolken auf das aktinische Strahlungsfeld der Atmosphäre

Band 44 *M. Barth, 2009*: Akustische Tomographie zur zeitgleichen Erfassung von Temperatur- und Strömungsfeldern

Band 45 *A. Raabe* (Hrsg.), 2009: Meteorologische Arbeiten (XIV) und Jahresbericht 2008 des Institutes für Meteorologie der Universität Leipzig

Band 46 *G. Stober, 2009:* Astrophysical Studies on Meteors using a SKiYMET All-Sky Meteor Radar

Band 47 *A. Raabe* (Hrsg.), 2010: Meteorologische Arbeiten (XV) und Jahresbericht 2009 des Institutes für Meteorologie der Universität Leipzig

Band 48 *A. Raabe* (Hrsg.), 2011: Meteorologische Arbeiten (XVI) und Jahresbericht 2010 des Institutes für Meteorologie der Universität Leipzig

Band 49 *A. Raabe* (Hrsg.), 2012: METTOOLS_VIII Tagungsband

Band 50 *A. Raabe* (Hrsg.), 2012: Meteorologische Arbeiten (XVII) und Jahresbericht 2011 des Institutes für Meteorologie der Universität Leipzig

Band 51 *A. Raabe* (Hrsg.), 2013: Meteorologische Arbeiten (XVIII) und Jahresbericht 2012 des Institutes für Meteorologie der Universität Leipzig

Band 52 *A. Raabe* (Hrsg.), 2014: Meteorologische Arbeiten (XIX) und Jahresbericht 2013 des Institutes für Meteorologie der Universität Leipzig

Band 53 *A. Raabe* (Hrsg.), 2015: Meteorologische Arbeiten (XX) und Jahresbericht 2014 des Institutes für Meteorologie der Universität Leipzig

Band 54 *A. Raabe* (Hrsg.), 2016: Meteorologische Arbeiten (XXI) und Jahresbericht 2015 des Institutes für Meteorologie der Universität Leipzig

Band 55 *A. Raabe, M.Wendisch* (Hrsg.), 2017: Meteorologische Arbeiten (XXII) und Jahresbericht 2016 des Institutes für Meteorologie der Universität Leipzig

Band 56 *A. Raabe, M.Wendisch* (Hrsg.), 2018: Meteorologische Arbeiten (XXIII) und Jahresbericht 2017 des Institutes für Meteorologie der Universität Leipzig

Band 57 *A. Raabe, M.Wendisch* (Hrsg.), 2018: Meteorologische Arbeiten (XXIV) und Jahresbericht 2018 des Institutes für Meteorologie der Universität Leipzig